# Shocked Molecular Hydrogen in the Orion "Bullets"

Jonathan Andrew Tedds

Presented for the Degree of Doctor of Philosophy
at the University of Edinburgh
1996

This thesis is solely my own composition, except where specifically indicated in the text.

Jonathan A. Tedds,
November 1996.

# Acknowledgments

First and foremost, I thank Peter Brand for providing enough scientific inspiration for life and for his unstinting help and support at all times, not to mention beers! I also wish to remember Franz Kahn at the University of Manchester for his faith in my ability which was greatly valued. Invaluable assistance was often sought and always reciprocated by Michael Burton, Antonio Chrysostomou and Amadeu Fernandes. Back at base, from day one, always willing to help were UKIRT and CGS4 experts Suzie Ramsay-Howat and Phil Puxley, not to mention Starlink software expert Horst Meyerdierks, whose patience in navigating me through the trickier elements of computer world (da-da da-dah-da..) was invaluable. Tom Geballe, Gillian Wright, Thor Wold, Dolores Walter, Tim, Frossie and the rest of the UKIRT crew helped to make each observing trip in Hawaii better than the last. I thank my second supervisor David Emerson for his friendly support and encouragement throughout.

I count myself extremely fortunate to have studied at the University of Edinburgh within such a fine institution as the Royal Obsevatory Edinburgh. For the breadth of expertise from cutting-edge development of instrumentation to the finest theoretical wanderings, there can be few places to match it. Long may it continue. It is a wonderful place to work and who better to work, rest and play with than my friends and office-mates Thackers (Andrew Thackrah), Maccas (Steve McNally) and Harry (Andrew Harrison); Henry Buckley for musical and theoretical fiddling, Rob Ivison for being fair to piddling, Eelco van Kampen for flying through the middle and Elspeth Minty on the Jimmy riddle; Mike Hawkins for saying the wrong thing at the right time and introducing me to the pleasures of sailing on the Forth; Liz Gibson (astronomy), Alan Heavens, John Peacock, John Cooke, Mark Casali, John Barrow, Andy Longmore, Sue Tritton and the ROE Visitor Centre; Andy Taylor, Hugh Jones, Phil James; Shona, Sally, Angus and Sarah in the library; Aberdeen Bill and Scott "Finney" at the lodge; Alistair "Murphys" Glasse, Mike "Thunderbolt" Read, James "Brassneck" Dunlop and Kenny "McCoist" Laidlaw and co for Portybelly specials; Mike McCartney: somewhere, out there..., Rachel 'Lovely' Johnson, Alison, Bill, Richard, Han Ying, Elese, Jo, Helen, Ross and the student faction.

School days are warmly remembered and relevant to this tale. As are the Heavenly views of the Ribble Valley, Lancs. So let the tales begin: Once upon a time there was a little village school called Linthurst in Blackwell; then Colmore Juniors and King Edward VI Five Ways Grammar School, Birmingham. All deserve thanks for helping to steer me through the finest education a man could wish for. Individual thanks to Mr Holmes, Mrs Sandra Maycock, Mrs Saville, Geoff Sanders, DATMAN, Obi-one Ken Oakley, Peter Hall, Dai Hughes and Billy Preston.

Love and thanks to Mum and Dad who have always encouraged me to follow my dreams and supported me in doing so! My Dad has helped me more than all the above put together and for as long as I can remember, sharing it all with me ever since. By 'eck, thaz a rum'n. My mum is brill and that's all there is to it (not to mention considerably better at remembering things than me). Brother and best friend Dan and sister Jane (let me know when I get back to Planet Earth!) and their young families, not forgetting the love and support of my Grandparents. Friend since schooldays and fellow Edinburgh PhD Graham Smith; Christina and Jo Prescott; Amanda Carter, Floss, Chris Scudds aie the Glasgae/Embra mob - life's a breeze with cheesy peas..., Sandra Gadd, Steve Bond (raincoat), Gail Nolan, Abina Crean, Fiona Mitchell, Flo Bonjean. Greetings to the and THE Manchester United, especially Adrian Sach, Perry Harper, Neil Othen, Jim, Kathy Romer, Olli in Hamburg and la musica electronica; back in Brum, Rich Shardlow and Karen, Steve and Liz Bailey, Margerat Schellenberg for piano and life as fun fun fun!; Brighton belles KT, Nicky, Ros, Rich Graves and Kathryn in DC, Thanasis, Julia and last, but not least, Miss Stephanie Dawson; lifelong friend Graeme Daniels and family in San Fran, not forgetting Karin and Ingeberg in Berlin.

I would like to acknowledge HMG of the UK via PPARC, SERC and elsewhere as I have regarded it as a great privilege to be funded to pursue this astronomical research. Cheers!

# Abstract

The physics of shocked outflows in molecular clouds is one of the fundamental astrophysical processes by which the cycle of star formation in our Galaxy is regulated. I outline the basis of our understanding of the star formation process and the violent outflow always associated with it, the physics of shocks in molecular gas, and the consequent excitation of molecular hydrogen ($H_2$). It is demonstrated that molecular hydrogen is the best observational diagnostic of this hot, shocked molecular gas and an introduction is given to the observational techniques of near-infrared spectroscopy required in its measurement. I describe a detailed observational study of the physics of shocked $H_2$ excitation and dynamics in the nearby massive star forming region of the Orion giant molecular cloud, the brightest source of its type, using the recently upgraded CGS4 near-IR spectrometer at UKIRT.

We have demonstrated that integrated [FeII] 1.644$\mu$m line profiles in the Orion "bullets" are consistent with theoretical bow-shock predictions for two different "bullets". We have identified a uniform, broad background component pervading the region in both $Fe^+$ and $H_2$ which is inconsistent with a fluorescent component due to the ionizing radiation of the Trapezium stars alone. A collisionally broadened background component of unidentified origin is measured to be Gaussian in profile with an average FWHM of $26\pm2.5 kms^{-1}$ in the $H_2$ 1-0 S(1) line after deconvolution of the instrumental profile and a peak velocity of $2.5\pm0.5 kms^{-1}$, close to the local ambient rest velocity. Crucially, the extended $H_2$ "bullet" wakes have allowed us to dissect individual molecular bow shock structures but the broad (intrinsic FWHM$\leq 27 kms^{-1}$), singly-peaked $H_2$ 1-0 S(1) profiles observed in the two most clearly resolved, plane-of-sky oriented wakes challenge our present understanding. It is very difficult to reconcile *any* steady-state molecular bow shock model with these observations in Orion. To fit a single C shock absorber model to individual $H_2$ profiles implies a magnetic field strength far in excess of observed estimates and is not consistent with the bow-shaped wake morphology.

Alternatively, we may still not be resolving multiple $H_2$ shock fronts along the line-of-sight. For example, multiple overlapping bullet wakes could give rise to merged sets

of doubly-peaked profiles resulting in approximately Gaussian shaped profiles. However, given the appearance of single bow shaped wakes at many observed positions, the accuracy of single Gaussian line-fits, the velocity resolution of our observations (FWHM=23.1±0.3kms$^{-1}$) and that we see this phenomenon in *two* different wakes, this explanation is expected to be excluded.

If we cannot fit the profiles in Orion with steady state molecular shocks it may be necessary to model the effects of instabilities and turbulence. This will have important consequences. Not only will line profiles be broadened but level populations of shocked species will be altered and hence the observed column densities over a range of transitions.

Observations of a range of $H_2$ column densities in the K band have confirmed the existence of a near-constant background excitation mechanism pervading the entire Orion "bullets" region. The background $H_2$ emission can be modelled by a combination of fluorescent and shock excited mechanisms, in agreement with the broad $H_2$ line profiles observed. It is thermalized in the $v$=1 levels but higher levels are dominated by fluorescence. Measurement of the $H_2$ excitation in the "bullet" wakes M42 HH126-053 and M42 HH120-114 shows a near constant emission spectrum, within each wake, that may be modelled by a combination of shocked and fluorescent excitation, now more strongly dominated by collisional processes but also containing an intrinsic wake-only fluorescent component. The column density ratios clearly show a range of gas temperatures as expected for cooling, post-shock gas. Furthermore, the uniformity of these ratios on small-scales (these observations) and also on large scales, contradicts combinations of fundamentally different types of shock. However, the near constancy of this excitation with position *within* each individual wake is inconsistent with bow C shock models previously fitted at OMC-1, in which significantly different line ratios occur depending on the shock velocity which varies in the bow.

# Contents

# Chapter 1

# Introduction

The purpose of this thesis is to investigate the physics of shocked outflows in molecular clouds, one of the fundamental astrophysical processes by which the cycle of star formation in our Galaxy is regulated. In this chapter I outline the basis of our understanding of the star formation process and the importance of understanding the outflow stage always associated with it. In Chapter 2, I then summarise current theoretical understanding of the physics of shocks in molecular gas caused by outflows and the consequent excitation of molecular hydrogen by which we observe the process. It will be demonstrated that molecular hydrogen is the best observational diagnostic of this hot, shocked molecular gas and an introduction is given to the observational techniques of near-infrared spectroscopy required in its measurement. In Chapters 3 and 4 I describe a detailed observational study of the physics of shocked $H_2$ excitation and dynamics in the nearby massive star forming region of the Orion giant molecular cloud, the brightest source of its type. I present the first such measurements of the molecular shocks in the newly identified bow-shaped "wake" structures associated with the Orion "bullets". In Chapter 5 I summarise the conclusions of these studies and outline the implications for our understanding of molecular cloud physics in Orion. Finally, an outline of future intentions and associated observations required to further this work is provided.

## 1.1 Star Formation

The youngest stars are observed to have formed in dense, molecular clouds of interstellar gas and dust. An understanding of this most fundamental of astronomical processes has remained elusive because young protostars themselves are extremely difficult to identify unequivocally, embedded as they are in the densest regions of molecular clouds, impeding direct observation.

Infra-red and radio emission, for which optical depths are low enough to permit radiation to escape from molecular clouds, have demonstrated that this protostar phase is but one part of the full cyclic and multiply-fed-back system which regulates the conversion of gas to stars, as summarised by McKee (1989). The cycle begins with the aggregation of molecular clouds, perhaps triggered by supernova blasts of previously fragmented clouds and intercloud material. Star formation is envisaged to begin when giant molecular clouds, supported by magnetic fields and internal energy sources, can collapse to dense cores where ionization is low enough that ambipolar diffusion may proceed, *i.e.* neutral material can contract gravitationally to a protostar since angular momentum is dissipated via ion-magnetic field interactions to the surrounding cloud (Alfvén waves). The timescale for this process is of the order of $10^7$ years.

Consequent contraction of the cloud increases the fraction of the cloud susceptible to collapse due to the associated increase in optical depth lowering ionization rates. However, observations of rapidly-moving and shocked gas suggest that all forming stars produce a molecular outflow (Lada 1985) which re-energises the cloud and therefore acts against cloud contraction. Hence, a balance between collapse and expansion emerges determining a steady rate of star formation. The creation of massive OB ($\geq 10 M_{\odot}$) stars and an associated ionised hydrogen (HII) region will, however, rapidly erode the remaining cloud (Whitworth 1979). Such regions are indeed observed and when built into a cyclic scheme can give satisfactory agreement with the overall, observed galactic rate of star formation.

Clearly, to determine more accurately the conditions under which a star is born and hence be able to extrapolate to different situations (*e.g.* elliptical galaxies and the early

universe), we must derive diagnostic measures of the protostellar environment. These phenomena occur at large visual optical depths and therefore only infrared (IR) and radio techniques are useful. Advances in IR detection technology, particularly the advent of efficient and many-pixelled arrays sensitive to radiation in the 1-5 $\mu$m wavebands, has now advanced the observational astronomy at these wavelengths to levels of sophistication previously only possible at optical wavelengths.

## 1.2 Clouds

Molecular clouds exist where UV starlight is sufficiently extinguished that molecules, in particular $H_2$, can form. The extinction of starlight is a consequence of the scattering and absorption of starlight by dust grains in the interstellar medium. It is expressed in terms of the intensity of light reaching the observer ($I_{obs}$) compared with the observed intensity if the line of sight were dust free ($I_0$)

$$I_{obs} = I_0 e^{-\tau_\lambda} \tag{1.1}$$

where $\tau_\lambda$ is referred to as the optical depth. The observed form of the extinction law for wavelengths from 0.002$\mu$m to 250$\mu$m is shown in Figure 1.1 (Mathis 1990), with the extinction displayed in magnitudes ($A_\lambda = 1.086\tau_\lambda$) as a fraction of the visual extinction at ~6000Å. It is immediately apparent that the extinction at near-infrared (NIR) wavelengths, $\lambda \simeq$1-5$\mu$m , is greatly reduced compared to at visual wavelengths. Thus, highly obscured star forming regions within molecular clouds can be observed in the infrared, making this the ideal waveband for studies of embedded sources such as protostars (Rayner *et al.* 1990).

The existence of molecular clouds when $A_V > 1$ was confirmed observationally by Spitzer *et al.* (1973) who measured the atomic/molecular hydrogen fractions of diffuse clouds in front of bright stars via UV absorption using the *Copernicus* satellite. They are typically located throughout the disk of our Galaxy, although warm clouds containing IR sources usually reside in spiral arms like HII regions (Solomon *et al.* 1985). A typical giant molecular cloud (GMC) has mass in the range $10^3 M_\odot < M < 10^6 M_\odot$ and size

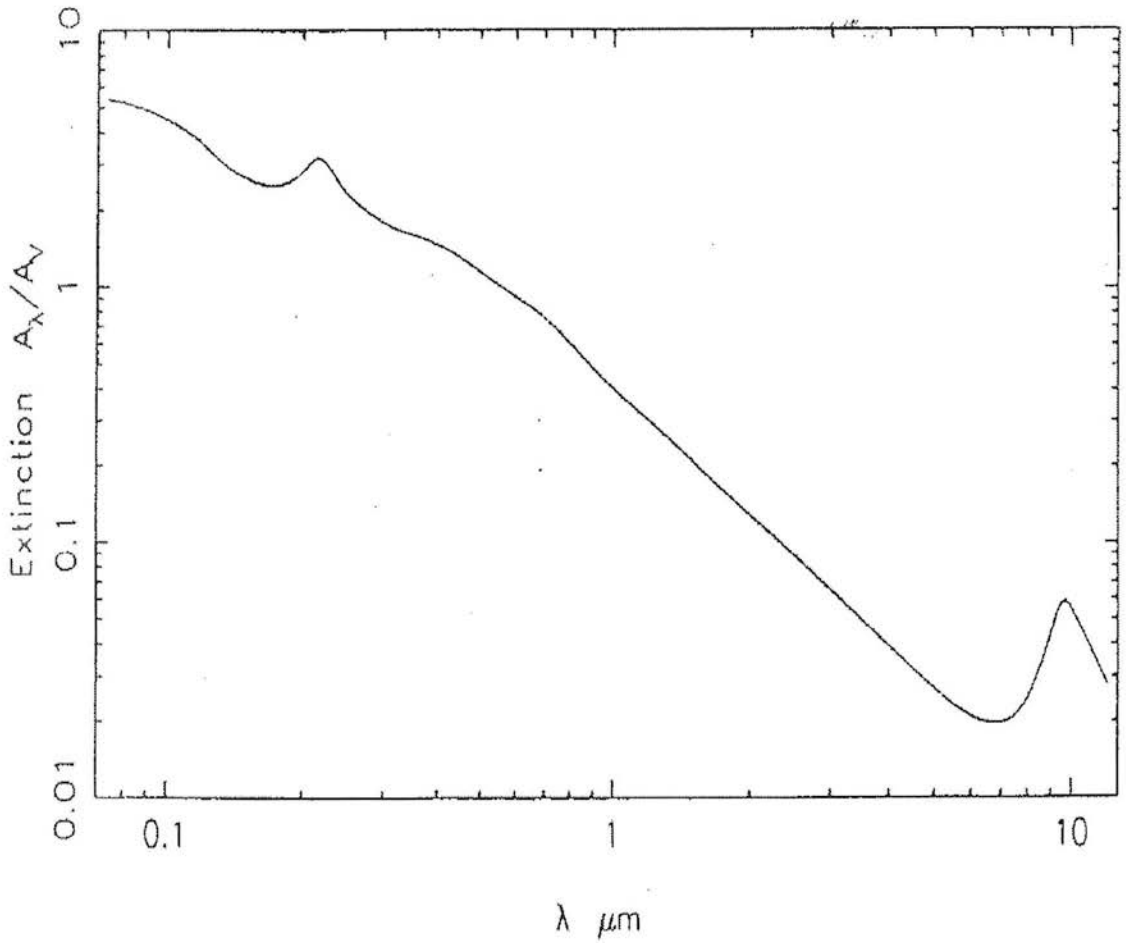


Figure 1.1: Extinction (relative to visual extinction) due to interstellar dust as a function of wavelength (Mathis *et al.* 1990), illustrating the advantages of near infrared astronomy ($\lambda \simeq$1-5$\mu$m ) over optical astronomy for observing obscured sources.

$1pc < R < 100pc$. They are known to be the sites of star formation in the Galaxy yet the gravitational collapse time of the clouds has to exceed their free fall time in order that the star formation rate be as low as is observed (Zuckerman and Palmer 1974). We wish to elucidate the processes responsible for supporting the clouds against gravitational collapse and hence regulating the star formation process. The observed line widths in such regions are generally highly supersonic and must be turbulent since these motions cannot be due to cloud collapse alone (Zuckerman and Evans 1974).

### 1.2.1 Properties of Molecular Clouds

The basic relations observed for mass($M$), size($R$) and velocity dispersion of molecular clouds extend over six orders of magnitude in mass and include clumps within clouds. They are summarised by Larson (1981) as follows:

1. Clouds are in approximate virial equilibrium

$$\sigma^2 \propto \frac{GM}{R}, \tag{1.2}$$

where $\sigma$ is the one-dimensional velocity dispersion and $G$ is the gravitational constant;

2. line width increases with size according to the relation

$$\sigma \propto R^p, \tag{1.3}$$

where $p \simeq 0.38$;

3. mean density decreases with size

$$\overline{n}_{\rm H} \propto R^{-q}, \tag{1.4}$$

where $q \simeq 1.1$, such that the column density

$$N_{\rm H} = \frac{4}{3}\overline{n}_{\rm H} R \tag{1.5}$$

is approximately constant.

These relations were subsequently confirmed to within factors of 3 in the coefficients and 0.3 in the exponents (Myers 1985). To understand the structure of molecular clouds and star formation it is clearly necessary to explain the line-width size relation (1.3), as illustrated in Solomon *et al.* (1987). Interestingly, the equivalent constancy of the column density (1.5) is naturally explained if the clouds are supported against gravitational collapse by magnetic fields of order $30\mu$G (e.g. Shu 1987). We will see that magnetic fields may also crucially influence the structure of molecular shock fronts in such regions (Chapter 2.2).

### 1.2.2 Gravitational Collapse and the Influence of Magnetic Fields

Larson (1969) and later Shu (1977) modelled the gravitational collapse of a singular isothermal cloud resulting in a theoretical Jeans mass for the cloud. The Jeans wavenumber of a perturbation is

$$k_J = 2\pi/\lambda_J = \sqrt{4\pi G\rho_0}/v_s, \tag{1.6}$$

where $\lambda_J$ is the Jeans wavelength, $\rho_0$ is the initial cloud density and $v_s$ is the sound speed. The resultant Jeans mass is the mass inside a volume $\lambda_J^3$ and is consistent with stellar values. However, it was recognised that the initial conditions, although in equilibrium, are highly unstable.

Following from the initial work of Mestel & Spitzer (1956) on magnetic fields and star formation in molecular clouds, the effects of stresses exerted by magnetic fields were considered. This includes a pressure term ($B^2/2\mu_0$) perpendicular to the field lines and tension ($B^2/2\mu_0$) parallel to them, where $B$ is the magnetic field strength and $\mu_0$ is the permeability of free space. Interstellar magnetic fields are difficult to measure, but observed Zeeman splitting of the 21cm line of atomic H and of the 18cm transitions of OH (Heiles *et al.* 1993) suggests that interstellar magnetic fields in clouds vary approximately as

$$B \propto (n_H)^{\frac{1}{2}}. \tag{1.7}$$

In molecular cloud conditions, these field lines are effectively "frozen in" to the ionized gas. A field distorted perpendicular to the field lines generates *Alfvén* waves of velocity

$$v_A = \sqrt{B^2/\mu_0\rho} \approx 1 - 3\mathrm{kms}^{-1}. \tag{1.8}$$

Conversely, compressive waves travelling perpendicular to the field lines are *magnetosonic* waves of velocity $v_{MS} = v_A$. If such magnetic stresses dominate, energy and information are transported by Alfvén and magnetosonic waves, while if thermal stresses dominate, sound waves are the carriers. The criterion is

$$p_B/p_{\mathrm{thermal}} = (v_A/v_s)^2. \tag{1.9}$$

Therefore magnetic stresses will dominate if the Alfvén velocity is large.

If magnetic fields provide the majority of the pressure preventing gravitational collapse of a cloud of ionized gas, a *critical mass*

$$M_{crit} \simeq \Phi/\sqrt{\mu_0 G}, \tag{1.10}$$

may be determined above which a cloud must collapse in gravitational freefall, where $\Phi$ is the flux of order $BR^2$. Clouds of lower mass are supported against such collapse. If the gas is only partially ionized then, as only the ions will be frozen to the field lines, the neutrals will be constrained to move with the ions by collisions. If the magnetic field supports the ionized gas against gravity then neutrals are pulled to the centre in preference to the ions and a slow drift of the neutrals relative to the ions called *ambipolar diffusion* results. The timescale for this process ($t_{AD}$ in seconds) is independent of the mass and size of the cloud but depends on the degree of ionization, $x_e$, only:

$$t_{AD} \sim 10^{14} x_e. \tag{1.11}$$

This leads eventually to the situation where the combined forces of magnetic fields and gas pressure can no longer resist the inward gravitational pull of the central concentration of material so that the inner portion of the cloud collapses. Furthermore, since a majority of observed stars are members of binary or triple systems, it is possible that the cloud decouples from the magnetic field when enough angular momentum has been transferred outwards in order that multiple star systems or single stars with planetary systems may then form.

It is possible to model such molecular clouds by polytropes (Maloney 1988, Elmegreen 1989), in which the total pressure in the cloud $p$ (both thermal and turbulent) is assumed to vary as a power of the density ($\rho$),

$$p \propto \rho^{\gamma_p} \tag{1.12}$$

where $\gamma_p$ is the polytropic index (of value unity for an isothermal sphere). Both Elmegreen (1989) and Fleck (1988) successfully incorporated magnetic fields into the isothermal

cloud model. However, polytropic models do not enable us to determine what provides the energy for the cloud motions and how the cloud evolves.

### 1.2.3 Photoionization-regulated Star Formation

McKee (1989) tackled these problems by advancing an elegant model of photoionization-regulated star formation in which the rate of low-mass star formation is governed by ambipolar diffusion in magnetically supported clouds and therefore depends on the ionization of the cloud. He showed that this ionization is due to photoionization by the far-ultraviolet (FUV) radiation field, not to cosmic rays. Hence, the rate of low-mass star formation depends on the attenuation of this radiation by dust and will be related to clump density.

Interstellar clouds grow through coalescence (Field and Saslaw 1965) by cloud-cloud collisions and accretion of intercloud material. They become predominantly molecular when the extinction $A_V$ becomes of order unity (Elmegreen 1985a). The ionization within such clouds is maintained at a relatively high level by the FUV interstellar radiation field which suppresses ambipolar diffusion and inhibits low-mass star formation (Nakano 1984; Shu, Adams and Lizano 1987). Molecular clouds contract to higher column density as the internal motions which support them are dissipated through shocks (Scalo and Pumphrey 1982) and the damping and radiation of Alfvén waves (Elmegreen 1985b). As individual clumps contract, a larger fraction of their mass is shielded from the external FUV radiation field and so ambipolar diffusion can proceed and allow star formation. Once formed, such stars inject energy back into the clouds and when $A_V \sim 4-8$, the rate of energy injection is sufficient to stop the contraction of the clouds. In addition, massive stars formed in associations must disrupt the cloud in which they are located (Field and Saslaw 1965; Whitworth 1979). In the extreme, hot OB stars form and generate photons capable of ionizing atomic hydrogen and rapidly ending further star formation in the parent molecular cloud.

Alternative scenarios to the McKee picture have been proposed including a model by Silk & Norman (1983) in which pre-main sequence X-ray emitting stars observed in molecular clouds provide the bulk of the ionization regulating star formation. Mouschovias

(1991 and references therein) describes a numerical treatment of ambipolar diffusion and Alfvén wave damping during cloud contraction as opposed to the semi-analytical approach, initially without magnetic fields, by Shu (1977) described previously. Shu *et al.* (1987) describe neutral material drifting through the magnetic field under gravity and being left with residual angular momentum. When the resultant centrifugal force becomes equal to gravity the collapse is halted. The characteristic radius at which this occurs denotes the size of an *accretion disc* oriented perpendicular to the angular momentum vector. Matter circulates within this disc but viscous stresses gradually move matter inwards whilst transferring angular momentum outwards (Lynden-Bell and Pringle 1974) leading to the growth of a slowly rotating core. This central core asymptotically approaches a singular isothermal sphere without ever reaching it (as such an end state is unstable) and is transparent to its own thermal radiation. Therefore it may be modelled in hydrostatic equilibrium ( radius $r$) with the simple solution

$$\rho \propto r^{-2}. \tag{1.13}$$

When the core exceeds the Jeans mass it collapses, "inside out", and sends a rarefaction shock outwards through the surrounding layers. Infalling matter must pass through an accretion shock as it falls onto the central star. Together with accretion within the disc this provides the main source of luminosity for low-mass protostars and is in agreement with mid and far infrared observations of a steeply negative curve in the spectral energy distribution of the reprocessed light (Lada 1991). Submillimetre observations (reviewed by André 1995) of an initial "Class 0" protostellar state, at which there is virtually no emission at wavelengths shorter than $\sim 10\mu$m, is consistent with a single blackbody at $T \sim 15 - 30$K. However, recent observations of flat-topped density profiles in pre-stellar cores (André *et al.* 1996) may indicate the singular isothermal sphere assumption to be invalid. In the central core itself, where thermal pressure balances gravity, the core evolves towards the main sequence. We now discuss the corresponding outflow generated during this evolution.

## 1.3 Supersonic Motions and Winds From Young Stars

We have seen that newly formed stars inject energy into molecular clouds via photoionization. We now discuss the injection of energy via winds from newly forming stars which must act in concert with photoionization mechanisms to regulate the structure of molecular clouds. We wish to determine the effect of this energy injection on the evolution of star forming molecular clouds.

Shu *et al.* (1987) review the observational evidence, including direct observations of disks around young stellar objects and the interpretation of the infrared spectra of many young stellar objects, that implies stars form in a state of rapid rotation. However, observations of the relatively slow rotation rates of (recently formed) T Tauri stars (Vogel and Kuhi 1981; Hartmann *et al.* 1986) imply that the star formation process must entail the release of large quantities of kinetic energy. Norman and Silk (1980) suggested that winds from young stars, particularly T Tauri stars, could inject enough energy into the ambient molecular cloud to prevent its collapse. The subsequent discovery of highly energetic outflows from young stellar objects (see review of Lada 1985) strengthened the possibility of regulating the star formation rate by this mechanism (Franco and Cox 1983). Outflows appear to be driven by strong stellar winds and are directly related to the rapidly moving Herbig-Haro (HH) objects, high velocity water maser sources, shock-excited molecular hydrogen emission regions and optically visible jets appearing to emanate directly from the circumstellar material of the young driving stars.

In the picture of Shu *et al.* (1987), as a protostar accretes matter the convection and differential rotation of the star may combine to produce a dynamo and the star can naturally evolve towards a state with a stellar wind. Infalling material suppresses initial breakout but, as it falls preferentially onto the disk rather than the star, the stellar wind will rush through the channels of weakest resistance at the rotational poles resulting in collimated jets and bipolar outflows. The underlying processes that may trigger such stellar winds are little understood. Rather, theorists have concentrated their efforts on the more tractable problems of the interaction of such a wind with the molecular cloud and the nature of the resultant molecular outflows.

Initially, in the early 1970s, molecular outflows were traced by carbon monoxide (CO) emission which, although second to hydrogen ($H_2$) in abundance (by mass), is an asymmetric molecule which emits dipole radiation and as such is more easily observed than $H_2$. Having no permanent dipole moment, $H_2$ emits only via faint electric quadrupole transitions and is excited only in very hot regions (see Chapter 2.1). At this time the astronomical technology for observing the near infrared transitions of excited molecular hydrogen was in its infancy.

The first indications of the dynamical state of gas in a molecular cloud were deduced by measuring the full width at half maximum intensity (FWHM) of molecular emission line profiles, using the $J = 1 - 0$ $^{12}$CO line profile for example (Lada 1985). In a GMC, such line widths are typically between 1 and 3 $\mathrm{km\,s^{-1}}$. Temperatures derived from CO and $NH_3$ observations are typically around 10K. Yet the sound speed in such a cold gas is $< 1$ $\mathrm{km\,s^{-1}}$, much less than the observed line widths. A fundamental feature of molecular clouds is therefore that of supersonic motions dominating the dynamics. Indeed, in regions of active star formation, localized gas motions are often observed with line widths of up to $8\mathrm{km\,s^{-1}}$ and were initially interpreted as being related to cloud collapse (Goldreich and Kwan 1974). Then, in 1975, the $^{12}$CO emission line in Orion was measured and found to show wings extending over $150\mathrm{km\,s^{-1}}$ full-width at zero intensity (FWZI) within $1^{\circ}$ centred on an embedded cluster of infrared sources (Kwan and Scoville 1976; Zuckerman *et al.* 1976). It was realised that localised, supersonic molecular gas flows of this magnitude were too fast to be explained by collapse or any other gravitationally induced motion and the almost simultaneous discovery of shock-excited molecular hydrogen in the same region (Gautier *et al.* 1976) confirmed that an energetic outflow of some form must be responsible. Within ten years well over sixty other localized high velocity molecular flows had been confirmed (e.g. Bally and Lada 1983) and it was clear that these were as fundamental to a molecular cloud as the overall supersonic bulk motions discovered previously.

As more sources were detected and measured in more dynamical detail, it emerged that such high velocity flows tended to be bipolar (e.g. Snell *et al.* 1980), consisting of two spatially separate lobes of emission. One lobe containing predominantly blueshifted gas and the other predominantly redshifted gas are oriented symmetrically about an

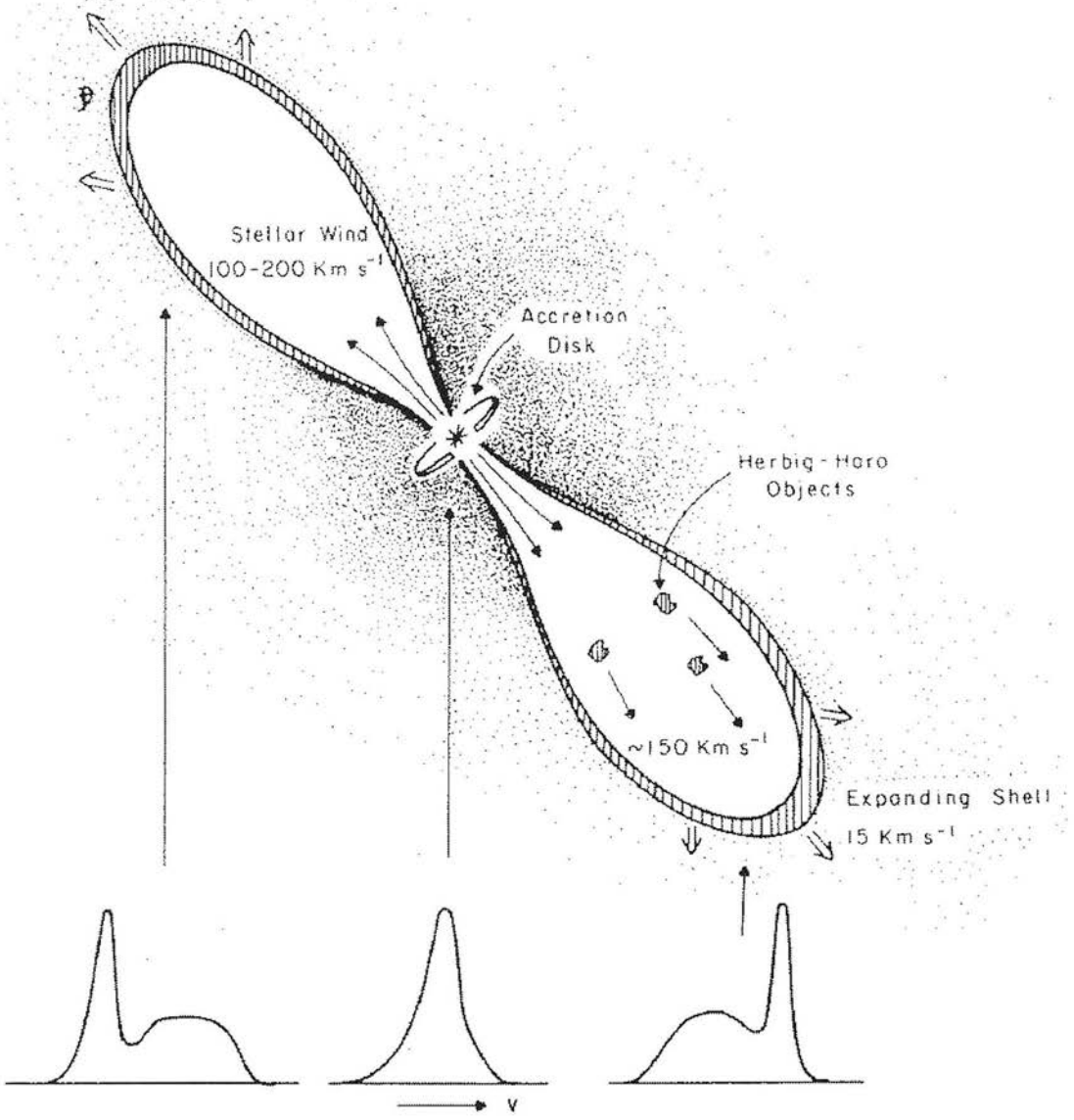


Figure 1.2: A schematic picture of a bipolar outflow and associated Herbig-Haro objects driven by protostellar outflow in the source L1551 from Snell *et al.* (1980) including the $^{12}$CO emission line profiles expected at different positions across the source.

embedded infrared source or young star (Figure 1.2). The degree of collimation of such bipolar outflows varies considerably although most are generally not well collimated (Bally and Lada 1983), having minor axis radii exceeding half the major axis radii (Lada 1985). The cause for this wind collimation may be related to the interaction between a wind and a disk, as described by Shu *et al.* (1987). The sizes of flow sources themselves vary from 0.1pc in Orion up to 4pc in Mon R2 and so therefore may operate on scales comparable to typical GMC sizes themselves (50 – 100pc).

The latest Hubble Space Telescope images (Ray *et al.* 1996) show optical jets that are well resolved in the lateral direction (with FWHM diameters $\lesssim 0.2''$) as far as they can be followed to their source which, in the case of HH 30, is as close as $0.25''$ (35 AU). Assuming the jet has essentially zero angular width at its origin, one can deduce a lower bound for the initial opening angle, and the values obtained are very large indeed (e.g. $\gtrsim 60°$ for the HH 30 jet and counterjet). These observations support models in which the jet is initially poorly focused before being asymptotically collimated into a column with a diameter of order a few tens of AU.

In addition to dynamical properties, physical parameters of the high velocity molecular outflow gas, including the mass, density and temperature are determined by observing a range of molecular spectral lines and, in particular, the relative intensities of the $^{12}CO$ and $^{13}CO$ isotopes (reviewed by Lada 1985). Other indirect observational tracers of molecular gas are optical extinction by dust (associated with $H_2$ formation) or of infrared continuum emission by dust (e.g. André 1995). The discovery of shocked molecular hydrogen emission, although comprising only a very small percentage of the outflowing material by mass, opened up the possibility of analysing the highly energetic phenomena in such deeply embedded outflows at higher spatial resolution than is possible with the millimetre and radio telescopes required to observe the CO emission. Here is a clear case of the feedback of energy from the star formation process back into the surrounding cloud mediated via radiative cooling of the predominant molecule behind shocks fronts driven into the gas.

## 1.4 Shocks in Molecular Outflows

The outflows observed from young stars exceed the local sound speed and must therefore be stopped in a shock front and possibly further cascades of shock fronts produced by the chaotic geometry of the interaction of wind and clumpy molecular cloud. Such outflows tend to be collimated and in some instances appear jet-like with internal shocks and Mach disks (Ray *et al.* 1996). As long as the shocks are not so violent as to dissociate $H_2$ then strong $H_2$ line emission will be produced.

Numerous IR transitions have been conclusively identified with shock waves, including the vibrational and rotational transitions of $H_2$ ($\lambda \simeq 1 - 5\mu$m and 12 $\mu$m), high J-transitions of CO ($\lambda \geq 100\mu$m), v=1-0 CO (4.7 $\mu$m), low-J OH transitions (50-160 $\mu$m), atomic and ionic fine structure and forbidden transitions, including [FeII] at 1.644 $\mu$m, [SiII] at 35 $\mu$m, [OI] at 63 $\mu$m and the Brackett $\alpha$ and $\gamma$ lines of atomic hydrogen (Hollenbach *et al.* 1988).

Rapid progress has recently been made in imaging high excitation species, including [OI] and [SII] transitions in the optical regime, by employing the high resolution capabilities of HST, unimpeded by the Earth's atmosphere. The first infrared instrumentation for HST is expected to become available during 1997 and will complement the recently launched, although smaller aperture Infrared Space Telescope (ISO). Ray *et al.* (1996) describe HST [SII] 6716, 6731Å and [OI] 6300Å emission line observations of the HL Tau, HH30, HH1 and HH34 jets. Many of the knots observed within the HH 1 and HH 34 jets resemble internal bow shocks, far away from their driving source ($\gtrsim 5''$ and $10''$ in the case of the HH1 and HH34 jets, respectively). This is consistent with models in which the knots are attributed to internal working surfaces caused by temporal variations in the outflow from the source.

IR emission from vibrationally excited $H_2$ was first observed in Orion at peak 1 (OMC-1) by Gautier *et al.* (1976) and in NGC7027 by Treffers *et al.* (1976). Measurements of the relative intensities of the lines in Orion showed that the gas was thermally excited (Gaultier *et al.* 1976; Grasdalen and Joyce 1976; Beckwith *et al.* 1978) and initial models based on shock excitation were developed (Hollenbach and Shull 1977; Kwan 1977; London *et al.* 1977). These will be described in Chapter 2.2. Detailed observations of this region have continued, as technology has improved, since it is the brightest such region by an order of magnitude. Recent $H_2$ observations in the massive outflows of DR21 (Davis & Smith 1996), Cepheus A (Hartigan *et al.* 1996) and NGC2071 (Garden *et al.* 1990) have shown complex morphology including irregularly spaced knots of emission within distinct lobes and apparent changes of outflow direction between different regions. This is perhaps indicative of the inhomogeneous, clumpy nature of molecular clouds themselves. Intriguingly, Richter *et al.* (1995a,b) measure shocked $H_2$ excited in the supernova remnant IC443 to have similar upper energy level populations to OMC-1

(Brand *et al.* 1989), suggesting a common underlying process may be present in each case. A more detailed comparison of these datasets with theory follows the description of shock modelling in Chapter 2.2.

In star forming regions, we have seen that the dense molecular gas is subject to both outflows generating high temperatures and to intense ultraviolet radiation fields. Both of these processes occur with sufficiently high energy densities to emit at relatively short IR wavelengths, thus enabling observations to be made at the highest possible subarcsecond spatial resolution, as necessary to resolve shock-phenomena. Initial theoretical predictions were of fluorescent $H_2$ emission associated with the rotational-vibrational cascade following electronic excitation by UV photons (Black and Dalgarno 1976). The first IR measurements of $H_2$ in Orion (Treffers *et al.* 1976; Gautier *et al.* 1976), however, indicated a thermal origin and shocks travelling at velocities of tens of $km\,s^{-1}$ produce the necessary high temperatures to thermalize dense gas at around 2000K. IR fluorescence of $H_2$ was not confirmed observationally until 1987 by Gatley *et al.* This is because the surface brightness of fluorescence in star forming regions tends to be lower than the corresponding shocked emission, although typically accounting for an order of magnitude more energy in total. I describe the theory of the excitation of $H_2$ in more detail in Chapter 2.1. The structure of interstellar shocks depend on the ambient magnetic field strength, the ionization fraction, the shock velocity and the gas density, all of which change within the flow. Considering the non-linear interactions of the various coolants, ionization mechanisms and chemical reactions, computer modelling is essential. We analyse the theoretical structure of molecular shocks more fully in Chapter 2.2. The observational techniques employed to test such models are reviewed in Chapter 2.3.

## 1.5 Relation of Shock Observations To Theories of Star Formation

We have seen that protostellar outflows must represent an important feedback process in the self-regulation of star formation and therefore star formation will affect the subsequent evolution of the parent molecular clouds, which in turn will affect further star

formation. Outflows also serve as important diagnostics of their surroundings and enable the determination of basic physical properties, such as the mass, density and temperature of the gas involved. In principle, these properties can be directly obtained from observations of a sufficient number of selected molecular spectral lines. In practice such determinations are complex and require detailed knowledge of the excitation conditions, clumpiness and abundances of the emitting gas. CO observations trace high velocity molecular flows around young stellar objects that are extremely massive (1-100$M_{\odot}$) flows of cold (10-90K), low-to-moderate density (300-3000cm$^{-3}$) molecular material (Lada 1985). Shocked $H_2$ line emission probes the hottest (T$\sim 10^3$K) and most dense ($\sim 10^{3-7}$cm$^{-3}$) phenomena associated with protostellar outflow.

Mass outflow is directly implicated as the cause of high velocity molecular flows by the association of individual molecular flow sources with Herbig-Haro objects and water maser sources. Indirect but strong evidence linking high velocity molecular flows to an outflow process is the detection of vibrationally excited $H_2$ in these regions. The fact that the brightest $H_2$ emission is typically found at the outer edge of the bipolar CO flow shows that observation of $H_2$ at the interface of outflow and ambient cloud represents the high energy range of the feedback process in star formation. The energetics of molecular outflows are a measure of the total, time-averaged energetics of early stellar mass ejection activity. Molecular outflows therefore provide unique information concerning the importance of such outflow activity around recently formed stars. The frequency of occurrence of high-velocity molecular outflows having short dynamical timescales of order $10^3$ years demonstrates that this process is very commonly associated with low mass as well as high mass star formation. The magnitude of the energy involved in outflow will be related to the cessation of inflow and to the final mass of the resultant star.

An understanding of interstellar shock waves is crucial in determining the structure of the interstellar medium. Radiative shocks, of typical shock speed $v_s \lesssim 200 \mathrm{km\,s^{-1}}$, are particularly important to astronomers because virtually all the energy flux crossing the shock front is converted into radiation that is potentially observable. By causing the gas to radiate, interstellar shocks provide valuable diagnostics of both the physical conditions in the interstellar medium and the energy source that produced the shock. The interstellar plasma through which such a shock passes is of a highly complex nature,

depending on the degree of ionization, molecular abundances, the presence of small dust grains and cosmic rays, and the magnetic field. This leads to a variety of possible geometrical and physical structures for interstellar shocks and makes their dissection a central problem in understanding interstellar physics.

### 1.5.1 Focus of Present Research

In the past two decades, observations and theory have combined to advance our understanding of many phenomena associated with interstellar shocks, including particle acceleration, the structure and chemistry of shocks in molecular gas, the effect of geometry on the spectra of shocks associated with Herbig-Haro objects in outflows from young stellar objects, the heating and destruction of dust grains in shocks, the stability of shocks, maser emission and so on. The aim of this project is to better understand the intrinsic physics of shocked outflows in starforming molecular clouds by detailed measurements of IR emission from excited molecular hydrogen and associated emission, *e.g.* high energy shocked [FeII] transitions. This project has become possible with the large increase in sensitivity and spatial resolution provided by the Cooled Grating Spectrometer (CGS4) with recently upgraded 256x256 array mounted on the UK Infrared Telescope (UKIRT).

On the basis of this, we have conducted a comprehensive study of shocked $H_2$ emission lines in the K IR-band in the brightest known source of its type, Orion, to test the physical basis of shock models. By observing both individual shocked emission line profiles at the highest available spectral and spatial resolution and employing long integration times to obtain higher signal-to-noise measurements of column densities of a range of shocked $H_2$ emission lines, we have dissected individual bow shocks to constrain current shock models, including the faintest but crucial transitions from the higher upper energy levels ($T_j = 10,000 - 40,000$K) where they diverge. Comparison between sources such as the bright but complex Orion OMC-1 region and observations of other fainter sources such as Herbig-Haro 7 will provide more accurate estimates of any possible small contributions from UV-excited fluorescence to the column densities at these energies. We investigate bow-shock models (Chapter 2.2) by searching for expected changes in $H_2$ line profiles

and ratios with position in the bow and orientation of the bow on the sky, and the measurement of any small differences between bow-peak velocities and ambient cloud velocity for a given orientation.

We wish to determine how some $H_2$ molecules survive the strongest shocks and how shock waves affect the evolution of molecular clouds. This requires a knowledge of the shock structure and is the focus of this work. Since the winds and explosions that give rise to shocks are common features of protostellar evolution we assume they play a significant role in maintaining internal velocities in clouds and limiting the rate of secondary star formation. By measuring the emission resulting from many different cases of strong molecular shocks it will be possible to reliably estimate the fraction of shock energy transmitted to cloud turbulence and to build up a more accurate estimate of the stellar birthrate in molecular clouds and on galactic scales. Ultimately, the evolution of galaxies themselves depend on the star formation regulated exchange of matter between stars, gas and dust that we are investigating.

# Chapter 2

# Theory and Observational Techniques

## 2.1 Excitation Of Molecular Hydrogen

In Chapter 1 we described the continuous exchange of matter between stars and the interstellar medium via winds and explosions on the one hand and by gas then coalescing back into clouds and eventually undergoing gravitational collapse to form new stars on the other. The state of the clouds and the rate at which they evolve depend on heating and cooling of matter composed almost entirely of $H_2$ .

### 2.1.1 $H_2$ and the Interstellar Medium

Molecular hydrogen was first observed in absorption in the ultraviolet (UV) using rocket observations by Carruthers (1970). Spitzer *et al.* (1973) then used the *Copernicus* satellite to determine the atomic to molecular fractions of clouds in front of bright stars. They showed that the gas became molecular when the near UV extinction through the cloud exceeded an optical depth of unity. This supports the idea of molecular formation as a phase transition. Indeed, $H_2$ cannot form in its ground state radiatively but requires that its formation be mediated by a third body. The surface catalyst for such

a mechanism is believed to be interstellar dust grains which are uniformly mixed with the gas (Hollenbach and Salpeter 1970, 1971; Goodman 1978; Smoluchowski 1981; Watson 1976). Molecule formation proceeds rapidly for grain temperatures $\lesssim$ 100K since, above this value, atoms evaporate from the grain surface before forming $H_2$ (Hollenbach and Salpeter 1971; Burke and Hollenbach 1980). Gas phase reactions are the only source of $H_2$ when grains are not present. Formation of $H_2$ during cloud collapse in the early Universe (Tegmark *et al.*, *in press*) is thought to have proceeded via the following reactions:

$$H^+ + e^- \rightarrow H + h\nu \qquad \text{(Hutchins 1976)} \tag{2.1}$$

$$H + e^- \rightarrow H^- + h\nu \qquad \text{(Hutchins 1976)} \tag{2.2}$$

$$H^- + H \rightarrow H_2 + e^- \qquad \text{(Hirasawa 1969)} \tag{2.3}$$

$$H^+ + H \rightarrow H_2^+ + h\nu \qquad \text{(Shapiro \& Kang 1987)} \tag{2.4}$$

$$H_2^+ + H \rightarrow H_2 + H^+ \qquad \text{(Karpas } etal. \text{ 1979).} \tag{2.5}$$

Equations (2.2) and (2.3) are the preferred formation route at low densities. Other reactions, including three-body reactions, may form $H_2$ in the gas phase (Black 1978) but their rates are much slower in low-temperature, low-density regions. The above $H^-$ reaction (2.3) may also play an important role in the formation of $H_2$ in the interfaces between ionized and neutral gas (Black 1978).

The first UV absorption studies of $H_2$ were necessarily investigating diffuse clouds of relatively low optical depth since the dense giant molecular clouds in which we are most interested lie in the plane of the Galaxy and are too opaque to allow enough UV radiation through for the satellite to detect. The molecular outflows in such dense clouds were first traced by carbon monoxide (CO) emission (Kwan *et al.* 1976 and Zuckerman *et al.* 1976) which, although second to hydrogen $H_2$ in abundance (by mass), is an asymmetric molecule which emits dipole radiation and as such is more easily observed than $H_2$

. Having no permanent dipole moment, $H_2$ emits only via faint electric quadrupole transitions (Section 2.1.2). However, the lack of spatial resolution of millimetre and radio telescopes, necessary to observe the dominant CO emission, allowed no further progress to be made until near IR observations were possible. Following the first infrared detection of $H_2$ by Treffers *et al.* (1976) and Gautier (1976), the rapid development of infrared techniques including ever more efficient and many-pixelled arrays sensitive to radiation in the one to five micrometres wavebands (and increasingly now in the mid to far infrared) has now advanced the observational astronomy at these wavelengths to levels of sophistication previously only possible at optical wavelengths. Section 2.3 describes the techniques used for this work in more detail. We now turn to the fundamental properties of $H_2$ that facilitate the investigations described in this thesis.

### 2.1.2 Properties of the $H_2$ Molecule

The detailed quantum mechanics of homonuclear molecules are described by Herzberg (1950) and the notation used in the following overview of $H_2$ is taken from Field *et al.* (1966). In the classical picture of a diatomic molecule, only the component of the electronic orbital angular momentum $\Lambda$ about the internuclear axis, $\mathbf{k}$, constitutes a constant of the electron motion (Shu 1991). The other two components of electronic angular momentum feel nonvanishing components of torque from the axisymmetric electric field of the two nuclei, which causes a precession of the vector angular momentum. When $\Lambda \neq 0$, there exists an internal magnetic field induced by the orbital motion of the electrons. The interaction of the electron spin $\Sigma$ with the magnetic field associated with $\Lambda$ splits the energies of a given level into $(2S+1)$ states.

The ground electronic state of $H_2$ is denoted quantum mechanically by $X^1\Sigma_g^+$, and excited states are labelled alphabetically, i.e. the ground state receives an $X$, then each excited state is labelled $B, C, D, ..$ and so on while the lowest unbound state is labelled $b$. The symbols ($\Sigma$, $\Pi$, $\Delta$) denote the total electron angular momentum such that $\Sigma$=0, $\Pi$=1, $\Delta$=2 in units of Planck's constant $h$, projected on $\mathbf{k}$. The total spin angular momentum quantum number for the two electrons takes the values $S$=0,1. The left superscript of the term symbol is the value of $(2S+1)$. The subscripts $g$ or $u$ and the

superscripts + or - (for $\Sigma$ states) refer to the symmetry of the electronic wavefunction as follows. A plane through **k** in a diatomic molecule must be a plane of symmetry. For a $\Sigma$ state, the electronic eigenfunction remains unchanged (+) or changes sign (-) when reflected about **k**. Similarly, if the two nuclei in the molecule have the same charge the field in which the electrons move has a centre of symmetry. The electronic eigenfunctions will change ($u$) or remain unchanged ($g$) when reflected about this plane of symmetry.

Hence, the ground state of $H_2$ ,$X^1\Sigma_g^+$, has no component of electronic angular momentum along **k**, has symmetric electronic wavefunction to a reflection in the plane through the centre of symmetry perpendicular to the axis, and has zero electronic spin (thus $2S+1=1$). This is the normal state for the molecule in the interstellar medium. The first allowed transitions out of this state are to the $B^1\Sigma_u^+$ state at 11.2eV (the Lyman bands, E/k$\simeq$130,000K) and to the $C^1\Pi_u$ state at 12.3eV (the Werner bands, E/k$\simeq$143,000K) above the ground state. These transitions can occur due to absorption of UV photons of wavelength $\lambda < 1120$Å for the Lyman bands and $\lambda < 1120$Å for the Werner bands.

### Ortho and Para forms

The electronic states are split by vibration and rotation of the nuclei. Collisions between molecules can populate the vibrational and rotational levels of the ground electronic state, as happens behind a shock front. The statistical weight of a given level depends on the rotational quantum number $J$ and the nuclear spin $I$ and is $(2J+1)(2I+1)$. $H_2$ is a homonuclear species having nuclei which are identical fermions so the overall wavefunction of the state must be antisymmetric to an exchange of nucleons. Therefore Pauli's exclusion principle places additional restrictions on the states that the system can occupy and the transitions that it may undergo. For even values of $J$ the rotational wavefunction is symmetric and hence the nuclear spin wavefunction must be antisymmetric, requiring $I=0$. These are known as "para" states (antiparallel nuclear spins). Conversely, for odd $J$, $I=1$ and the states are "ortho" states (parallel nuclear spins).

For a gas in thermodynamic equilibrium at high temperatures, the ortho form will have an abundance three times as great as the para form. Hence, the existence of

nuclear spin is of fundamental importance for the statistics of the $H_2$ molecule, although the energy splits so introduced are very small. Radiative transitions between the two forms are forbidden and so under astrophysical conditions one may expect to observe differing ratios of the two species between one region and another, depending on initial formation conditions and local history. At low temperatures, for example, collisions with protons provide a mechanism for ortho-para ($J = 0 \leftrightarrow 1$) conversion.

### Selection Rules for Electronic Dipole and Quadropole Transitions

The electronic dipole transitions of a diatomic molecule satisfy the selection rules: $\Delta\Lambda$=0, $\pm$1 while $\Delta$S=0; *g* states combine only with *u* states and vice versa; and $\Sigma^+$ states cannot combine with $\Sigma^-$ states (Field *et al.* 1966). The $\Delta S$ rule forbids dipole transitions between different vibrational and rotational levels for $H_2$ in its ground electronic state as found in molecular clouds. However, electric quadropole transitions between levels may occur, albeit with much lower probabilities, according to the selection rules

$$\Delta J = 0, \pm 2 \tag{2.6}$$

with $J$=0-0 transitions forbidden. There is no strict selection rule on changes in the vibrational quantum number, $v$, due to anharmonicity in the electronic potential function. Thus, $H_2$ cannot photodissociate via $X^1\Sigma_g^+ - b^3\Sigma_u^+$, which protects the molecule and makes it more stable than it might otherwise be. However, collisional dissociation can occur by this route given an adequate supply of hot electrons from a shock, for example. Figure 2.1 shows a partial energy level diagram for the $H_2$ molecule. The levels are displayed in temperature units, in order to show directly the high temperatures required for thermal population of the vibrationally excited states. The notation is that the change in vibrational number is written first (e.g. 1-0) and the rotational change second. The last number (in brackets) indicates the final rotational level occupied, such that *S* denotes a change of $\Delta J = -2$, Q of 0 and O of +2. Hence S(1) means $J$ goes from 3 to 1. The lowest rotationally radiating state of hydrogen is at 510K, hence the need for energetic phenomena in order for it to be observed in emission.

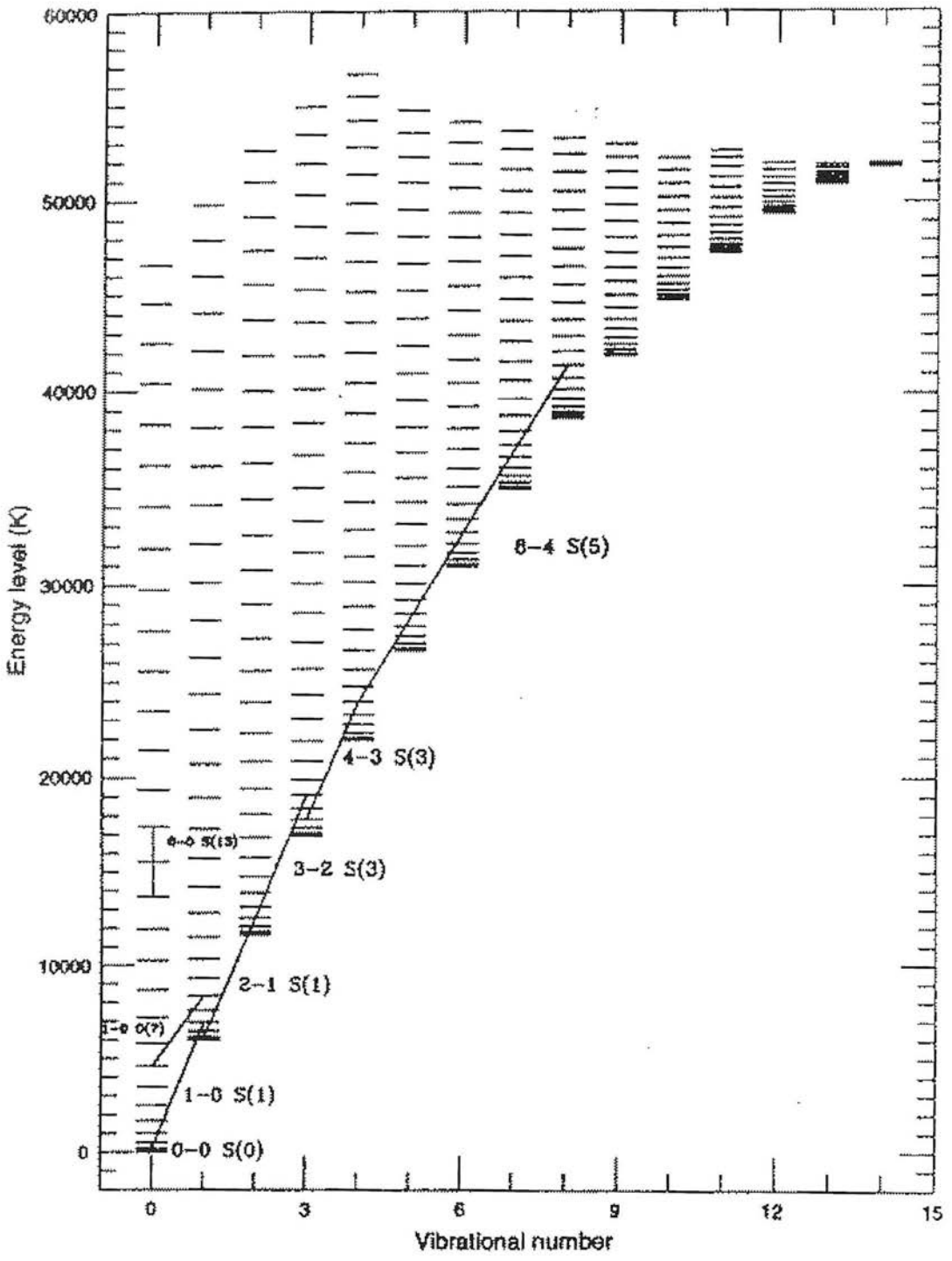


Figure 2.1: Energy level diagram for the ground electronic state of the hydrogen molecule from Burton (1992). Vibrational number (from $v$=0 to 14) increases along the $x$-axis and rotational number increases vertically from $J = 0$ within each vibrational level. The energy level is given in degrees Kelvin (1K $\equiv$1.4cm$^{-1}$). The vibrational continuum ($v > 14$) is at an energy of $\sim 52,000$K above the ground state. Examples of commonly observed quadrupole transitions are indicated.

The energy of each level can be written as an expression in quantum numbers called a "term value" (Huber and Herzberg 1979)

$$T(v,J) = T_e + \omega_e(v+\frac{1}{2}) - \omega_e x_e(v+\frac{1}{2})^2 + \omega_e y_e(v+\frac{1}{2})^3 + ... \qquad (2.7)$$

$$+B_v J(J+1) - D_v J^2(J+1)^2 + H_v J^3(J+1)^3 + ...$$

where $T_e$ is the electronic energy corresponding to the minimum in the potential curve and $\omega_e$, $x_e$, $y_e$, $B_v$, $D_v$, $H_v$ are constants. Accurate energy levels for $v \leq 4$ and $J \leq 30$ were calculated by Dabrowski and Herzberg (1984). Transitions with $\Delta v = \pm 1$ have energies $\sim$ 6000K and occur near $2\mu m$. The (0-0) rotational lines fall between $3\mu m$ and $28\mu m$, the wavelength of the 0-0 S(0) line. The most commonly observed line, due to its relative brightness and ease of observation, is the 1-0 S(1) line at 2.1218 $\mu$m. The $(v,J) = (0,2)$ level is at 512K above the ground state and is the first level from which a transition is allowed (the 0-0 S(0) line). Thus, in the typical cold, quiescent molecular cloud the molecules will all be in the $J$=0 or 1 levels and do not emit line radiation. Lines are only emitted after the molecule has been subjected to an energetic event. There are 14 vibrational levels in the ground electronic state with the vibrational continuum ($v > 14$) at 4.48 eV ($\sim 52,000$K) above the ground level. This is the energy required to dissociate the molecule. As $H_2$ is the lightest molecule it has a relatively low moment of inertia resulting in a wide spacing of the excited states in energy and therefore in emitted wavelength. Most lines can thus be identified individually with medium resolution near-IR spectroscopes (see Section 2.3).

Transition probabilities for radiative decay have been calculated by Turner *et al.* (1977) and Abgrall & Roueff (1989). Decay rates are typically of order $10^{-7}s^{-1}$, and so the cooling time for hot molecular hydrogen is about one year. Consequently, observed $H_2$ radiation traces the current location of a very recent exciting event which is responsible for transfer of energy to the molecule. Rate coefficients for the collisional excitation and dissociation of the molecule are poorly known and a major obstacle in modelling emission spectra. Three sets of commonly used rate coefficients are to be found in Shull and Hollenbach (1978), Shull and Beckwith (1982) and Draine, Roberge and Dalgarno (1983).

### 2.1.3 $H_2$ Excitation

We now describe the excitation of $H_2$ as a diagnostic of physical conditions in the interstellar medium. There are several mechanisms which fall into two different categories: thermal and non-thermal excitation.

#### Thermal (Collisional) Excitation

$H_2$ can be collisionally excited by hot gas behind a shock front. The molecules are heated to a few thousand degrees and radiate near-IR lines with a cooling time of about 1 year. The emission lines therefore trace the location of shock waves associated with supersonic gas flow. The kinetic energy of the flow is converted into thermal energy and then radiated away as line emission. The spectrum and dynamical range of the resultant $H_2$ line emission varies according to the structure of the shock which excited it (Section 2.2). This is the main subject of this thesis and the derivation of $H_2$ column densities from observed line intensities is discussed in Section 2.2.3. $H_2$ starts to radiate significantly when the temperature has dropped below ~4000K. Above this temperature dissociation of the molecules provides the dominant cooling mechanism. $H_2$ line cooling ceases at temperatures below 510K as excited levels are no longer significantly populated.

#### Non-Thermal Excitation and Photodissociation regions (PDRs)

In addition to collisional excitation, the $H_2$ molecule can also be excited by UV excitation of an electronic level which then cascades down through the vibrational/rotational levels to the ground electronic state. Roughly 11% of such transitions result in a dissociation of the molecule. The destruction of $H_2$ is therefore a two-step process in which an allowed photoabsorption from the ground electronic state to a discrete excited level (usually the Lyman or Werner bands, $B^1\Sigma_u^+$ or $C\Pi_u$) is followed by a radiative decay to the unstable vibrational continuum of the ground electronic state. The remaining 89% of the cases lead to fluorescent radiation as the excited molecule cascades down through the bound vibrational states of the ground electronic state. The destruction of $H_2$ is balanced by $H_2$ molecule formation on the surfaces of dust grains leading to an assumed statistical

equilibrium. Since the first step involves a number of discrete bound-bound transitions, the molecule can protect itself against complete destruction by *self-shielding*. Molecules near the surface of a large cloud can continually dissociate and reform on grain surfaces using up the energetic line photons that would otherwise penetrate to the interior to destroy $H_2$ (Hollenbach and Salpeter (1971).

Photodissociation regions are hence located at the interface between a hot star (*e.g.* massive OB stars) and a parent molecular cloud surface. Since the first observational confirmation of IR fluorescent emission from PDRs (Gatley *et al.* 1987), the approximate properties of PDR models have been confirmed (e.g. Chrysostomou *et al.* 1992). In the Orion outflow, fluorescent emission accounts for more than an order of magnitude more energy than shocked emission and this has been found to be typical in other star-forming regions. The main complication lies in the importance of self-shielding of the UV flux by $H_2$ (and further in by CO), and the complex competition between the various heating processes (e.g. Burton *et al.* 1990). Of particular interest here is the magnitude of the probable contribution of such fluorescence to total line intensities of shocked $H_2$ in molecular outflows. Possible mechanisms by which such additional fluorescent contributions might become significant in a shocked region are described in Chapter 4.

To distinguish PDR emission from other mechanisms, initial work simply compared the ratio of the 2-1 S(1)/1-0 S(1) lines which is significantly higher in a PDR compared to shocked sources. However, the interpretation of fluorescent $H_2$ emission is complicated by the need to consider two processes, radiative excitation of the $H_2$ by far-UV, and its collisional de-excitation by H atoms (Burton 1992). In pure radiative fluorescence, as first investigated by Black and Dalgarno (1976) and in more detail by Black and van Dishoeck (1987), the molecules fluorescently emit near-IR photons as excited electrons cascade down the vibrational-rotational ladder, with a timescale of 1 year per decay, to the ground state. The 1-0 S(1)/2-1 S(1) line ratio is 1.7. If $n \gtrsim 10^5 \mathrm{cm}^{-3}$, however, the ratio becomes density-dependent and can approach the shocked value of 10, as collisional de-excitation by H atoms can proceed faster than radiative decay, with much of the vibrational-rotational energy transformed into heat. The spectrum is therefore modified as population of the levels approaches local thermodynamic equilibrium (LTE). In the absence of other indicators that might favour fluorescence over shocks, this ratio cannot

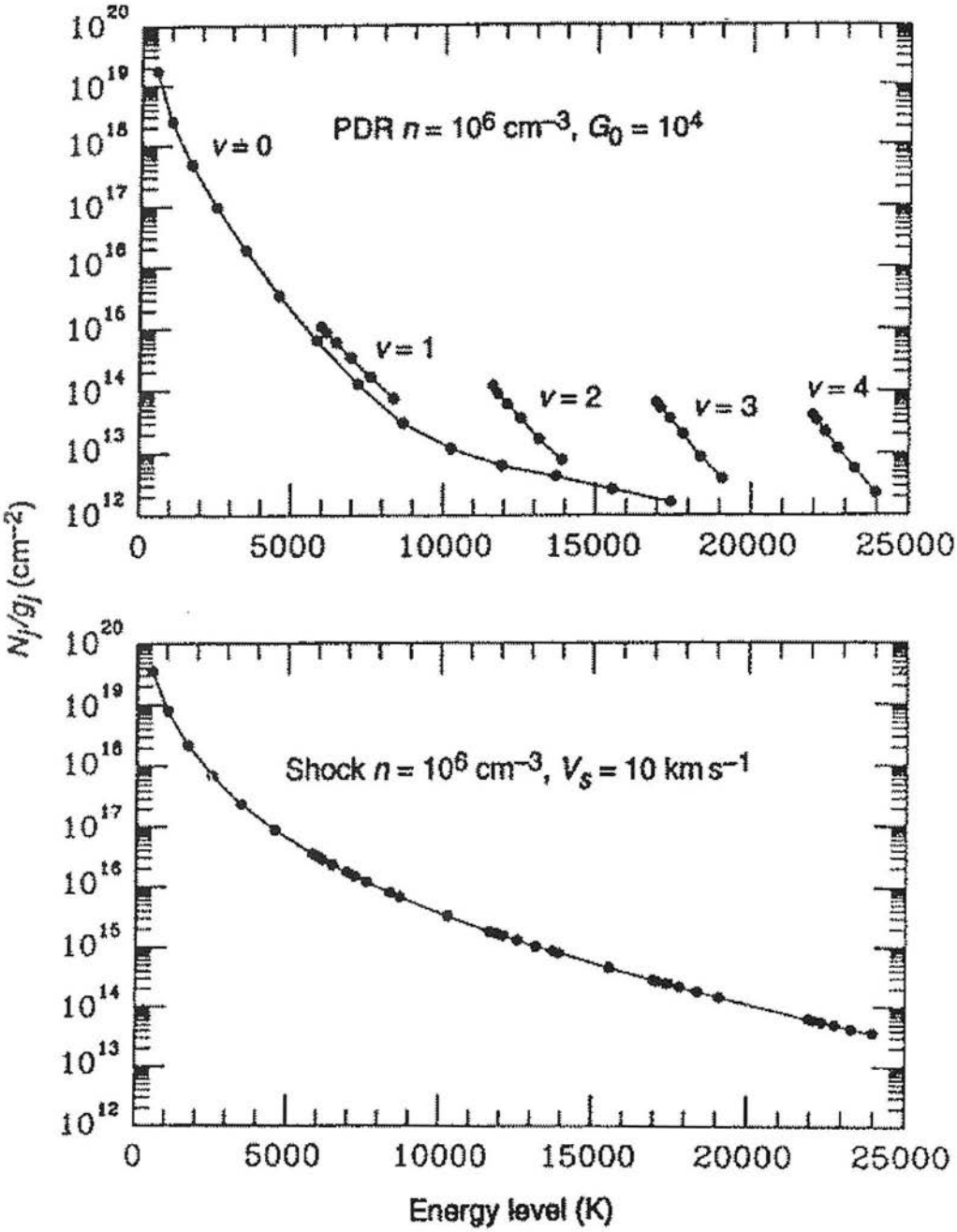


Figure 2.2: The run of model $H_2$ column densities (divided by statistical weights) with upper energy level for a PDR and shock assuming an ortho to para ratio of 3 and the physical conditions shown (from Burton 1992). For the PDR each vibrational series is labelled, and within each series the rotational levels increase from $J = 0$ (except for $v = 0$ where they start with $J = 2$). In the shock the levels are thermalised, as is the case for the lower levels in the PDR. The higher levels of the PDR ($v \geq 2$) show the characteristic fluorescent distribution.

simply be used to discriminate between these two excitation mechanisms.

Figure 2.2 illustrates the differences in the resultant $H_2$ column densities between model calculations (Sternberg and Dalgarno 1989; Burton *et al.* 1992) for purely shocked and fluorescent emission over a range of upper energy levels. A thermal distribution of energy levels is seen in the shock and the vibrational series cannot be distinguished in the diagram. In the PDR, however, just the $v = 1$ series is merged with the $v = 0$ series, where collisions have thermalised their populations. Higher vibrational levels ($v \geq 2$) still retain their fluorescent distribution, having populations considerably greater than the thermal values. The density dependence of PDR line ratios above $n \gtrsim 10^5 \mathrm{cm}^{-3}$ for a fixed UV flux is illustrated in Figure 2.3 and hence the need to measure lines resulting from $v \geq 3$ levels in order to distinguish between excitation mechanism.

Models of excited $H_2$ line emission have neglected the unknown contributions of $H_2$ formation. Duley and Williams (1986) modelled the formation of $H_2$ on the surfaces of amorphous silicate dust grains with about 2eV of energy, placing them in an excited state with $v = 4$ and leading to a kinetic energy of $\sim 0.2$eV after ejection from the dust surface. The model predicts an overpopulation of the $v = 0$ and 1 levels with $J \leq 6$ after collisional relaxation which might be distinguished observationally.

An alternative non-thermal process is excitation by impact of energetic photoelectrons produced by the absorption of X-rays. The emission from high vibrational levels is similar to UV pumping, while emission from $v = 1$ and 2 levels in a gas of low fractional ionization is dominated by direct electron impact excitation. Lepp and McCray (1983) modelled this emission and showed that $\sim 20\%$ of the absorbed X-ray luminosity can be reradiated in 0-0 and 1-0 vibrational lines due to excitation by thermal collisions with X-ray heated gas. They predict a consequent 1-0/2-1 S(1) line ratio $\sim 45$. More recently, Gredel and Dalgarno (1995) calculate an intensity ratio of the 1-0 S(1)/2-1 S(1) of $\sim 16.7$ in a gas of low fractional ionization and $\sim 1.85$ in a gas of high fractional ionization. Such a mechanism has yet to be detected observationally but may be expected to become significant for $H_2$ line emission from quasars, Seyfert galaxies and BL Lac objects. The X-ray pumping mechanism differs from the UV pumping mechanism in that electronic states in addition to the $B^1\Sigma_u^+$ and $C^1\Pi_u$ states are populated, and excitations

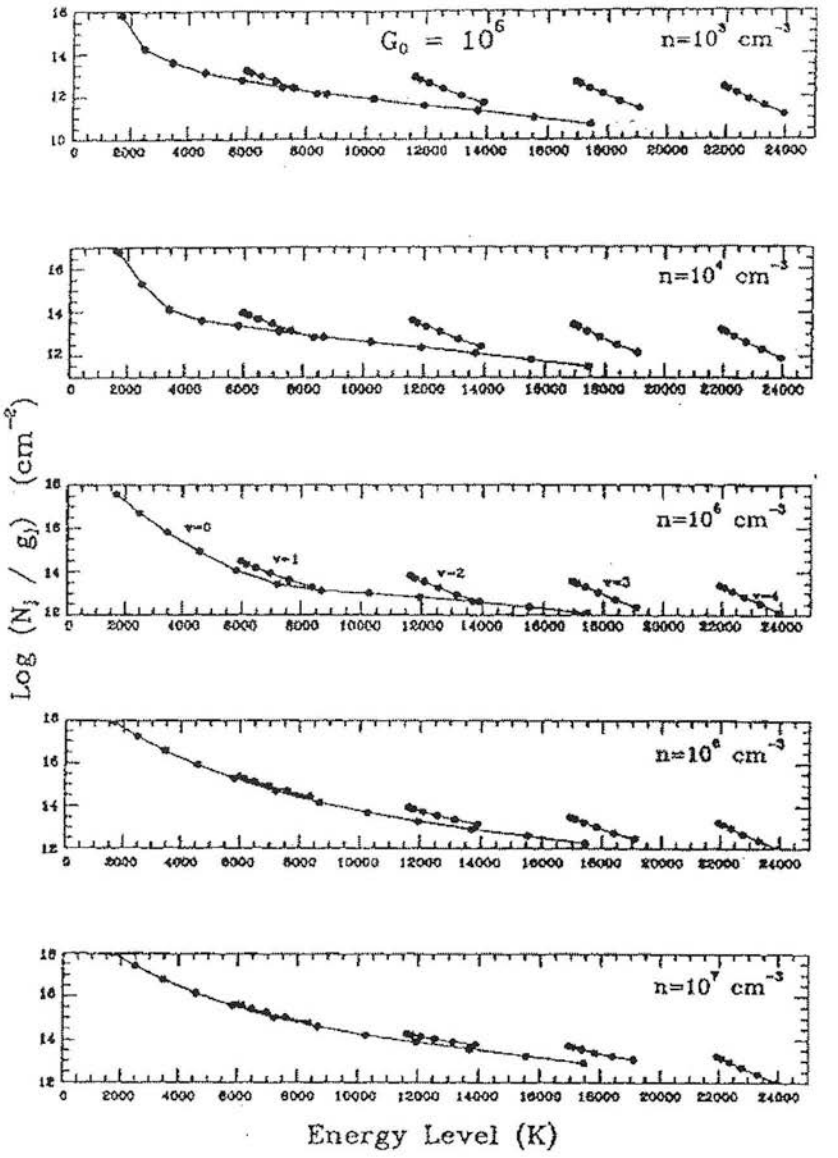


Figure 2.3: Plots of model PDR $H_2$ column densities (divided by statistical weights) against energy level (from Burton *et al.* 1990) for a range of densities from $n = 10^3 - 10^7 \mathrm{cm}^{-3}$, assuming an ortho to para ratio of 3 and a fixed UV flux of $G_0 = 10^5$ times the value of the ambient interstellar radiation field (ISRF) as measured by Habing (1968).

in the ground state occur by direct impact excitation as the electrons lose energy. In a sufficently dense gas, of course, the $H_2$ spectrum alone cannot distinguish between a shock-heated gas and an X-ray heated gas, because of the thermalization by collisions. But, in dilute gas in which collision processes do not modify the level populations before they decay radiatively, the above conclusions should hold.

### Summary

$H_2$ is the best diagnostic of shocked molecular outflows because

1. The vibration-rotation splitting of the ground electronic state of $H_2$ are widely spaced in energy and the rather uniform population of the energy levels gives many lines at a large range of energy in the near- and mid-IR part of the spectrum, where extinction becomes low enough to permit examination of the cloud-embedded processes.

2. The homopolar $H_2$ molecule emits electric quadrupole radiation with such a small oscillator strength that self-absorption is negligible - allowing accurate determination of column densities.

3. The radiator is the dominant constituent of molecular clouds and hence the diagnostic carries most of the mass and momentum.

## 2.2 Physics of Molecular Shocks

A shock wave forms when mass is injected into the interstellar medium at a velocity, $v_s$, that exceeds the velocity of propagation of signals in the medium (e.g. Spitzer 1979). Therefore the Mach number of the shock ($M$), which is the ratio of $v_s$ to the signal velocity, is greater than 1. The gas ahead of the shock is unaware of its approach and is "surprised", although energetic particles or radiation from the shock may provide an early warning. Upon impact by the shock wave, in the simplest case of a single non-magnetised hydrodynamical fluid, a discontinuous jump in the density, pressure,

temperature and velocity of the gas occurs. The conditions behind the shock front are related to those ahead by a set of algebraic relations expressing the conservation of mass, momentum and energy.

Dynamical equations in which the gas is treated as a non-magnetised single fluid are formulated with temperature $T$, density $\rho$ and velocity $v$ (perpendicular to the shock plane) in a frame fixed relative to the shock structure. If subscript '0' refers to properties ahead of the shock, $v_s$ is the speed of the upstream gas relative to the shock and the rate of energy loss per unit volume of the hot gas behind the shock is $L$, the equations of conservation of mass, momentum and energy are as follows (*e.g.* Landau and Lifshitz 1959a):

$$\rho v = \rho_0 v_s \tag{2.8}$$

$$P + \rho v^2 = \rho_0 v_s^2 \tag{2.9}$$

$$\frac{d}{dt}\left(\sum_k w_k + \frac{1}{2}v^2\right) = -\frac{L}{\rho} \tag{2.10}$$

These are the *Rankine-Hugoniot* conditions for a strong shock ($M \gg 1$) in which the pressure behind the shock is about equal to the ram pressure, $P \simeq \rho_0 v_s^2$, and is almost independent of the initial pressure ($P_0$ can be neglected). Additional magnetic pressure terms ($B^2/2\mu_0$) are incorporated into the momentum and energy conservation equations for a single magnetised fluid in which all components (including atoms, ions and electrons) can be approximated as having a common flow velocity, although the magnetic pressure becomes negligible in a very strong shock and the hydromagnetic jump conditions reduce to the gas dynamic ones (Hollenbach & McKee 1979). $w_k$ is the enthalpy per species $k$ (He, H and $H_2$ are relevant here). In the case of the non-magnetised fluid, it can be shown that the bulk energy is negligible compared to the enthalpy of the molecular gas (Burton *et al.* 1988) and the $v^2$ term disappears. The velocity of the shocked gas measured relative to the unshocked gas is comparable to but slightly smaller than the shock velocity $v_s$. If the shock is weak ($M \simeq 1$), as in the case of a sonic boom, then the gas is almost unchanged across the shock front.

The density and temperature of the shocked gas depend on the nature of the shock. In the simple case of all species of particles in the gas having a common velocity and kinetic temperature then the density in a strong molecular shock increases by a factor of 6 (McKee & Hollenbach 1980), since

$$\frac{\rho_s}{\rho_0} = \frac{\gamma + 1}{\gamma - 1} \tag{2.11}$$

where the assumed adiabatic exponent is $\gamma$=7/5 for a diatomic molecule. The associated temperature increases to

$$kT_{eq} = \frac{2(\gamma - 1)}{(\gamma + 1)^2}\mu v_s^2 = \frac{5}{36}\mu v_s^2 \tag{2.12}$$

so that the sound speed in the shocked gas is comparable to the shock velocity (McKee & Draine 1991). Here $k$ is Boltzmann's constant, $\mu$ is the mean mass per particle and the subscript $eq$ indicates that all the different species - electrons, ions and neutrals - are in equipartition (they have the same temperature). If, on the other hand, the shock occurs in a multifluid plasma such as a weakly ionized plasma (section 2.2.2) then the temperature and velocity vary from one species to another and radiative losses in the shock front may be important.

### 2.2.1 Overview of Shock-structure

A strong, single fluid interstellar shock is envisaged to comprise four regions (Burton *et al.* 1986), as shown in Figure 2.4, which may or may not be distinct: (a) the *pre-shock zone*, which may be irradiated by a UV-precursor and/or heated by the effect of a magnetic precursor; (b) the *shock front*, a relatively thin region in which elastic collisions excite the translational degrees of freedom of the gas, heating it up and increasing the density and entropy as the relative kinetic energy of shocked and unshocked gas is dissipated; (c) a region in which the rotational and vibrational states of the molecular species are excited by inelastic collisions; and (d) the *post-shock relaxation layer* in which the gas radiatively cools with corresponding changes in chemical state and increase in density. If the age of the shock exceeds the time for electrons to undergo radiative collisions then this region

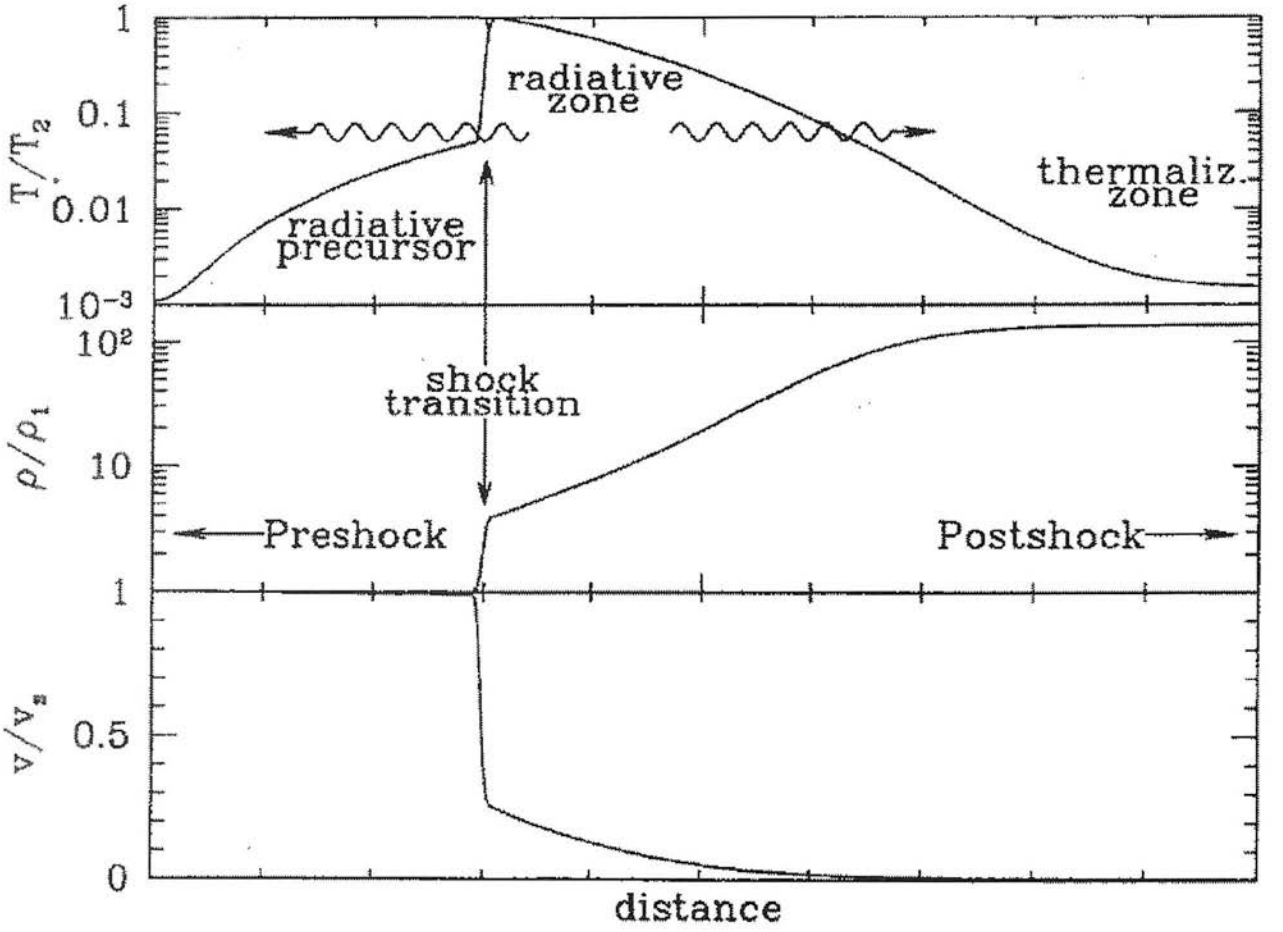


Figure 2.4: Schematic structure of a strong, single-fluid shock wave (Draine & McKee 1993) in terms of temperature $T$, density $n$, and velocity $v$ relative to the shock front.

will be important and a final thermalisation zone may result in which radiation from the post-shock relaxation layer is absorbed and then reradiated.

### 2.2.2 Shock Type and the Influence of the Magnetic Field

In dense clouds of hydrogen density, $n_H \sim 10^2$ to $10^6 cm^{-3}$, most of the mass is in the form of $H_2$ and fractional ionizations range from $10^{-4}$ to $10^{-8}$. Although the ions and electrons contribute only a small fraction of the mass and pressure, the plasma is dynamically important as it is directly coupled to the magnetic field. When the fractional ionization is low, the neutral-ion collision rate is small and the coupling between ions and neutrals becomes weak enough to treat the ions and neutrals as two distinct but

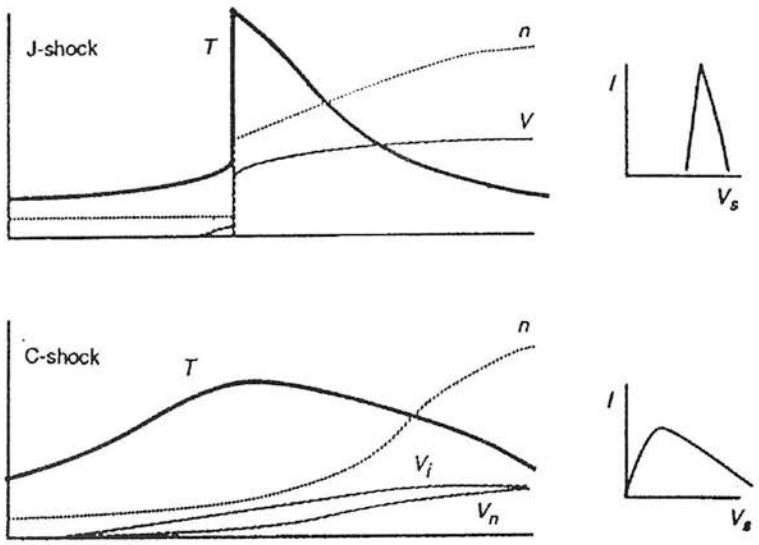


Figure 2.5: Characteristic structure of a planar J shock (top) and C shock (bottom) from Burton (1992). Distance increases along the $x$-axis, from pre-shock to post-shock, with the $y$-axis showing the variation in three physical parameters: temperature $T$ (thick line), density $n$ (dotted line and flow velocity $V$ (dashed line) in the ambient gas rest frame. For the C shock, both the ion velocity ($V_i$) and the neutral velocity ($V_n$) are shown, illustrating the relative drift which causes drag heating of the gas over a distance much greater than the mean free path of the gas for which J shock transitions occur. To the right of each is shown the corresponding $H_2$ velocity profile, significantly broader in the case of a C shock.

interpenetrating fluids (Draine 1980). If the differential acceleration of the ions and neutrals, referred to as ion-neutral slip, significantly heats and accelerates the neutral fluid then the neutral fluid can be brought to its downstream accelerated and compressed state without the need for a hydrodynamic jump. These are C (or continuous) shocks. Unlike Alfvén waves however, there is an irreversible change in neutral entropy due to the randomizing collisions causing the friction (related to the molecular viscosity). Hence, in addition to single-fluid hydrodynamic J (or jump) shocks, full magnetohydrodynamic (MHD) modelling of two-fluid shock waves in predominantly neutral gas (Draine 1993) is necessary and makes important predictions which may be tested observationally.

1. J-type shocks

   J-type shocks are distinguished by a discontinuous *jump* in the neutral hydrodynamic variables (velocity, density, temperature) within a thickness of one molecular

mean free path as a result of particle-particle collisions in which bulk energy is converted to thermal energy. In a single-fluid model, gas more than a few mean free paths ahead of the jump is essentially undisturbed from the pre-shock state and the cooling rate is determined only by the local constitution of the gas (the cooling function). In the case of a two-fluid model, the region ahead of the jump is referred to as a *magnetic precursor*. The low-ionization preshock gas may be heated slowly enough that the molecular material can survive and radiate until arriving at the jump, at which point $H_2$ is dissociated.

2. C-type shocks

   A *continuous* C-type shock results if the magnetic field is so strong, and the fractional ionization sufficiently small, that there is no jump transition (Figure 2.5). The hydrodynamic variables vary smoothly from pre-shock to post-shock values in an irreversible change (entropy increases) as ion-neutral collisions dissipate energy in a drag region which is long compared with the cooling length. As the shock transition and radiative cooling zone coincide, $H_2$ can be accelerated to high velocities without being dissociated since the fluids are at far lower temperatures than in the case of a J shock. However, if the heating by ion-neutral collisions raises the neutral gas temperature, and therefore the sound speed, enough that the neutral flow (which was initially supersonic) becomes subsonic then either a neutral J shock with magnetic precursor results (see above) or, under some circumstances, the neutral fluid can make the supersonic—subsonic transition smoothly. Such shocks are labelled as C* type (Chernoff 1987, Roberge & Draine 1990).

C shocks have a significantly different temperature profile to J shocks. $H_2$ excited by a C shock may therefore be approximated as a slab at approximately the peak temperature, and with a range of velocities which, like the peak temperature itself, is shock velocity dependent. C shocks are therefore less likely to destroy the molecules but will still do so above a maximum shock speed of $v_s \gtrsim 40 \mathrm{km\,s^{-1}}$ in typical molecular cloud conditions (Draine *et al.* 1983). Figure 2.6 illustrates the density and velocity bounds within which these different shock types are expected to occur. Clearly, interstellar shocks depend on the ambient magnetic field strength, the ionization fraction, the shock velocity and the

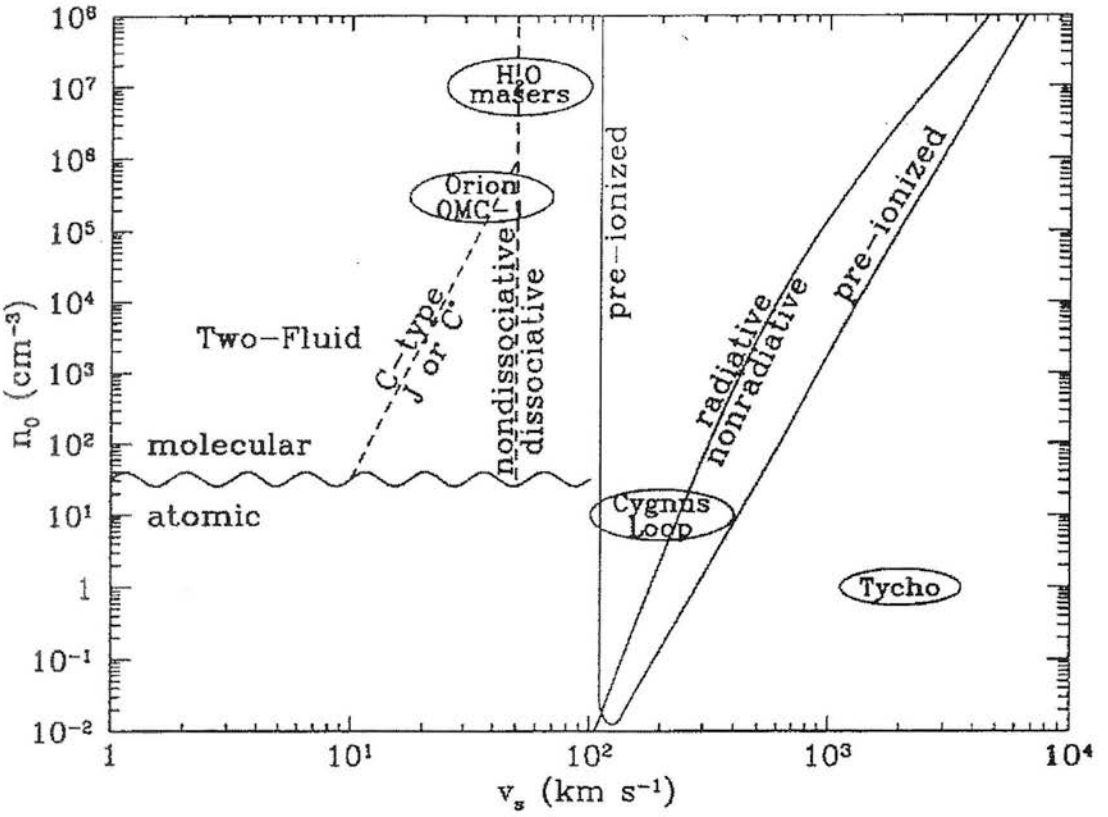


Figure 2.6: Location of different shock types on the $v_s - n_0$ plane from McKee & Draine (1991). The line labelled radiative/nonradiative separates radiative and nonradiative shocks (for shocks assumed to be driven by a $10^{44}$J supernova explosion). The line labelled preionized encloses the conditions under which the radiation emitted by the shock wave is able to preionize initially neutral preshock gas. Strong two-fluid shocks are possible only if the gas is primarily molecular, which typically requires densities well in excess of $10\text{cm}^{-3}$; in atomic gas, strong shocks are J type. The approximate locations of the Cygnus Loop and Tycho supernova remnants, the $H_2$ line-emitting region in OMC-1 and the $H_2O$ masers in star forming regions are shown.

gas density, all of which change within the flow. Considering the non-linear interactions of the various coolants, ionization mechanisms and chemical reactions, computer modelling is essential.

### 2.2.3 $H_2$ Line Emission

#### Predictions For a Planar J Shock

$H_2$ is shocked to a temperature which reaches its highest value just behind the hydrodynamic jump, and then rapidly cools to its final value. The cooling rate is set by the local constitution of the gas (the cooling function $L(T)$), and the final temperature is negligibly small compared to the temperatures required to excite $H_2$ . It is assumed that the vibrational and rotational levels of $H_2$ are in local thermodynamic equilibrium as long as the following requirements are met. Firstly, the density is high enough ($\geq 10^6 \mathrm{cm}^{-3}$) that many downward collisions take place per radiative transition from the levels occupied by the majority of the gas molecules just behind the shock. Secondly, the cooling rate must be slower than the collision rate.

To derive column densities ($N_j$) of the upper level of the $H_2$ transition (directly related to emission line intensities), one applies the Rankine-Hugoniot conditions (equations 2.5-2.7) to the jump and then applies theoretical estimates of the cooling rates by line emission and dissociation (*e.g.* Burton 1986; Roberge and Dalgarno 1982) to the post-shock cooling zone. The densities are normalised by division of the statistical weights ($g_j$) of energy-levels $kT_j$ to yield an equation of the form (Burton *et al.* 1988):

$$\frac{N_j}{g_j} = n_0 v_s \int \frac{e^{-T_j/T} dw}{Q(T)L(T)} \tag{2.13}$$

where $Q(T)$ is the partition function for $H_2$ and the expression is integrated with respect to the enthalpy per species $w$. The partition function is the sum of all possible states $i$ in a Boltzmann equilibrium given by $\sum_i g_i e^{-E_i/kT}$. For $H_2$ , with an $H_2$ ortho:para ratio of 3:1, $Q(T)$ can be approximated by

$$Q(T) = \frac{T/T_{\mathrm{H_2}}}{1 - e^{-T_v/T}} \tag{2.14}$$

where $T_v \simeq 6000$K is the vibrational level interval of the lowest levels of $H_2$ and $T_{\mathrm{H_2}}$=39.5K (Landau & Lifshitz 1959b). Equation (2.13) can be simplified further by substituting for

$Q(T)$ and letting $T_{\max} \rightarrow \infty$ to give

$$\frac{N_j}{g_j} \propto T_j^{-s} - (T_j + T_v)^{-s}, \tag{2.15}$$

where $s$ is the exponent of an assumed power law for cooling $L = L_0 T^s$ (Hollenbach & McKee 1979).

Hence, each IR $H_2$ line will be significantly excited only above a temperature which is proportional to the upper energy level of the line. Once this criterion is met, however, the column density depends on $n_0 v_s$ and molecular properties and not on temperature, shock speed or density independently except that $n_0$ must be high enough to maintain local thermodynamic equilibrium. The relationship between column density and $H_2$ upper energy level is therefore a map of the cooling function of the gas. The effects of dissociational cooling are proportional to $n^2 = n(nT)/T$, and with $nT$ proportional to pressure behind the shock and assumed constant, dissociation must have the same density dependence as $H_2$ line cooling so that it can readily be included in equation(2.13). Observed $H_2$ shock speeds are thus confined to a narrow window, $10 \lesssim v_s \lesssim 23 \mathrm{km\,s^{-1}}$ (Kwan 1977). Below this range $H_2$ is not sufficiently excited to significantly radiate. Above this range and the shock is so intense that cooling is dominated by dissociation of $H_2$ . A strong diagnostic result is that J shocks dissociate $H_2$ at significantly lower velocities than C shocks.

### Extension to a Planar C Shock

In the simplest case, C shock modelling requires the extension of the conservation equations to include a magnetic pressure term $B^2/2\mu_0$ as the field is distorted perpendicular to the field lines generating Alfvén waves (equation 1.8). Following Draine (1980), Chernoff (1987) and Smith *et al.* (1990) it is useful to parameterize the flow through a C shock by the shock velocity $V_s$ and the Alfvén Mach number defined by

$$M_A^2 = \frac{V_s^2}{B^2/\mu_0 \rho_n}. \tag{2.16}$$

where '0' refers to preshock values, and 'i' and 'n' refer to ions and neutrals respectively. The length scale over which ion drag accelerates the predominant neutral material is

$$l = \frac{(m_i + m_n)B^2}{\mu_0 \rho_{n0} \rho_{i0} \langle \sigma v \rangle V_s}, \tag{2.17}$$

where $\sigma$ is the ion/neutral collision cross section. The ion and neutral velocities are scaled $u_i = v_i/V_s$, $u_n = v_n/V_s$. Tóth (1994) has recently performed numerical simulations that successfully reproduce steady state C shocks.

If we now assume that the flow is "cool", i.e. very supersonic (Smith *et al.* 1990), the equation of momentum conservation becomes

$$u_n = 1 - (u_i^{-2} - 1)/2M_A^2 \tag{2.18}$$

which enables simple estimates of the amount of heating (proportional to $(u_n - u_i)^2$) and other quantities. The heating rate will grow slowly and then die away giving the characteristic flat-topped C shock temperature profile, and so the emission of the gas can be approximated by a uniform temperature zone in contrast to that from a J shock. The distribution of column densities of $H_2$ will also be velocity sensitive because the heating rate due to friction increases as the shock velocity increases. We now compare shock models with observational data.

### 2.2.4 Comparison to Observations

The majority of detailed observational work has been done in Orion since it is the brightest region of shocked emission by an order of magnitude. Since the first detection by Gaultier *et al.* (1976), technological progress has allowed the measurement of column densities resulting from a range of excitation energies at Orion Peak 1 (Brand *et al.* 1988; Burton *et al.* 1988). Figure 2.7 shows a plot of the ratios of observed, dereddened $H_2$ column densities at Peak 1 to those for a Boltzmann distribution at 2000K (normalised so that the $1 - 0S(1)$ line ratio is unity) versus upper energy level. The solid line is the best-fit planar J shock model as fitted by Brand *et al.* (1988). The excess of hot gas above 2000K is seen by the rise at higher energy level. Planar C shock models, by

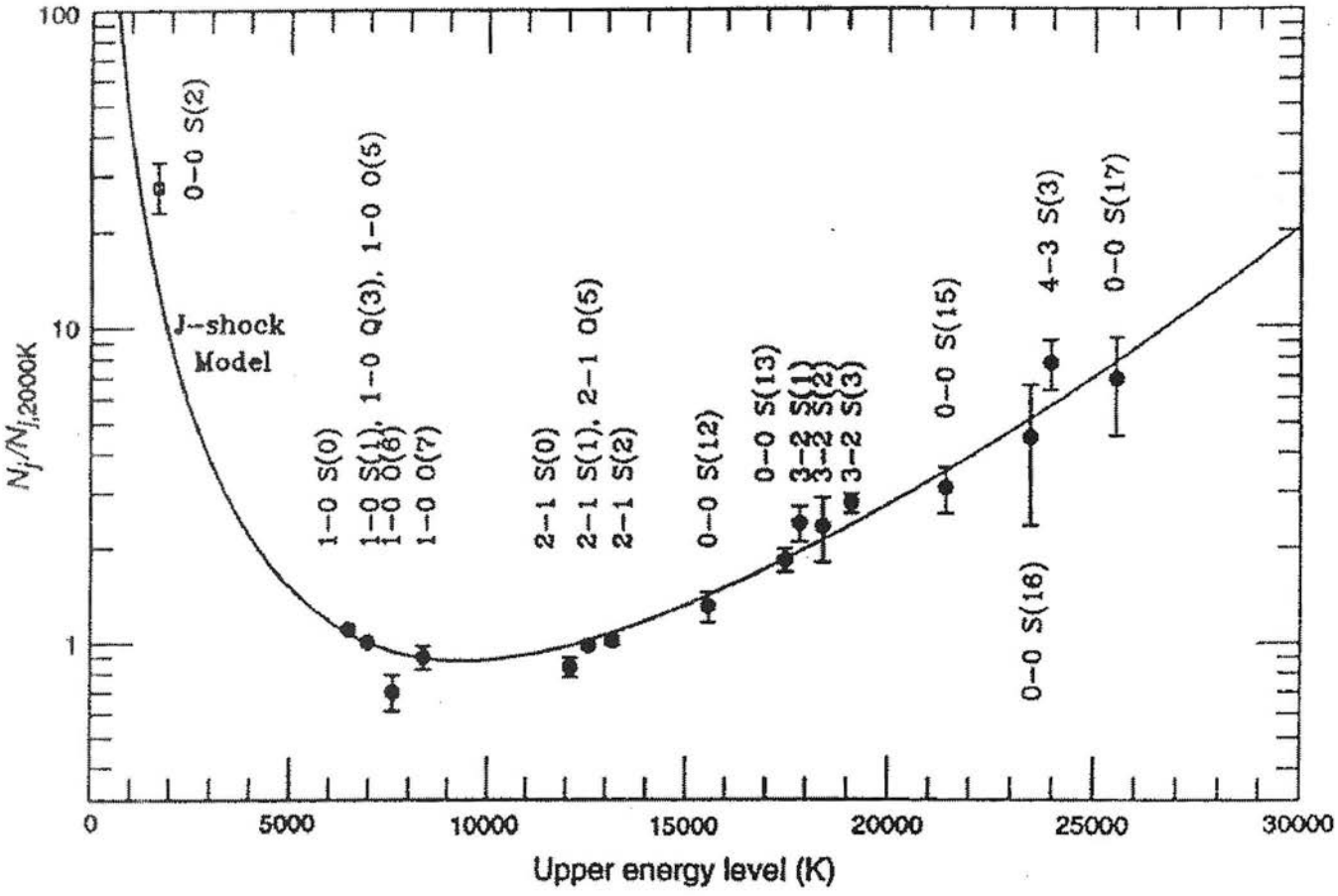


Figure 2.7: $H_2$ line ratios in OMC-1 from Brand *et al.* (1988), plotted as column density ratio versus energy level, and labelled by transition. The observed column density is divided by the column expected for gas in LTE at 2000K and then normalised so that the intensity of the 1-0 S(1) line is unity. The continuous line is a best fit planar J shock fit to the data which depends only on one free parameter, the driving pressure behind the shock. In contrast, planar C shock models predict a relative deficit in column density at the highest upper energy levels.

contrast, predict a deficit. Any possible fluorescent contribution to the column densities at higher energies would introduce intrinsic scatter. At OMC-1 any such contribution is constrained to be relatively small, if present, by these observations.

This success in predicting $H_2$ line ratios, however, poses severe theoretical problems. A J-shock should only exist under these conditions if the magnetic field is unreasonably low ($B \leq 10\mu$G), or if the ionization fraction is unreasonably high (Burton 1992). We expect fields of order 1mG, which must have an important effect on the dynamics and ne-

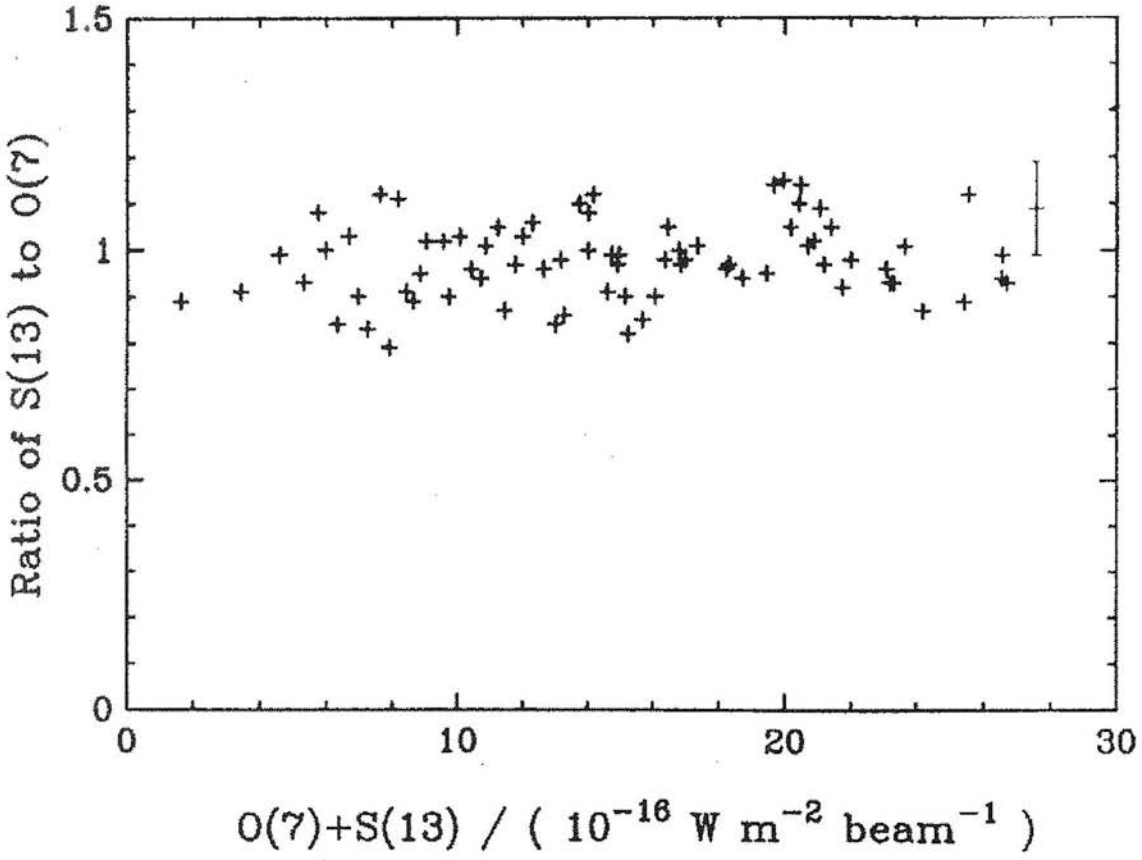


Figure 2.8: The ratio of $H_2$ 0-0 S(13) to 1-0 O(7) intensity versus mean intensity in the region of OMC-1 from Brand *et al.* (1989a). The lack of variation with intensity in the map implies a lack of variation with position.

cessitates a multi-fluid model. This model also assumes that $H_2$ is the dominant coolant but chemical studies indicate that under certain circumstances cooling via $H_2O$ and OH could significantly alter the emission spectrum (Draine & McKee 1993). Modelling of the shocked $H_2$ emission in Orion must also explain a map over the brighter parts of the outflow (Brand *et al.* 1989a) in which the ratio of two of the more highly excited lines, 0-0 S(13) [17,000K] to 1-0 O(7) [8,300K], remains constant (figure 2.8) to within the observational errors ($\sim 10\%$). This would not seem unreasonable if planar J shocks were responsible as it would imply a constant cooling function.

The most important objection to J shock models lies in the large observed widths ($\sim$140km s$^{-1}$ ) of shocked $H_2$ velocity profiles at OMC-1 (Brand *et al.* 1989b), as shown in Figure 2.9. These huge widths are inexplicable for single planar shocks of any variety,

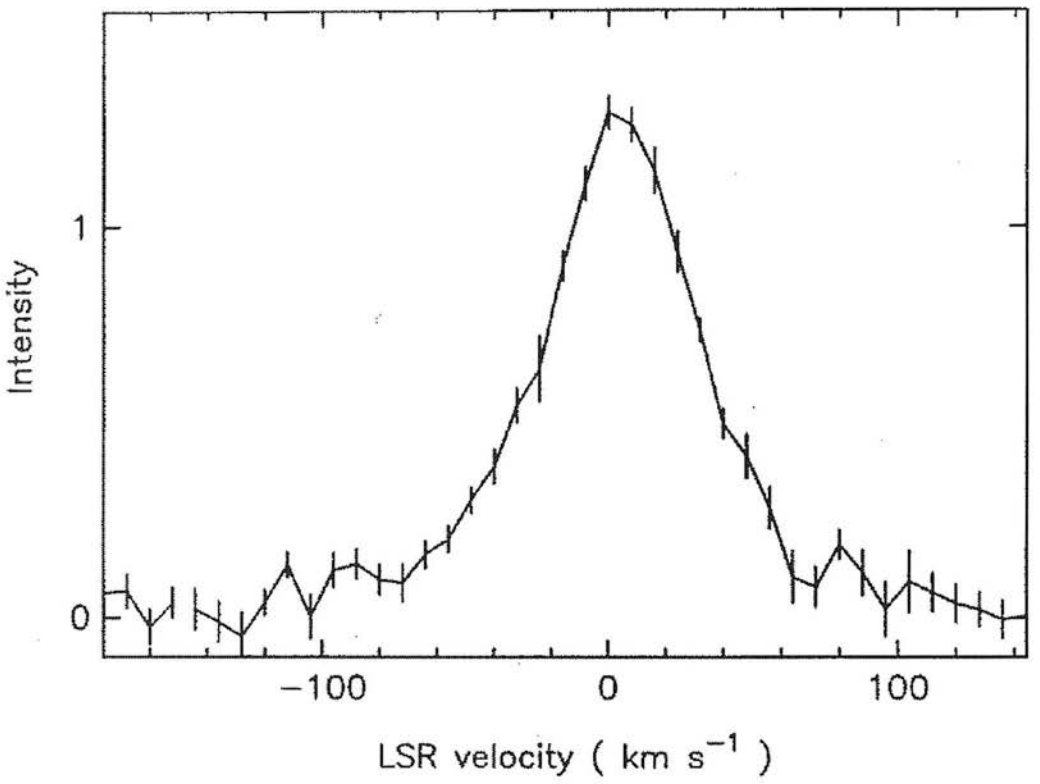


Figure 2.9: The velocity profile of the $H_2$ 1-0 S(1) line in a $5''$ aperture at OMC-1 from Brand *et al.* (1989b).

since $H_2$ dissociates above velocities of $\lesssim$24km s$^{-1}$ in J-shocks and $\lesssim$60km s$^{-1}$ in C-shocks given the constraints on physical conditions in Orion (Smith *et al.* 1991b). This difficulty was tackled by the introduction of bow-shock models, implying more than one shock front along a given line-of-sight.

### 2.2.5 Bow-shock Models

In order to reconcile the large observed velocity widths with the excitation spectrum of $H_2$ observed at OMC-1, Smith and Brand (1990a,b,c) and Smith *et al.* (1991a,b) modelled fast C bow shocks. A dense knot of gas driven at high velocity into ambient molecular gas (or, conversely, a fast wind impacting a dense clump) creates a bow shock structure around the leading edge of the clump. Emission from each point along the bow is computed according to the appropriate component of shock velocity and magnetic field and then summed over the entire structure. It is expected that $H_2$ is dissociated

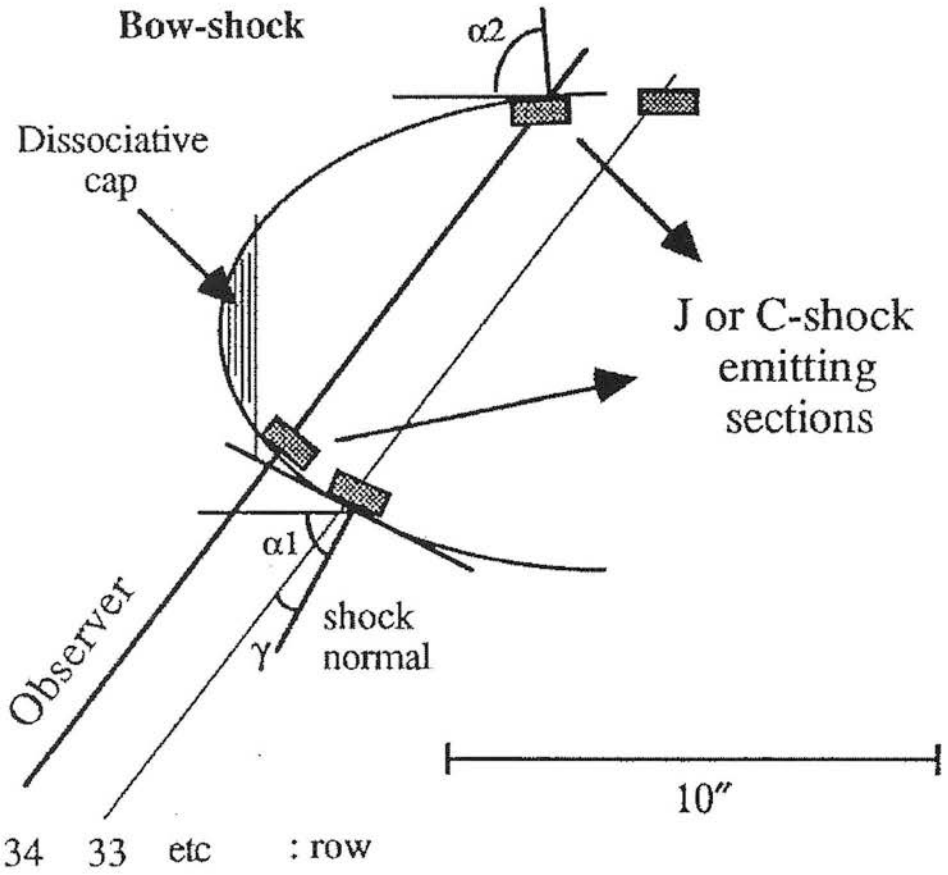


Figure 2.10: Plan view of a bow shock propagating through molecular gas from Fernandes (1993). A given line of sight through the bow shock will here intercept two oppositely directed shock fronts. The gas in each component will see an effective shock velocity that is proportional to the bow velocity and varies according to the angle subtended by the shock normal to the bow and direction of propagation of the bow ($\alpha$).

in the head of the bow and so emission is only observed further along the bow-structure (Figure 2.10).

Smith *et al.* (1991b) went on to fit a bow C shock model to both $H_2$ line intensities and velocity profiles at Orion Peak 1, but only by assuming a very high magnetic field and that the beam size employed samples the full range of velocities and shock excitation conditions integrated over the entire bow surface. Now supported further by bow-shaped IR images of $H_2$ emission in Herbig-Haro objects (Hartigan *et al.* 1989) and bow-shaped $H_2$ wakes associated with the $Fe^+$ "bullets" in Orion (Allen & Burton 1993)

there are, however, serious concerns about the rigid requirements of the geometry and the abnormally high magnetic field required to fit bow C shock models at OMC-1. The bow shape is tightly constrained in addition to the requirement that the entire bow must be in the entrance aperture of the spectrometer. Finally, the effects of any turbulent boundary layer (with unresolvable heating and subsequent cooling zones) created within such bow-structures are, as yet, little explored.

### 2.2.6 Instabilities

We now consider the possibility that the plane-parallel, steady-state conditions assumed above are unsuitable to describe the observed shocks. Wardle (1990; 1991a,b) pursued this possibility by investigating the dynamic stability of plane-parallel steady C type shock waves to a deformed magnetic field.

#### Wardle Instability

If a plane-parallel shock is crossed perpendicularly by a magnetic field such that $B_{||} = 0$ and the fractional ionization is low enough that the ion inertia and pressure may be neglected, the net force on the ions must be zero. The dominant forces on the ion-electron fluid are the magnetic force $\mathbf{J} \times \mathbf{B}/c = -\nabla B^2/8\pi$, where $\mathbf{J}$ is the current density, and the drag force between the ions and neutrals, which is proportional to $\rho_n \rho_i (\mathbf{v}_n - \mathbf{v}_i)$. If the straight magnetic field lines are now perturbed as illustrated in Figure 2.11, the drag force now has a component parallel to the magnetic field that cannot be balanced by the $\mathbf{J} \times \mathbf{B}$ force. Ions will thus be accelerated along the field lines and accumulate in magnetic "valleys". As $\rho_i$ increases at these points, the corresponding drag force increases and the field lines are hence unstable to distortion. Wardle (1990) showed that these shocks and also oblique shocks having $B_{||} \neq 0$ (Wardle 1991b) are generally stable if the Alfvénic Mach number, $M_A = v_s/v_A \lesssim 5$, but are unstable to dynamic instability for $M_A \gtrsim 5$. The nonlinear development of such an instability has been determined by Tóth (1995) who confirms Wardle's original linear analysis. However, the perturbation grows most rapidly for wavelengths approximately equal to the shock thickness and so, after this

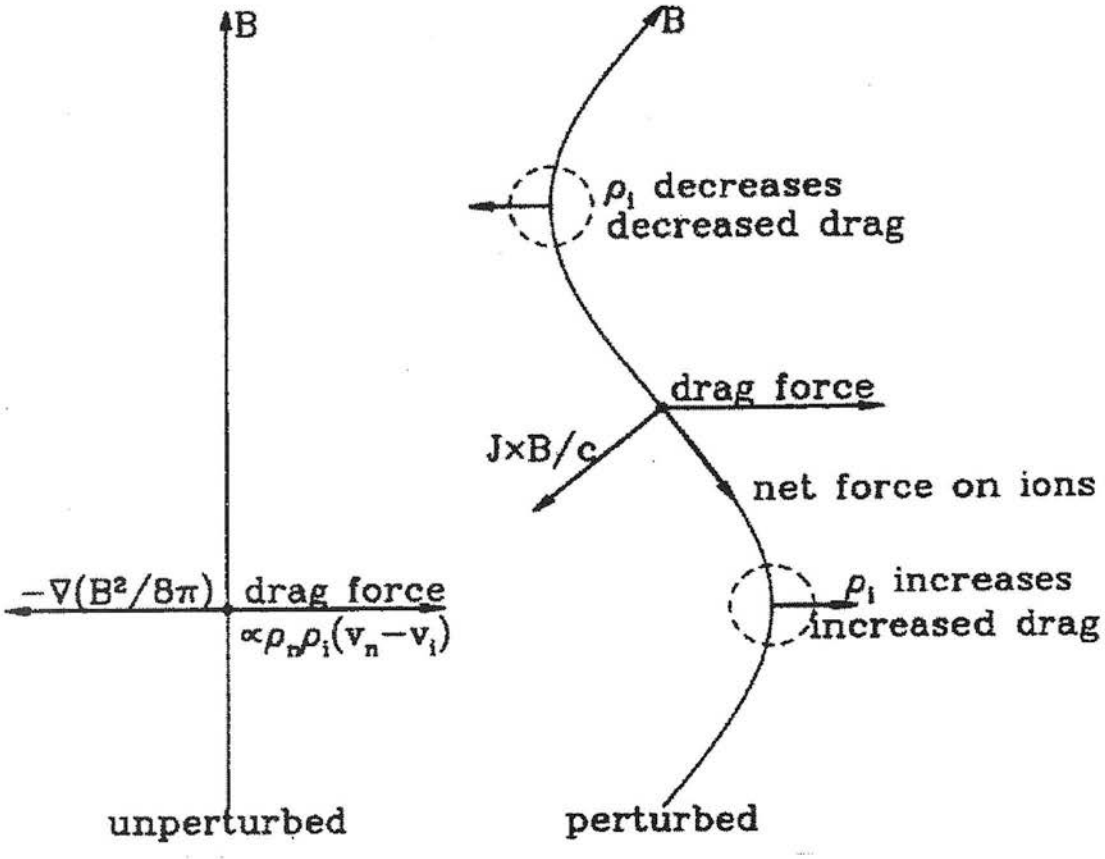


Figure 2.11: Mechanism for the Wardle instability in two-fluid MHD shock waves, from Draine and McKee (1993).

instability has grown to saturation, the emission spectrum from the shock front may be quite different to those computed for the unperturbed steady-flow solution.

### Thermal Instability

Draine & McKee (1993) describe thermal instabilities in shocks due to radiative cooling. Thermal instability results when the cooling time of the gas decreases with decreasing temperature (Field 1965, Balbus 1986) and may only apply locally on a scale small enough that the dynamics of the shock are unaffected. On larger scales, however, variations in the shock velocity can grow and increase the shock velocity over the steady state value, depending on the downstream boundary conditions imposed on the shock. Linear

stability analysis and numerical simulations of magnetized plane-parallel shocks by Tóth & Draine (1993) show that the magnetic field is not strong enough to stabilize shocks in the high density gas we are studying here, should this instability be significant.

## 2.3 Near-Infrared Spectroscopic Instrumentation and Observing Techniques

In order to measure a range of shocked $H_2$ transitions at molecular shock fronts it is necessary to use near-IR spectroscopy. The following section describes the observational techniques and instrumentation required, concentrating on the instrument of choice for this work: the near-IR Cooled Grating Spectrometer CGS4 mounted on the United Kingdom Infrared Telescope (UKIRT) at Mauna Kea (Hawaii). A detailed description of CGS4 is given in Mountain *et al.* (1990).

### 2.3.1 Atmospheric Transmission

The most important limitation on infrared observing is the absorption of light by atmospheric gases, especially $H_2O$ and also $CO_2$, $CH_4$, $N_2O$, CO, $O_3$ and $O_2$. IR Telescopes are therefore optimally situated at dry, cold sites. Isolated mountain tops are ideal since airflow is smooth and light pollution is low. The IR wavelength region is divided into a series of windows by major absorption troughs at which atmospheric transmission falls (and may vary) dramatically. Of concern to us are the near-IR bands centred on the wavelength bands ($\lambda_c$) shown in Table 2.1.

In this work we have concentrated on $H_2$ emission within the K band. As can be seen in Figure 2.12, observed emission lines may coincide with atmospheric absorption features even within an atmospheric window. Furthermore, atmospheric transmission is temporally variable and so observations must be continually recalibrated using procedures described in section 2.3.4.

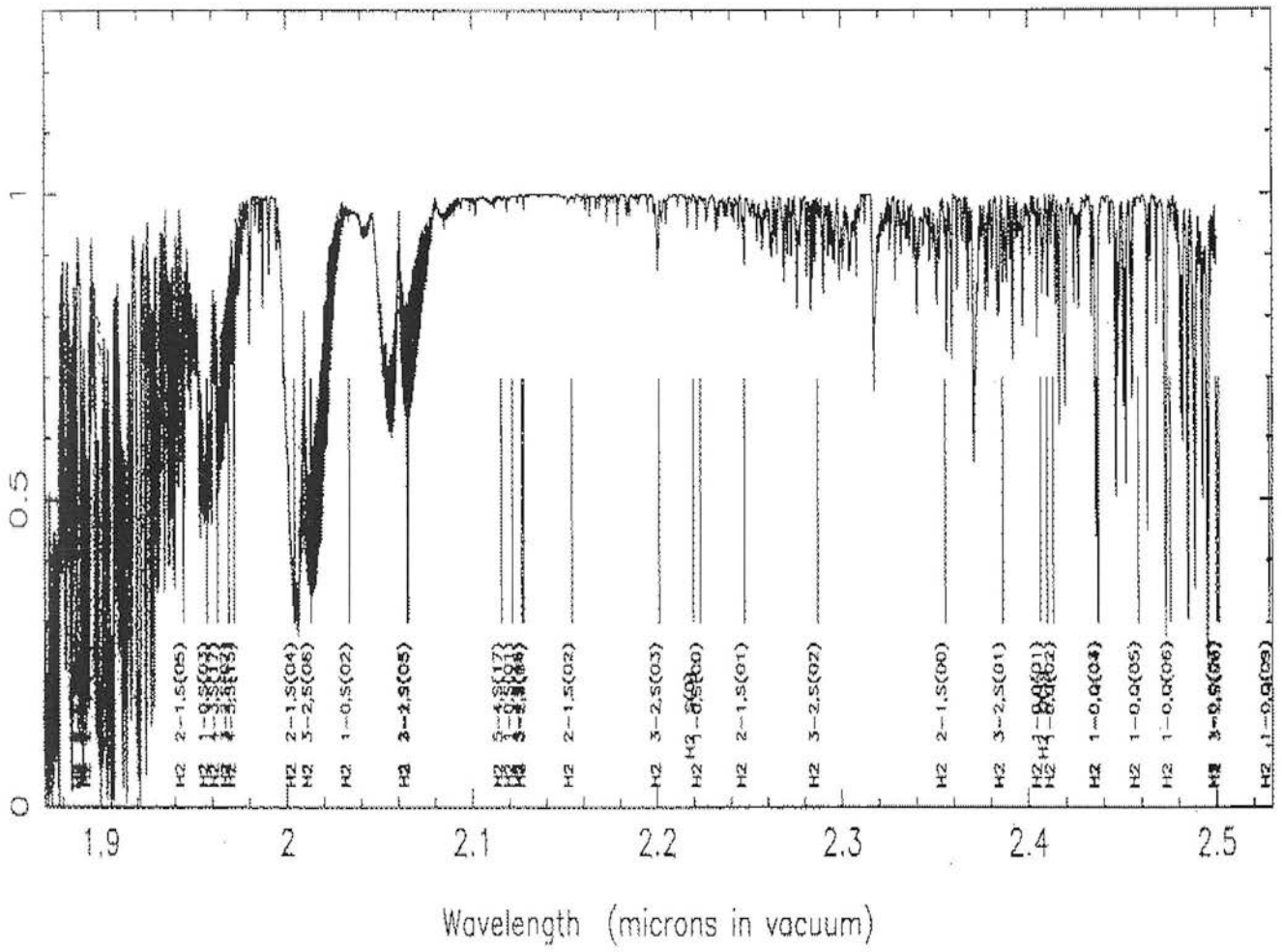


Figure 2.12: Atmospheric transmission in the K band centred at 2.2$\mu$m.

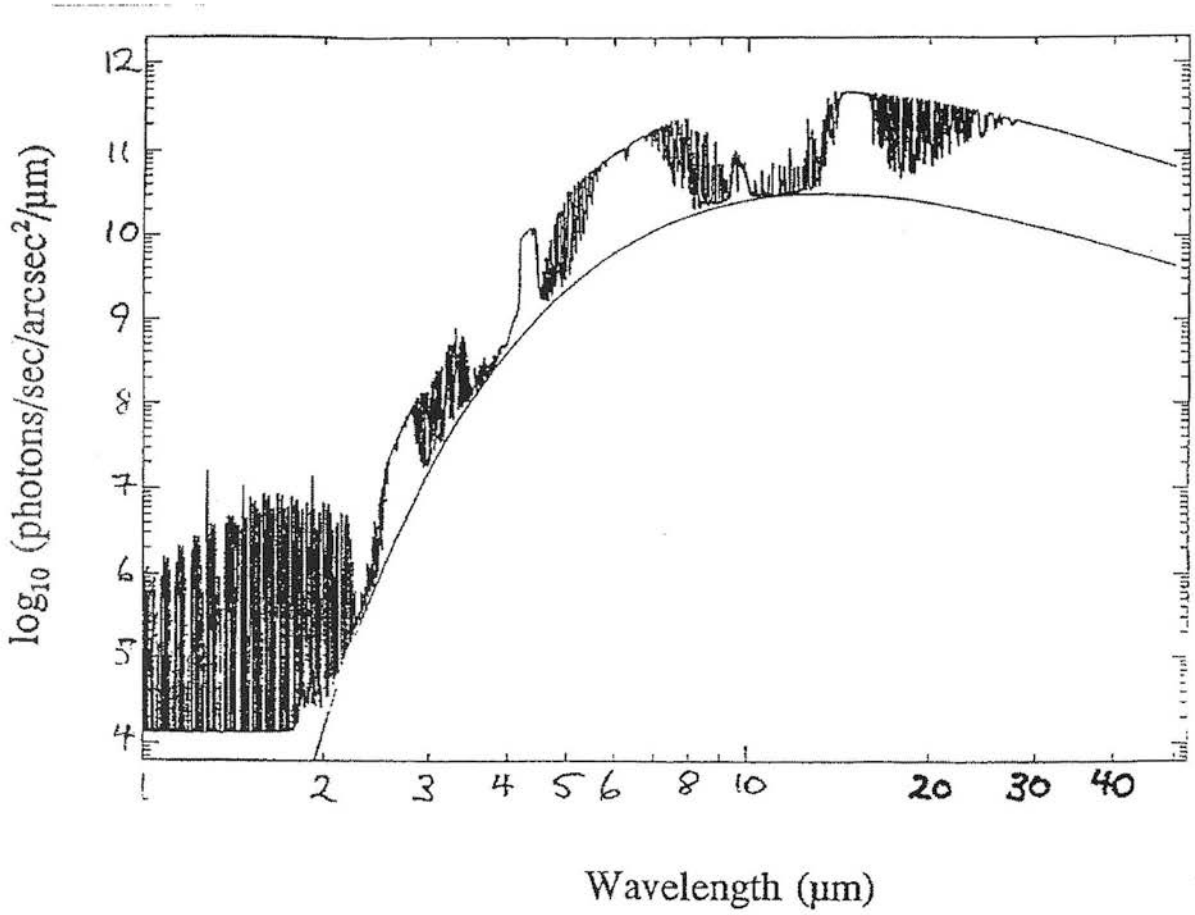


Figure 2.13: IR background at Mauna Kea including OH and thermal emission.

### 2.3.2 Sky and Telescope Background Emission

The classical difficulty of IR astronomy is that the background usually completely dominates the signal being observed (Figure 2.13). Even at an optimum location such as Mauna Kea, the UKIRT background intensity at K is $\simeq$12.5 mag/arcsec$^2$. To observe a 20th magnitude object at K therefore implies a sensitivity 1000 times greater than the sky emission and requires stable instrumentation. The background is also temporally variable (on timescales of a few minutes) and so the object and background must be measured more frequently than the variability timescale. There are two main components to the background emission:

#### OH Airglow

These are narrow molecular transitions at $\lambda < 2.3\mu$m, generated by gravity waves in the upper atmosphere followed by radiative cascade. The emission is variable in intensity by up to 10% over a 10 minute timescale and all the lines vary together.

#### Thermal Emission

Thermal background due to both sky and telescope emission resulting in a grey body emission spectrum (black body with fractional emissivity) at $\lambda > 2.3\mu$m. The telescope contribution may be reduced by decreasing the emissivity of any warm surfaces (e.g. silver has an emissivity $\simeq$0.7% whereas aluminium$\simeq$3%). Division of observations by a standard stellar spectrum observed with the same instrumental configuration includes all of these effects but, in practice, an exact cancellation of thermal absorption is not possible. This is because the sky contribution is temporally variable due to the difference in temperature between parcels of atmosphere crossing a telescope beam at varying altitude and velocity.

### 2.3.3 Instrumentation and Detectors

To reduce the infrared background the optics and detector of CGS4 are cooled with liquid nitrogen to $\sim$ 77K. IR arrays consist of a hybrid of a number of components including a silicon multiplexer to readout electronic levels and InSb or HgCdTe detector materials joined by columns of indium by bump bonding. The fundamental difference to optical detectors is the method of readout because IR detectors are readout directly whereas optical detectors use charged couple device chips (CCDs), which readout via charge transfer. CGS4 has a 256x256 InSb array which can be used in single or multiple non-destructive readout modes (see below). There is a built-in calibration unit containing a blackbody source for flat-fielding and several arc lamps used for wavelength calibration (Mountain *et al.* 1990). The spectrometer includes 75 and 150 lines per mm gratings and a high resolution echelle grating giving resolving powers in the range 150 to 40,000 depending on grating and camera focal length configuration. The resultant slit subtends

approximately $1\,\hat{''}$ by $90\,\hat{''}$ on the sky and an individual pixel subtends $\sim 1.2\,\hat{''} \times 1.2\,\hat{''}$ on the sky for the 75 and 150 lines/mm gratings and roughly $0.9\,\hat{''} \times 1.6\,\hat{''}$ for the echelle.

#### Non-Destructive Readout (NDR)

This technique allows the measurement of accumulated signal on individual pixels without affecting the signal level. Each pixel well is gradually 'filled up' as incident photons are converted to electron-hole pairs. Each measurement has an associated read noise uncertainty associated with it. By taking $n$ measurements, uniformly spaced in time, and fitting a simple slope to these independent measurements (error $\sigma_{rd}$), the effective noise ($\sigma_{ndr}$) may be significantly reduced such that for large $n$:

$$\sigma_{ndr} \simeq \frac{\sigma_{rd}}{(n/12)^{\frac{1}{2}}} \tag{2.19}$$

For example, a $60e^-$ read noise with the current 256x256 CGS4 array is reduced to $12e^-$ with 300 non-destructive reads.

### 2.3.4 Observational Techniques and Data Reduction

For a single exposure of a patch of sky (a frame), the measured signal comprises several components:

- Bias: this is a DC level on which the signal is integrated (defining the bottom of a potential well). This bias is automatically removed using the NDR method described above.
- Dark current (and instrumental background): this is a signal which integrates over time and would be measured even if the detector were completely shielded from outside radiation. For broad-band observations the dark current is generally much lower than the detected signal.
- Sky (and telescope) background: this is reasonably uniform across the array.
- Astronomical signal.

- Pixel-to-pixel gain variation: different pixels measure a different signal even for uniform illumination and so all of the detected signal (sky background and object signal) are subject to a pixel-to-pixel gain variation which is wavelength dependent.
- Non-linear detector response: at the few % level, a constant intensity does not produce a linear increase in detected signal with current near-IR detectors.

The following section describes the basic procedures involved in data reduction for the long-slit near-infrared spectrometer CGS4 on the United Kingdom Infrared Telescope (UKIRT), as used for the work presented in this thesis. A more detailed account of the dedicated CGS4 data reduction software is given in Puxley *et al.* (1992).

### Data Reduction

Every frame read (a reading of the charge accumulated in each pixel of the detector array) includes a background signal due to the electronics of the instrument and chip. This signal is known as the dark current and increases with time. It is necessary to remove this signal from every frame. The dark signal is measured by closing the instrument shutter, so that no photons fall onto the chip, and reading the array for the same length of time as will be used for the object exposures.

Next, the frames read must be flatfielded which involves removing the pixel-to-pixel variations that are intrinsic to the particular array and filter configuration in use. A flatfield is produced by exposing the chip to a uniform (flat) source of radiation. In CGS4 an internal blackbody source is observed which uniformly fills the slit via an integrating sphere. The bias (see above) and dark current is removed from this frame and the resultant image (normalised by a blackbody function) is the intrinsic pixel-to-pixel gain variations of the array as a function of wavelength. This flatfield is removed from each subsequent object, sky and arc lamp observation by dividing thus:

$$\frac{\text{object} - (\text{dark} + \text{bias})}{\text{flat}} \tag{2.20}$$

Bad pixels due to "hot" pixels on the array or cosmic ray events must also be removed. A bad pixel mask is created by plotting a histogram of the errors in the pixel values for a

relatively short exposure (a few seconds) of the dark current. Points which lie outside the range by $3\sigma$ or greater are flagged as bad. The resultant bad pixel mask is a map of the pixels to be ignored during subsequent reduction. In practice, the detector chip is also translated in the dispersion direction during an observation in order that spectral lines are sampled in sufficient detail and to compensate for bad pixels by interpolation. For example, 3 integrations at positions spread over 2 pixels provides a compromise between adequately defining the line shapes, allowing the longest on-chip exposure times before the variation in OH lines requires a sky observation to be made and eliminating the effects of bad pixels.

After flatfielding, Starlink FIGARO routines (Shortridge 1991) are employed to subtract consecutive pairs of object and sky observations. This practice also serves as an effective method of removing the dark current from the object frame, since over such a short period of time the dark current on the object and sky observations will be the same. Depending on the spatial extent of the object, a further secondary correction may be made by removing any residual sky emission from pixels at the edge of the slit and clear of the object. Next, the same pixel row from each sky subtracted object frame is extracted and placed into a separate frame.

Ripples present in the spectra must next be removed. These are caused by the object moving in and out of the slit between detector positions during the same integration so that absolute fluxes on each integration in the observation differ. The image motion occurs as a result of wind shaking the telescope or changes in atmospheric seeing. The ripple spectrum is defined on a level region of the emission (e.g. the continuum) by measuring the deviation of each point from the mean for given position in the ripple period. The ripple spectrum is then divided into the object spectrum over the entire observed range.

Finally, all of the spectra at a given spectral position are combined to give the mean spectrum using a technique called coadding. Firstly, the mean number of counts of each spectrum in the frame is determined and then each spectrum in the frame is normalised relative to the average value from all spectra. The error on each spectral point is then equal to the scatter from the mean. Normalisation accounts for the passage of a cloud

across the beam which might otherwise result in unrealistically large errors in the final spectra. Further corrections for the small effects of optical distortions in the CGS4 optics are made during wavelength and flux calibration, as described below.

### 2.3.5 Corrections for Optical Distortions

The recent introduction of a 256x256 array for CGS4 means that it is now possible to resolve and correct for small magnitude optical distortions in both the spatial and dispersive directions on the array. The corrections are made using FIGARO routines after the basic data reduction described previously and before final wavelength and flux calibration.

#### Spatial Distortion

This optical distortion manifests itself as a slight j-shaped curvature (Figure 2.14) in the spatial direction which causes spillage into neighbouring rows of the array. Hence, the spectrum of a point source does not lie perfectly along one row of the detector and the dispersion is therefore slightly dependent on the row of the array. The resultant curvature amounts to $\sim 0.5$ pixels across the 256 pixels in the spatial direction. It is measured by tracing out the spatial position of the peak emission of a stellar spectrum (using the standard star observation required for flux calibration) across the wavelength range in the given configuration and then rebinning the image data across the entire array in order to minimise this deviation.

#### Slit Curvature Correction

Observations of arc lamp lines across the detector (the arc fills the instrumental aperture) are used to wavelength calibrate spectra (see below) but show slight pin-cushion shaped curvature with respect to the direction of dispersion. The misalignment with the columns due to curvature is about 0.2-0.5 pixels across the array, depending on grating angle, and is a maximum at the edges. Therefore, after fitting a single spatial row near the centre of the array, FIGARO commands are used to derive the fit for each row across the

detector, working from the centre outwards. For each spatial row, the program looks for a given emission line peak close to where it was found in the previous fit. Finally, the image is rebinned to the linear wavelength scale determined by wavelength calibration (see below) using a set of polynomial fits to the two-dimensional arc in order to obtain the wavelength-channel relationship for each cross-section in the image.

### 2.3.6 Signal-to-Noise

The final signal-to-noise of an observation is comprised of three separate noise contributions which all add in quadrature in the absence of background variations. These are the intrinsic photon noise $N$ on a signal $S$, which is derived from Poisson statistics by

$$N = \sqrt{S}, \tag{2.21}$$

the noise on the dark current $I_d$ (also derived according to Poisson statistics) and the detector read noise $n_{rd}$. The total noise in the pixel with peak object signal is therefore

$$N_{tot} = \sqrt{S_{tot} + n_{rd}^2 + (I_d \times t_{exp})}, \tag{2.22}$$

given consistent units, where $S_{tot}$ is the total (object peak + sky) signal and $t_{exp}$ is the exposure time. Similarly, the noise in a sky pixel is

$$N_{sky} = \sqrt{S_{sky} + n_{rd}^2 + (I_d \times t_{exp})} \tag{2.23}$$

and for a software aperture covering $n_{pix}$ pixels

$$N_{ap} = N_{sky} \times \sqrt{n_{pix}}. \tag{2.24}$$

The signal-to-noise ratio in the peak pixel, $S_{pk}$, integrated within an aperture is thus

$$\frac{S_{pk}}{N_{tot}} = \frac{S_{obj}}{N_{ap}} \times \frac{1}{\sqrt{2}}. \tag{2.25}$$

Ideally, if the photon noise on the (background + object) dominates, observations are background noise limited and signal-to-noise is given simply by

$$\frac{S}{N} \propto \sqrt{t_{exp}}. \tag{2.26}$$

As the background level will vary, the optimum signal-to-noise ratio is achieved by dividing long integrations lasting up to several hours into a series of short, background-limited exposures subject to telescope and data acquisition considerations in order that overheads associated with telescope motion and data storage are minimised.

### 2.3.7 Wavelength and Flux Calibration

#### Wavelength Calibration

The wavelength scale of a given observed spectrum is calibrated by making observations of the known transitions from either an argon or krypton arc lamp. The wavelengths of the transitions are identified using the lists published by Outred (1978). The calibrated wavelength scales from the lamp observations are then used to replace the estimated wavelength scale of the observations provided by the online reduction software at the telescope. The wavelength calibration is typically accurate to better than $\pm 5 \times 10^{-4} \mu$m ($\sim 0.1$ pixels).

#### Flux Calibration

Astronomical source intensities are calibrated against a known flux standard (star) which themselves have been calibrated against a very few measurements of fundamental standard stars such as Vega (Mountain *et al.* 1985) which is defined to be at 0.0 magnitudes in all bands. Calibration against a furnace gives a resultant flux $F_\lambda$ of

$$\frac{F_\lambda}{(Wm^{-2}\mu m^{-1})} \simeq \frac{1.965 \times 10^{-8}}{(\lambda/\mu m)^5[(exp(1.4388/\lambda) - 1]} \tag{2.27}$$

at wavelength $\lambda$. A star of apparent magnitude $m$ is then flux calibrated via

$$F_\lambda(m) = F_\lambda(Vega) \times 10^{-0.4m} \tag{2.28}$$

and hence a standard star is observed as near on the sky to the object as possible and the object is fluxed relative to this standard.

Before the standard spectrum can be used as a flux calibrator, stellar absorption features must be removed. For the K band observations described in this work, the only stellar feature present is the HI Brackett $\gamma$ recombination line absorption feature which is removed by interpolating across the continuum either side of it using the 'isedit' routine in FIGARO. Atmospheric absorption features are not removed because they are intrinsic to the atmosphere and so will also be present in the object spectrum. Division of the object spectrum by the stellar spectrum will remove these features. The stellar spectrum is then divided by a blackbody function at the effective temperature of the standard star, which is normalised so that only the slope of the stellar spectrum is removed. The flux density as a function of wavelength is then calculated from the magnitude at K and divided into the stellar spectrum. The resultant spectrum is then divided into the object spectrum converting the number of data counts into a flux density. A flux at a given wavelength is thus calibrated according to

$$\frac{F_{obj}}{F_{*}} \times \text{B.B(norm)} \times S_{\lambda} \tag{2.29}$$

where $F_{obj}$ is the object flux in data counts, $F_{*}$ is the stellar flux in data counts, B.B(norm) is the normalised blackbody function and $S_{\lambda}$ is the stellar flux density.

### Line Fitting

Using the medium resolution gratings, as is the case for measuring a range of $H_2$ transitions in the K band (Chapter 4), the CGS4 instrumental profile is triangular in shape. This is because the slit has a top hat profile which is being projected onto the array whose pixels also have top hat profiles. Sampling slides the detector across the top hat profile of the slit and therefore produces a convolution of the two profiles, which is triangular. For higher spectral resolution observations of individual line profiles using the echelle grating in CGS4 (Chapter 3), the instrumental profile is Gaussian. The profile is the sum of more than one Gaussian if a number of velocity components are present.

To determine the intensities and widths of the individual transitions, spectral lines are fitted using the appropriate routine from the Starlink SPECDRE software library.

### 2.3.8 Interstellar Extinction

Before final determination of column densities, line fluxes must be corrected for the effects of interstellar extinction due to scattering and absorption of photons by dust grains (Mathis *et al.* 1977). The extinction is assumed to follow a power law of the form

$$\tau_\lambda = E\lambda^{-\beta} \tag{2.30}$$

where E is constant. The power law index, $\beta$, is determined empirically but is not well defined. Whittet (1988) analysed data in the literature and derived a best fit for $\beta = 1.70 \pm 0.08$. Draine (1988), adopted a value of $\beta \sim 1.75$ using a different dataset, for wavelengths of 0.7 to 5.0$\mu$m . Finally, He *et al.* (1995) have recently confirmed these previous results between 0.9 and 2.2$\mu$m and suggest that extinction curves converge to a single functional form in the infrared, well described by a power law of index $\beta = 1.73 \pm 0.04$, using photometric studies of 154 highly obscured OB stars in the southern Milky Way. We shall adopt this latter value in this work.

A measure of the differential extinction over the K band wavelength range studied here ($\sim$ 1.9 to 2.54$\mu$m ) is obtained directly by measuring the flux ratio of $H_2$ lines having a common upper state, which depends only on the differential extinction between the two lines, the Einstein A values, and the energies of the transitions. Using the bright $H_2$ 1-0 S(1) line at 2.1218$\mu$m and the 1-0 Q(3) line at 2.4237$\mu$m , for example, the flux ratio is expressed as

$$\frac{I_{S(1)}}{I_{Q(3)}} = \frac{\lambda_{Q(3)}}{\lambda_{S(1)}} \frac{A_{S(1)}}{A_{Q(3)}} e^{-(\tau_{S(1)} - \tau_{Q(3)})}. \tag{2.31}$$

In practice, care must be taken to avoid using lines strongly affected by atmospheric absorption features. This is discussed in Chapter 4. Combining the deduced extinction at K (2.2$\mu$m ) with the extinction law then the extinction $\tau_\lambda$ at wavelength $\lambda$ is given by

$$\tau_\lambda = \tau_K \left( \frac{\lambda}{2.2} \right)^{-1.73}. \tag{2.32}$$

Finally, the dereddened intensity $I_0$ is related to the observed intensity $I_{obs}$ using equation (1.1).

# Chapter 3

# Shocked $H_2$ & $Fe^+$ Line Profiles in the Orion "Bullet" Wakes

## 3.1 Abstract

New observations of $H_2$ velocity profiles in the Orion "bullet" wakes are extremely difficult to reconcile with existing steady-state shock models. We have observed [FeII] 1.644$\mu$m velocity profiles of selected bullets and $H_2$ 1-0 S(1) 2.122$\mu$m velocity profiles for a series of positions along and across the corresponding bow-shock wakes. Integrated [FeII] velocity profiles of the brightest bullets are consistent with theoretical bow shock predictions. Observations of broad, singly-peaked $H_2$ 1-0 S(1) profiles in the most clearly resolved bullet wakes challenge our understanding of molecular shocks. It may be necessary to model the effects of instabilities and turbulence in the Orion "bullet" wakes in order to fit our observations.

## 3.2 Introduction

The nature of molecular shocks, which play an important role in the processes of momentum and energy transfer within star forming molecular clouds (McKee 1989), is still uncertain (Draine & McKee 1993). The Orion molecular cloud is the brightest known source of shocked $H_2$ emission and as such has been the primary test bed for theoretical models. In this Chapter we describe the history of shocked $H_2$ observations in Orion and, in particular, the fundamental obstacle in modelling its excitation: namely the extremely broad velocity profiles observed. With the discovery of the Orion "bullets" and associated $H_2$ wakes, we describe an experiment to test previous models to breaking point by detailed observations of $Fe^+$ and $H_2$ line profiles using CGS4 with the new 256x256 array at UKIRT.

### 3.2.1 Overview of the Orion Outflow

The outflow associated with the KL infrared nebula in Orion is the best studied as its closeness (1500 light years) permits higher spatial resolution and signal-to-noise ratios than are possible in other massive star forming regions. It is located about 0.4 light years ($1\hat{}$) in projection to the northwest of the Trapezium cluster of young OB stars that excites the M42 ionized region. The KL nebula was first detected by Rieke *et al.* (1973) as an infrared nebula extending over about $0.5\hat{}$ with several emission peaks. These include massive young stars (BN and IRc2) embedded in molecular material and lower luminosity young stars together with dense young clumps of gas heated by BN and IRc2. IR emission peaks may also coincide with holes in the cooler foreground dust distribution (Wynn-Williams *et al.* 1984). The larger scale distribution of molecular gas is arranged in a ridge running northeast to southwest that is part of a giant molecular cloud extending for more than 200 light years. The radial velocity of the gas along the ridge shows a shift at the position of the KL region that has been interpreted as either rotation seen edge-on around the KL region or as the collision of two clouds of different radial velocities (Ho and Barrett 1978, Bastien *et al.* 1981). The distribution of velocities close to the KL nebula corresponds to the motions of gas orbiting about a central condensation of material with a mass of more than $20M_{\odot}$ (Vogel *et al.* 1985).

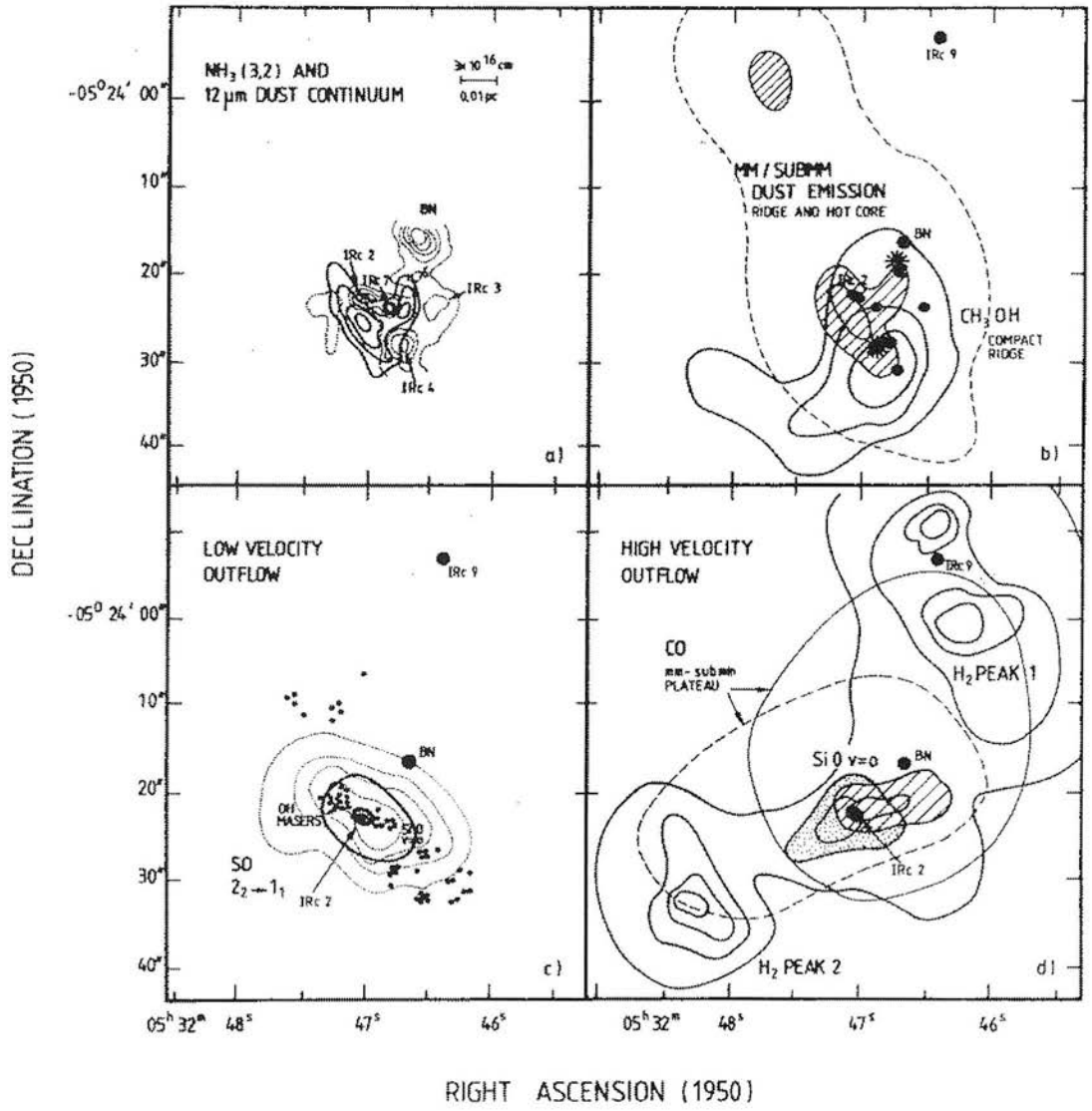


Figure 3.1: Composite of spatial distributions of different gas components at the core of BN-KL from Genzel & Stutzki (1989) including standard source designations. (a) Comparison of a $0.9''$ resolution $12\mu$m infrared continuum image (dotted contours) with a $1.2''$ VLA map of the 1.2cm $(J, K) = (3, 2)$ inversion transition of $NH_3$ (heavier contours). (b) Quiescent gas/dust maps in which shaded regions denote the hot core and extended ridge traced by 3mm dust emission. Filled circles indicate the positions of compact IR sources. (c) The low velocity outflow traced in 1.3cm $H_2O$ masers (dots), 18cm OH masers (asterisks), 3mm SiO $v = 0, J = 2 - 1$ emission (heavy contours), and SO $2_2$-$1_1$ 3mm line emission (dotted contours). (d) High velocity flow and shocked gas. The blueshifted (shaded) and redshifted (stipled) high velocity gas close to IRc2 is traced in the 3mm SiO $v = 0, J = 2 - 1$ transition while the extended high velocity "plateau" is traced in the mm transitions of CO and $HCO^+$. Outside the plateau are the $6''$ resolution contours of the $2.122\mu$m $H_2$ 1-0 S(1) line emission mapped by Beckwith *et al.* (1978).

Genzel and Stutzki (1989) review the parameters of the outflowing gas and distinguish a low velocity ($18 \mathrm{km\,s^{-1}}$) "expanding doughnut" flow, a high velocity flow or "plateau" and high velocity shocked gas. Each component is identified with a different pattern of spatial distribution (Figure 3.1), kinematics and excitation. Measurements of the proper motions of $H_2O$ masers (Genzel *et al.* 1981) and of Herbig-Haro objects (Axon & Taylor 1984) together with spectroscopic evidence of blueshifted, high velocity gas in absorption against the dust continuum (e.g. Scoville *et al.* 1983) demonstrate that the flows represent gas streaming away from the BN-IRc2 cluster. The centre of the outflows is within a few arcseconds of IRc2 and the dynamical age is of order $10^3$ years. The inferred mass loss rate, as derived from that age and the total mass involved is $10^{-3\pm0.3} \mathrm{M_\odot\ yr^{-1}}$.

The low velocity flow extends northeast-southwest along the dense quiescent ridge (Figure 3.1c) and can be traced from within $0.2\hat{''}$ of IRc2 to $\sim 20\hat{''}$ from the star with a constant velocity range of $\sim 35 \mathrm{km\,s^{-1}}$ (Genzel & Stutzki 1989). The flow is modelled as a spherically symmetric outflow which impacts the dense molecular ridge at $R = 10^{17}$cm and lead to the formation of the "expanding doughnut" having a hydrogen density $\gtrsim 10^7\ \mathrm{cm^{-3}}$ (Stutzki *et al.* 1988). The second flow has a much larger velocity range ($\Delta v \leq 250 \mathrm{km\,s^{-1}}$) and stretches approximately northwest-southeast, i.e. perpendicular to the low velocity flow and ridge, with the characteristic bipolar structure seen in many star forming regions (Chapter 1.3). The two flows have been interpreted as the channeling of one single high velocity flow by the surrounding cloud (Cantó *et al.* 1981) but they remain distinct to within $2\hat{''}$ ($10^{16}$cm) of IRc2, far inside the outflow cavity. Therefore the two flows may originate from different stars or else the gas has to be channeled in the immediate environment of the star, perhaps by a circumstellar disk.

The high velocity flow associated with the shocked gas (Figure 3.1d) impacts the surrounding cloud about $30\hat{''}$ from the dynamical centre, creating high velocity $H_2O$ masers and a region of shocked molecular gas cooling in infrared and submm lines including $H_2$ (Shull & Beckwith 1982) and the far-infrared lines of rotationally excited CO and OH (Watson *et al.* 1985). In addition to the main outflow source of size $\leq 30\hat{''}$, Wiseman & Ho (1996) have recently measured straight, elongated filaments consisting of bead-like chains of dense gas extending out more than 0.5pc from the central core of the cloud

in the inversion transitions of $NH_3$ (1,1) and (2,2). It is unclear if these are connected with the outflow associated with the Herbig-Haro objects in this region (Axon & Taylor 1984).

### 3.2.2 Previous Shocked $H_2$ Observations in Orion

Following the initial discovery, Beckwith *et al.* (1978) mapped the $H_2$ 1-0 S(1) line emission over a $2\hat{'}$ x $2\hat{'}$ field about BN-KL at $5\hat{''}$ spatial resolution, identifying the brightest region as Peak 1 (OMC-1) centred on $05^h\,32^m\,46.09^s$, $-05^\circ\,23'\,57.3''$ [1950] at which to concentrate further studies. Here, they were able to measure the intensities of the brightest near-infrared $H_2$ emission lines including the 1-0 S(0), 1-0 S(1), 1-0 S(2), 1-0 Q(3) and the 2-1 S(1) transitions. By calculating the ratio of intensities of these lines, a vibrational $H_2$ excitation temperature of $T_{vib} = 2000 \pm 300$K was found to be consistent with a thermalised Boltzmann distribution of level populations for an average column density of $\sim 10^{19}$ cm$^{-2}$. Pure radiative excitation, as described by Black & Dalgarno (1976) was ruled out.

In 1979, Nadeau & Geballe published high spectral resolution ($\sim 20$km s$^{-1}$ ) velocity profiles of the $H_2$ 1-0 S(1) profiles in this region. After deconvolution of the instrumental profile, the intrinsic full width at half maximum (FWHM) velocities of the lines was found to lie in the range 18 to 58km s$^{-1}$ . They deduced two separate components to the profiles (depending on position) at this resolution having expansion velocities from BN-KL of $\sim$40km s$^{-1}$ and a much smaller component at $\sim$100km s$^{-1}$ . Hence, it was clear that the excitation of the observed $H_2$ could not be caused by a single plane shock front moving at or below the dissociation speed limit of $H_2$ for hydrodynamic J shocks of $v_s \lesssim 24$km s$^{-1}$ (Chapter 2.2). Furthermore, the observed asymmetries of the line profiles were shown by Beckwith *et al.* (1979) to be inconsistent with models having variable extinction across the source alone. The magnitude of foreground extinction, however, was revised significantly downwards by Scoville *et al.* (1982) to $A_{2.1\mu m} \simeq 1.2-2$ magnitudes and shown to vary by a factor of 2 on scales of $\sim 4\hat{''}$. The average excitation temperature was confirmed as $T_{vib} = 2010 \pm 50$K for the transitions measured.

Nadeau *et al.* (1982) presented higher spatial resolution ($5\hat{''}$ ) velocity profiles of the

$H_2$ 1-0 S(1), 1-0 S(0) and 2-1 S(1) profiles for a range of positions about OMC-1. In addition to the broad (FWZI $\geq$100km s$^{-1}$ ), asymmetric profiles observed previously at OMC-1 itself, they noted narrower, symmetric profiles towards the periphery of the region having an intrinsic FWHM = 22$\pm$2km s$^{-1}$ . The profiles were all identical in shape and found not to vary temporally. Since thermal broadening alone at $\sim$2000K results in a line profile of FWHM $\leq$7km s$^{-1}$ , it was concluded that the high velocity $H_2$ comes from shocked gas in the flow while the low velocity $H_2$ comes from shocked gas in the molecular cloud. Geballe *et al.* (1986) later ruled out scattering due to intervening dust grains as an explanation of the broad lines since they found the $H_2$ 1-0 O(7) line at 3.81 $\mu$m to be broader than the 1-0 S(1) line at 2.12$\mu$m in the centre of the cloud. Scattering of photons by dust particles must decrease at longer wavelengths. First spectropolarimetric measurements by Burton *et al.* (1988) found no evidence for a change in polarisation across the $H_2$ 1-0 S(1) profile as would be associated with dust scattering. They proposed that the extended blue wings were produced by fast moving clumps embedded within the outflow while the symmetric line core resulted from shocked gas at the edges of an expanding outflow cavity.

Following the initial detection of $H_2$ line emission (Gautier *et al.* 1976, Beckwith *et al.* 1978), models for their excitation were advanced involving planar hydrodynamic jump(J) shocks (Hollenbach & Shull 1977, Kwan 1977, London *et al.* 1977). These models give shocked $H_2$ line ratio predictions including that the 1-0 S(1)/2-1 S(1) line ratio is of order $\sim$ 10 for a 10km s$^{-1}$ shock wave moving into gas of density $10^5$ cm$^{-3}$. However, as described in Chapter 2, such a shock must dissociate $H_2$ at velocities exceeding $\sim$ 24 km s$^{-1}$ . Therefore, when Nadeau & Geballe (1979) observed individual $H_2$ line profiles in this region having FWZI line widths exceeding 150 km s$^{-1}$ this model was quickly brought into doubt. Since molecular clouds have measurable magnetic fields carried by ions, such difficulties might be overcome by modelling magnetohydrodynamic shocks having continuous C-type shock fronts (Draine & Roberge 1982, Chernoff *et al.* 1982, Draine *et al.* 1983).

A major problem of fitting planar C shocks to the Orion observations is that the predicted excitation spectrum greatly underestimates the higher energy level populations (and hence column densities) observed towards OMC-1 (Brand *et al.* 1988). Secondly,

such a model predicts the line ratios of two high excitation lines must vary considerably given small changes in local physical conditions, whereas Brand *et al.* (1989a) demonstrated that the ratio of the 1-0 O(7) to 0-0 S(13) $H_2$ lines, at excitation energies of 8300K and 17000K respectively, remains constant over the outflow. These two difficulties are naturally explained by a simple J shock (Brand *et al.* 1988) assuming higher density gas than the early models. Of course, such a model is inconsistent with the observed profiles and also implies that $H_2$ is the dominant coolant compared to $H_2O$ or CO.

A solution that might reconcile the contradictory evidence thus far presented is to propose that we observe one or more bow shocks along a given line of sight. If the outflow is at least partly composed of dense clumps of material either ejected or swept up by a wind, then a bow shock will form around the leading edge of each clump as it drives through the molecular gas. The shock velocity and hence degree of excitation must vary as the normal component of the clump velocity, depending on the geometry of the bow. Hence, in observations unable to spatially resolve individual clumps, the complete range of excitation conditions would be observable at any position, from a dissociated cap with atomic line emission, through to molecular line emission from cooler gas further down the wake. Line ratios would also be constant if all bows conformed to a generic shape. A series of papers (Smith & Brand 1990a, 1990b, 1990c, Smith *et al.* 1991a, 1991b, Smith 1991) had an impressive array of successes accounting for a number of observational features with such bow C shock models.

However, the fast C bow shock solutions create their own difficulties. To fit the broad FWZI $H_2$ 1-0 S(1) profile width of 140km s$^{-1}$ observed with a $5''$ aperture at OMC-1 by Brand *et al.* (1989b) requires C shocks that do not dissociate $H_2$ at velocities in excess of 60-70km s$^{-1}$ . This, in turn, implies a very high magnetic field of $\gtrsim$50mG, somewhat higher than recent estimates of $\sim$10mG determined from the dispersion of the position angles of the $H_2$ polarization vectors (Chrysostomou *et al.* 1994). The measured value is sensitive to estimates of the density and turbulent velocity. The value quoted is determined by assuming $n \sim 10^6$cm$^{-3}$, which is in agreement with shock modelling (Brand *et al.* 1988) and detection of $J = 3 - 2$ transitions of HCN and $HCO^+$ (White *et al.* 1986). The turbulent velocity is estimated to be of the order of $\sim$ 1 km s$^{-1}$ from the FWHM of the Doppler-broadened lines of CS $J = 2 - 1$ transitions (Mundy *et al.* 1988).

However, if the velocity is as high as 3 km $s^{-1}$ this combines with a maximum uncertainty of up to a factor of 10 in the density to give a range of $\sim$ 3-95 mG for the strength of the magnetic field. Ionization fractions in excess of $10^{-5}$ to $10^{-4}$ in the pre-shock gas will tie the neutral fluid to the ionized fluid, effectively freezing the magnetic field. This would eliminate the magnetic precursor and make the shock front J type (Smith 1994).

There are further difficulties. The full range of observed shocked $H_2$ excitation conditions (Brand *et al.* 1988) must be sampled within the $5''$ beamsize placing rigid geometrical requirements on the (unknown) bow geometry at OMC-1. Furthermore, the shock front in a given bow will be oblique along the bow which may give rise to the Wardle instability in the case of C shocks (Wardle and Draine 1987, Wardle 1991a,b).

Recent near-IR imaging of Orion with $0.5''$ spatial resolution in the emission lines of $H_2$ (2.122 $\mu$m) and [FeII] (1.644 $\mu$m) has significantly advanced our view of the shocked molecular outflow (Allen & Burton 1993). Images of the region to the Northwest of OMC-1, at which we shall concentrate our studies, are displayed in Figures 3.2 and 3.3. Many new Herbig Haro-type objects were revealed, visible as $Fe^+$ "bullets", at the heads of wakes of $H_2$ emitting gas. The "bullets" (apparently originating within $5''$ of IRc2) appear to have been ejected over a wide opening angle. Considering also the [OI] 6300Å line widths of up to 380 km $s^{-1}$ measured towards the brightest "bullets" previously identified in this region (Axon & Taylor 1984), an explosive origin in the core of Orion within the last $10^3$ years is suggested. We cannot yet identify the cause of this event although an FU-Orionis event (Hartmann & Kenyon 1985) is speculated.

### 3.2.3 Outstanding Problems and Observational Aims

We have established that planar C(magnetised)-shock models cannot explain the $H_2$ line intensities in Orion or any other outflow, while planar J-shock models can (Brand *et al.* 1988). However, neither planar nor bow J-shock models can reproduce the line profiles observed at Peak 1 in Orion (Brand *et al.* 1989b). It is just possible to fit both $H_2$ line profiles and ratios in this region using highly magnetised C-shock models (Smith *et al.* 1991b). Measurements of $H_2$ excitation conditions which remain constant throughout the bright part of the Orion outflow, however, are not easily explained by any bow shock

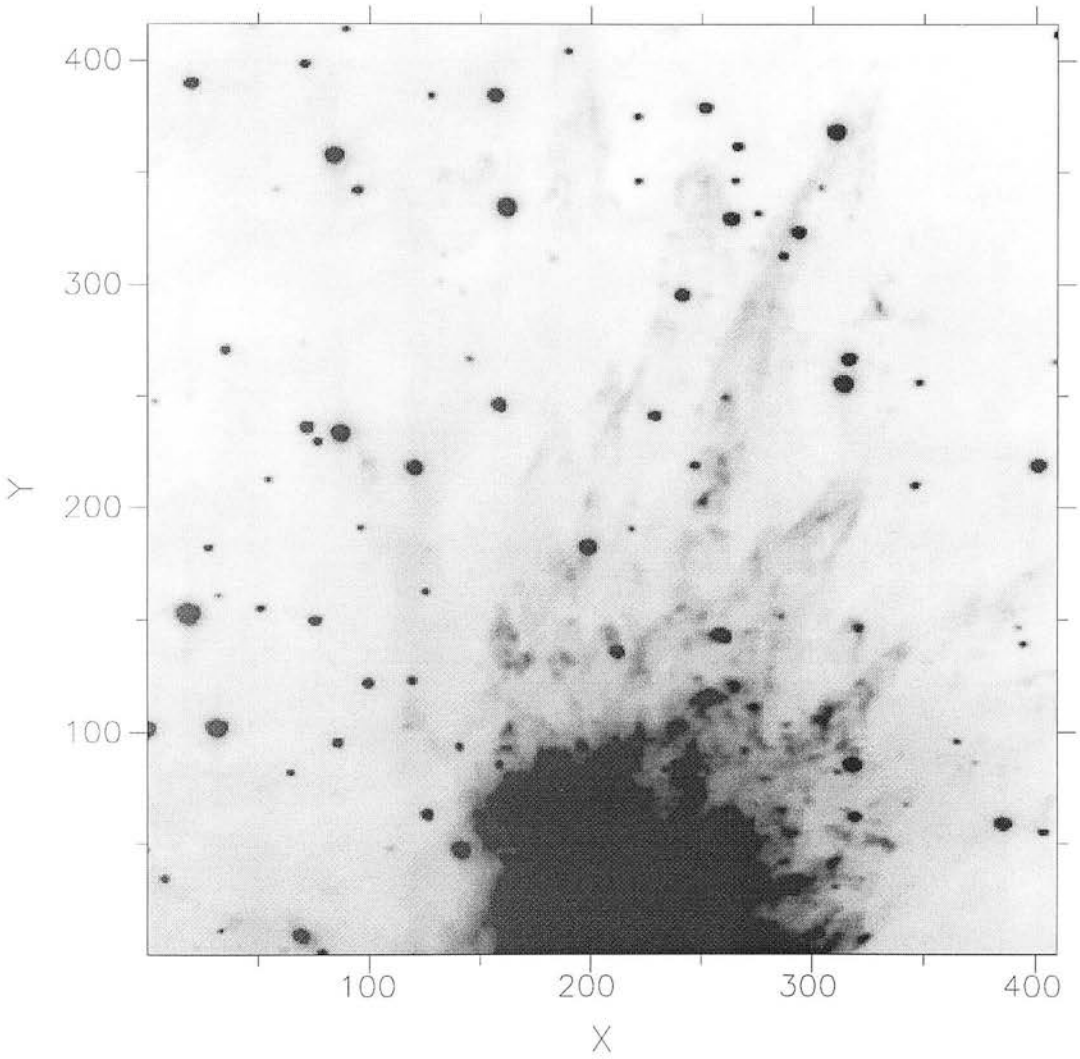


Figure 3.2: Narrowband image in the $H_2$ 1-0 S(1) line at 2.12$\mu$m of the northern outflow from OMC-1, consisting of 16 frames taken with the IRIS near-infrared camera on the 3.9m Anglo Australian Telescope (Allen & Burton 1993). Right Ascension and Declination axes are labelled by pixel number where the image scale is $0.27''$ per pixel. OMC-1 is located in the brightest region, centred on (229,13). At least 20 hollow structures or "wakes" are resolved, closely resembling bow shocks. Compact [FeII] emission knots coincident with the tips of these wakes are obvious in Figure 3.3.

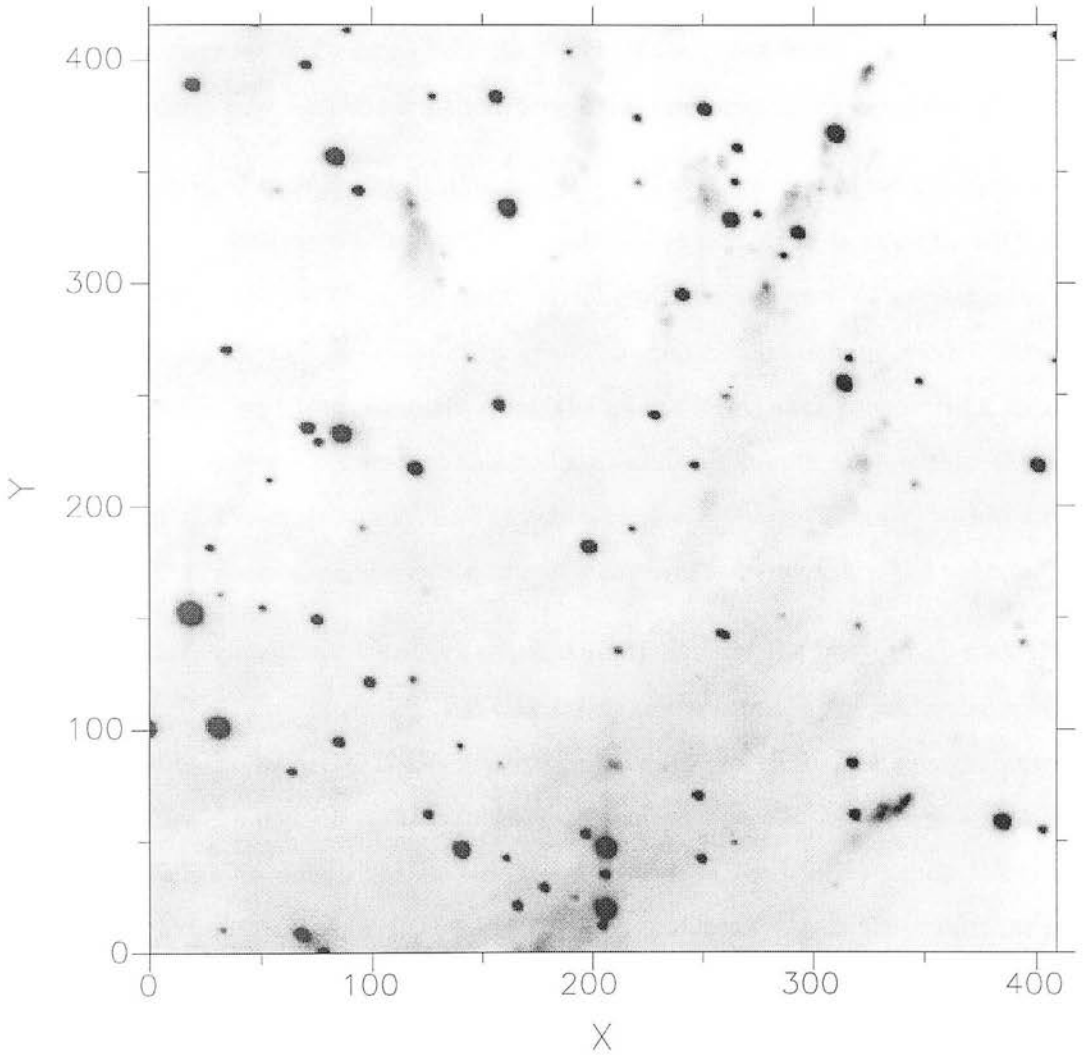


Figure 3.3: As Figure 3.2 but now imaged in the [FeII] $a^4F_{5/2} - a^4D_{7/2}$ line at 1.64$\mu$m (Allen & Burton 1993). The "bullets" appear as knots of bright emission coincident with the tips of the $H_2$ wakes in Figure 3.2. Much of the diffuse nebulosity is due to the 12-4 transition of HI which also lies within this filter bandpass.

models (Brand *et al.* 1989b, McKee 1989).

Crucially for molecular shock studies, the newly discovered "bullets" and wakes are resolved spatially to be typically 2-4$''$ in size and the wakes or "fingers" a factor of two or so longer behind them. This corresponds to a scale of 0.005 to 0.01 pc for each bullet at the distance of Orion. While the width of the shock front remains unresolved, if these are indeed bow shocks then their properties may now be determined along their wakes.

The $H_2$ 1-0 S(1) line profile in OMC-1 has been measured through a 5$''$ beam at 12 $\mathrm{km\,s^{-1}}$ channel resolution by Brand*et al.* (1989b). It is smooth with an enhanced blue wing and FWZI of 140 $\mathrm{km\,s^{-1}}$ . There is no evidence of sub-structure within the profile. As already discussed, this cannot be reconciled with any planar shocks. Even an ensemble of emitting cloudlets along the line of sight, each contributing its own velocity profile, requires an unreasonable redistribution of momentum within the source. The individual cloudlets would have to achieve velocities of $\pm 70 \mathrm{km\,s^{-1}}$ within a cylinder 0.01 pc in diameter along the entire line of sight everywhere within the source.

Alternatively, a bow shock can naturally explain the large profile width. Given the 1.2$''$ spatial and 23 $\mathrm{km\,s^{-1}}$ FWHM spectral resolution achieved using CGS4 with the echelle and new array, it has become possible to search for the changes expected within the Orion "bullet" $H_2$ wakes, if they are indeed bow shocks. Given the known physical constraints on conditions in Orion, we expect to see the $H_2$ shock velocity vary from the maximum for J or C shocks ($25 \lesssim v_s \lesssim 50 \mathrm{km\,s^{-1}}$ ) to the minimum necessary to excite the lines at all ($\gtrsim 8 \mathrm{km\,s^{-1}}$ ). Each line of sight will sample a range of conditions (and velocities) and so this must be incorporated into any interpretation. This problem has been carefully analysed for atomic line emission by Hartigan *et al.* (1987), who show that the FWZI of the integrated profile over a single bow shock must be equal to the speed of the "bullet" itself. By also measuring the maximum and minimum velocity one can further deduce the orientation to the line-of-sight. Therefore, measurement of $Fe^+$ profiles for a "bullet" provides an estimate of the velocity and orientation of the associated $H_2$ bow and therefore it is possible to compare measured and expected variations in the $H_2$ shocks with position in the bow in some detail.

Fernandes and Brand (1995a) have demonstrated that molecular hydrogen emission

from the bow shock-shaped HH7 is well explained as a C-shock in a bow configuration in which the 'cap' is completely dissociated, and $H_2$ fluorescence produced by Lyman alpha resonance pumping in the hot post-shocked layers (Black & van Dishoeck 1987) in the cap irradiate the downstream flow. The same type of shock + fluorescent spectrum as seen in HH7 has been seen in DR21 (Fernandes 1993). It was expected that the bow shocks in Orion could be similarly excited.

### 3.2.4 Object Classification

In this work I shall refer to the "bullets" and associated wakes in Orion by a new system of designation of compact sources and stars in M42, proposed by O'Dell *et al.* (1994). This is important as there is now a proliferation of observations in this region, many having separate classification schemes. Possible confusion and difficulty of cross referencing are avoided in the new system, based on the E2000 position on the sky. The first three digits indicate the position of right ascension (E2000), and the second three digits indicate the declination, with the box so designated subtending $1.5\,\widehat{\mathrm{m}}$ in right ascension and $1.0\,\widehat{\mathrm{m}}$ in declination. The common values for the inner region of M42 of $5^{\mathrm{h}}\,35^{\mathrm{m}}$ and $-5^{\circ}\,20'$ are not included. Hence, a Herbig Haro object located at $5^{\mathrm{h}}\,35^{\mathrm{m}}\,23.123^{\mathrm{s}}$, $-5^{\circ}\,27'\,38.9''$ would be M42 HH231-739. Extra digits are included before those above in the case of objects lying outside the common range. Individual slit and profile positions within the "bullets" and wakes are referred to by their Allen & Burton (1993) image coordinates (Figures 3.2 and 3.3).

## 3.3 Observations

High resolution, near-infrared, long-slit echelle spectra were measured of the [FeII] $a^4F_{5/2}-a^4D_{7/2}$ line profile at $1.644\mu$m on two of the most prominent "bullets" associated with the most clearly defined $H_2$ wakes. $H_2$ 1-0 S(1) profiles were then measured at a range of positions along and across the associated wakes. The observations of the [FeII] emission from the "bullet" M42 HH126-053 (previously denoted M42 HH7) were carried out at UKIRT on the night of 19th September 1992 by Amadeu Fernandes with the cooled grat-

ing spectrometer CGS4 and the old (62x58) detector array. The [FeII] observations for the "bullet" M42 HH120-114 (no previous designation) and the observations of the $H_2$ wakes associated with both "bullets" were carried out at UKIRT on the nights of 5-8th October 1995 with CGS4. At this time CGS4 had been fitted with the new 256x256 pixel array and was used in the echelle mode with the short 150mm focal length camera giving a pixel scale of $\sim 1.7''$ (exact scale depending on wavelength) in the spatial direction and $\sim 0.9''$ in the dispersion direction. Spectra were fully sampled by physically shifting the array by 1/2 pixel, so that two detector positions were observed per resolution element. Each spectral image was bias subtracted and flat-fielded using a black-body calibration source. As the background and array bias varies between the two detector positions used to sample profiles, the baselines in the resultant interlaced spectra can exhibit a sawtooth profile. If present, this is corrected for by fitting linear baselines to the odd and even pixels on either side of the emission line in each row of each spectral image respectively (Chapter 2.3). Removing the odd and even pixel baselines, row by row, corrects for the ripple in the final reduced spectra. All profiles were velocity calibrated relative to the dynamical Local Standard of Rest.

The [FeII] profile observations of the "bullet" M42 HH126-053 required five groups of object-sky-sky-object observations at one slit position only. An offset sky position at $+300''$ West in Right Ascension (RA) was used, in order to be clear of M42 nebula emission. The slit was positioned so that the middle row on the array was fixed at the brightest "bullet" intensity and oriented at an angle of $+25.5^\circ$ West of North on the sky, along the associated $H_2$ wake axis. Wavelength calibration was achieved by observing an Argon arc lamp with the same instrumental configuration and measuring the emission line at $\lambda_{air} = 1.6441\mu$m together with OH emission lines present in sky spectra at $\lambda_{air} = 1.6415$ and $1.6442\mu$m . It was not necessary to correct for optical distortions with the old array as they are unresolved. A standard star (BS1784) was observed in order to flux calibrate this observation but was later determined to be dominated by stellar absorption features at this wavelength and so not used. A relative, rather than an absolute flux calibration only was sufficient in this case. The spatial scale of a single CGS4 pixel in this configuration was measured by sliding a star by 20 pixels along the slit and measuring the resultant shift in Declination (DEC). It was determined to be $2.16''$ for a $1.1''$ wide

slit.

The [FeII] profile observations of the fainter "bullet" M42 HH120-114 required nine groups of object-sky-sky-object observations at two slit positions. In each case, an offset sky position at $+600''$ West in RA was used, as necessary to be fully clear of M42 nebula emission. Slit positioning was achieved by small step offsets from the nearby IR reference objects: BN and IRc9, whose positions are exactly known. In addition, pointing checks were made at approximately hourly intervals by offsetting to three nearby stars and measuring any drift in RA or DEC from the expected position. The drift was found to be typically $\lesssim 0.5''$ and rarely exceeded $1.0''$. The slit was oriented at an angle of $+22°$ West of North, along the associated $H_2$ wake axis. Wavelength calibration was achieved by observing an Argon arc lamp with the same instrumental configuration and measuring the emission lines at $\lambda_{air} = 1.6441\mu$m , $1.6524\mu$m . OH emission lines present in sky spectra were also used to check the wavelength calibration. It was necessary to rebin the resultant images to correct for small optical distortions in both the spatial and dispersive directions of the array using routines in the STARLINK Figaro Software Library before proceeding to wavelength calibrate the data. The nearby UKIRT standard star BS1937 (K= 4.47 mag) was also observed at the same airmass as Orion to flux calibrate the data. No stellar absorption features are present in this wavelength range. With a slit width of 1 pixel ($\sim 0.9''$), a velocity resolution of 14.1 $\mathrm{km\,s^{-1}}$ per pixel was obtained. The effective velocity resolution with this instrumental configuration was determined to be $21.7 \pm 0.4 \mathrm{km\,s^{-1}}$ by measurement of the FWHM of the best Gaussian fit to unresolved Argon arc lines. This was found to be consistent with fits to unresolved sky OH lines. The spatial scale of a single CGS4 pixel in this configuration was determined, using the method described previously, to be $1.689''$ for a $0.9''$ wide slit.

For the $H_2$ 1-0 S(1) profile observations in both "bullet" wakes, five groups of object-sky-sky-object observations were taken per on-source slit position using the same sky offset of $+600''$ West in RA and oriented at the previously given position angles on the sky. All other observing procedures were identical to above except that wavelength calibration was achieved by observing a Krypton arc lamp in 26th order with the same instrumental configuration and measuring the emission lines at $\lambda_{air} = 2.1215\mu$m and $2.12391\mu$m . OH emission lines present in sky spectra were also used to check the wave-

length calibration. As before, it was necessary to rebin the resultant images to correct for small optical distortions in both the spatial and dispersive directions of the array using routines in the STARLINK Figaro Software Library before proceeding to wavelength calibrate the data. With a slit width of 1 pixel ($0.9\widehat{''}$), a velocity resolution of 14.1 $\mathrm{km\,s^{-1}}$ per pixel was obtained. The effective velocity resolution with this instrumental configuration was determined to be $23.1\pm0.3\mathrm{km\,s^{-1}}$ by measurement of the FWHM of the best Gaussian fit to unresolved Krypton arc lines. This was found to be consistent with fits to unresolved sky OH lines. The spatial scale of a single CGS4 pixel in this configuration was determined, as previously described, to be $1.744\widehat{''}$ for a $0.9\widehat{''}$ wide slit. An artificial, instrumental "ghost" feature was newly identified on both arc lamp and object spectra. It was measured to be a blueshifted secondary at $-51.9\pm9.5\mathrm{km\,s^{-1}}$ relative to the primary line and to have a flux of 4.5% relative of the primary (real) line. It was therefore only detectable at the brighter on-wake positions and could be accounted for during line-fitting.

The $H_2$ trails behind the "bullets" studied in Orion are of order $40\widehat{''}$ long, $10\widehat{''}$ wide so it was necessary to observe at 5 slit positions per wake in order that resultant velocity profiles could be compared for a range of positions both along and across the wakes to search for the predicted changes within the proposed bow shock structure.

## 3.4 Results

### 3.4.1 M42 HH126-053 [FeII] 1.644 $\mu$m Profiles

Observations of the [FeII] 1.644$\mu$m line profiles from the bullet M42 HH126-053, shown in Figure 3.4(a) alongside its corresponding $H_2$ wake (Figure 3.4b), apparently oriented in or close to the plane of sky, are displayed in Figure 3.5. The profiles are broad and strongly peaked at a velocity of $\simeq 8\mathrm{km\,s^{-1}}$, close to rest velocity of the ambient medium of $+9\mathrm{km\,s^{-1}}$ (Goldsmith *et al.* 1975), measured relative to the dynamical local standard of rest. It can be seen that total velocity range is highest at the leading edge of the emission (top rows), as is expected at the head of a bow shock where the gas is shocked at velocities approaching the full driving velocity of the "bullet" in two components,

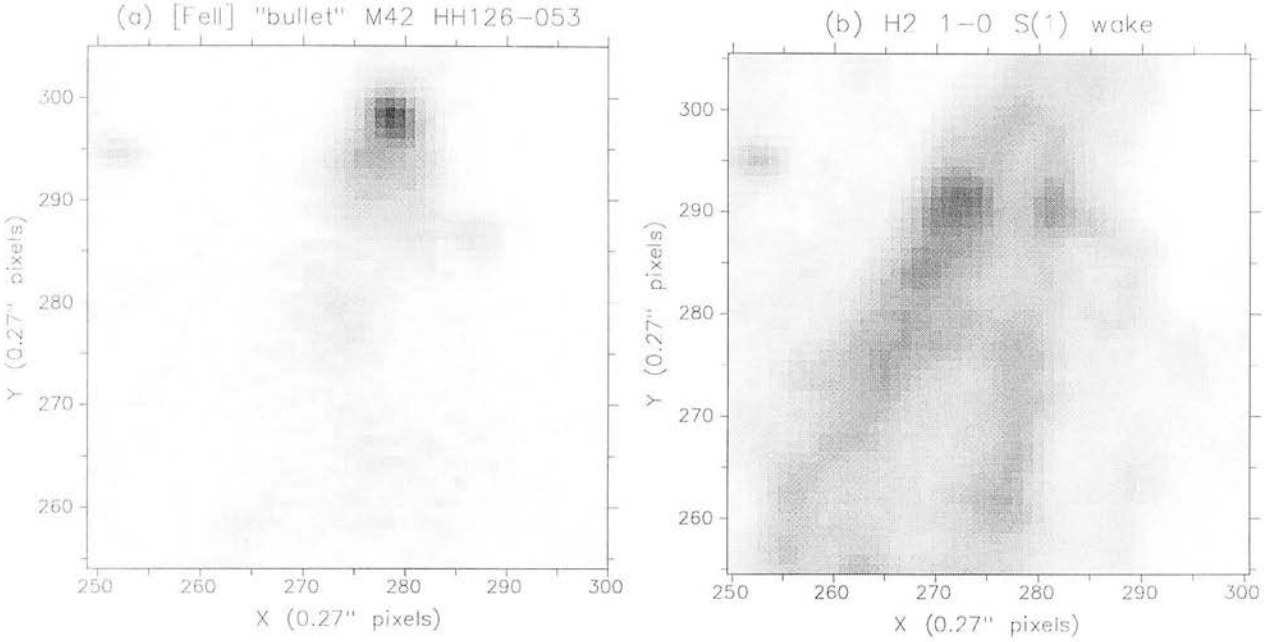


Figure 3.4: Close-up of M42 HH126-053 region in (a) [FeII] 1.644$\mu$m emission and (b) $H_2$ 1-0 S(1) emission from images of Allen & Burton (1993).

oppositely directed from one another. Further down the "bullet", the velocity range narrows (bottom of Figure 3.5) as the ambient gas sees a lower effective shock velocity (the normal component of the shock velocity decreases moving down each side of the bow-shaped shock front geometry).

### Derivation of "Bullet" Velocity and Orientation

The two most important parameters in modelling integrated bow-shock line profiles are the incident shock velocity, $v_s$ and the orientation to the line-of-sight, $\alpha$. Observationally, we can directly measure $v_s$ since it is equal to the full width near zero intensity (FWZI) of the integrated emission over an entire bow shock front independent of the shape of the bow-shock, orientation angle, pre-shock density, elemental abundances and reddening (Hartigan et al. 1989). Furthermore, by measuring the maximum ($MX$) and minimum ($MN$) radial velocities for the integrated line profile we obtain both $v_s$ and $\alpha$. The appropriate formulae for the observed maximum and minimum radial velocities for a

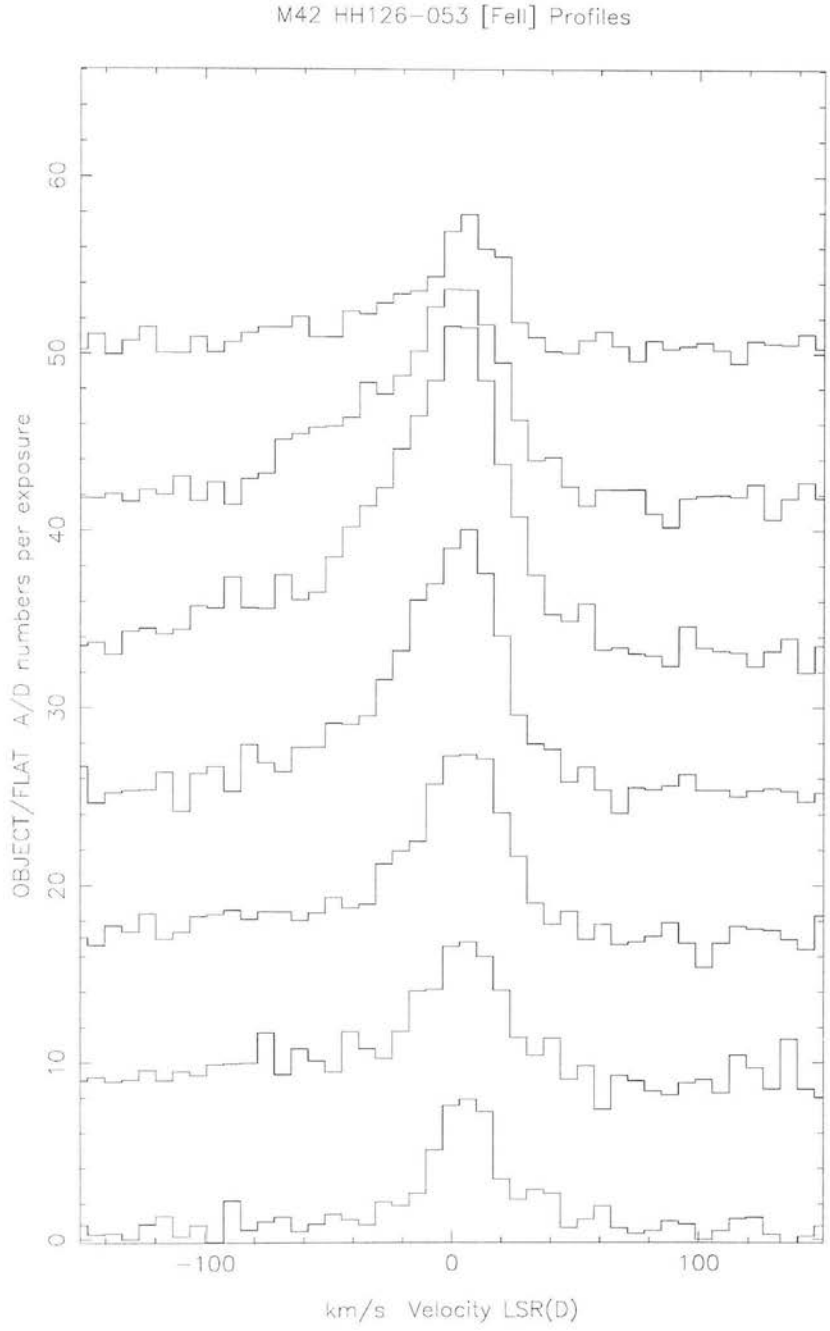


Figure 3.5: M42 HH126-053 [FeII] 1.644$\mu$m velocity profiles running from North (top) to South (bottom) along "bullet" axis with peak intensity at "bullet" tip. Profiles are relatively but not absolutely flux calibrated in this case (see text).

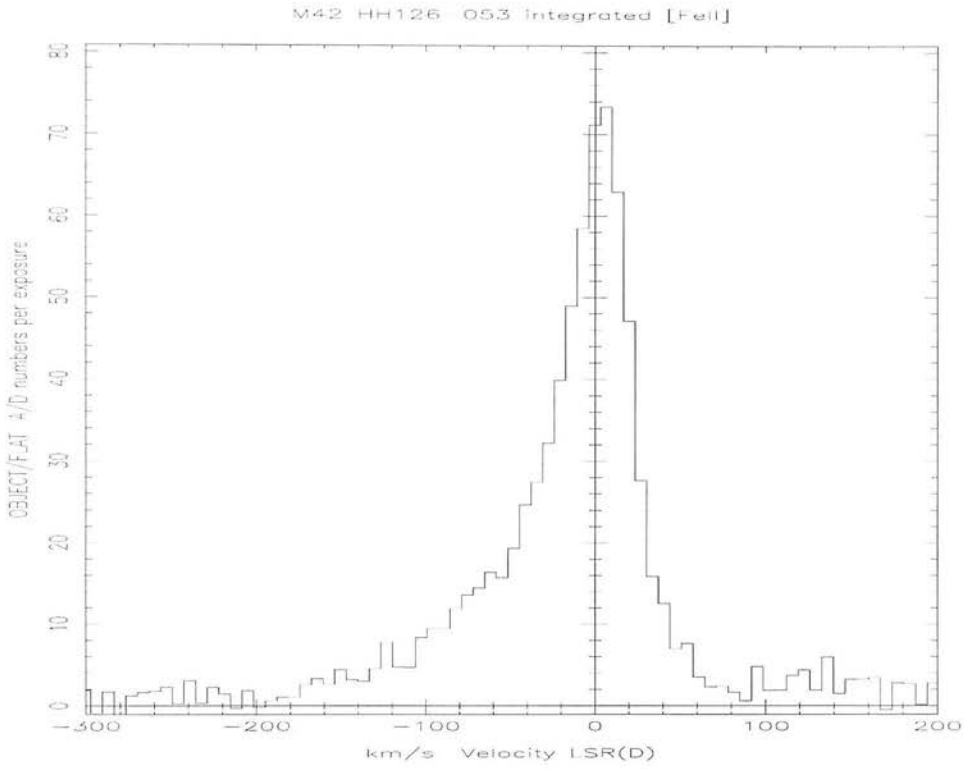


Figure 3.6: M42 HH126-053 integrated [FeII] 1.644$\mu$m velocity profile showing total velocity range in "bullet".

bullet ploughing into a stationary medium are given by Hartigan *et al.* (1987) as

$$MX = \frac{v_s}{2}(1 + \cos\alpha) - v_s \cos\alpha \tag{3.1}$$

and

$$MN = -\frac{v_s}{2}(1 - \cos\alpha) - v_s \cos\alpha. \tag{3.2}$$

The total velocity range is

$$FWZI = MX - MN = v_s. \tag{3.3}$$

In addition, the effects of thermal and instrumental broadening are accounted for by setting the values of MX and MN to

$$MX = MX_{0.1} - \frac{SM}{2}, \tag{3.4}$$

and

$$MX = MN_{0.1} + \frac{SM}{2}, \tag{3.5}$$

where $MX_{0.1}$, $MN_{0.1}$ are the maximum and minimum velocities at 0.1 of the observed peak intensity and $SM$ is the FWHM of the instrumental smoothing ($21.7 \mathrm{km\,s^{-1}}$ ).

In this case, the integrated [FeII] profile (Figure 3.6) corresponds to a shock velocity of $v_s = 150 \pm 15$ km s$^{-1}$ and an orientation angle of $\alpha = 70 \pm 10°$ to the line-of-sight. Note that $\alpha = 90°$ for a bow shock oriented exactly in the plane-of-sky. A comparison of this observed [FeII] profile shape with radiative bow-shock model predictions (Hartigan *et al.* 1989) is hampered in this case because of the difficulty in subtracting a background emission component (not clearly identified for this observation). An unambiguous identification of this component in the following section, however, indicates that the observed values of MN and MX above will remain unaltered and the resultant shock velocity and orientation therefore stand. It is also clear that the strongest peak emission lies near zero radial velocity, as predicted in bullet models, as opposed to models in which the molecular gas flows past an obstacle. Encouragingly, the observed profile is similar in shape to the theoretical integrated velocity profile generated for $v_s = 200 \mathrm{km\,s^{-1}}$ , $\alpha = 60°$ (Hartigan *et al.* 1987), with a suitably reduced FWZI velocity range.

### 3.4.2 M42 HH120-114 [FeII] 1.644 $\mu$m Profiles

The "bullet" M42 HH120-114 is shown in Figure 3.7(a) alongside its corresponding $H_2$ wake in Figure 3.7b. As with M42 HH126-053, the wake is apparently oriented in or close to the plane of sky. It is possible to discern other "bullet"-like condensations close to the prominent M42 HH120-114 "bullet" at (323,218) in figure 3.7a. Indeed a weak [FeII] feature centred at (318,203) is associated with a second $H_2$ wake feature that partially overlaps with that of M42 HH120-114. Observations of the [FeII] 1.644$\mu$m line profiles at two adjacent slit positions including the "bullet" M42 HH120-114 are shown in Figure 3.8, superimposed on the Allen & Burton (1993) image. Each profile is displayed in a box centred on the exact position of the corresponding CGS4 slit row. The common flux and velocity scales of each profile are illustrated in the "key" box. This method of displaying

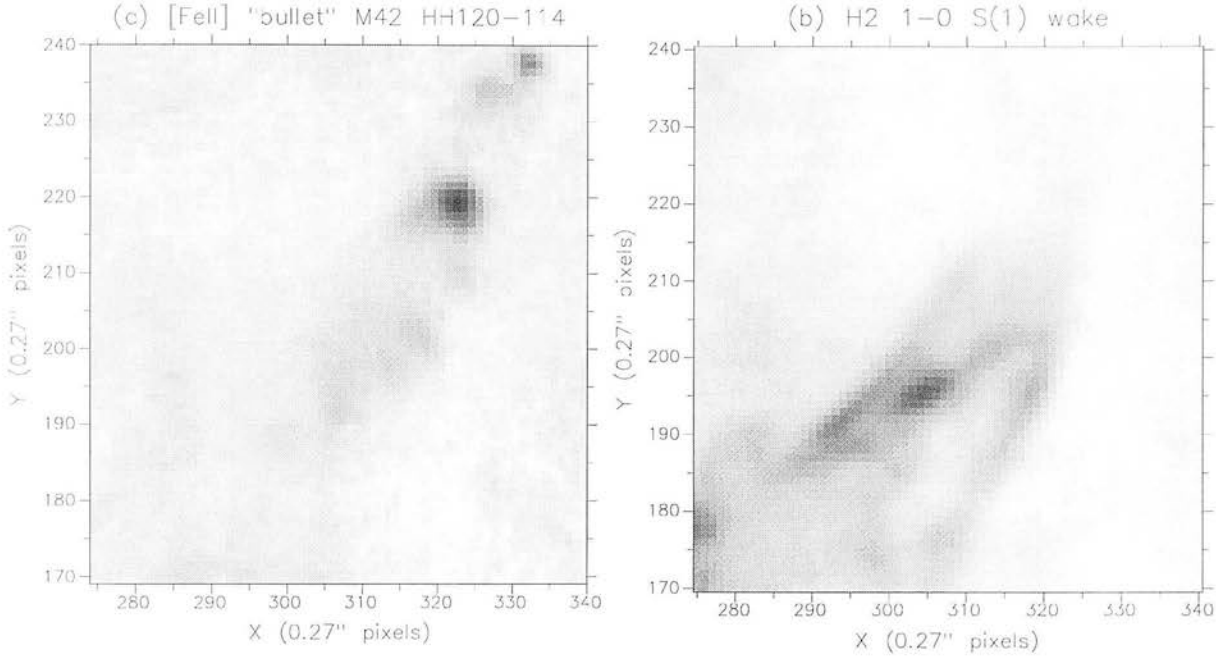


Figure 3.7: Close-up of M42 HH120-114 region in (a) [FeII] 1.644$\mu$m emission and (b) $H_2$ 1-0 S(1) emission from images of Allen & Burton (1993).

the relative flux and velocity scales of profiles for a given position on a "bullet"/wake in the region will be used throughout the remainder of this chapter. In addition to the broadened velocity profiles associated with the "bullet", it is immediately apparent that the entire region is pervaded by a constant "background" emission feature. Individual profiles on the "bullets" themselves are displayed in Figure 3.9. As for M42 HH126-053, "bullet" profiles are broad and strongly peaked at a velocity of $\simeq 8 \mathrm{km\,s^{-1}}$, close to the rest velocity of the ambient medium of $+9 \mathrm{km\,s^{-1}}$, determined by Goldsmith *et al.* (1975) from $^{12}$CO and $^{13}$CO radio observations. The emission profiles narrow as one moves downstream from each individual "bullet" tip. At rows to the north and south of the "bullet" positions the profile is dominated by the narrow background component centred at zero velocity.

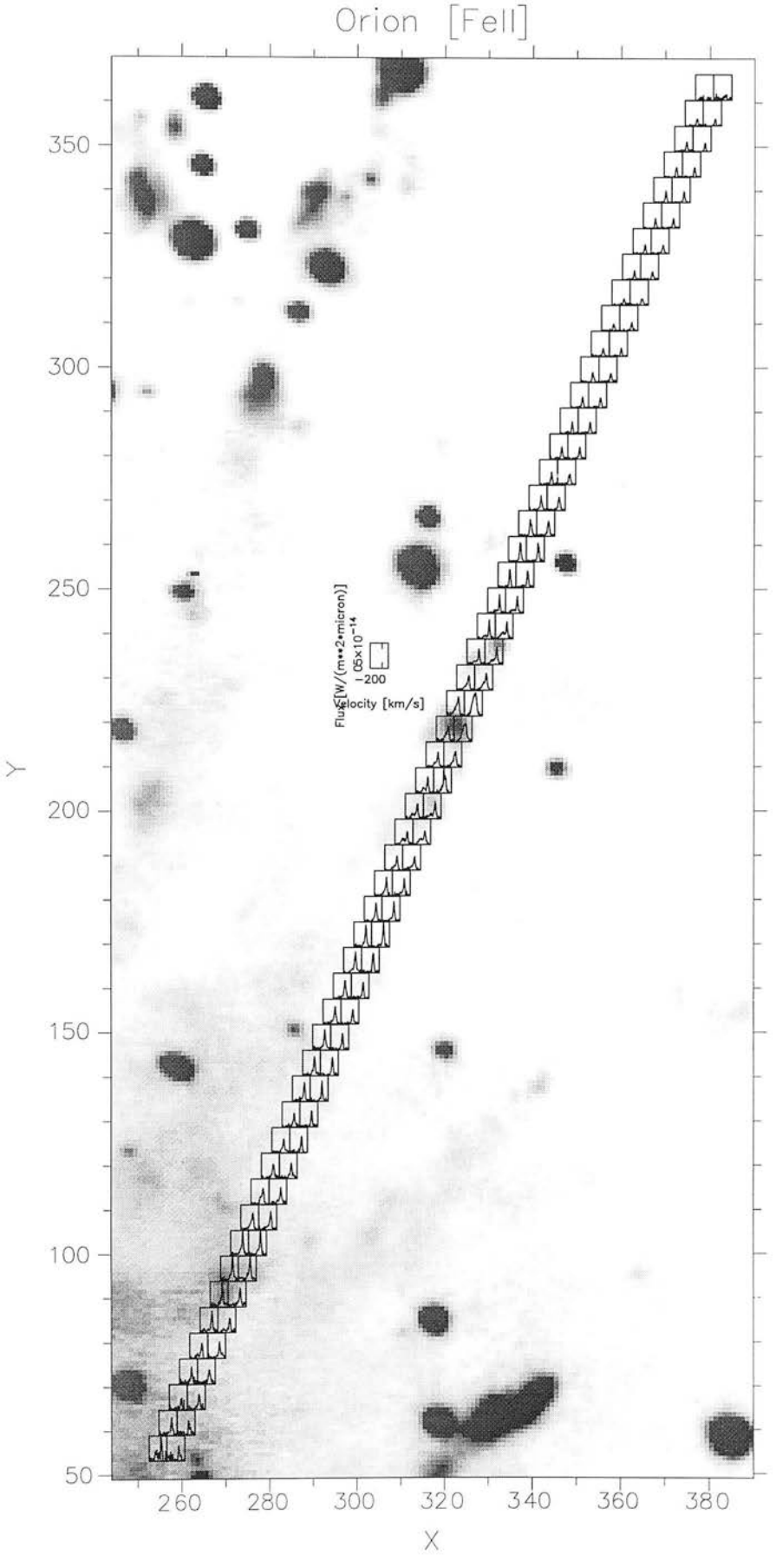


Figure 3.8: Region including M42 HH120-114 centred at (318,223) imaged in [FeII] 1.644$\mu$m (Allen & Burton 1993) with corresponding [FeII] velocity profiles at two slit positions superimposed. Each profile box is centred on the appropriate CGS4 pixel row and has equal flux and velocity scale as indicated by the key. Note constant component North of "bullet".

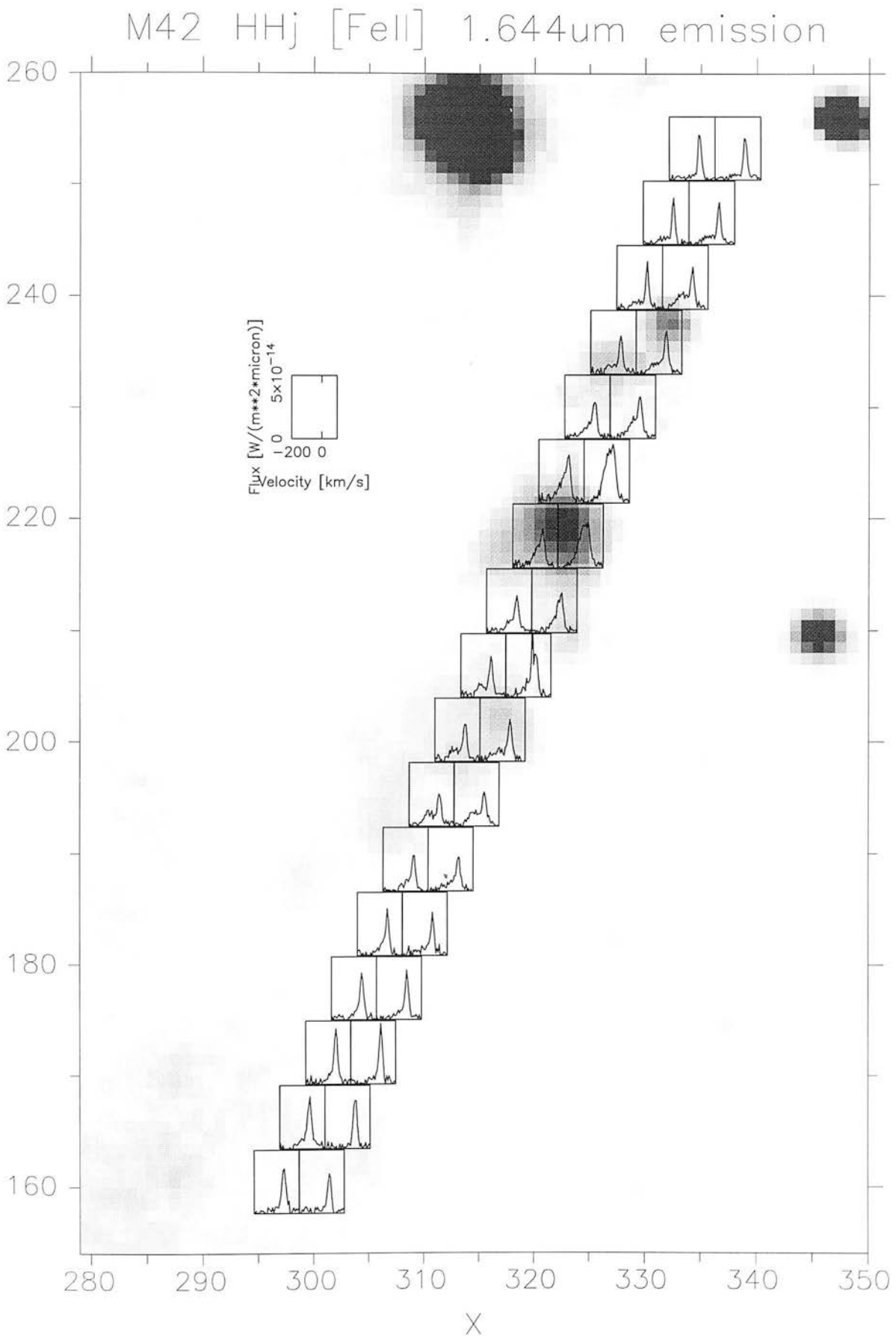


Figure 3.9: Observed M42 HH120-114 [FeII] 1.644$\mu$m "bullet" velocity profiles (background component not removed).

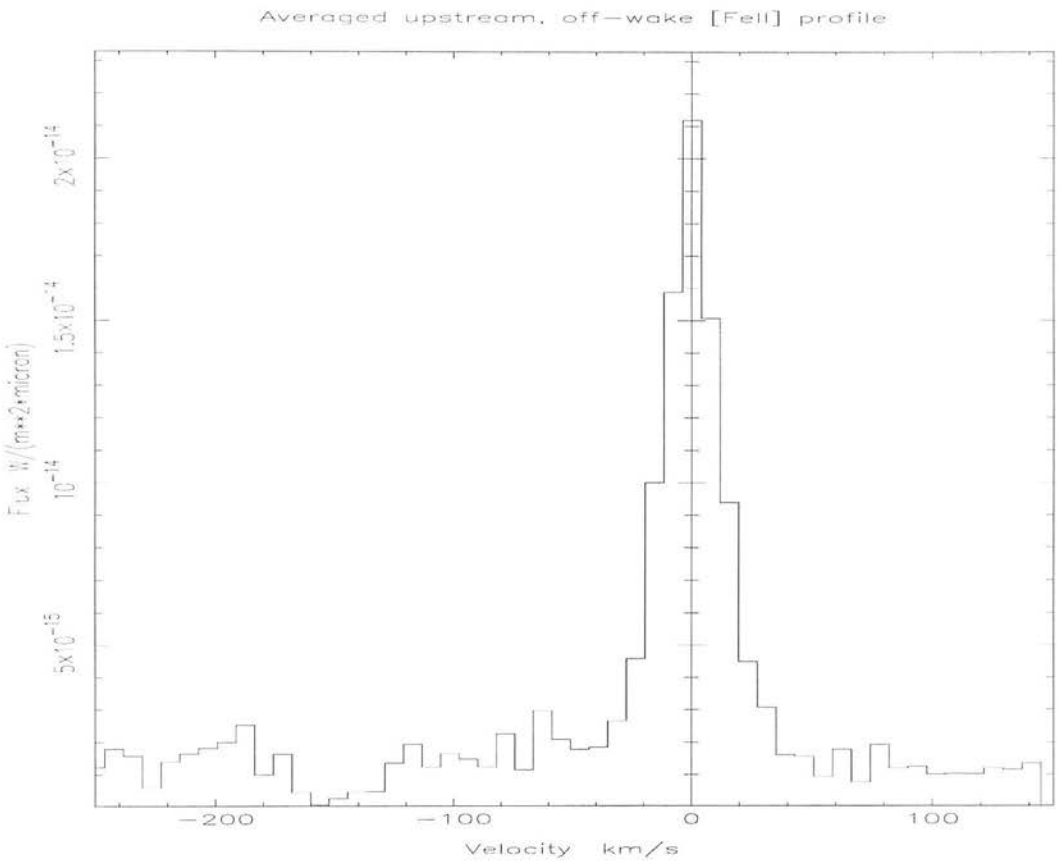


Figure 3.10: Averaged background [FeII] 1.644$\mu$m velocity profile, upstream of M42 HH120-114.

### Subtraction of Background Component: "Bullet"-only emission

In order to accurately determine the velocity range of emission resulting from the "bullet" alone, it is necessary to isolate the background emission pervading the entire region. For this purpose, the slits shown in Figure 3.8 were positioned so that a significant area upstream of the "bullets" emission was sampled. The averaged upstream profile was found by coadding all observed profiles upstream of the "bullets" at these positions and is displayed in Figure 3.10. The background profile is centred at -0.4±0.2km s$^{-1}$ (weighted mean) and is well fitted by a single Gaussian profile of FWHM = 31.1±0.6km s$^{-1}$ . After deconvolution of the instrumental profile the intrinsic FWHM is 22.3±0.7km s$^{-1}$ . The line flux is $(3.4 \pm 0.2) \times 10^{-18}$Wm$^{-2}$ in a $1.689\hat{''} \times 0.9\hat{''}$ CGS4 pixel row.

This averaged background profile was therefore subtracted from each observed profile

in order to isolate "bullet"-only emission. Figure 3.11 shows the same region as Figure 3.9 but this time the "bullet"-only emission profiles are displayed. The resultant profiles consist of at least two components as expected for bow shock emission profiles. Variations in background emission show as relatively small spikes and dips at zero velocity if significantly different to the average. The integrated profiles summed over the M42 HH120-114 "bullet" are shown in Figures 3.12 (total observed emission) and Figure 3.13 (background component subtracted).

### Derivation of "Bullet" Velocity and Orientation

Using the methods described previously, the background-subtracted integrated [FeII] profile for the "bullet" M42 HH120-114 (Figure 3.13) corresponds to a shock velocity of $v_s = 120 \pm 10$ km s$^{-1}$ and an orientation angle of $\alpha = 60 \pm 10°$ to the line-of-sight, after small corrections for thermal and instrumental broadening. A comparison of this observed [FeII] profile shape with radiative bow-shock model predictions (Hartigan *et al.* 1989) shows good agreement with the theoretical integrated velocity profile generated for a $v_s = 100$km s$^{-1}$ , $\alpha = 60°$ bow shock (Hartigan *et al.* 1987). In particular, peak emission is blueshifted by up to $\sim 40$km s$^{-1}$ for the observed profile, consistent with a similar but slightly larger blueshift of $\sim 50$km s$^{-1}$ for the theoretical profile.

## 3.4.3 Shocked $H_2$ 1-0 S(1) Profiles in Associated "Bullet" Wakes

Figures 3.14 and 3.15 show the observed $H_2$ 1-0 S(1) 2.1218 $\mu$m line profiles at positions both along, across and upstream of the clearly resolved bow-shock wakes associated with each of the "bullets" M42 HH126-053 and M42 HH120-114. As with the [FeII] emission, a roughly constant emission feature clearly pervades regions upstream and adjacent to the wake itself, while profile intensity increases by a factor of ten or more up to a maximum of $1.68 \pm 0.01 \times 10^{-16}$Wm$^{-2}$ in a $1.744\,\hat{n} \times 0.9\,\hat{n}$ CGS4 pixel at positions on the wakes themselves. The emission profiles are dominated at all positions by a broad, single peak centred at or close to zero velocity relative to the local standard of dynamical rest. Before analysing the profiles in more detail it is necessary to determine and subtract the constant background feature, as for the [FeII] profiles.

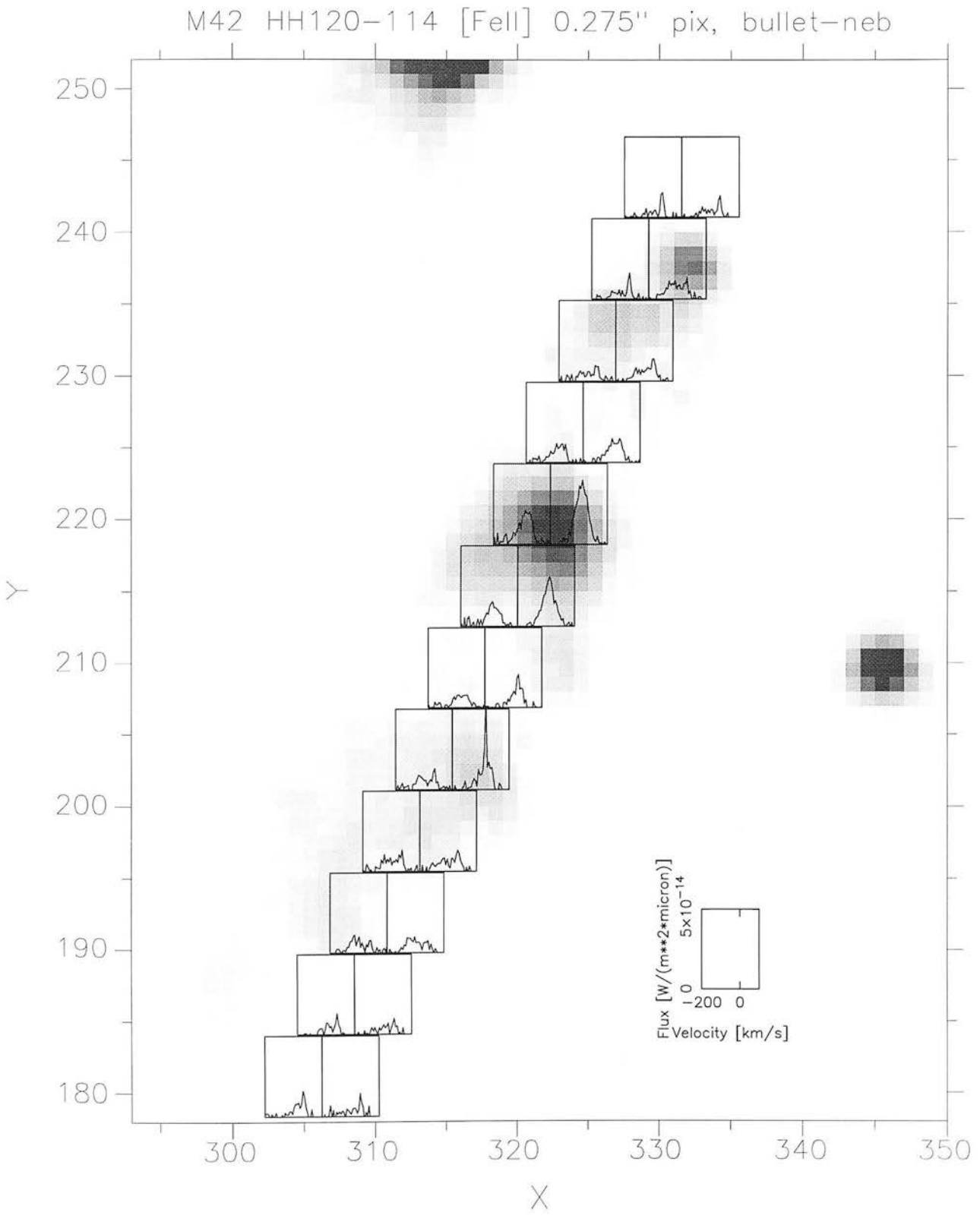


Figure 3.11: M42 HH120-114 [FeII] 1.644$\mu$m "bullet" - "background" velocity profiles.

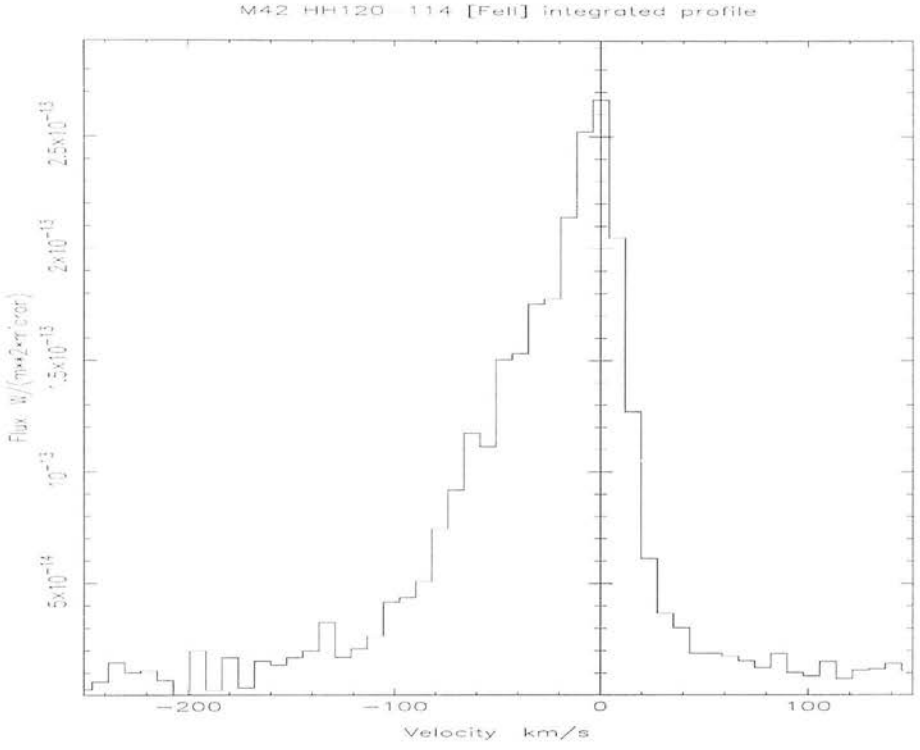


Figure 3.12: M42 HH120-114 [FeII] 1.644$\mu$m integrated "bullet" + "background" velocity profile.

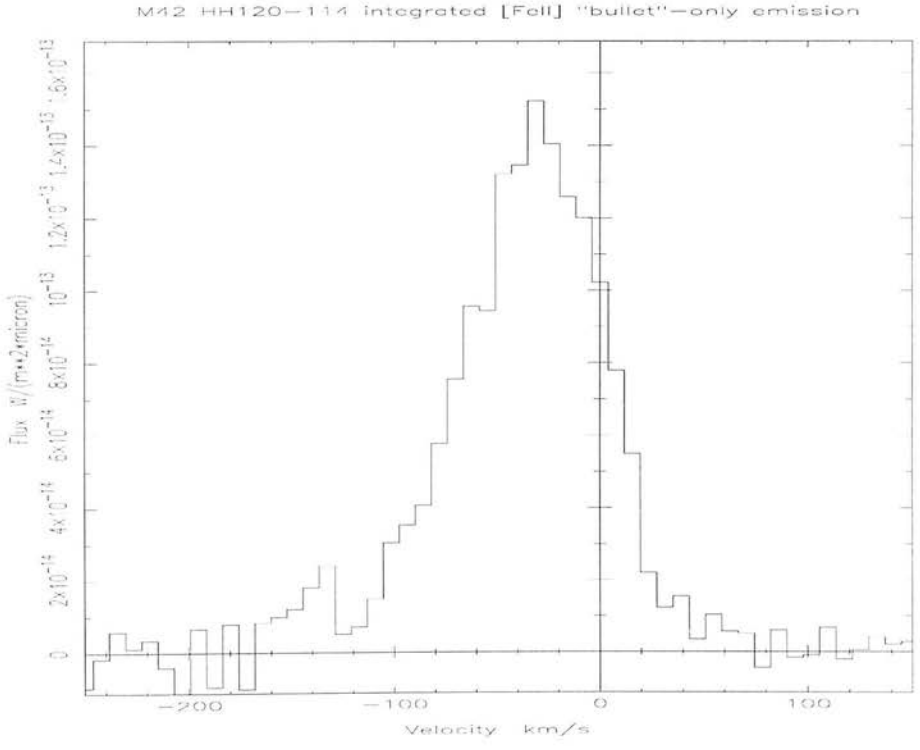


Figure 3.13: M42 HH120-114 [FeII] 1.644$\mu$m integrated "bullet"-only velocity profile.

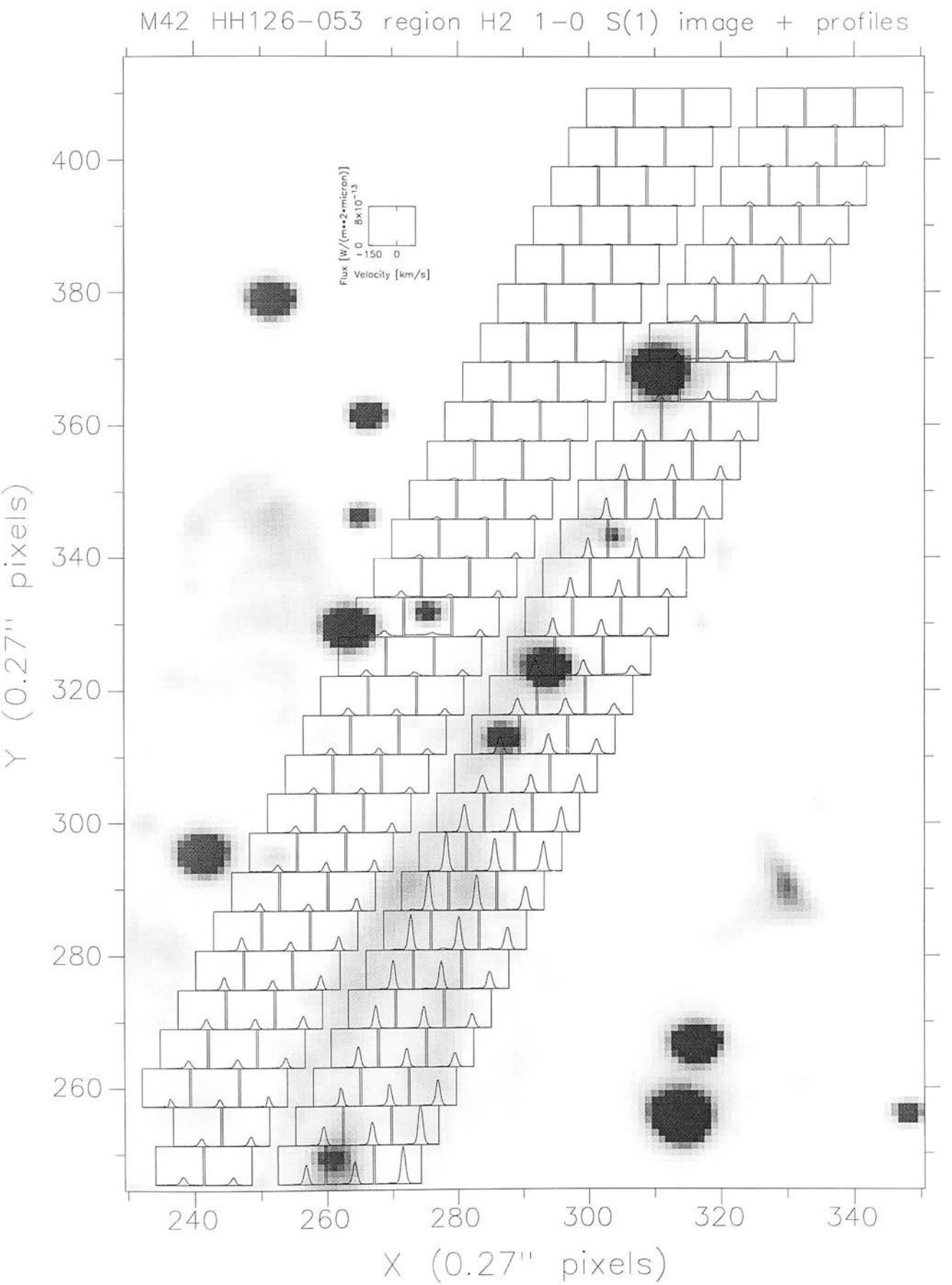


Figure 3.14: Region including M42 HH126-053 imaged in $H_2$ 1-0 S(1) 2.122$\mu$m (Allen & Burton 1993) with velocity profiles superimposed.

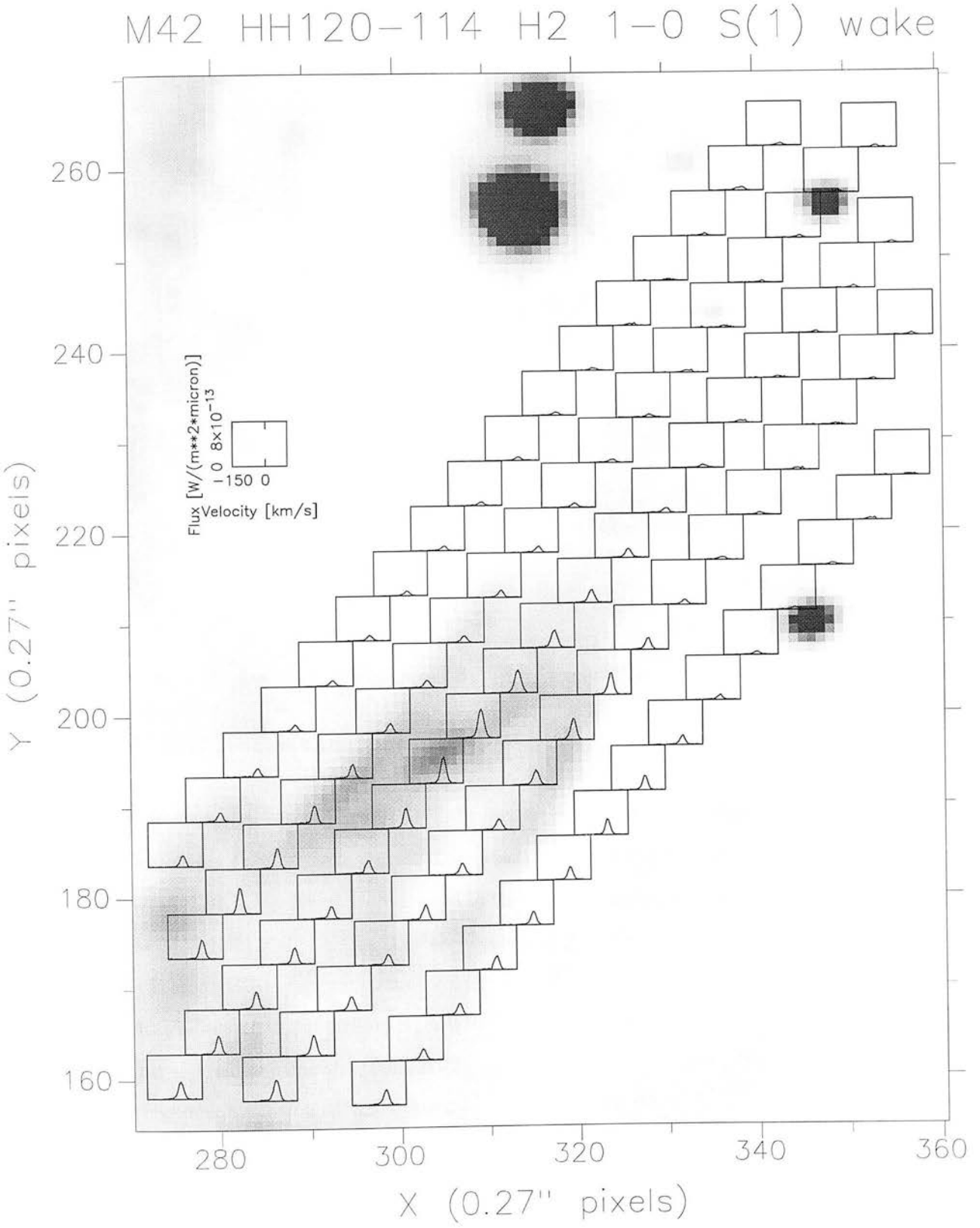


Figure 3.15: M42 HH120-114 $H_2$ 1-0 S(1) velocity profiles superimposed on the $H_2$ narrowband image of Allen & Burton (1993).

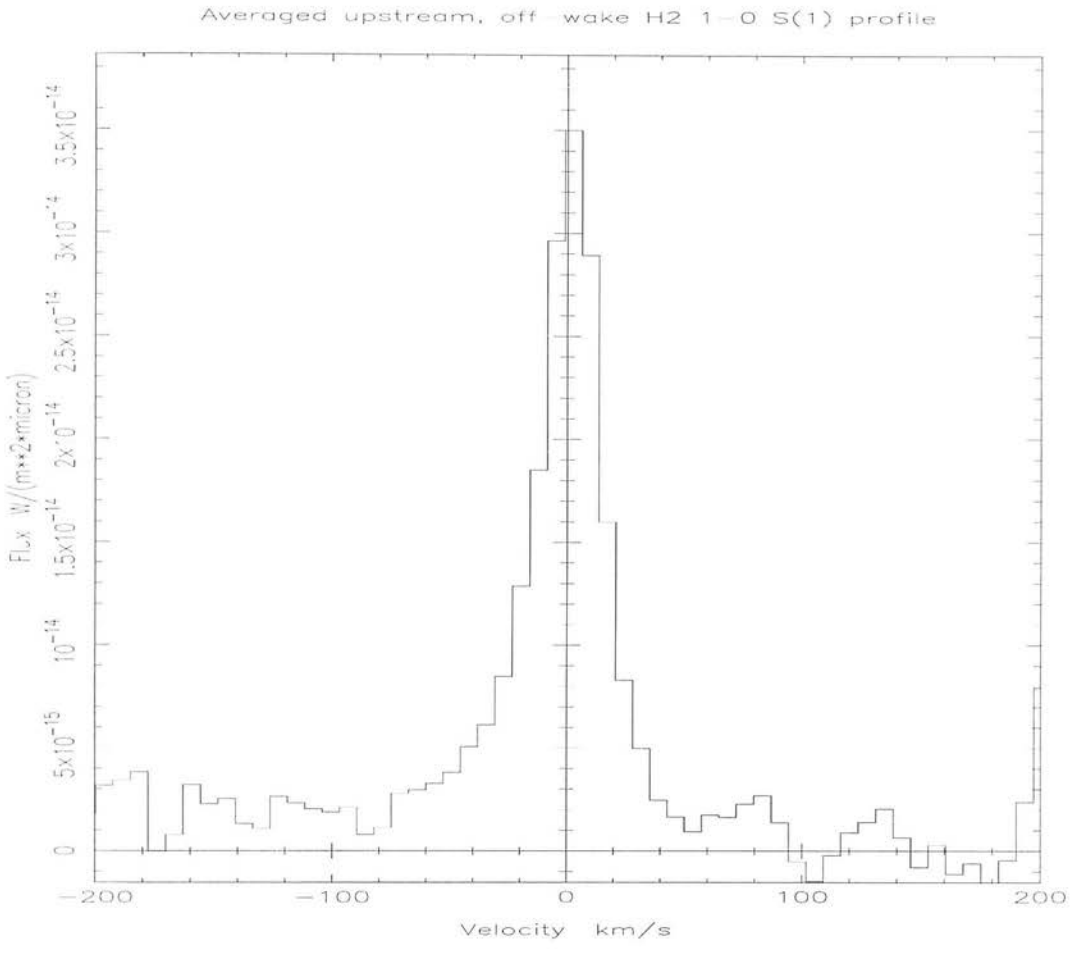


Figure 3.16: Averaged "background" $H_2$ 1-0 S(1) velocity profile, upstream of M42 HH120-114.

### $H_2$ Background Component

The averaged, upstream $H_2$ 1-0 S(1) profile was found by averaging profiles at positions well clear of the wake features. The consequent profiles are almost identical for both regions. The majority of profiles used in this determination are at positions far upstream of the M42 HH120-114 wake. The resultant profile is shown in Figure 3.16 and is well fitted by a single Gaussian centred at $2.5\pm0.5\mathrm{km\,s^{-1}}$ , close to the value of $+4\mathrm{km\,s^{-1}}$ found by Moorhouse *et al.* (1990) for $H_2$ 1-0 S(1) profiles at OMC-1, and in close agreement with that determined for the [FeII] background component. The FWHM is $34.0\pm2.5\mathrm{km\,s^{-1}}$ . After deconvolution of instrumental broadening (FWHM = $23.1\pm0.3\mathrm{km\,s^{-1}}$ ), the intrinsic FWHM of the background component is therefore $26.0\pm2.5\mathrm{km\,s^{-1}}$ , slightly higher than for the [FeII] 1.644$\mu$m background component. The average background flux in the $H_2$ 1-0 S(1) transition is $9.9\pm0.6\times10^{-18}\mathrm{Wm^{-2}}$ in a $1.744''\times0.9''$ CGS4 pixel.

| Slit Row | Slit (272,307) | | Slit (283,307) | | Slit (290,307) | | Slit (297,307) | |
|---|---|---|---|---|---|---|---|---|
| | $v_{peak}$ /km s$^{-1}$ | intrinsic FWHM /km s$^{-1}$ | $v_{peak}$ /km s$^{-1}$ | intrinsic FWHM /km s$^{-1}$ | $v_{peak}$ /km s$^{-1}$ | intrinsic FWHM /km s$^{-1}$ | $v_{peak}$ /km s$^{-1}$ | intrinsic FWHM /km s$^{-1}$ |
| 19 | -1.1±0.3 | 23.1±0.7 | 0.2±0.1 | 26.8±0.4 | 2.7±0.3 | 21.9±0.8 | 1.4±0.1 | 23.0±0.4 |
| 20 | -2.8±0.2 | 14.3±0.5 | -2.7±0.1 | 21.1±0.4 | -1.1±0.1 | 24.3±0.4 | 0.3±0.1 | 22.2±0.4 |
| 21 | -1.8±0.2 | 11.2±0.6 | -4.0±0.1 | 14.0±0.4 | -2.6±0.1 | 18.2±0.4 | 0.5±0.2 | 20.8±0.5 |
| 22 | -0.8±0.2 | 5.0±0.5 | -4.5±0.7 | 14.0±0.3 | -4.3±0.9 | 16.8±0.4 | -1.0±0.1 | 23.7±0.4 |
| 23 | -1.7±0.2 | U | -4.6±0.6 | 13.2±0.3 | -4.9±0.8 | 16.3±0.4 | -2.0±1.0 | 24.3±0.4 |
| 24 | -4.4±0.2 | 14.0±0.5 | -4.7±0.6 | 11.4±0.3 | -4.9±1.0 | 14.6±0.4 | -3.6±0.9 | 22.1±0.4 |
| 25 | -4.7±0.2 | 19.8±0.5 | -4.0±0.6 | 11.8±0.3 | -4.4±0.1 | 12.2±0.4 | -3.9±0.1 | 20.6±0.4 |
| 26 | -2.0±0.2 | 10.0±0.6 | -3.1±0.8 | 11.2±0.4 | -2.9±1.0 | 13.4±0.4 | -2.8±0.1 | 20.4±0.4 |
| 27 | - | - | -0.6±0.2 | U | 0.5±0.3 | U | 0.9±0.2 | 13.4±0.6 |
| 28 | -0.5±0.2 | 15.6±0.5 | -0.1±0.1 | 12.4±0.4 | 1.2±0.9 | 14.5±0.4 | 1.1±0.1 | 15.8±0.4 |

Table 3.1: Gaussian line-fits to main velocity component of background-subtracted $H_2$ 1-0 S(1) wake profiles in M42 HH126-053. CGS4 slit row 19 (top row displayed in Figure 3.17) corresponds to the Allen & Burton (1993) image coordinates indicated above each column. Row 28 is the bottom row displayed in Figure 3.17. Velocities are calibrated relative to the local standard of dynamical rest (LSR). "U" indicates profile unresolved.

### Wake-only Emission

*(i) M42 HH126-053*

The averaged background component (Figure 3.16) was subtracted from all positions on the $H_2$ wakes to determine the characteristics of the wake-only emission. Figure 3.17 shows the resultant profiles superimposed on the $H_2$ wake of M42 HH126-053. Profile intensity increases for on-wake positions up to a maximum of $1.58\pm0.01\times10^{-16}$Wm$^{-2}$ in a $1.744'' \times 0.9''$ CGS4 pixel (after background subtraction). Detailed Gaussian line-fits of peak velocity and FWHM were possible for the emission profiles at all positions. Routines in the SPECDRE Starlink software library were employed and the results, including intrinsic FWHM after deconvolution of instrumental broadening, tabulated in

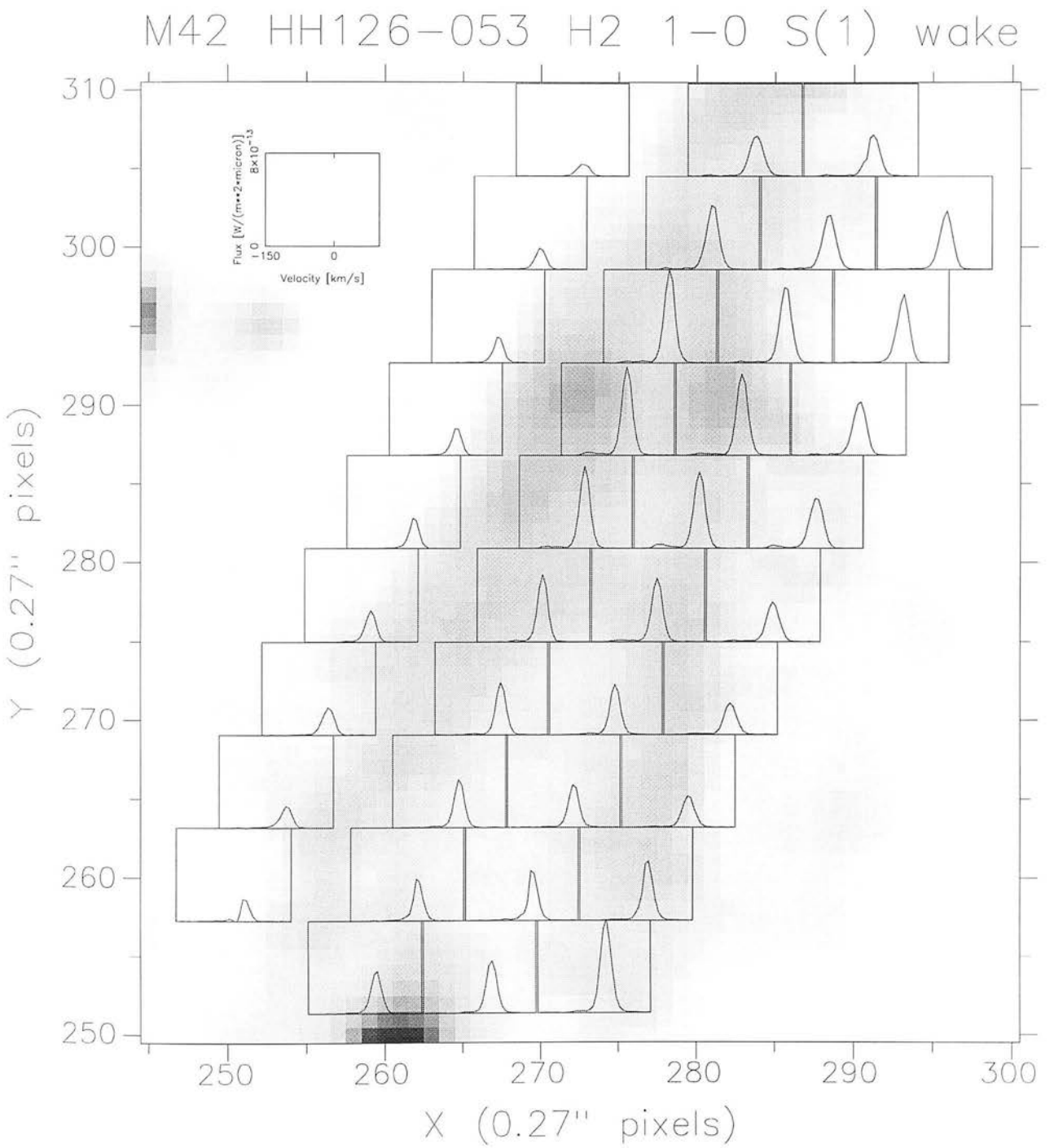


Figure 3.17: M42 HH126-053 "wake" - "background" $H_2$ 1-0 S(1) velocity profiles.

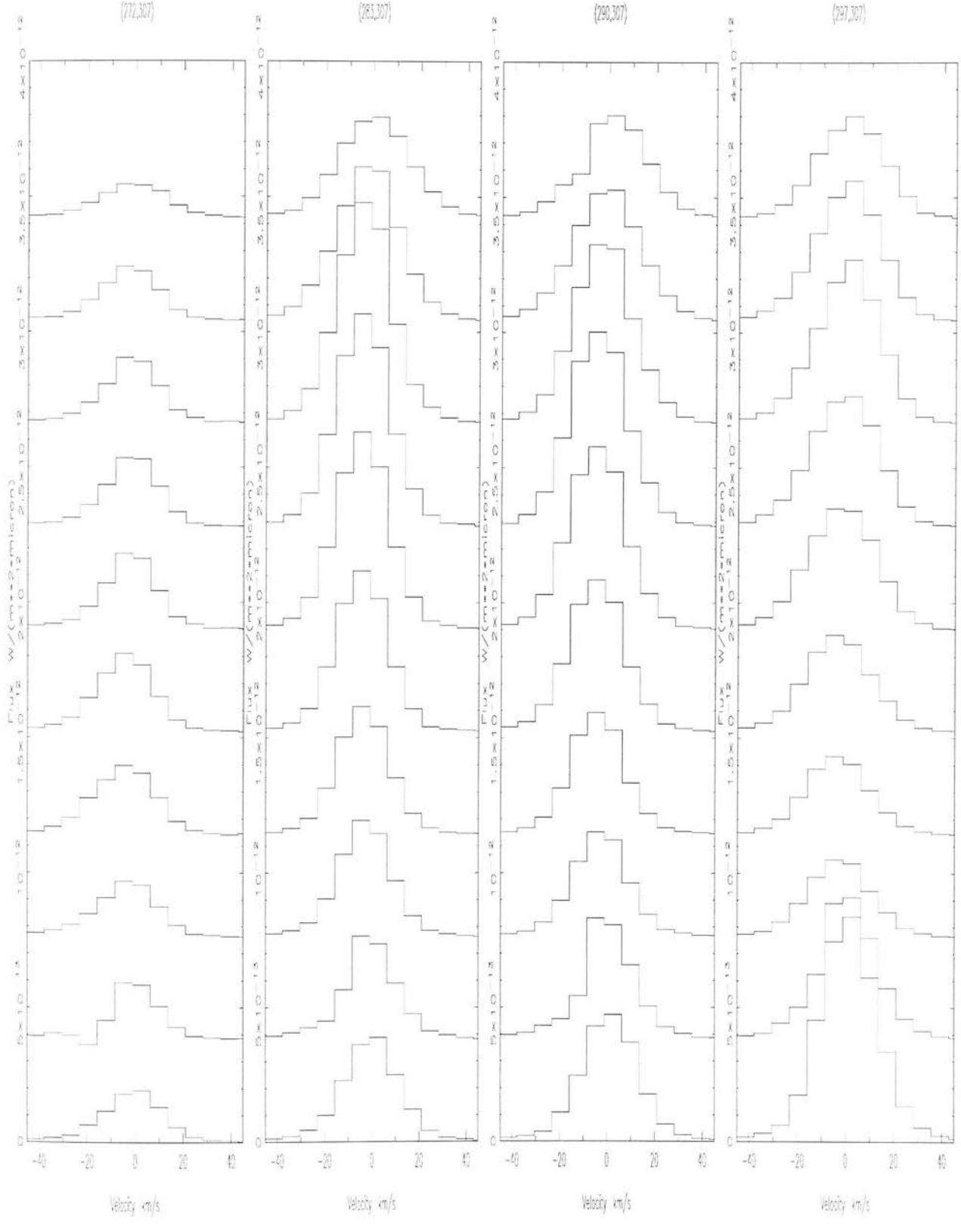


Figure 3.18: M42 HH126-053 "wake" - "background" $H_2$ 1-0 S(1) velocity profiles running from NW(top) to SE(bottom) along wake axis highlighting peak velocity shifts. Profiles are those shown in Figure 3.17 with image pixel centre of top row labelled accordingly.

Table 3.1 for the main peak emission centred at or close to zero velocity. The small peak velocity shifts measured can be seen by comparing the same profiles displayed in columns in Figure 3.18. For each slit position, a small but significant blueshift is observed up to a peak velocity of -4.9±1.0km s$^{-1}$ compared to the off-wake peak of +2.5±0.5km s$^{-1}$ , corresponding to a blueshift of up to 7.4±1.1km s$^{-1}$ and up to 14km s$^{-1}$ from the ambient cloud velocity in this region measured in CO. The maximum blueshift occurs at positions corresponding to the brightest regions at the tips of the $H_2$ emission and almost coincident (along the line-of-sight) with the [FeII] 1.644$\mu$m "bullet". In moving down the wake, profiles weaken and peak velocity approaches the background peak velocity once again. At no point on the wake is there any evidence of the double-peaked profile structure in the dominant emission profile centred near zero-velocity, as would be expected for bow shocks.

The decrease in intensity and blueshift of the profiles at the central on-axis wake positions is coincident with a corresponding decrease in the intrinsic FWHM of the profiles, ranging from a maximum of 24.3±0.4km s$^{-1}$ near the tip of the wake down to 10.0±0.6km s$^{-1}$ at the tail of the wake for the two on-wake slits centred at image coordinates (283,307) and (290,307). Slit (272,307) lies along the edge of the main wake emission associated with M42 HH126-053 and shows a less clear trend in profile that is perhaps due to the irregular shape of the underlying wake geometry. Slit (297,307) follows the general trend of the central positions but appears to be coincident with an additional wake feature corresponding to a secondary [FeII] clump (Figure 3.4) which confuses interpretation.

Additional and much weaker components are identified at velocities significantly blueshifted from the dominant single peak and highlighted in Figures 3.19 and 3.20. These features are strongest at the correspondingly brightest main peak positions. One of these components remains fairly constant and is identified as the "ghost" feature previously observed in arc lamp spectra and centred at about -51km s$^{-1}$ , and whose intensity is proportional to the main peak intensity and up to $\sim$ 5% in relative flux intensity, consistent with the arc line fits. However, a component centred at velocities as great as -106±3km s$^{-1}$ is also observed and is often stronger than the "ghost" feature. Results of Gaussian line-fitting to any weak component which is clearly distinguished from the

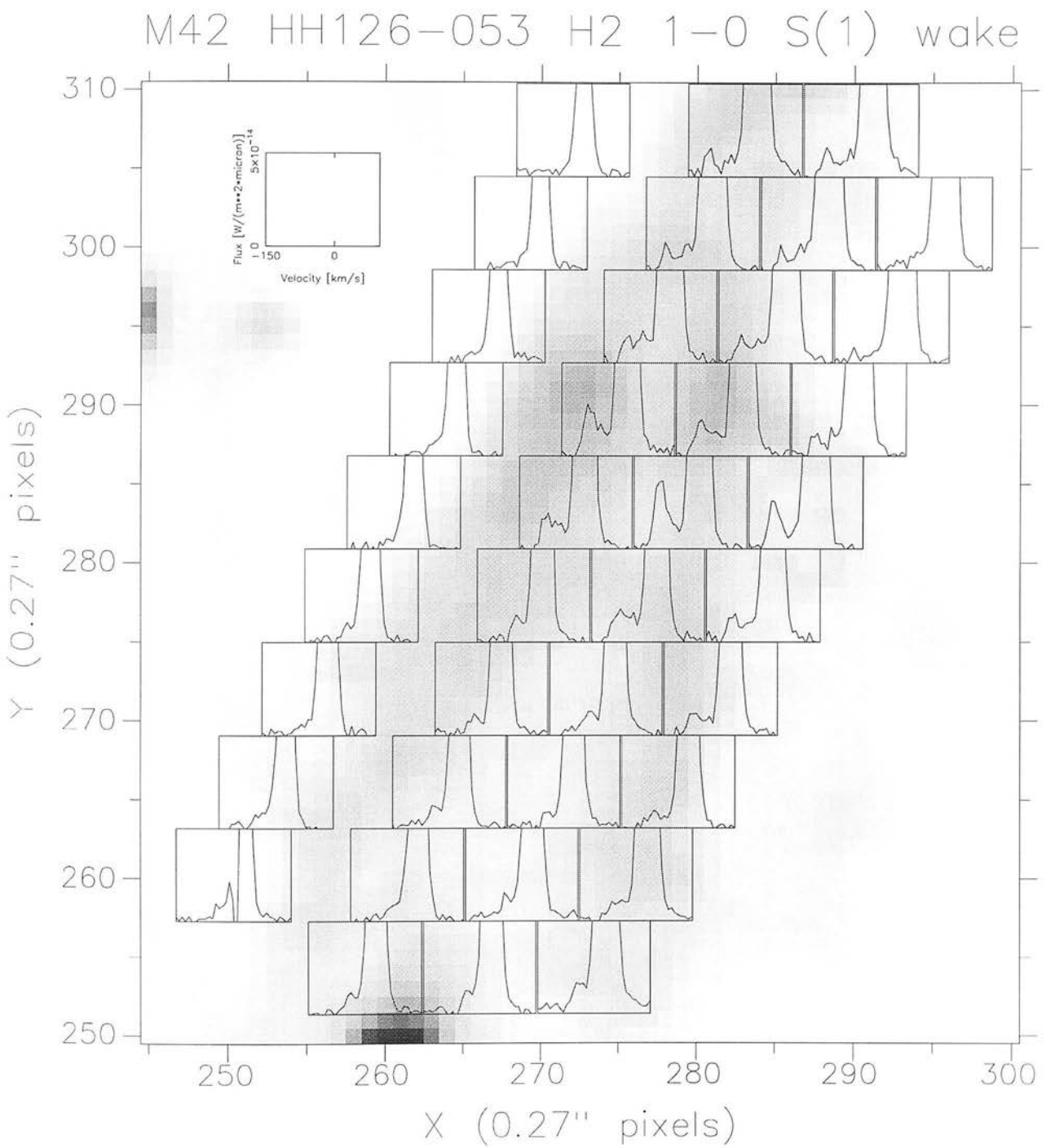


Figure 3.19: M42 HH126-053 "wake" - "background" $H_2$ 1-0 S(1) emission highlighting weak velocity features.

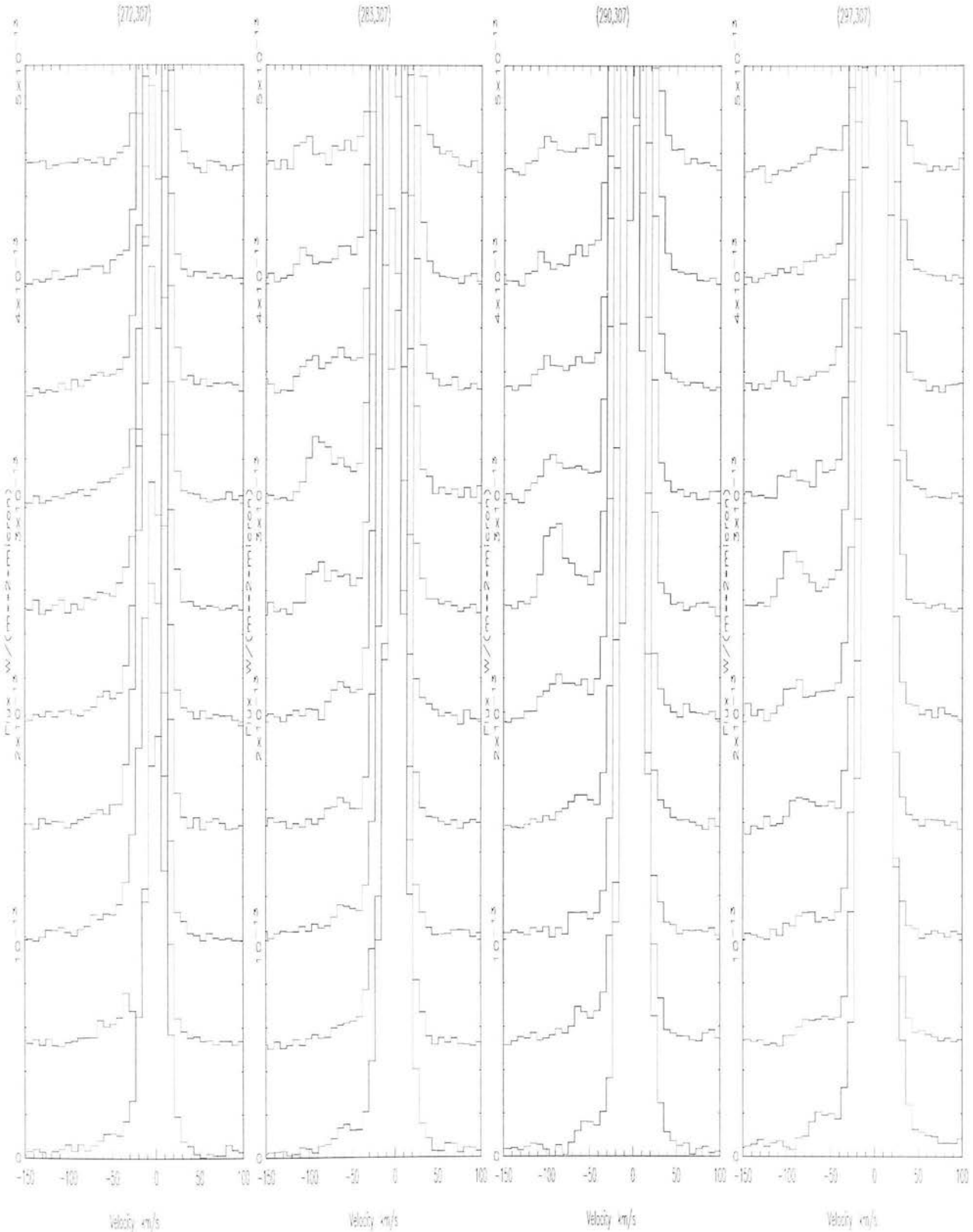


Figure 3.20: M42 HH126-053 "wake" - "background" $H_2$ 1-0 S(1) velocity profiles running from NW(top) to SE(bottom) along wake axis highlighting weak blueshifted velocity components. Profiles are those shown in Figure 3.17 with image pixel centre of top row labelled accordingly.

| Slit Row | Slit (272.307) | | Slit (283.307) | | Slit (290.307) | | Slit (297.307) | |
|---|---|---|---|---|---|---|---|---|
| | $v_{weak}$ LSR /km s$^{-1}$ | intrinsic FWHM /km s$^{-1}$ | $v_{weak}$ LSR /km s$^{-1}$ | intrinsic FWHM /km s$^{-1}$ | $v_{weak}$ LSR /km s$^{-1}$ | intrinsic FWHM /km s$^{-1}$ | $v_{weak}$ LSR /km s$^{-1}$ | intrinsic FWHM /km s$^{-1}$ |
| 19 | - | - | -104.1±2.3 | 6.1±5.3 | -96.8±8.6 | 19.8±20.3 | - | - |
| 20 | - | - | -103.4±6.0 | 9.5±14.1 | -105.5±3.0 | U | - | - |
| 21 | - | - | -94.1±7.7 | 24.9±19.3 | -96.4±6.6 | 26.2±16.1 | - | - |
| 22 | -22.6±2.3 | U | -88.9±2.1 | 16.1±5.2 | -92.2±4.5 | 28.0±11.4 | -95.9±5.3 | 14.5±12.7 |
| 23 | -25.5±2.1 | 10.9±2.1 | -88.8±2.7 | 15.0±6.6 | -91.2±1.4 | 17.6±3.4 | -93.7±1.6 | 17.5±3.8 |
| 24 | - | - | - | - | -89.0±4.1 | 23.8±10.5 | -90.4±2.2 | 17.3±5.3 |
| 25 | - | - | - | - | - | - | -83.8±2.5 | 15.5±6.3 |
| 26 | -25.3±1.4 | 10.3±1.5 | - | - | - | - | -80.2±3.7 | 12.1±9.3 |
| 27 | - | - | -31.5±4.5 | U | -30.2±6.5 | U | -78.6±11.8 | U |
| 28 | - | - | -28.8±3.2 | U | - | - | - | - |

Table 3.2: As Table 3.1 but for Gaussian line-fits to any weak velocity component of background-subtracted $H_2$ 1-0 S(1) wake profiles in M42 HH126-053. "U" indicates profile unresolved. An instrumental "ghost" feature is not included (see text).

constant "ghost" feature associated with the much brighter, zero-velocity centred component are shown in Table 3.2. It is noted that both the peak velocities and the intrinsic FWHM of these components follow the trends found for the main peak emission as one moves down and outwards from the tip of the wake, although accurate determinations are difficult due to the much lower signal-to-noise.

*(ii) M42 HH120-114*

Figure 3.21 shows the background subtracted $H_2$ 1-0 S(1) profiles superimposed on the $H_2$ wake of M42 HH120-114. As for M42 HH126-053, emission is dominated by a broad but singly-peaked profile. Profile intensity increases for on-wake positions up to a maximum of $1.21\pm0.02\times10^{-16}\mathrm{Wm}^{-2}$ in a $1.744''\times0.9''$ CGS4 pixel after subtraction of the averaged background intensity. Detailed Gaussian line-fits of peak velocity and FWHM were made to the emission profiles as before and the resultant peak velocities and deconvolved FWHM values tabulated in Table 3.3 for the main peak emission centred at or close to zero velocity. Once again, at no point on the wake is there any evidence of the double-peaked profile structure in the dominant emission profile centred near zero-velocity, as would be expected for bow shocks.

Small peak velocity shifts are again observed (Figure 3.22). However, in this case, the peaks are slightly redshifted compared to the background emission peak. For each slit position, a small but significant redshift is observed for the peak up to $10.5\pm0.1\mathrm{km\,s}^{-1}$ compared to the average off-wake peak of $2.5\pm0.5\mathrm{km\,s}^{-1}$ corresponding to a redshift of up to $8.0\pm0.6\mathrm{km\,s}^{-1}$ . The largest shifts from row to row again occur at the head of the wake and are again almost coincident (along the line-of-sight) with the main [FeII] 1.644$\mu$m "bullet" emission. Although less clearly defined than for M42 HH126-053, since for positions westward of slit (324,230) a second "bullet" and wake significantly overlaps, there is a clear trend for the peak velocities to reduce and approach the background peak velocity once again in moving down the wake.

The decrease in intensity and redshift of the profiles at the central on-axis wake positions of the main wake M42 HH120-114 is again coincident with a corresponding decrease in the intrinsic FWHM of the profiles, in this case ranging from a maximum of typically $26.1\pm2.4\mathrm{km\,s}^{-1}$ near the leading edge of the wake down to $12.4\pm1.2\mathrm{km\,s}^{-1}$ at

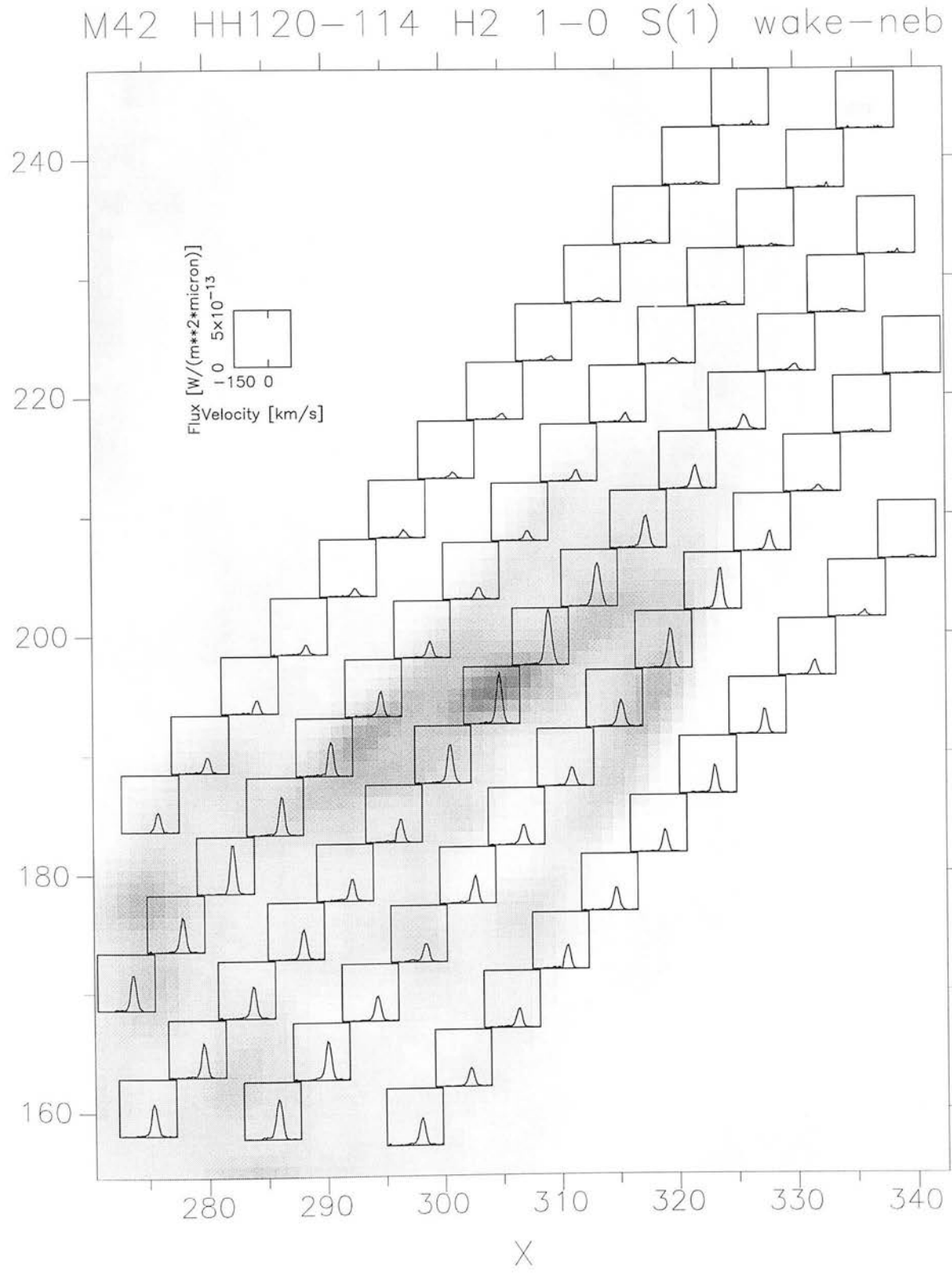


Figure 3.21: M42 HH120-114 "wake" - "background" $H_2$ 1-0 S(1) velocity profiles.

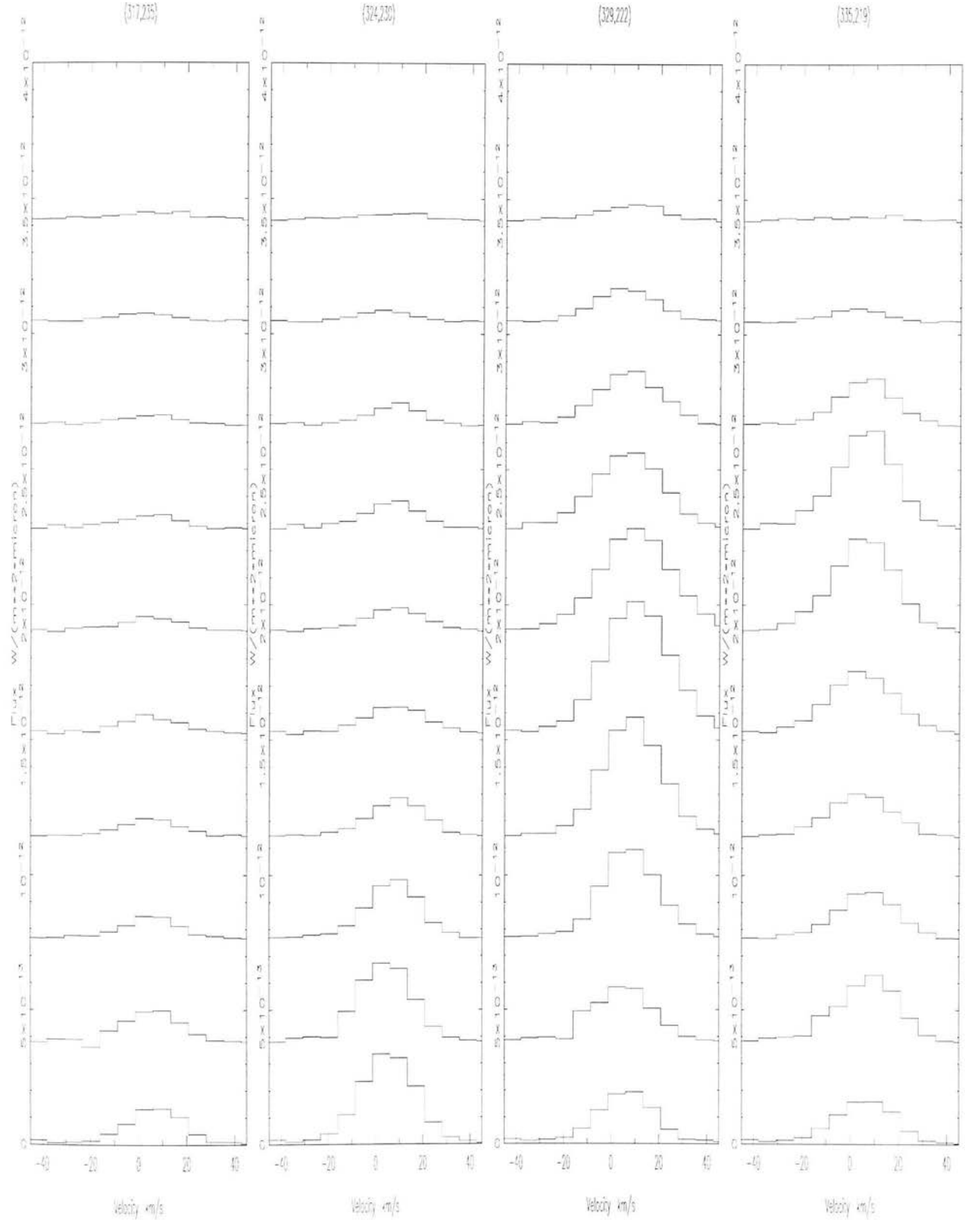


Figure 3.22: M42 HH120-114 "wake" - "background" $H_2$ 1-0 S(1) velocity profiles running from NW(top) to SE(bottom) along wake axis to highlight peak velocity shifts. Profiles are four of those shown in Figure 3.21 with image pixel centre of top row labelled accordingly.

| Slit Row | Slit (317.235) | | Slit (324.230) | | Slit (329.222) | | Slit (335.219) | | Slit (344.214) | |
|---|---|---|---|---|---|---|---|---|---|---|
| | $v_{peak}$ /km s$^{-1}$ | intrinsic FWHM /km s$^{-1}$ | $v_{peak}$ /km s$^{-1}$ | intrinsic FWHM /km s$^{-1}$ | $v_{peak}$ /km s$^{-1}$ | intrinsic FWHM /km s$^{-1}$ | $v_{peak}$ /km s$^{-1}$ | intrinsic FWHM /km s$^{-1}$ | $v_{peak}$ /km s$^{-1}$ | intrinsic FWHM /km s$^{-1}$ |
| 19 | 5.3±2.3 | 44.5±5.4 | 5.4±2.1 | 36.4±5.0 | 7.5±0.9 | 25.5±2.2 | -4.4±4.6 | 69.3±10.9 | -7.6±6.6 | 91.5±15.6 |
| 20 | 1.4±1.6 | 35.0±3.8 | 3.0±1.0 | 26.1±2.4 | 4.9±0.3 | 22.6±0.9 | 1.7±1.0 | 26.0±2.3 | -1.7±4.6 | 80.1±10.9 |
| 21 | 4.0±1.5 | 26.1±3.5 | 7.9±0.5 | 12.9±1.3 | 6.9±0.2 | 23.1±0.6 | 6.1±0.3 | 15.9±0.7 | 6.8±1.1 | 16.7±2.5 |
| 22 | 4.1±0.8 | 18.4±2.0 | 6.7±0.5 | 14.1±1.1 | 6.7±0.2 | 25.1±0.5 | 6.0±0.2 | 17.2±0.6 | 6.6±0.4 | 15.7±0.9 |
| 23 | 4.8±0.9 | 20.9±2.1 | 8.1±0.5 | 19.6±1.1 | 9.8±0.1 | 27.3±0.4 | 5.2±0.2 | 19.9±0.5 | 6.6±0.2 | 12.6±0.5 |
| 24 | 4.5±0.6 | 20.4±1.5 | 8.3±0.4 | 21.4±0.9 | 10.5±0.1 | 24.1±0.4 | 4.3±0.2 | 23.3±0.5 | 5.9±0.2 | 10.4±0.5 |
| 25 | 4.9±0.6 | 19.1±1.4 | 9.2±0.3 | 16.3±0.8 | 8.5±0.1 | 18.3±0.4 | 4.1±0.3 | 21.6±0.7 | 4.4±0.2 | 13.1±0.5 |
| 26 | 5.3±0.5 | 16.1±1.3 | 7.4±0.2 | 13.3±0.6 | 7.6±0.2 | 16.6±0.5 | 6.9±0.3 | 19.4±0.7 | 5.5±0.2 | 16.8±0.6 |
| 27 | 5.8±0.5 | 12.4±1.2 | 4.0±0.2 | 13.5±0.5 | 4.6±0.4 | 19.0±0.9 | 7.6±0.3 | 18.8±0.8 | 6.0±0.4 | 15.8±1.0 |
| 28 | 7.0±0.3 | 15.6±0.5 | 5.3±0.1 | 14.7±0.4 | 6.3±0.2 | 15.2±0.7 | 6.3±0.3 | 17.0±0.7 | 6.6±0.3 | 14.9±0.7 |

Table 3.3: Gaussian line-fits to main velocity component of background-subtracted $H_2$ 1-0 S(1) wake profiles in M42 HH120-114. CGS4 slit row 19 (top row displayed in Figure 3.21) corresponds to the Allen and Burton (1993) image coordinates indicated above each column. Row 28 is the bottom row displayed in Figure 3.21. Velocities are calibrated relative to the local standard of dynamical rest (LSR).

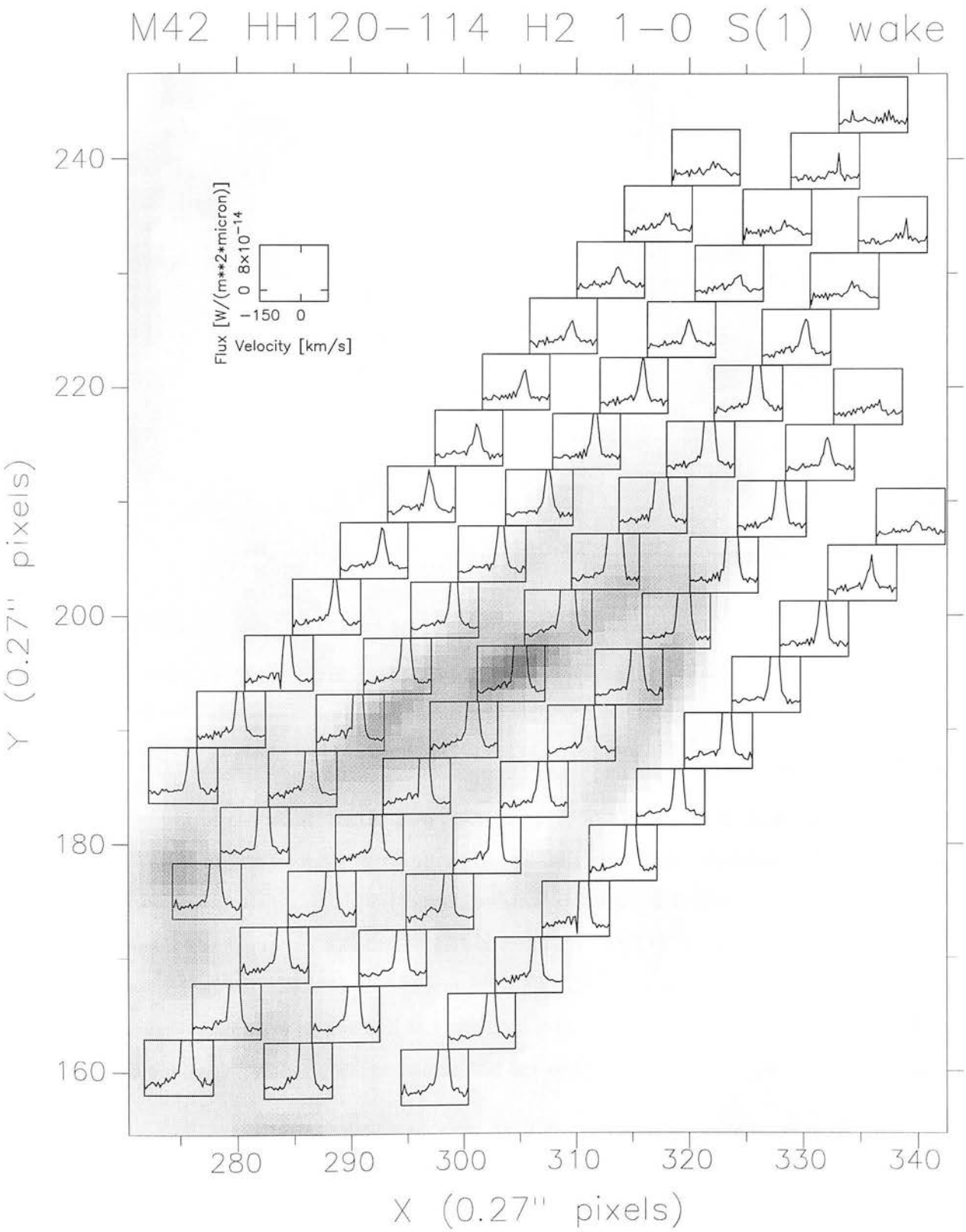


Figure 3.23: M42 HH120-114 "wake" - "background" $H_2$ 1-0 S(1) velocity profile emission highlighting weak $H_2$ 1-0 S(1) velocity features.

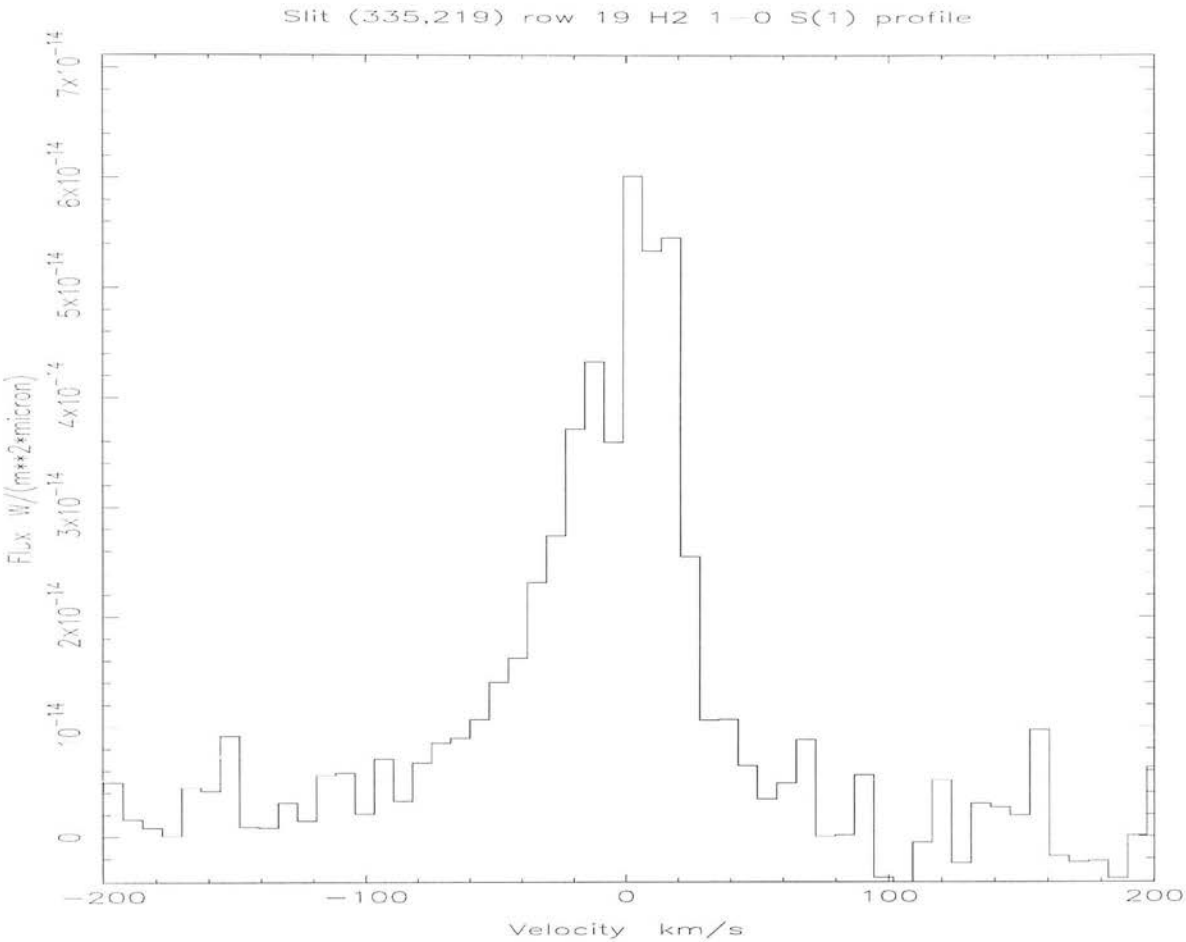


Figure 3.24: Slit (335,219) row 19 $H_2$ 1-0 S(1) velocity profile, upstream of prominent M42 HH120-114 wake emission and without background subtraction. Note the very large total velocity range near zero intensity and the similarity to the corresponding [FeII] profile (Figure 3.12).

the tail of the wake for the two on-wake slits. We note, however, a significantly higher FWHM at the lowest row numbers 19 and 20 than is seen elsewhere. This is due to the presence of a very weak but broad pedestal in addition to the weak main profile which biases the Gaussian line-fits to give a resultant FWHM as high as $91.5\pm10.9\mathrm{km\,s^{-1}}$ for row 19 of slit (344,214). Also, at slit (335,219) for example, the FWHM of the line emission appears to rise and fall twice with increasing row number, correlated with the two different wakes observed along the line-of-sight at these positions.

Unlike the wake associated with M42 HH126-053, additional velocity components are not clearly identified on the main wake region itself (Figure 3.23) apart from the weak, artificial "ghost" feature. However, real secondary components are visible on the confused region just downstream of the actual wake(s). The broad but very weak

emission noted above for the lowest row numbers in figure 3.23 are, however, visible. At these positions, ill-defined in the $H_2$ image but coincident with the strongest [FeII] "bullet" emission, it appears that the total velocity range at close to zero intensity is similar to the [FeII] 1.644$\mu$m profile, *i.e.* as high as $130\pm20 \mathrm{km\,s^{-1}}$ ! Figure 3.24 shows row 19 of slit (335,219) but with the background not subtracted to show the weak high velocity emission at higher signal-to-noise. We note the similarity both in shape and velocity range to the corresponding [FeII] "bullet" profile (Figure 3.12) at the same position. Retention of the background component does not contribute to the high velocity emission we are interested in here. The small dip near the peak of the profile is artificially introduced by a very weak and unresolved $H_2$ emission source centred at zero velocity in the sky position used and so again will not affect the high velocity emission. This sky feature was carefully checked for all relevant positions in this wake and confirmed to be approximately constant but negligible in intensity compared to even the background component.

## 3.5 Discussion

### 3.5.1 Nature of Background Contribution(s) to Profiles

In front of the shocked line emission from OMC-1 there is a zone of fluorescent $H_2$ line emission, resulting from the UV excitation of the molecular cloud by the Trapezium stars. While in the line of sight to OMC-1 it is clear that shocked/thermal emission dominates, it is important to estimate the contribution of fluorescent emission, especially as its profile should be unresolved by our observations, being intrinsically narrow compared to collisionally broadened $H_2$ emission. Large scale diffuse $H_2$ mapping by Luhman *et al.* (1994) over the entire Orion A cloud in the 6-4 Q(1) line at 1.601$\mu$m and 1-0 S(1) line shows that UV fluorescence dominates the emission in the outer parts of the cloud and accounts for $\sim 98-99\%$ of the global $H_2$ emission. Burton & Puxley (1990) showed that shocks alone would produce relatively more 1-0 S(1) emission contributing $\sim 7\%$ of the total line flux. The line profiles of the fluorescent emission from the Orion Bar are unresolved spectrally with FWHM $\leq 17$ km s$^{-1}$ (Burton *et al.* 1990a) and are centred at

the ambient cloud velocity. This is in clear contrast to the 140/kms wide with broad blue-wing shock profile at OMC-1 (Brand *et al.* 1989b). Hence, if fluorescence were dominating the emission in any of the profiles we measured we would expect to see a significantly enhanced, narrow component to the profile at the rest velocity compared to the shock profiles.

Following the analysis of Burton & Puxley (1990), the fluorescent contribution to the 1-0 S(1) line at the peak of OMC-1 is only about 1%, but moving to the edges of the strong emission regions it rises to about 10%. At the region containing the observed "bullet" wakes the strength of the fluorescence has not been measured in detail. In both tracers measured here the profile of the background emission pervading the observed "bullets" region is well-fitted by a single Gaussian profile centred within $3\mathrm{km\,s^{-1}}$ of zero velocity relative to the local standard of dynamical rest. However, the $H_2$ profile is not unresolved, as would be the case if it were excited by fluorescence alone, but is significantly broadened by $26.0\pm2.5\mathrm{km\,s^{-1}}$ at FWHM. Therefore the background component can perhaps be modelled as a combination of an unresolved fluorescent component together with a uniform, collisionally broadened component. If the broadening is interpreted as purely thermal, this corresponds to an rms velocity, $v_{rms}= 16.8\mathrm{km\,s^{-1}}$ and uniform excitation temperature of $\simeq$34,000K!

Alternatively, the broad component may be the result of an expanding bubble, centred near the BN-IRc2 complex, which pushes a shock front through the molecular gas as it traverses the entire observed region. If the emission is due to cooling upon passage of a uniform, plane J or C shock front, we would expect the peak velocity of the resultant profiles to vary with position in the region as the line-of-sight intersects components deflected at differing angles and varying apparent shock velocity. One would also expect to see two different components, separated in velocity, along a given line-of-sight intersecting two different sides to the bubble. This appears to rule out this explanation as even though the underlying cloud geometry is unknown it is difficult to model the emission resulting in such a spatially uniform, singly-peaked profile. The broadening may therefore only be explained by a single and constant, highly magnetised planar C shock or as the result of supersonic turbulence or instabilities. These processes are little understood and may be expected to significantly alter the excited $H_2$ level populations

compared to steady-state models. We shall go on to measure the $H_2$ excitation spectrum of this background component in Chapter 4.

### 3.5.2 Comparison of $H_2$ wake Profiles to Steady State Bow Shock Models

We have demonstrated that integrated [FeII] 1.644$\mu$m line profiles in Orion are entirely consistent with theoretical bow-shock predictions for two different values of $v_s$ and $\alpha$. Motivated by clearly resolved bow-shaped $H_2$ wakes associated with the [FeII] "bullets", it was expected that observations of individual $H_2$ line profiles within the wakes should enable a clear distinction between competing models of the shock excitation within these structures. Indeed, Carr (1993) was able to successfully interpret the $H_2$ 1-0 S(1) 2.122$\mu$m profile emission in the bow-shaped object HH7 (NGC1333) as a bow shock in this way. Such models predict broad, double-peaked emission profiles to be observed in the $H_2$ wakes associated with the Orion "bullets", since a line-of-sight should intersect two distinct and oppositely directed shock fronts on either side of the bow shock wake. However, we have observed $H_2$ 1-0 S(1) line profiles at positions along the brightest and most clearly resolved $H_2$ wakes but find them to be dominated by singly-peaked, broad profiles centred within 10km s$^{-1}$ of the peak background emission. This cannot be reconciled with any steady state bow shock models.

Referring to Figure 3.25, it is straightforward to show that the effective radial velocity ($v_{rad}$) observed for gas shocked by one side of a simple parabolic bow structure is given by the expression

$$v_{rad} = v_s \sin\psi \sin(\alpha - \psi) \tag{3.6}$$

where $v_s$ is the shock speed through the (stationary) ambient medium, $\psi$ is the angle between the tangent to the bow at that point and the bow-axis, and $\alpha$ is the angle between the bow-axis and line-of-sight (orientation). For a line-of-sight that intersects regions on both sides of a wake, the radial velocity to the observer is oppositely directed for each component. Therefore two separate components are observed as long as the

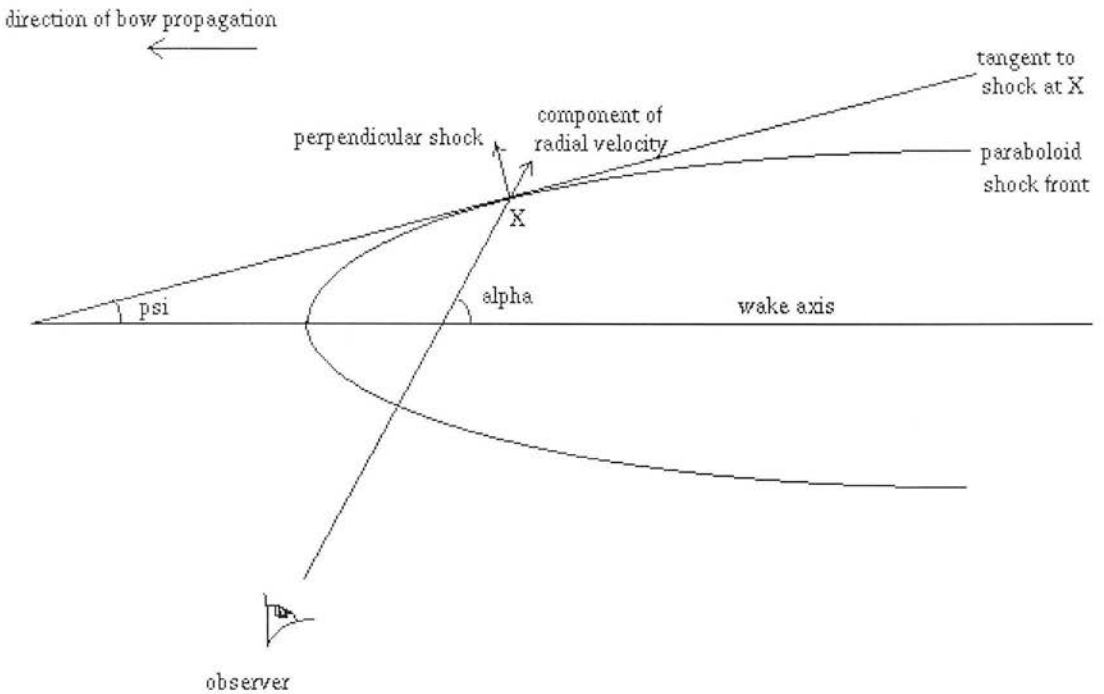


Figure 3.25: Diagram of theoretical bow shock front (assumed paraboloid) passing at velocity $v_s$ through a stationary medium and imparting a velocity $v_\perp = v_s \sin\psi$ perpendicular to the bow at X. The observer sees an effective radial velocity $v_{rad}$ (see text). The observer sees an oppositely directed component of shocked gas (not shown here) from the intersect of the line-of-sight to the near side of the wake.

effective shock velocity is not so high as to dissociate $H_2$ in either component, as is the case for all positions in the Orion "bullet" wakes except those close to the tip associated with the [FeII] 1.644$\mu$m emission itself.

At positions near the head of the $H_2$ wake emission, *e.g.* row 20 of slit (283,307) in Table 3.1 for M42 HH126-053 (Figures 3.17,3.18), one can use the "bullet" speed and orientation determined from the $Fe^+$ profiles together with the approximate bow position (hence $\psi$) in equation 3.6 to determine the peak velocity of the expected emission. In the simplest case of a J shock this is equivalent to the shock velocity "seen" by the gas. If we take a value of $\psi$ ~45° on the far side of the wake and $\psi$ ~ -30° for the near side, then the peaks will be centred at ~96 and -48km s$^{-1}$ respectively ($v_s$=150km s$^{-1}$

, $\alpha$=70°). Figure 3.26 shows model profiles calculated in this way over the relevant shock range sampled in a single CGS4 pixel for both M42 HH126-053 and M42 HH120-114 at row 20 of slits (283,307) and (324,230) respectively. No dissociation speed limit has been imposed so that the models merely indicate the wide peak separation and the relatively low emission strength near to the pre-shock velocity (set to zero), in contrast to the observed $H_2$ emission. While a peak velocity separation of this magnitude can be accomodated within the widest [FeII] profiles at the tips of the "bullet", they clearly cannot explain the singly-peaked $H_2$ profiles given the relatively high velocity resolution ($14\mathrm{km\,s^{-1}}$ per velocity channel or $23\mathrm{km\,s^{-1}}$ FWHM) of these observations compared to the profile widths. We should clearly resolve two separate peaks. In any planar shock the peak $H_2$ emission velocity is shifted from that of the ambient cloud since it is the downstream gas that is emitting. Although the peak emission for a C shock occurs at velocities below the shock speed itself, it will still be at velocities significantly shifted from the pre-shock velocity of the gas, and always oppositely directed for each component sampled at positions in the near plane-of-sky wakes observed here.

We note that it is only just possible to fit the observed profiles by theoretical C bow shock models even if the line-of-sight includes the entire bow shock and therefore the full, integrated velocity range. This can be seen by comparing to Figure 11 of Smith & Brand (1990c) and assuming that the bow is oriented close to the plane-of-sky and moving at $v_s$=$120\mathrm{km\,s^{-1}}$, as determined from the $Fe^+$ profiles. Our observations, however, dissect small cuts through the bow, rather than the full range of shocked velocities sampled over the total bow surface. To fit a single C shock absorber model (Smith *et al.* 1991b) at these positions would imply an $H_2$ dissociation speed in excess of $\sim 80\mathrm{km\,s^{-1}}$, with an implied magnetic field strength far in excess of observed estimates (Chrysostomou *et al.* 1994). Furthermore, an explanation for the appearance of limb-brightened bow-shaped wakes is then required, especially given the success of the bow shock model in explaining the $Fe^+$ emission.

Theoretical bow shock models further predict that peak separation will decrease from a maximum value near the head of the wake (exact position depending on orientation) to a minimum towards the tail where the gas is only weakly shocked due to the highly oblique angle between shock front and direction of propagation of the bow. Hence, the

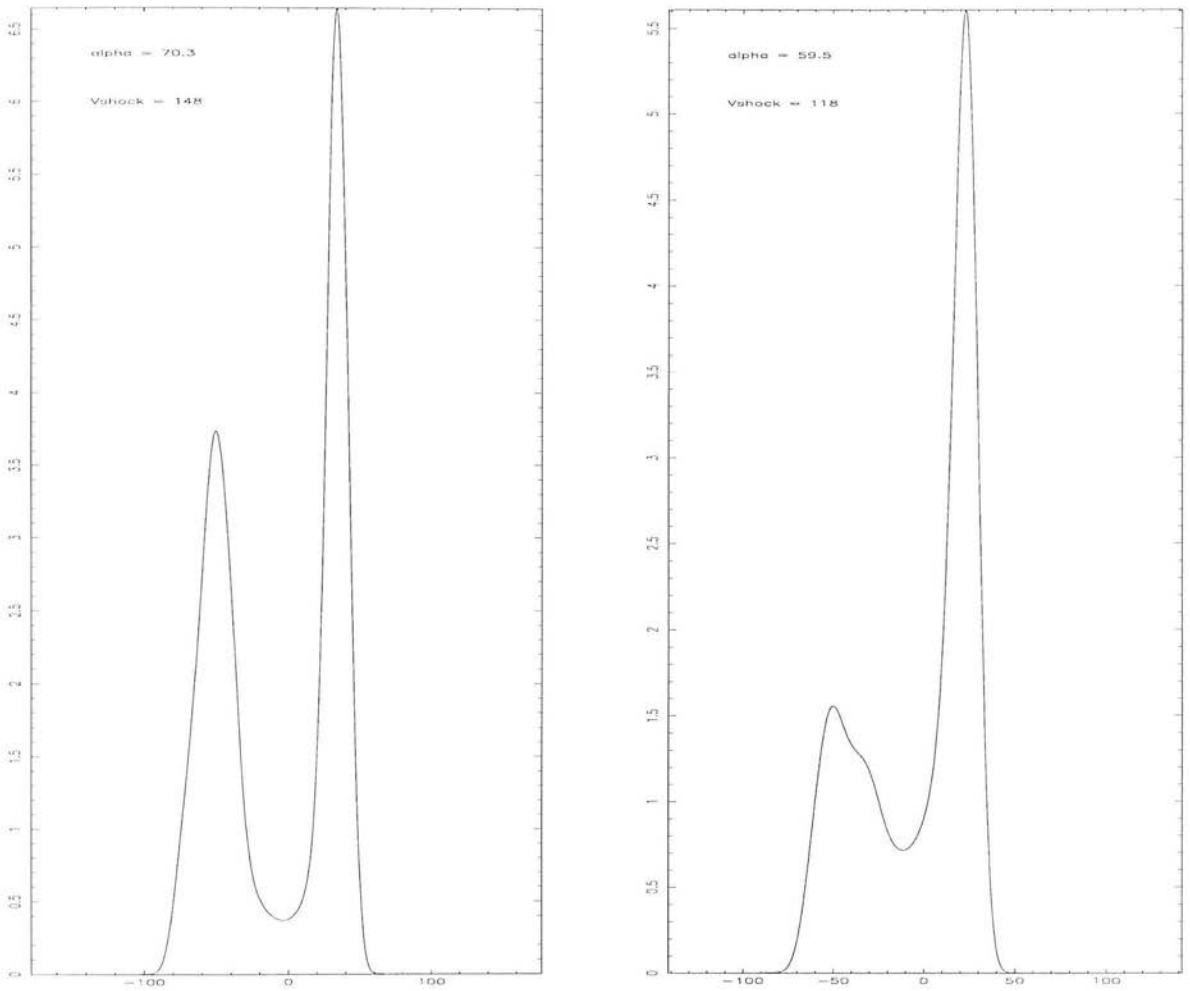


Figure 3.26: Model Predictions of possible shocked $H_2$ 1-0 S(1), 2.122 $\mu$m line profiles in following pixel positions. *Left:* M42 HH126-053 Slit (283,307) row 20; *Right:* M42 HH120-114 Slit (324,230) row 20. The model assumes post-shock relative velocity is negligible and that the shocks move into a stationary medium. No dissociation speed limit has been imposed on the shocked $H_2$ and profiles are not smoothed by instrumental broadening.

profile width, proportional to the effective shock speed, will decrease for each component as one moves down the bow axis. A decrease in peak separation is also predicted in moving across from central axis positions to the outer limbs of the wake, perpendicular to the bow axis, as direction of shock impulse converges for each side of the wake. Singly peaked profiles are therefore not inconsistent with bow shock models for positions in the wake extremities, but the widths must be considerably more narrow. Our observations do show a gradual decrease in profile FWHM in moving down the wake, although this

is less clear in the case of M42 HH120-114 due to the presence of two wakes for some positions. Within individual wakes, however, this relation holds.

The detection of weak but extremely high velocity (peak velocity$\lesssim$ -105km s$^{-1}$ ) $H_2$ emission features at positions close or coincident with the [FeII] "bullet" emission in both wakes is inexplicable with any steady state molecular shock models unless we are not resolving multiple shock fronts along the line-of-sight. However, peak velocity of the individual features identified in M42 HH126-053 clearly moves closer to the main emission peak in moving down the wakes and so appears to be associated with the "bullets". The presence of the instrumental "ghost" feature in between the strong and weak components together with the relatively poor signal-to-noise, however, prevents a more detailed analysis. When resolved, the FWHM of Gaussian line-fits to these components shows no clearly discernable trend with position, but never exceeds the FWHM of the strong, zero-velocity centred emission.

### Dust Extinction?

In the absence of the expected double-peaked $H_2$ profiles, we now examine the possibility that the "fingers" of $H_2$ may contain dust at a density that is high enough to completely extinguish $H_2$ emission from the far side of the wake (relatively redshifted emission). To estimate the implied gas density required for this, we set the optical depth, $\tau$, given by

$$\tau = \int_{pathlength} N\sigma_{ext} dx \tag{3.7}$$

to unity. Here, $\tau$ is a function of the mass column density $N$ (gcm$^{-3}$) and the dust opacity at 2.122$\mu$m $\sigma_{ext}$ (cm$^2$g$^{-1}$) integrated over the pathlength ($x$) of intervening material between each face of an idealised bow shock structure. Examining the Allen & Burton (1993) images, the wake structures are of order $10^{17}$cm across. If we take an estimate for the dust opacity of $\sigma_{ext} = 3.25 \times 10^3$cm$^2$g$^{-1}$ at 2.512$\mu$m (Ossenkopf & Henning 1994) this gives an implied mass density of $3.08 \times 10^{-21}$gcm$^{-3}$. Using the typical interstellar medium value $\rho_{dust} \simeq 0.01\rho_{gas}$ and knowing $m_{H_2} = 3.3 \times 10^{-24}$g therefore implies an $H_2$ gas number density of $\sim 10^5$cm$^{-3}$, which is similar to the inferred densities in the OMC-1 region. Clearly this possibility will require further investigation.

### 3.5.3 Summary

We have demonstrated that integrated [FeII] line profiles in the Orion "bullets" are consistent with theoretical bow-shock predictions for two different values of $v_s$ and $\alpha$. We have identified a uniform, broad background component pervading the region in both $Fe^+$ and $H_2$ which is inconsistent with a fluorescent component due to the ionizing radiation of the Trapezium stars alone. A collisionally broadened background component of unidentified origin is measured with an average FWHM of $26\pm2.5\mathrm{km\,s^{-1}}$ in the $H_2$ 1-0 S(1) line and a peak velocity of $2.5\pm0.5\mathrm{km\,s^{-1}}$ , close to the local ambient rest velocity. The extended $H_2$ bullet wakes have allowed us to dissect individual molecular bow shock structures but the broad, singly-peaked $H_2$ 1-0 S(1) profiles observed in the two most clearly resolved, plane-of-sky oriented wakes challenge our present understanding. It is very difficult to reconcile *any* steady-state bow shock model with these observations in Orion. To fit a single C shock absorber model to individual profiles implies a magnetic field strength far in excess of observed estimates and is not consistent with the bow-shaped wake morphology.

Alternatively, we may still not be resolving multiple shock fronts along the line-of-sight. For example, multiple overlapping bullet wakes could give rise to merged sets of doubly-peaked profiles resulting in approximately Gaussian shaped profiles. However, given the appearance of single bow shaped wakes at many observed positions, the accuracy of pure Gaussian line-fits, the velocity resolution of our observations and that we see this phenomenon in *two* different wakes, this explanation is expected to be excluded.

If we cannot fit the profiles in Orion with steady state molecular shocks it may be necessary to model the effects of instabilities and turbulence. This will have important consequences. Not only will line profiles be broadened but level populations of shocked species will be altered and hence the observed column densities over a range of transitions. New observations of $H_2$ column densities in these "bullet wakes" (Chapter 4) address this.

# Chapter 4

# Shocked $H_2$ Excitation in the Orion "Bullet" Wakes

## 4.1 Abstract

We have measured the excitation of $H_2$ via K band transitions in the Orion "bullets" region and find a near-constant background spectrum which can be modelled by a combination of fluorescent and shock-excited mechanisms. Measurement of the $H_2$ excitation in the "bullet" wakes M42 HH126-053 and M42 HH120-114 shows a near constant emission spectrum, within each wake, that may be modelled by a combination of shocked and fluorescent excitation, now more strongly dominated by collisional processes but also containing an intrinsic wake-only fluorescent component. However, the near constancy of this excitation with position *within* each individual wake is inconsistent with bow C shock models previously fitted at OMC-1, in which significantly different line ratios occur depending on the shock velocity which varies in the bow. This is in agreement with $H_2$ 1-0 S(1) line profiles measured at these positions and suggests that it may be necessary to model the effects of instabilities and turbulence in the Orion "bullet" wakes in order to fit our observations.

## 4.2 Introduction

The nature of molecular shocks, which play an important role in the processes of momentum and energy transfer within star forming molecular clouds (McKee 1989), is still uncertain (Draine & McKee 1993). The Orion molecular cloud is the brightest known source of shocked $H_2$ emission and as such has been the primary test-bed for theoretical models, as reviewed in Chapter 3. The discovery of [FeII] "bullets" in the Orion outflow (Allen & Burton 1993) emphasised the importance of bow shock morphology and allowed the first measurements of bow-shock dynamics in this bright source. In Chapter 3 we showed that broad, singly-peaked $H_2$ 1-0 S(1) velocity profiles in clearly resolved bow-shock structures of the Orion "bullet" wakes are extremely difficult to reconcile with existing steady-state shock models. In this Chapter we describe detailed observations of a range of $H_2$ lines in the K band to determine the nature of the $H_2$ excitation in the same Orion "bullet" wakes using CGS4 with the new 256x256 array at UKIRT.

In previous work, concentrated at the position of peak $H_2$ brightness in the Orion outflow (OMC-1), it has been established that planar C(magnetised)-shock models cannot explain the $H_2$ line intensities in Orion or any other outflow, while planar J-shock models can (Brand *et al.* 1988). However, neither planar nor bow J-shock models can reproduce the line profiles observed at OMC-1 (Brand *et al.* 1989b). It is just possible to fit both $H_2$ line profiles and ratios in this region using highly magnetised C-shock models (Smith *et al.* 1991b). Measurements of $H_2$ excitation conditions which remain constant throughout the bright part of the Orion outflow, however, are not easily explained by any bow shock models (Brand *et al.* 1989b, McKee 1989).

Fernandes and Brand (1995) have demonstrated that molecular hydrogen emission from the bow shock-shaped HH7 is well explained as a C-shock in a bow configuration in which the 'cap' is completely dissociated, and $H_2$ fluorescence produced by Lyman alpha resonance pumping in the hot post-shocked layers (Black & van Dishoeck 1987) in the cap irradiate the downstream flow. The same type of shock + fluorescent spectrum as seen in HH7 has been seen in DR21 (Fernandes 1993). It was expected that the bow shocks in Orion could be similarly excited.

We used CGS4 in its echelle mode to obtain [FeII] line profiles of many of the bullets together with $H_2$ line profiles in the two most clearly defined bow shock wakes (Chapter 3). Observations of the integrated [FeII] 1.644 $\mu$m line profile of the "bullets" M42 HH126-053 and M42 HH120-114 oriented close to the plane of sky, show a width (FWZI) of up to 150 kms$^{-1}$. We have observed $H_2$ 1-0 S(1) 2.122 $\mu$m line profiles at positions both along and across the corresponding bow-shock wakes. At these positions, a line-of-sight should intersect two distinct and oppositely directed shock fronts on either side of the bow shock wake and modelling gives a doubly-peaked line profile. In moving down the wake, away from the bullet, the model velocity width decreases as the normal component of bow shock velocity of each gas component decreases. However, unlike $H_2$ profiles observed in HH7 (Carr 1993), the observed profiles (resolution 14.1 kms$^{-1}$) at these positions are dominated by a broad (FWZI $\lesssim$ 80 kms$^{-1}$) BUT singly-peaked Gaussian-shaped line profile.

These observations appear irreconcilable with any steady-state bow shock model (the fluorescent component fitted to $H_2$ intensities in HH7 will not explain the broad line profiles seen in Orion). It may be necessary to model the effects of instabilities and turbulence in the Orion "bullet" wakes in order to fit the observations. We expect the excitation of these molecular shocks to be unusual so it is essential to measure this. We therefore used the CGS4 spectrometer at UKIRT with the 75 l/mm grating to measure a range of $H_2$ emission in the K-band at the brightest positions in the Orion "bullet" wakes for which we have profile data, including the fainter transitions corresponding to the highest upper energy levels, as necessary to distinguish excitation mechanism. Resultant spectra can be compared for a range of positions along and across the wakes to search for any changes in excitation within the bow structure, and also summed for an entire wake in order to achieve maximum signal to noise on the faintest transitions.

## 4.3 Observations

Near-infrared, long-slit K band spectra were measured of the $H_2$ line emission associated with the two most clearly defined Orion "bullet" wakes. The observations were made for a range of positions both along and across the associated $H_2$ wakes, to search for the

predicted changes within the proposed bow shock structure and to complement previous $H_2$ 1-0 S(1) 2.122$\mu$m line profile observations at the same positions (Chapter 3). Observations of the wakes associated with the "bullets" M42 HH126-053 (previously denoted M42 HH7) and M42 HH120-114 (previously unidentified) were carried out at UKIRT on the nights of 5-8th October 1995 with the cooled grating spectrometer CGS4 and the new (256x256) detector array. At this time CGS4 was fitted with the short 150mm focal length camera and we used the 75 lines/mm grating in first order to measure $H_2$ lines in the K window, centred at 2.2$\mu$m , giving $\simeq$1.22$''$ wide pixels. In this configuration with the new array, the spectral coverage of 0.66 $\mu$m is sufficient to observe the entire K-window at one grating position and at a significantly improved spectral resolution of 0.0025$\mu$m, preventing blending of any of the important lines with background emission or other $H_2$ lines. Therefore all $H_2$ lines used in this experiment were observed simultaneously at a given position which eliminates problems associated with intercalibration of adjacent spectra, sky fluctuations and telescope pointing.

Spectra were oversampled and the number of bad pixels reduced by physically shifting the array by 1/3 pixel, so that six detector positions were observed over two resolution elements. Each spectral image was bias subtracted and flat-fielded using a black-body calibration source. As the background and array bias varies between the three detector positions used to sample profiles, the baselines in the resultant interlaced spectra can exhibit a sawtooth profile of period 3 pixels. If present, this is corrected for by fitting linear baselines to the continuum of a standard star and correcting each row of each spectral image respectively (Chapter 2.3). Removing the 3 pixel baselines, row by row, corrects for the ripple in the final reduced spectra. All spectra were wavelength calibrated by observing an Argon arc lamp in the same instrumental configuration and measuring a range of emission lines from $\lambda_{air}$ = 1.9823$\mu$m to $\lambda_{air}$ = 2.5668$\mu$m . OH emission lines present in sky spectra were also used as a secondary check. It was necessary to rebin the resultant images to correct for small optical distortions, resolvable in both the spatial and dispersive directions of the new array, using routines in the STARLINK Figaro Software Library before proceeding to wavelength calibrate the data (Chapter 2.3.5).

The nearby UKIRT standard star BS1937 at $05^h\,38^m\,53.0^s$, $-07^\circ\,12'\,47''$ [2000] and spectral type A4V (K= 4.47 mag) was observed at the same airmass as Orion for each

position to flux calibrate the data and remove telluric absorption features. No stellar absorption features are present in this wavelength range except the well-known Br$\gamma$ absorption line at 2.166$\mu$m , which was removed by manual interpolation, before flux calibration, using FIGARO software.

The $H_2$ trails behind the "bullets" studied in Orion are of order $40\,\widehat{''}$ long, $10\,\widehat{''}$ wide. Observations of the $H_2$ wake associated with the "bullets" M42 HH126-053 (Figure 3.4) and M42 HH120-114 (Figure 3.7) required between 9 and 13 groups of object-sky-sky-object observations at each different slit position per $H_2$ wake. The total on-source integration time was at least 180s, as necessary to obtain high signal-to-noise detections of the faintest higher energy $v = 4$ $H_2$ transitions, such as the $H_2$ 4-3 S(3) [23975K] line at 2.3445$\mu$m , with the new array. An offset sky position at $+600\,\widehat{''}$ West in Right Ascension (RA) was used, in order to be fully clear of M42 nebula background emission. The slit was positioned so that the middle row on the array was fixed midway along the $H_2$ wake in each case and oriented at an angle of $+25°$ and $+41°$ West of North on the sky for the "bullet" wakes M42 HH126-053 and M42 HH120-114 respectively. Slits were aligned parallel to the wake axis and coincident with our previous $H_2$ 1-0 S(1) line profile observations. Slit positioning was achieved by small step offsets from the nearby IR reference objects: BN and IRc9, whose positions are exactly known. In addition, pointing checks were made at approximately hourly intervals by offsetting to three nearby stars and measuring any drift in RA or DEC from the expected position. The drift was found to be typically $\lesssim 0.5\,\widehat{''}$ and rarely exceeded $1.0\,\widehat{''}$ .

## 4.4 Results

Figures 4.1 and 4.2 show a cut in wavelength from 2.1 to 2.18$\mu$m at selected positions for each of the wakes M42 HH120-114 and M42 HH126-053 respectively. These positions have been selected to sample the brightest and least confused regions near the head of the wakes. In the case of M42 HH120-114, a total of twelve positions are analysed in order to obtain high signal-to-noise spectra averaged over the wake and also to search for any variations in moving both along and perpendicular to the wake axis. In the rather more confused M42 HH126-053 wake, 6 rows running down the central wake axis

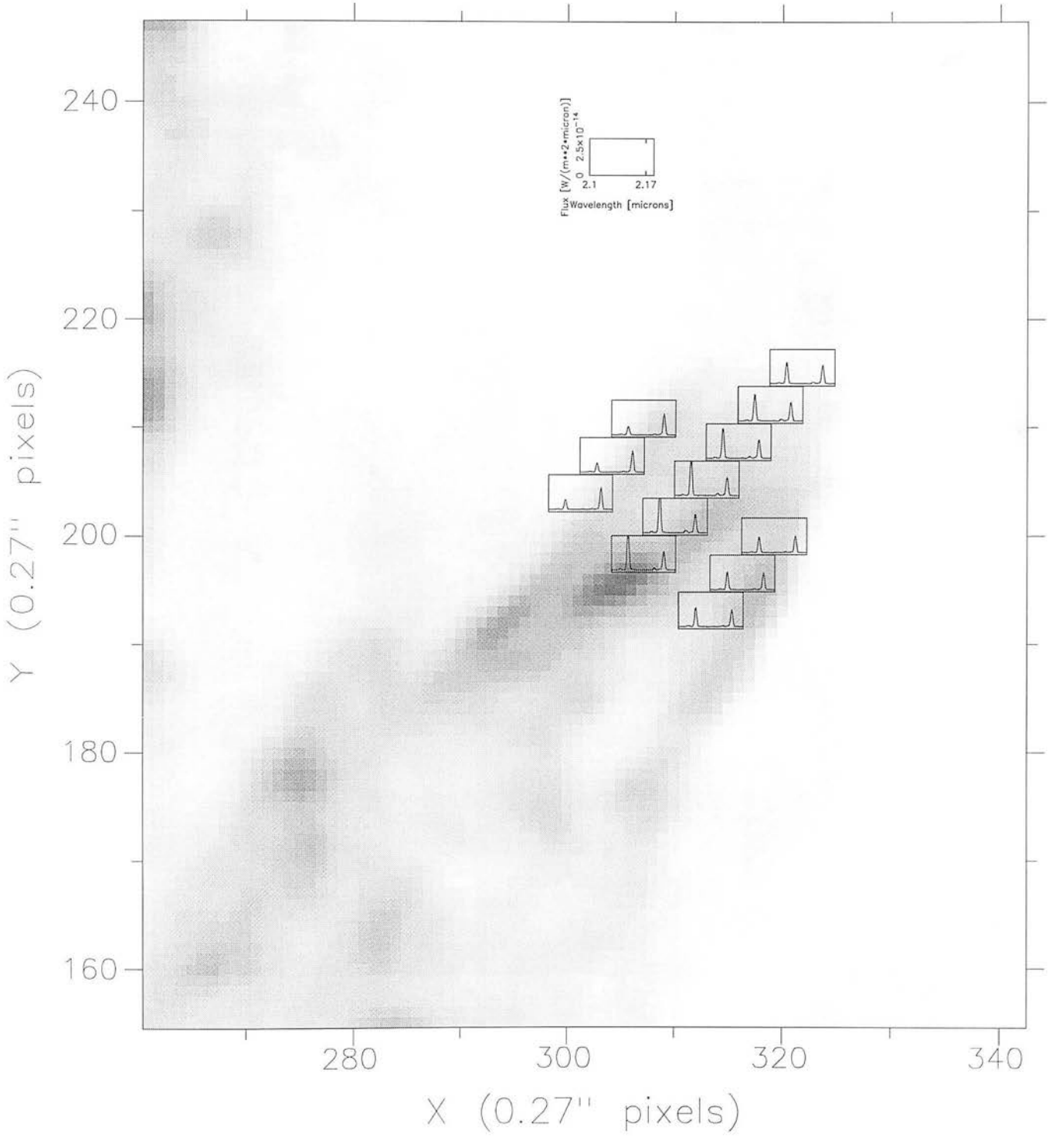


Figure 4.1: Selected M42 HH120-114 K band spectra cut to show the prominent $H_2$ 1-0 S(1) line at 2.122$\mu$m and Brackett $\gamma$ line at 2.166$\mu$m superimposed on the $H_2$ 1-0 S(1) narrowband image of Allen & Burton (1993). Boxes are centred at corresponding row of CGS4 slit position but are scaled in size for display purposes and therefore not equivalent to actual size ($1.22\hat{''} \times 1.22\hat{''}$) on sky. A key box indicates flux and wavelength scale of spectra.

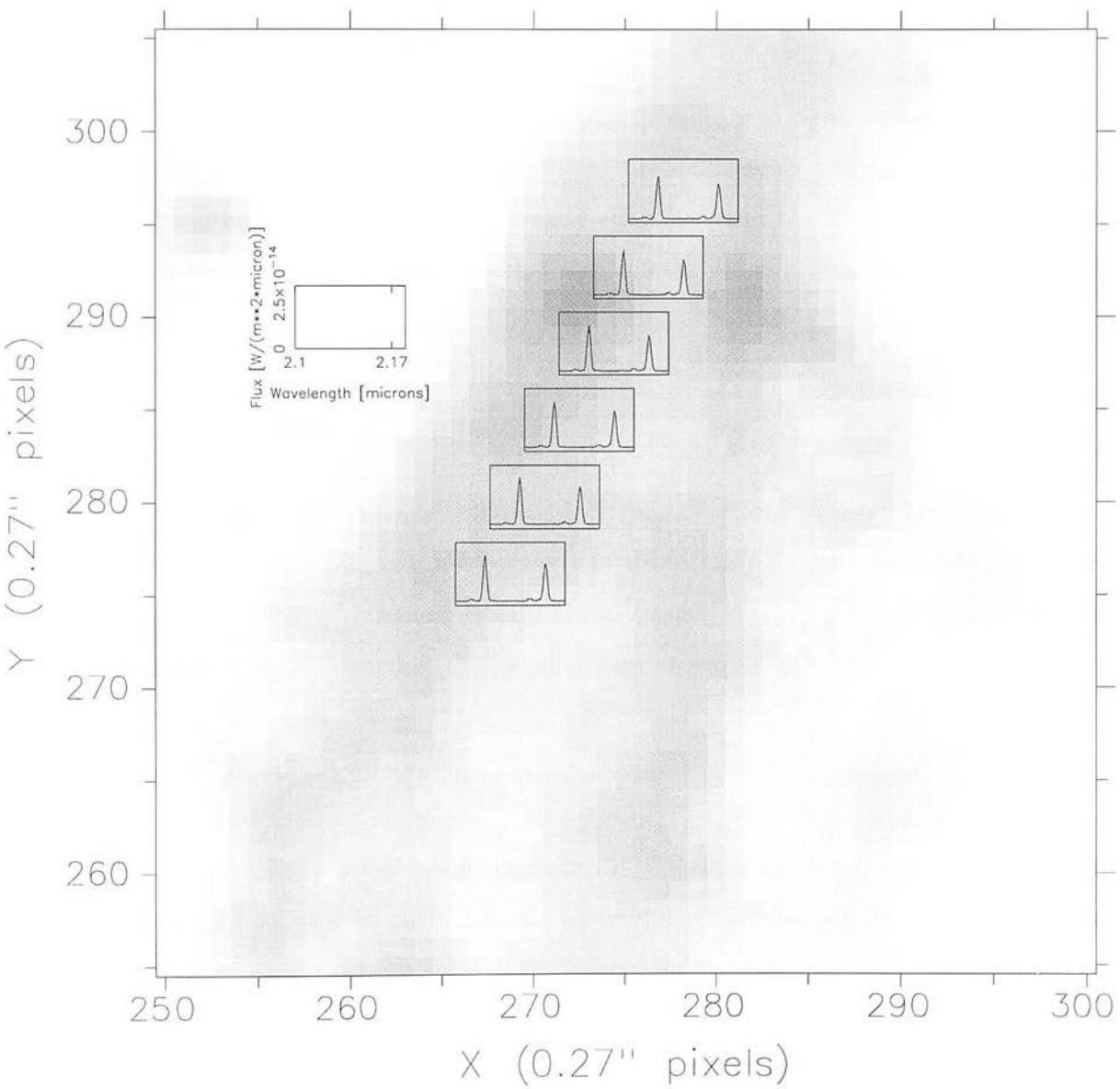


Figure 4.2: As Figure 4.1 but for selected M42 HH126-053 K band spectra cut to show prominent $H_2$ 1-0 S(1) and Br$\gamma$ emission lines. Detailed $H_2$ line-fits have been made and CDR diagrams plotted at each position shown in each wake (see text).

are analysed. The spectra are dominated at all positions by the $H_2$ 1-0 S(1) line at 2.1218$\mu$m and the Br$\gamma$ recombination line of neutral hydrogen at 2.166$\mu$m . However, whereas the Br$\gamma$ line intensity remains almost constant at all positions both on and off the "bullet" wakes, the $H_2$ 1-0 S(1) line intensity clearly fluctuates with wake intensity, in approximate correlation with the underlying $H_2$ 1-0 S(1) narrowband image of Allen & Burton (1993). The Br$\gamma$ line is thus associated with the background emission pervading the entire region noted in Chapter 3.

To calculate $H_2$ column densities along these lines of sight we can take advantage of the fact that the observed $H_2$ transitions are quadrupole and therefore optically thin. Hence, the radiative transfer is greatly simplified and the number of molecules $N_j$ in the excited levels $j$ (column density) is calculated directly from the measured line fluxes using the expression

$$\frac{N_j}{g_j} = \frac{4\pi}{hc}\frac{\lambda_{ji} I_{ji}}{A_{ji} g_j} \times 10^{0.4 A_\lambda}, \tag{4.1}$$

where $g_j$ is the degeneracy (or statistical weight) of level $j$, $h$ is Planck's constant, $c$ is the speed of light, $\lambda_{ji}$ is the wavelength of transition $j - i$ calculated from Dabrowski & Herzberg (1984), $I_{ji}$ is the intensity of transition $j - i$, $A_{ji}$ is the Einstein $A$ coefficient (Turner *et al.* 1977) and $A_\lambda$ is the extinction at wavelength $\lambda$.

### 4.4.1 Extinction Measurements

In order to study the physical conditions in the emission region, inferred column densities must be corrected for interstellar extinction. The observed flux ratio of lines having a common upper energy state depends only on the differential extinction between the two lines, the Einstein $A$ coefficients, and the energies of the transitions. Using calculated and laboratory measurements of the molecular parameters it is therefore possible to measure the differential extinction. Then, assuming an extinction law of the form $A_\lambda \propto \lambda^{-\alpha}$ with $\alpha$= 1.73 (He *et al.* 1995 following Draine 1988 and Whittet 1988), the differential extinction can be converted to a total extinction value at a given wavelength (e.g. Beckwith *et al.* 1979).

| East Slit | | Central Slit | | West Slit | |
|---|---|---|---|---|---|
| CGS4 Pixel Coords. (x,y) | $A_K$ (mag) | CGS4 Pixel Coords. (x,y) | $A_K$ (mag) | CGS4 Pixel Coords. (x,y) | $A_K$ (mag) |
| - | - | 322,216 | 0.81±0.14 | - | - |
| - | - | 319,212 | 0.99±0.17 | - | - |
| - | - | 316,209 | 0.84±0.16 | - | - |
| 307,211 | $\sim 0^a$ | 313,205 | 0.97±0.15 | 319,199 | 1.00±0.17 |
| 304,207 | $\sim 0^a$ | 310,202 | 0.83±0.12 | 316,196 | 1.06±0.15 |
| 302,204 | 0.13±0.06 | 307,198 | 0.84±0.15 | 313,193 | 0.86±0.16 |
| Mean | 0.13±0.06 | Mean | 0.88±0.04 | Mean | 0.97±0.06 |

Table 4.1: Extinction results from the $H_2$ 1-0 S(1)/1-0 Q(3) line ratio at the positions ($1.22'' \times 1.22''$) centred at Allen & Burton (1993) image coordinates of the 3 slit positions indicated in Figure 4.1 in the M42 HH120-114 $H_2$ wake. The weighted mean of the extinction for each slit is given. Superscript *a* indicates poor signal-to-noise hampering accurate determination of $A_K$.

| CGS4 Pixel Coords. (x,y) | $A_K$ (mag) |
|---|---|
| 278,297 | 0.44±0.16 |
| 276,293 | 0.49±0.15 |
| 274,288 | 0.42±0.14 |
| 272,284 | 0.39±0.15 |
| 271,280 | 0.55±0.16 |
| 269,276 | 0.58±0.16 |
| Mean | 0.48±0.03 |

Table 4.2: Extinction results from the $H_2$ 1-0 S(1)/1-0 Q(3) line ratio at the positions ($1.22'' \times 1.22''$) centred at Allen & Burton (1993) image coordinates indicated in Figure 4.2 in the M42 HH126-053 $H_2$ wake.

In the K band there are four separate $H_2$ line pairs with upper states $v$=1,$J$=2,3,4,5 from which the differential extinction can be measured. However, at least one line from each pair coincides with atmospheric absorption features to some degree. At this instrumental resolution, coincident atmospheric absorption lines are relatively narrow and therefore division by a standard star does not sufficiently correct affected $H_2$ lines. By calculating the effects of the atmospheric absorption on Gaussian emission lines of varying widths, Richter *et al.* (1995) estimated the errors involved with atmospheric correction of these $H_2$ transitions. For example, the atmosphere near a Q-branch line will absorb more flux on average from a continuum source than from a narrow emission line at the same wavelength. They found that the 1-0 S(1)/1-0 Q(3) value gives the minimum uncertainty of order ±6% of the actual value after correction. At worst, the $H_2$ 1-0 Q(5) line is undercorrected by a factor of 2-5 depending on the velocity of line centre with respect to the atmosphere and on the line's shape. In subsequent calculations, we will therefore adopt the extinction values given by the 1-0 S(1)/1-0 Q(3) ratio. In any case, as we shall concentrate further $H_2$ excitation analysis on line ratios and hence relative level populations, the effect of extinction uncertainty is small compared to the differences between model predictions. We present the derived extinction $A_K$ at each position shown in both wakes (Figures 4.1,4.2) in Tables 4.1 and 4.2.

In addition to the $H_2$ measurements of extinction in the "bullet" wakes, the extinction has also been measured independently, via measurements of the line ratio of the [FeII] 1.644 $\mu$m and 1.257 $\mu$m transitions, towards four of the brightest "bullets" including M42 HH126-053 (M.G. Burton, *private communication*). Both transitions are from the same upper energy level and undergo negligible self-absorption. These observations were carried out using the IRIS infrared imaging spectrograph on the Anglo Australian Telescope and the ratio used to determine directly the extinction to the source since the unextinguished ratio is 1.36 (Nussbaumer & Storey 1988). At M42 HH126-053 the observed 1.257/1.644$\mu$m line ratio is 0.66 and the differential extinction 0.78 magnitudes. The extinction at K, assuming the He *et al.* (1995) extinction law, is therefore $A_K$=0.80 mag. This is 0.32 mag higher than the mean value determined from the $H_2$ line pair in this wake (Table 4.2) but this might be expected if the $Fe^+$ emission traces the densest region of the "bullet" itself. The advantage of determining $A_K$ using the $Fe^+$ value is

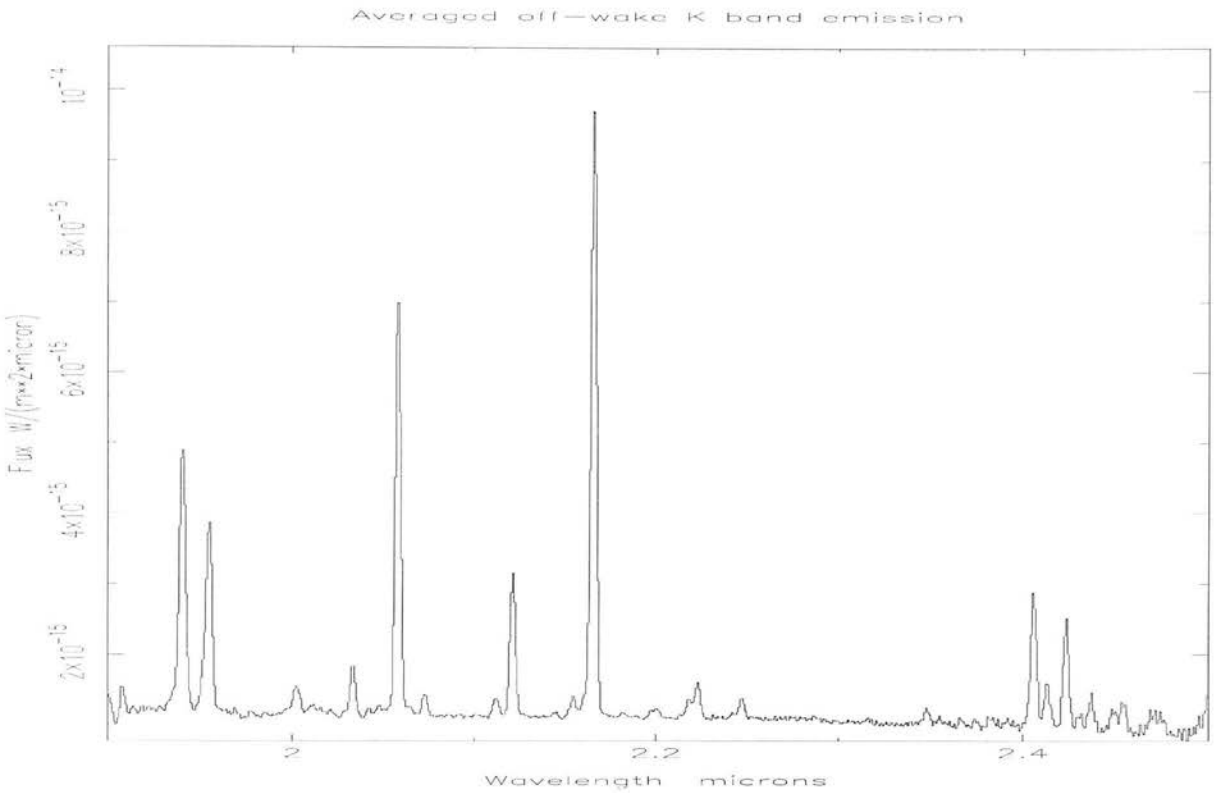


Figure 4.3: Averaged background K band emission spectrum

that, although the [FeII] 1.644$\mu$m transition is within 40km s$^{-1}$ of the OH(5,3)R$_1$(2) atmospheric feature, neither [FeII] line is as strongly affected by atmospheric absorption as the $H_2$ Q-branch lines. However, the small difference in the value of extinction adopted was found to be insignificant in the following line ratio analysis so the $H_2$ values, determined individually at each position in both wakes, were retained for consistency and in order to map any significant spatial variation.

### 4.4.2 Background Emission

In Chapter 3 we identified a constant background emission throughout this region in both $Fe^+$ and $H_2$ tracers. The slit positions at which we have measured K band spectra in the wakes are coincident with previous $H_2$ profile measurements and therefore also sample off-wake regions and, in particular, the large region to the northwest of the M42 HH120-114 wake at which it was possible to accurately determine the averaged $H_2$ background excitation conditions. As expected, the background K band emission was indeed uniform

| Wavelength /$\mu$m | $H_2$ Transition | Energy /K | Line Intensity in $1.2'' \times 1.2''$ beam $I_j$ ($10^{-18}$Wm$^{-2}$) | Dereddened Column Density $N_j/g_j$ ($10^{16}$m$^{-2}$) |
|---|---|---|---|---|
| 1.9121 | 3-2 S(18) | 40130 | 0.893±0.167 | 7.89±0.38 |
| 1.9692 | 3-2 S(7) | 23069 | 0.283±0.163 | 8.93±4.01 |
| 2.0041 | 2-1 S(4) | 14764 | 1.631±0.467 | 103.98±7.79 |
| 2.0065 | 4-3 S(15) | 38860 | 0.147±0.459 | 0.87±2.14 |
| 2.0130 | 3-2 S(6) | 21911 | 0.527±0.163 | 39.84±3.23 |
| 2.0338 | 1-0 S(2) | 7584 | 2.633±0.187 | 342.27±6.40 |
| 2.0475 | 4-3 S(17) | 42021 | 0.533±0.142 | 1.59±0.34 |
| 2.0656 | 3-2 S(5) | 20856 | 0.637±0.142 | 14.78±2.62 |
| 2.0735 | 2-1 S(3) | 13890 | 1.118±0.162 | 27.66±3.19 |
| 2.1218 | 1-0 S(1) | 6951 | 7.337±0.283 | 479.65±14.86 |
| 2.1542 | 2-1 S(2) | 13150 | 0.965±0.134 | 92.19±3.44 |
| 2.2233 | 1-0 S(0) | 6471 | 1.672±0.211 | 650.49±22.35 |
| 2.2477 | 2-1 S(1) | 12550 | 0.999±0.168 | 47.25±5.07 |
| 2.3445 | 4-3 S(3) | 23955 | 0.161±0.176 | 5.41±4.92 |
| 2.3558 | 2-1 S(0) | 12095 | 0.334±0.116 | 92.61±8.93 |
| 2.4066 | 1-0 Q(1) | 6149 | 7.252±0.277 | 416.90±13.35 |
| 2.4134 | 1-0 Q(2) | 6471 | 2.582±0.174 | 490.86±9.25 |
| 2.4237 | 1-0 Q(3) | 6951 | 5.387±0.241 | 305.23±11.47 |
| 2.4375 | 1-0 Q(4) | 7584 | 1.462±0.147 | 221.43±6.25 |

Table 4.3: Averaged background $H_2$ line intensities and dereddened column densities (assuming an $H_2$ ortho-to-para ratio of 3). $1\sigma$ errors are derived from the triangular line-fitting routine.

and it was therefore possible to increase signal-to-noise significantly by averaging over positions well clear of wake emission. It was also noted, however, that some field stars in this region showed enhanced continuum emission at K and that this emission could affect a number of neighbouring CGS4 pixels. Such pixels were excluded from our analysis.

The averaged background K band spectrum is shown in Figure 4.3. We first note the non-zero continuum upon which the emission lines are superimposed, which slightly

decreases with wavelength from ~1.3 down to 1.0 $Wm^{-2}\mu m^{-1}$ between 1.9 and 2.5$\mu$m . It can be seen that, in addition to the most prominent $H_2$ emission lines such as the 1-0 S(1) line at 2.1218$\mu$m and the Q-branch lines at $\lambda \gtrsim 2.4\mu$m , the brightest lines are the atomic emission lines at 2.166$\mu$m (HI Brackett $\gamma$) and the [HeI] transition at 2.0587$\mu$m . There is therefore a strong component of nebulous emission throughout the "bullets" region. We have also isolated excited $H_2$ emission, including transitions from very high excitation energy levels (E/k$\gtrsim$40,000K), throughout the region and independent of the "bullet" wakes.

Line intensities were determined by fitting triangular line profiles to each resolved $H_2$ line. Some of the lines were blended to some degree either with other $H_2$ lines or with one of the many weak nebular emission lines. Since all lines are unresolved spectrally, it is still sometimes possible to determine individual line fluxes, if only partially blended, as the profile shape and width of each component is constant and can be accurately determined on nearby bright, unblended lines. The measured line intensities and calculated column densities (assuming an $H_2$ ortho-to-para ratio of 3) for the averaged $H_2$ lines are presented in Table 4.3. The average extinction off-wake is found to be $A_K = 0.22\pm0.03$ mags.

### 4.4.3 "Bullet" Wake Emission

Sample on-wake K band spectra for bright points near to the head of the wakes M42 HH126-053 and M42 HH120-114 are presented in Figure 4.4. It is immediately apparent that the spectra are similar in both cases and that the $H_2$ emission now dominates over the background nebular emission. We also note that these observations resolve many more $H_2$ lines than was previously possible with the old CGS4 detector array. This is most easily seen by comparing the Q branch lines at $\lambda \gtrsim 1.4\mu$m to previous K band datasets of shocked sources (e.g. Fernandes & Brand 1995). The measured line intensities and calculated column densities (assuming an $H_2$ ortho-to-para ratio of 3) for the averaged $H_2$ lines from the brightest positions on the wake M42 HH120-114 are presented in Table 4.3. The average extinction on-wake, found by calculating the weighted mean of the six brightest positions (Table 4.1), is $A_K = 0.88\pm0.04$ mags. This is 0.66 mag higher than found at the averaged off-wake position. The $H_2$ wakes

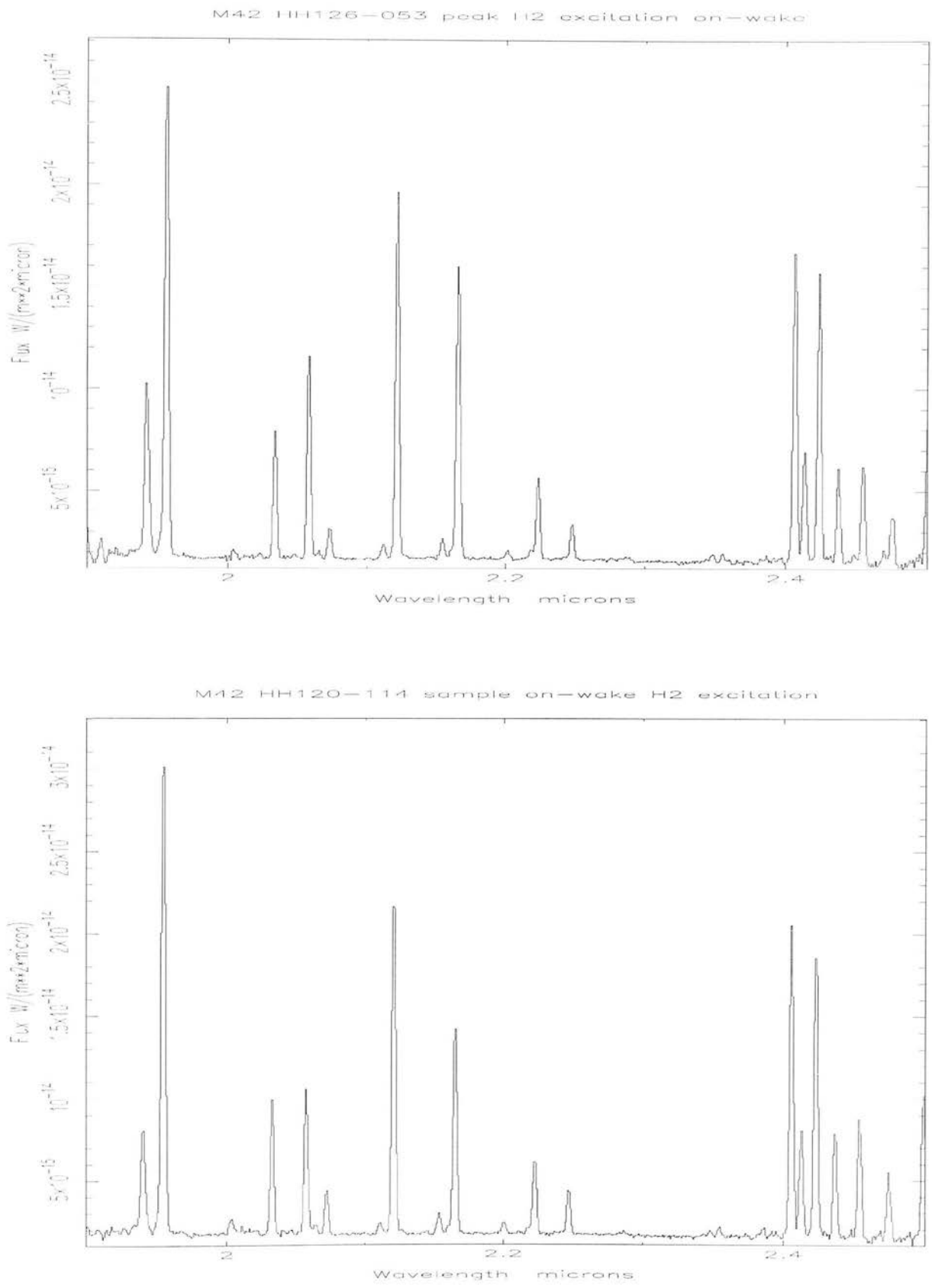


Figure 4.4: Sample on-wake K band $H_2$ emission spectrum for individual $1.22'' \times 1.22''$ CGS4 pixels near head of wakes M42 HH126-053 (top) and M42 HH120-114 (bottom).

| Wavelength /$\mu$m | $H_2$ Transition | Energy /K | Line Intensity in $1.2'' \times 1.2''$ beam $I_j$ ($10^{-18}$Wm$^{-2}$) | Dereddened Column Density $N_j/g_j$ ($10^{16}$m$^{-2}$) |
|---|---|---|---|---|
| 1.9121 | 3-2 S(18) | 40130 | 1.096±0.333 | 23.70±0.76 |
| 1.9449 | 2-1 S(5) | 15763 | 26.512±0.549 | 1262.05±8.50 |
| 1.9576 | 1-0 S(3) | 8365 | 102.678±1.475 | 7946.64±37.58 |
| 2.0041 | 2-1 S(4) | 14764 | 4.368±0.328 | 635.31±5.47 |
| 2.0065 | 4-3 S(15) | 38860 | 0.185±0.376 | 2.50±1.76 |
| 2.0130 | 3-2 S(6) | 21911 | 1.057±0.148 | 181.23±2.93 |
| 2.0338 | 1-0 S(2) | 7584 | 27.914±0.576 | 8108.43±19.71 |
| 2.0475 | 4-3 S(17) | 42021 | 0.863±0.136 | 5.70±0.32 |
| 2.0656 | 3-2 S(5) | 20856 | 2.156±0.143 | 109.46±2.64 |
| 2.0735 | 2-1 S(3) | 13890 | 9.885±0.235 | 532.19±4.63 |
| 2.1004 | 4-3 S(7) | 27706 | 0.327±0.177 | 42.53±8.61 |
| 2.1218 | 1-0 S(1) | 6951 | 77.260±1.784 | 10662.94±93.66 |
| 2.1280 | 3-2 S(4) | 19912 | 1.263±0.144 | 187.35±2.72 |
| 2.1542 | 2-1 S(2) | 13150 | 4.874±0.178 | 964.11±4.58 |
| 2.2014 | 3-2 S(3) | 19086 | 2.561±0.162 | 135.89±3.47 |
| 2.2233 | 1-0 S(0) | 6471 | 17.664±0.486 | 13690.38±51.49 |
| 2.2477 | 2-1 S(1) | 12550 | 9.521±0.209 | 885.68±8.10 |
| 2.2870 | 3-2 S(2) | 18386 | 0.620±0.122 | 118.26±3.32 |
| 2.3445 | 4-3 S(3) | 23955 | 0.548±0.150 | 34.52±4.19 |
| 2.3558 | 2-1 S(0) | 12095 | 2.094±0.133 | 1083.03±10.23 |
| 2.3864 | 3-2 S(1) | 17818 | 1.526±0.128 | 134.25±5.12 |
| 2.4066 | 1-0 Q(1) | 6149 | 70.271±1.769 | 7367.58±85.25 |
| 2.4134 | 1-0 Q(2) | 6471 | 25.563±0.726 | 8837.19±38.60 |
| 2.4237 | 1-0 Q(3) | 6951 | 66.145±2.047 | 6785.48±97.44 |
| 2.4375 | 1-0 Q(4) | 7584 | 22.911±0.999 | 6246.36±42.44 |

Table 4.4: M42 HH120-114 averaged on-wake $H_2$ line intensities and dereddened column densities (assuming an $H_2$ ortho-to-para ratio of 3). $1\sigma$ errors are derived from the triangular line-fitting routine.

are therefore associated with a higher density of material along the line-of-sight. This contradicts any expectation that a relative cavity might be cleared upon passage of a "bullet" driving a bow shock through the molecular material, unless the "background" emission occurs in a region in front of the "bullets" and wakes.

Comparison of averaged column densities on and off the M42 HH120-114 wake show that populations of the highest measured upper energy levels are similar in both cases and therefore significantly influenced by the same exciting mechanism as the background component(s). The excitation of the lowest energy levels such as the brightest $H_2$ 1-0 S(1) transition, is however over two orders of magnitude higher on-wake than off-wake and hence dominated by a different wake-only excitation mechanism(s).

## 4.5 Discussion

### 4.5.1 Column Density Ratio (CDR) Diagrams

In order to determine the nature of the excitation mechanism responsible for the $H_2$ line emission both on and off-wake we plot the ratio of the dereddened line intensities relative to the brightest 1-0 S(1) line and divide these values by those expected from an idealized thermal slab at 2000K. This choice of temperature is arbitrary but serves to show any deviation of the data from a pure thermalized case. The column density ratio may be inferred from the intensity ratio assuming the $H_2$ is in local thermodynamic equilibrium. The CDR diagrams allow a direct comparison of the physical processes that determine the local distribution of levels while being independent of any shock or fluorescent excitation model.

To facilitate comparison between positions and to investigate the nature of the $H_2$ excitation mechanism, we have plotted theoretical shock and fluorescence model predictions against each dataset presented. Firstly, we plot model calculations of the column density in the cooling zone behind a hydrodynamic shock, following the work of Brand *et al.* (1988), as used to successfully model the $H_2$ emission from OMC-1. We here model

a simple power-law cooling function of the form

$$\Lambda(T) = \Lambda_0 T^s \ \mathrm{W(H_2 molecule)^{-1}} \tag{4.2}$$

with $s$ set to 4.7 as an approximation to the calculations of Hollenbach & McKee (1979) and Burton (1986) of cooling by thermalized $H_2$ (Chapter 2.2.3). Assuming the shock is strong enough, it can be shown that the $H_2$ column density per state at level $j$ with energy $T_j$ degrees Kelvin is approximately given by

$$\frac{N_j}{g_j} \propto \int \frac{e^{-T_j/T}}{Q(T)\Lambda(T)} dT, \tag{4.3}$$

where the partition function $Q$ is approximated by

$$Q(T) \simeq AT(1 - e^{-T_v/T}) \tag{4.4}$$

with $T_v$ = 6000K, the vibrational level interval of the lowest levels of $H_2$ (Landau & Lifshitz 1959b), and $A$ is constant (Chapter 2.2.3). Column densities can therefore be modelled by the expression

$$\frac{N_j}{g_j} \propto T_j^{-s} - (T_j + T_v)^{-s}. \tag{4.5}$$

The temperature behaviour of the shocked molecular gas responsible for the $H_2$ line emission is determined by factors such as the initial density of the shocked gas, the shock velocity and the magnetic field strength. These may be expected to vary within the outflow region by large factors and therefore cause observable differences in the relative line strengths. Certainly, within an idealised bow shock structure such variations are predicted in sampling gas shocked at the highest velocity at the apex compared to the lowest effective velocity down in the flanks of the bow.

We also compare our results to theoretical predictions of UV-excited fluorescent $H_2$ intensities as modelled by Black & van Dishoeck (1987, hereafter BvD) model #14. The distribution of $H_2$ in these models is strongly affected by the importance of collisional processes (Burton *et al.* 1990b) which is related to the $n_0/G_0$ ratio, where $n_0$ is the

density and $G_0$ is defined to be the far-UV incident radiation field in units of the interstellar radiation field and is equivalent to a one-dimensional flux of $1.6\times10^{-3}$erg s$^{-1}$ cm$^{-2}$ = 1 Habing (Habing 1968). The fluorescent BvD model #14 parameters used are $n$= $3\times10^3$cm$^{-3}$ and $G_0$=$10^3$.

### 4.5.2 Background Component Excitation

Figure 4.5 is the CDR diagram for the averaged background $H_2$ emission in which the error bars are calculated directly from the $1\sigma$ errors in the triangular line-fitting procedure. The increased sensitivity of the new CGS4 array has enabled the detection of fainter high energy transitions, with E/k~40,000K, thus enabling the excitation to be mapped over a much larger energy range than has previously been possible in a given integration time. All line ratios are greater than unity with the higher line ratios arising from the higher energy levels. There is increased emission from levels at increasingly higher energies relative to the emission expected from the Boltzmann distribution environment of gas at 2000K.

The lowest energy $v$=1 levels (E/k $\lesssim$8000K) lie close to a straight line and are exactly fitted by the simple power-law cooling described in Section 4.5.1. The data are only matched by the fluorescent excitation model with an ortho-to-para $H_2$ ratio of 3.0 whereas the even upper energy levels are significantly underpopulated compared to a fluorescent model with a more commonly observed ortho-to-para ratio of 1.8. There are small discrepancies in equivalent upper level populations as measured by the 1-0 S and Q branch lines, but this is expected since the Q branch lines are much more strongly affected by atmospheric variations at $\lambda \geq 1.4\mu$m at the edge of the K window. The $H_2$ 1-0 S(3) line at 1.9576$\mu$m was excluded from this analysis due to a blend with the HeI nebular line at 1.9548$\mu$m .

The $v$=2 levels (12000$\lesssim$ E/k $\lesssim$15000K), however, show significant deviations from the smooth curve predicted in the J shock model and have relative populations intermediate between the shocked and fluorescent models. Indeed the scatter in these points follows the same pattern as that predicted by the fluorescent model having ortho-to-para (o/p) ratio 1.8 and is inconsistent with the o/p = 3.0 fluorescent model. The observed scatter

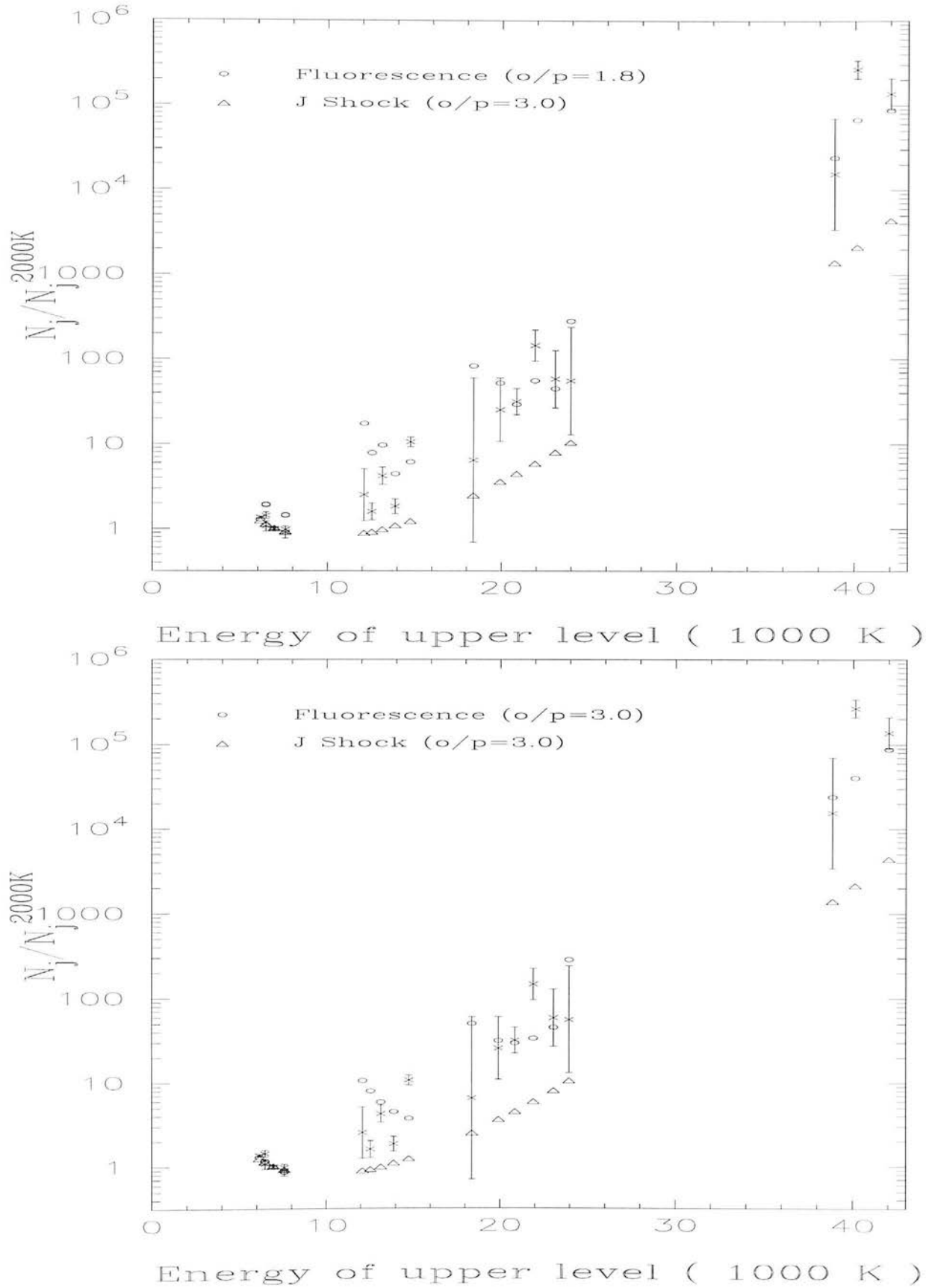


Figure 4.5: Averaged background CDR diagrams (see text) compared to theoretical models of simple power-law cooling behind a J shock (ortho-to-para ratio, o/p = 3.0) and BvD model #14 fluorescence for o/p = 1.8 (top) and 3.0 (bottom). Errors are derived from $1\sigma$ line-fits.

is significant since it is greater than the associated error bars. An o/p ratio of $\lesssim$2 implies a low fluorescent gas temperature of about 100K whereas the ortho-to-para abundance ratio is expected to saturate at a value of 3 if the gas is hotter than 300K due to the numerous collisions bringing the states to thermal equilibrium (Flower & Watt 1984). In cold gas ($\leq$50K) the abundance ratio depends strongly on temperature and on the time scales for the destruction of $H_2$ molecules and the spin-exchange reactions. A low ortho-to-para ratio is observed in several fluorescently excited regions including M17 (o/p=1.8), Hubble 12 (o/p=1.7) and NGC2023 (o/p=2.2) (Chrysostomou 1992).

The remaining $v$=3,4 relative level populations lie significantly in excess of the J shock model and appear to be dominated by fluorescent excitation although showing a less clear pattern as the signal-to-noise of these fainter transitions is low at these off-wake positions. We note an excess in the observed populations of the 2-1 S(2) and 2-1 S(5) levels at E/k = 13150K and 15763K respectively over the o/p = 1.8 fluorescent excitation model. In the case of the 2-1 S(2) line at 2.1542$\mu$m , the observed line strength may be artificially boosted to a relatively small extent during division by the standard star spectrum which has been edited to remove the nearby HI Br$\gamma$ recombination line of neutral hydrogen at 2.166$\mu$m . The 2-1 S(5) line intensity at 1.9449$\mu$m also appears to be overestimated due to a blend with the coincident HI 8-4 Br line at1.9451$\mu$m .

We can define an excitation temperature for any given $H_2$ line ratio. The excitation temperature ($T_{ex}$) derived from the dereddened 1-0 S(1)/2-1 S(1) line ratio is commonly quoted for shocked sources and is calculated from equation (4.1) as

$$T_{ex} \equiv (E_{21}/k - E_{10}/k)/\ln\left(\frac{I_{10}A_{21}\lambda_{10}g_{21}}{I_{21}A_{10}\lambda_{21}g_{10}}\right) \tag{4.6}$$

where $E/k$ is the upper state energy in temperature units and the subscripts 10 and 21 denote the 1-0 and 2-1 transitions having upper energies of 6951K and 12550K respectively. For the averaged background $H_2$ spectrum we find $T_{ex}$= 2416$\pm$173K. This is significantly higher than the equivalent excitation temperature of 1900-2100K derived by Burton *et al.* (1989) in any of the four shocked sources HH7, CRL618, OMC-1 or the supernova remnant IC443. Of course, we can see from the CDR diagram that the $H_2$ excitation cannot be fitted by one single temperature alone since this would require all

of the data points to lie along a straight line. This trend is therefore consistent with the existence of different temperature regions exciting $H_2$ within the shock and/or a fluorescence mechanism enhancing the $H_2$ emission from higher energy levels.

It is clear that the background emission cannot be accounted for by any one individual excitation process known but rather is a combination of at least two components, including both collisional and fluorescent excitation mechanisms. A single planar C shock model alone predicts a relatively flat distribution of level populations (Draine & Roberge 1982; Chernoff *et al.* 1982) and is therefore ruled out by these observations. Smith *et al.* (1991b) demonstrated, however, that it is possible to mimic the planar J shock model curve at OMC-1 if observing two different planar C shocks (having two different effective temperatures) within a bow shock structure. By combining two different C shock components and a fluorescent component Fernandes & Brand (1995) were able to accurately fit the $H_2$ level populations in HH7 in this manner, remaining consistent with the doubly-peaked $H_2$ 1-0 S(1) line profiles observed by Carr (1993). However, in Chapter 3 we showed that the $H_2$ 1-0 S(1) line profile of this background component within any given $1.744'' \times 0.9''$ CGS4 pixel at the Orion periphery is well fitted by a single-peaked Gaussian shaped profile. This is not consistent with this bow shock + fluorescence model. It might be possible to reproduce the observed spectrum if we are not resolving multiple shock fronts (J or C) within each CGS4 pixel, perhaps accelerated by a uniform wind, and there is a significant fluorescent background contribution.

### 4.5.3 "Bullet" Wake Excitation

The $H_2$ emission at OMC-1 can only be explained by a highly magnetised bow C shock model (Smith & Brand 1990b; Smith *et al.* 1991a,b). A similar but less magnetised model, incorporating an additional fluorescent component, has since been successfully fitted to emission from the HH7 bow-shaped Herbig-Haro object (Fernandes & Brand 1995) and also DR21 (Fernandes 1993). Furthermore, the $H_2$ emission properties calculated for the whole bow can successfully explain the observed line ratios and linewidths from several objects (Smith & Brand 1990a). Axisymmetric two-dimensional modelling of the C shock structure by Smith *et al.* (1991a) shows that the $H_2$ line ratios (summed

over the entire bow) are mainly sensitive to the bow shape and the cooling function. Importantly, the $H_2$ line ratios are independent of the bow velocity if it exceeds the dissociation speed of $H_2$ ($\lesssim$50-60km s$^{-1}$ for high Mach flows in Orion). It was therefore speculated that the Orion "bullet" wakes might be similarly excited, with the bow shock arising upon passage of the $Fe^+$ "bullet" travelling at supersonic speed relative to the ambient molecular gas.

Figure 4.6 is the CDR diagram for the averaged on-wake M42 HH120-114 $H_2$ emission. As with the background component, all line ratios are greater than unity with the higher line ratios arising from the higher energy levels. There is, again, increased emission from levels at increasingly higher energies relative to the emission expected from the Boltzmann distribution environment of gas at 2000K. However, the scatter of the data points is considerably reduced compared to the background CDR and is closer to, although in excess of, the model predictions for the smooth J shock cooling curve fitted to OMC-1.

The lowest energy $v$=1 levels (E/k $\lesssim$7000K) still lie close to a straight line fitted by the simple power-law cooling described in Section 4.5.1 but begin to show significant deviation for E/k $\gtrsim$7000K. The 1-0 S(3) line at 8365K is discounted as described previously. Similarly, there are again small discrepancies in equivalent upper level populations as measured by the 1-0 S and Q branch lines, caused by atmospheric variations. The $v$=2 to $v$=4 levels (E/k $\gtrsim$12000K) are significantly different to the background spectrum. A small but significant (relative to the error bars) scatter of the data points from a smooth curve in excess of the J shock model predictions is observed. However, the level populations are much closer to the collisionally excited model predictions. Only at high energies (E/k $\gtrsim$22000K) do data points begin to lie closer to fluorescent predictions, although still scattered about a smooth curve which rises more steeply with energy than the Brand *et al.* (1988) J shock model. The scatter in these points again follows the same pattern as that predicted by the fluorescent model having ortho-to-para (o/p) ratio 1.8 and is inconsistent with the o/p = 3.0 fluorescent model. The 2-1 S(2) and in particular the 2-1 S(5) points are considered unreliable for the reasons noted previously. The 3-2 S(18) line at 1.9121$\mu$m (E/k = 40130K) coincides with stronger atmospheric absorption troughs, similar to the 1-0 Q branch and is probably less reliable than the derived error

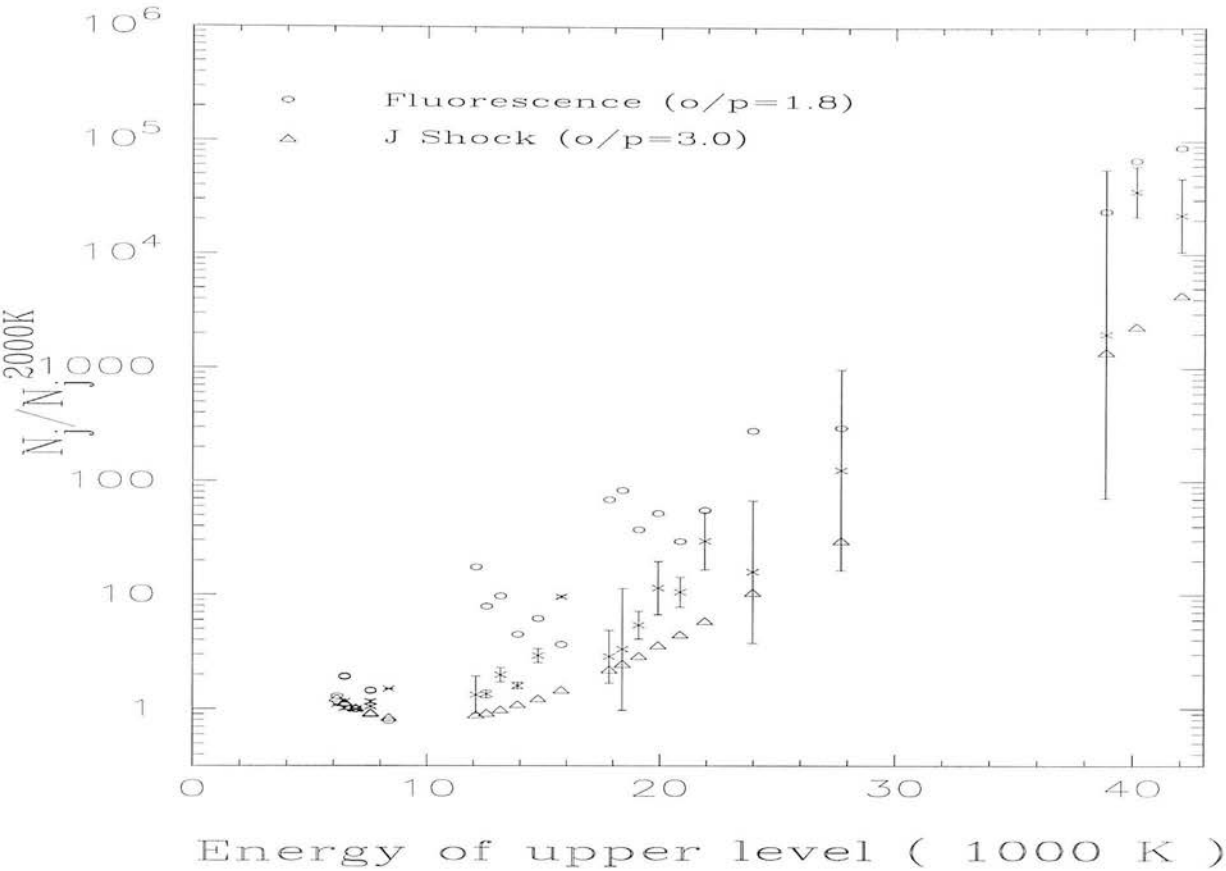


Figure 4.6: M42 HH120-114 averaged on-wake CDR.

bar shown.

Figure 4.7 shows the same data but this time with the averaged background component column densities subtracted. Unfortunately this increases the CDR diagram errors but demonstrates that even at the highest energies, the background component contributes only a small component of the on-wake flux, since any differences between the two diagrams are relatively small. It is clear that the spectra can be fitted by a composite C bow-shock + fluorescence model as fitted to HH7 (Fernandes & Brand 1995) but having a much smaller relative fluorescent contribution than the averaged Orion background component. Alternatively, it would be possible to fit a simple J shock power-law cooling model (Brand *et al.* 1988) with a higher pressure than at OMC-1 together with fluorescence, although a J shock should only exist under these conditions if the magnetic field is unreasonably low ($B \lesssim 10\mu G$), or if the ionization fraction is unreasonably high (Burton 1992). If the fields are at least of order 1mG, they must have an important effect on the dynamics and necessitate a multi-fluid model. None of the bow shock models,

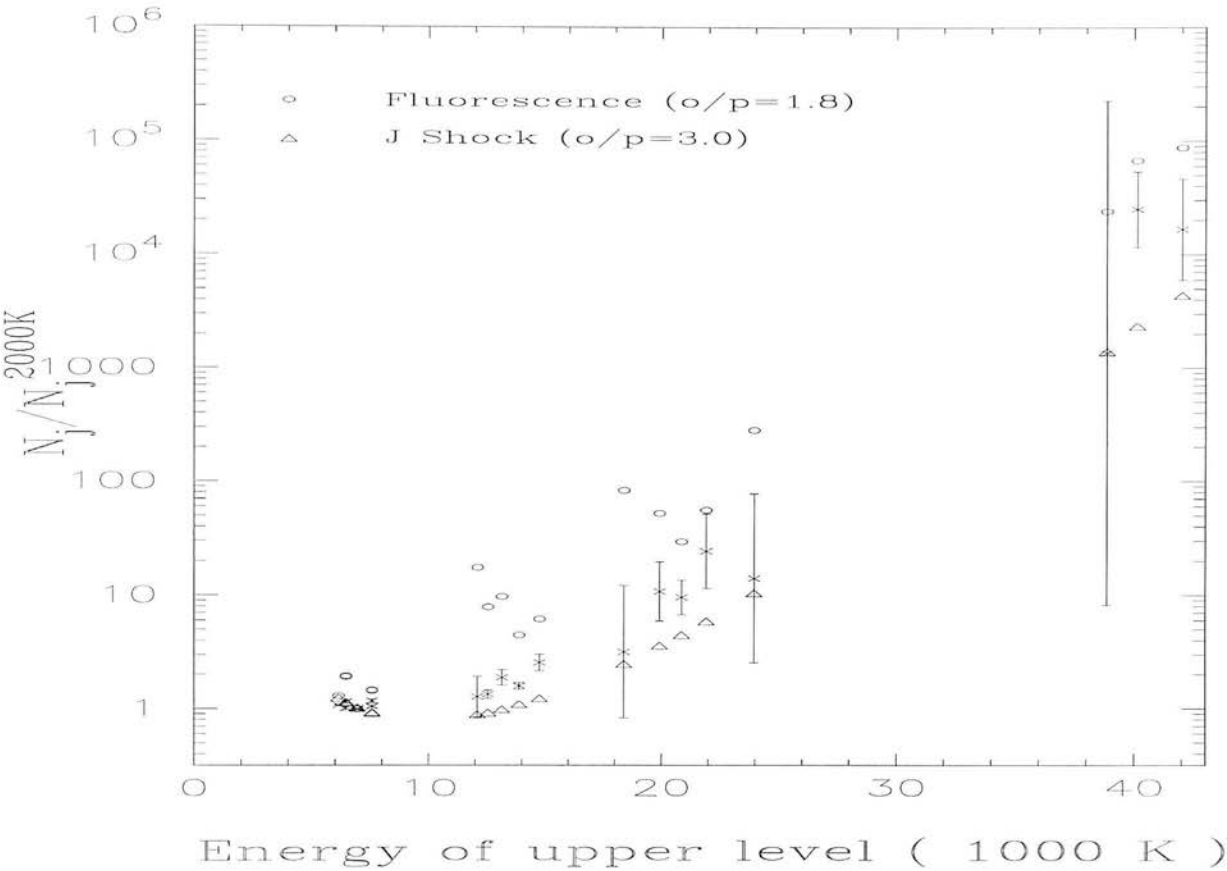


Figure 4.7: M42 HH120-114 averaged on-off wake CDR.

however, can be reconciled with the observed $H_2$ velocity profiles in Chapter 3. The fluorescent component cannot be accounted for by the contribution of the background alone, unless highly variable compared to off-wake positions, since there is a significant scatter in the level populations which is only slightly reduced by subtraction of the averaged background column densities.

### Wake-only fluorescent mechanism

We can account for a separate wake-only fluorescent excitation mechanism by invoking HI Lyman $\alpha$ (1215.67Å) and Ly$\beta$ (1025.18Å) resonances with the $H_2$ lines (BvD) as in the case of HH7 (Fernandes & Brand 1995) and also seen in DR21 (Fernandes 1993). It is speculated that HI Ly$\alpha$ emission will be produced in the strong shocks at the [FeII] "bullets" and irradiates $H_2$ molecules formed downstream in the cooling zone. The line fluorescence mechanism requires the presence of warm $H_2$ (2000-3000K) to provide a

thermal population of the ($v$=2,$J$=5) ground electronic state and that the radial velocity shift between the Ly$\alpha$ emitting region and the $H_2$ fluorescence region is small.

Since the morphology of the $H_2$ wakes suggests dissociation of $H_2$ near the tips of the "bullets", and that strong, high velocity $Fe^+$ emission is produced, it is clear that there are shocks present which are strong enough to cause low-excitation optical emission lines near the apex of the wake which may excite $H_2$ emission in both the pre-shock and post-shock gas through X-ray, ultraviolet heating and Ly$\alpha$ pumping (Wolfire & Königl 1991). It is possible that the non-ionizing far-UV radiation (6-13.6eV) produced at the bow apex can excite $H_2$ fluorescently in this way, implying densities of order $10^3$ to $10^4 cm^{-3}$, consistent with the PDR model densities given in BvD. Alternatively, if the fluorescence arises in re-formed $H_2$ in the post-shocked gas only then the fluorescent emission should arise from higher density gas of order $n_{H_2}$=$10^5$-$10^6 cm^{-3}$.

Finally we compare individual CDR diagrams within each of the wakes M42 HH120-114 and M42 HH126-053 at the highest signal-to-noise, therefore neglecting the small contribution of the background emission and allowing a true acid test of bow shock model predictions.

### CDR Variation within wakes

By employing power-law cooling mechanisms and incorporating ion-neutral and dust-neutral drag terms Smith *et al.* (1991a) showed that the most important parameters influencing the $H_2$ excitation summed over a bow C shock are the shape, cooling function and $H_2O$ abundance. $H_2$ line ratios are predicted to remain constant when summed over entire bows, because the maximum temperature ($\simeq$4000K) is always reached at some location in the bow, unless the bow speed is below the local $H_2$ dissociation speed ($v_{bow} \lesssim 60 km\,s^{-1}$ for highly magnetised C shocks in OMC-1). Whereas planar C shocks exhibit flat-topped temperature profiles which may be approximated by a single excitation temperature, Smith *et al.* (1991b) were able to fit the OMC-1 observations (Brand *et al.* 1988) by assuming a full range of individual C shock components is sampled over a bow surface within the 5″ beamsize, thereby sampling the total range of excitation conditions and hence excitation temperatures. We have now measured the excitation

from individual sections within the $H_2$ wakes, however, and should therefore observe variations in $H_2$ line ratios as the sampled gas temperature varies, given a proposed bow shock wake structure.

Figures 4.8-4.11 show the individual CDR diagrams for each of the positions indicated in Figure 4.1 for the M42 HH120-114 wake. Figures 4.8 and 4.9 show six positions in the central slit running along the axis from the tip of the wake, coincident with the $Fe^+$ "bullet", down to the brightest positions at which a secondary (associated?) wake begins to partially overlap. Surprisingly, the excitation is quite closely matched at each position and follows a rather uniform curve which slightly steepens with increasing level energy. This curve lies significantly in excess of the level populations fitted at OMC-1, indicative of higher pressure in a simple J shock model. In general, the scatter in data points about this smooth curve is barely significant compared to the $1\sigma$ error bars derived from line fitting, except for the unreliable transitions described previously and the highest energy levels which may be significantly affected by spatial variation in the background fluorescent contribution.

Excluding the 2-1 S(2) line at 13150K, there is a weak tendency for any significant scatter in the $v$=2,3 relative level populations to be minimised at positions of strongest underlying $H_2$ wake intensity. This is consistent with a relatively smaller background fluorescent contribution as a proportion of the total $H_2$ intensity. Figure 4.10, showing the CDR diagrams at three positions in the East slit just touching the limb of the M42 HH120-114 wake, is also consistent with this picture since the scatter is considerably larger and the wake intensity fainter, therefore the excitation more closely resembling the averaged background CDR. Figure 4.11, showing the CDR diagrams at three positions in the West slit at which the secondary wake overlaps, again shows increased scatter but this time the weakest intensity and largest CDR scatter is observed in the southernmost row, where the underlying wake intensity is smallest (here related to limb-brightening effects in an idealised bow shock model).

In Table 4.5 we present the excitation temperature derived from the 1-0 S(1)/2-1 S(1) line ratio as before at each of the positions in M42 HH120-114 shown in Figure 4.1. We find that $T_{ex}$ decreases significantly from ~2400K at the weakest positions in the

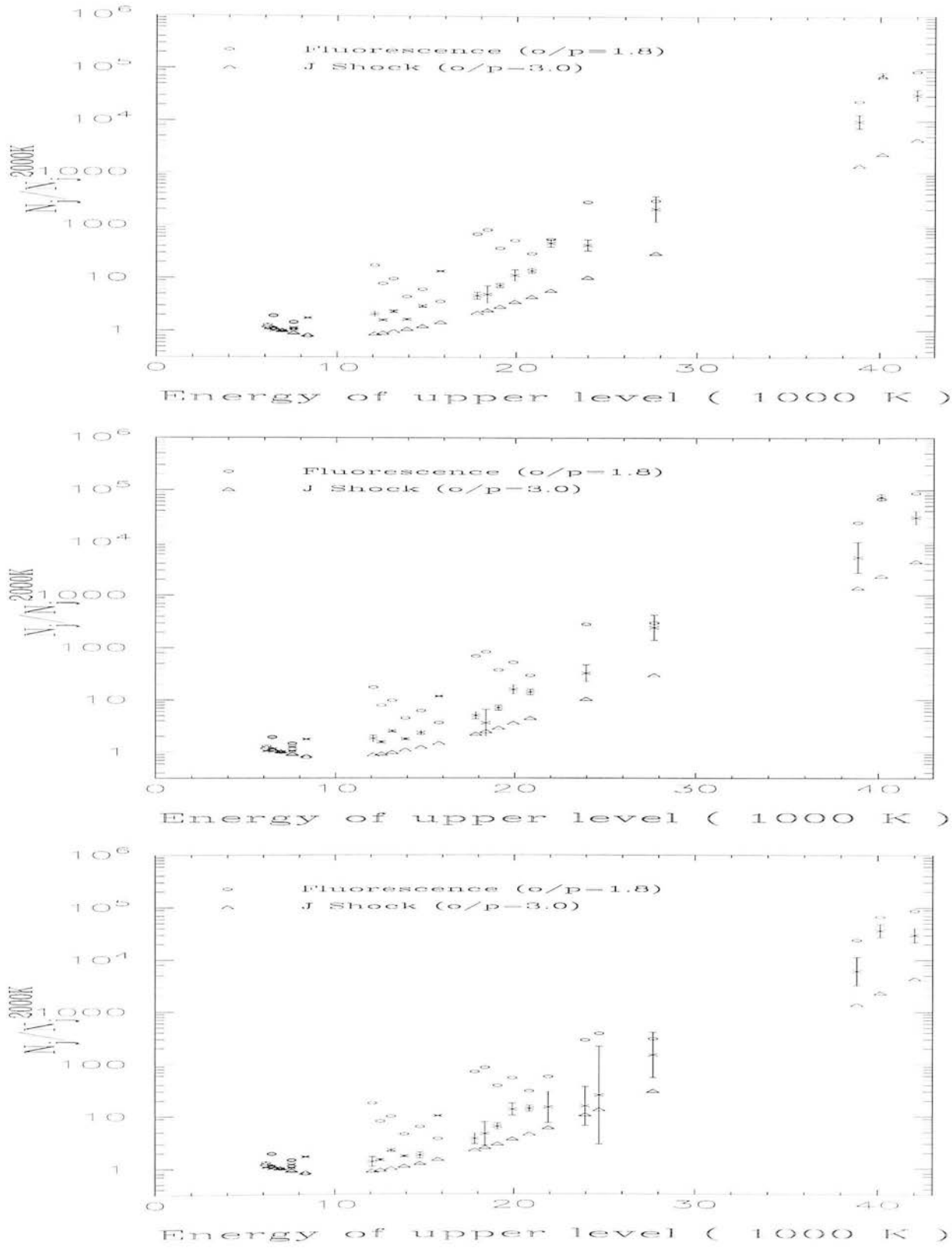


Figure 4.8: M42 HH120-114 - central slit - on wake CDR diagrams for rows 322,216 (top); 319,212 (middle); and 316,209 (bottom). Refer to Figure 4.1 for image coordinates.

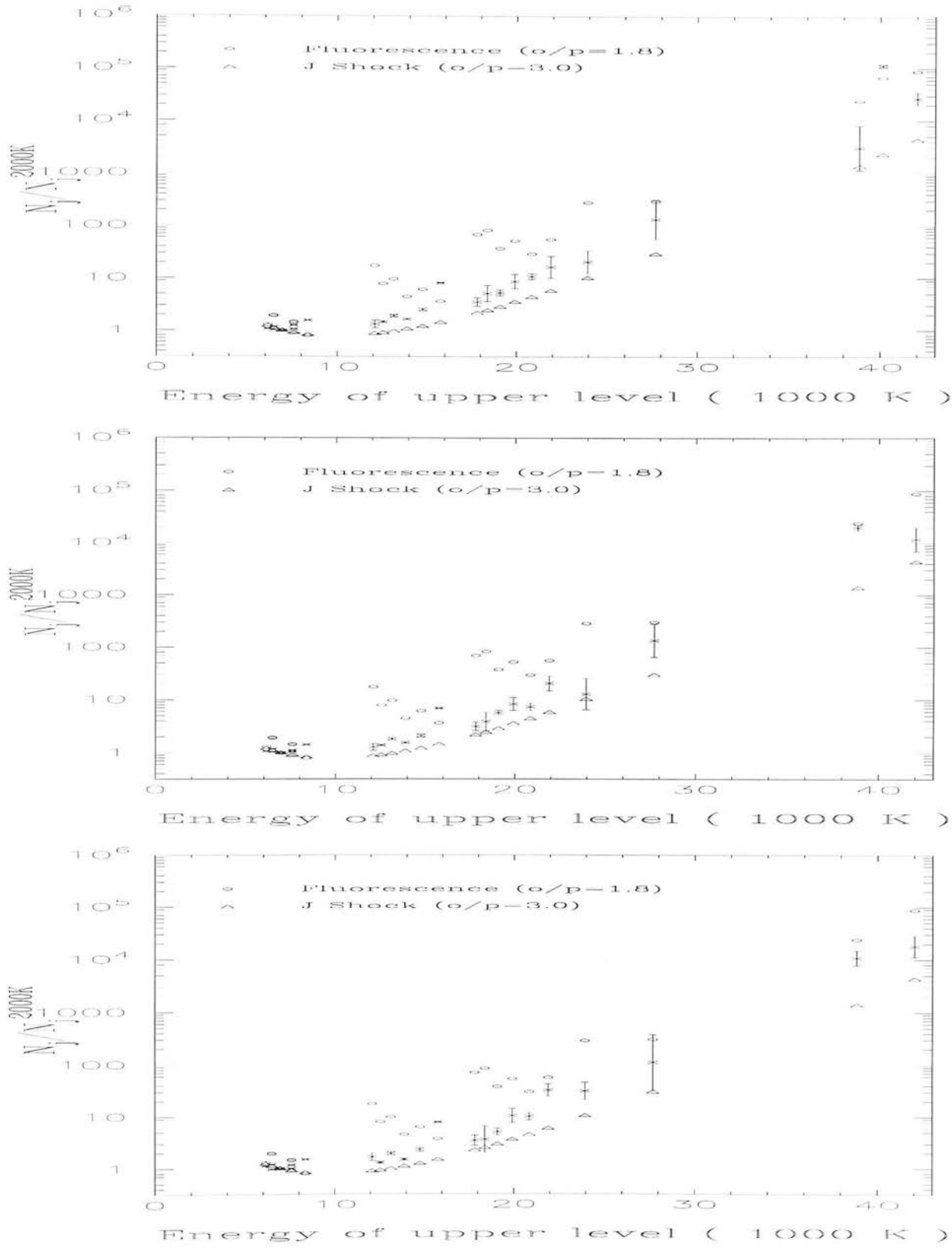


Figure 4.9: M42 HH120-114 - central slit - on wake CDR diagrams for rows 313,205 (top); 310,202 (middle) and 307,198 (bottom).

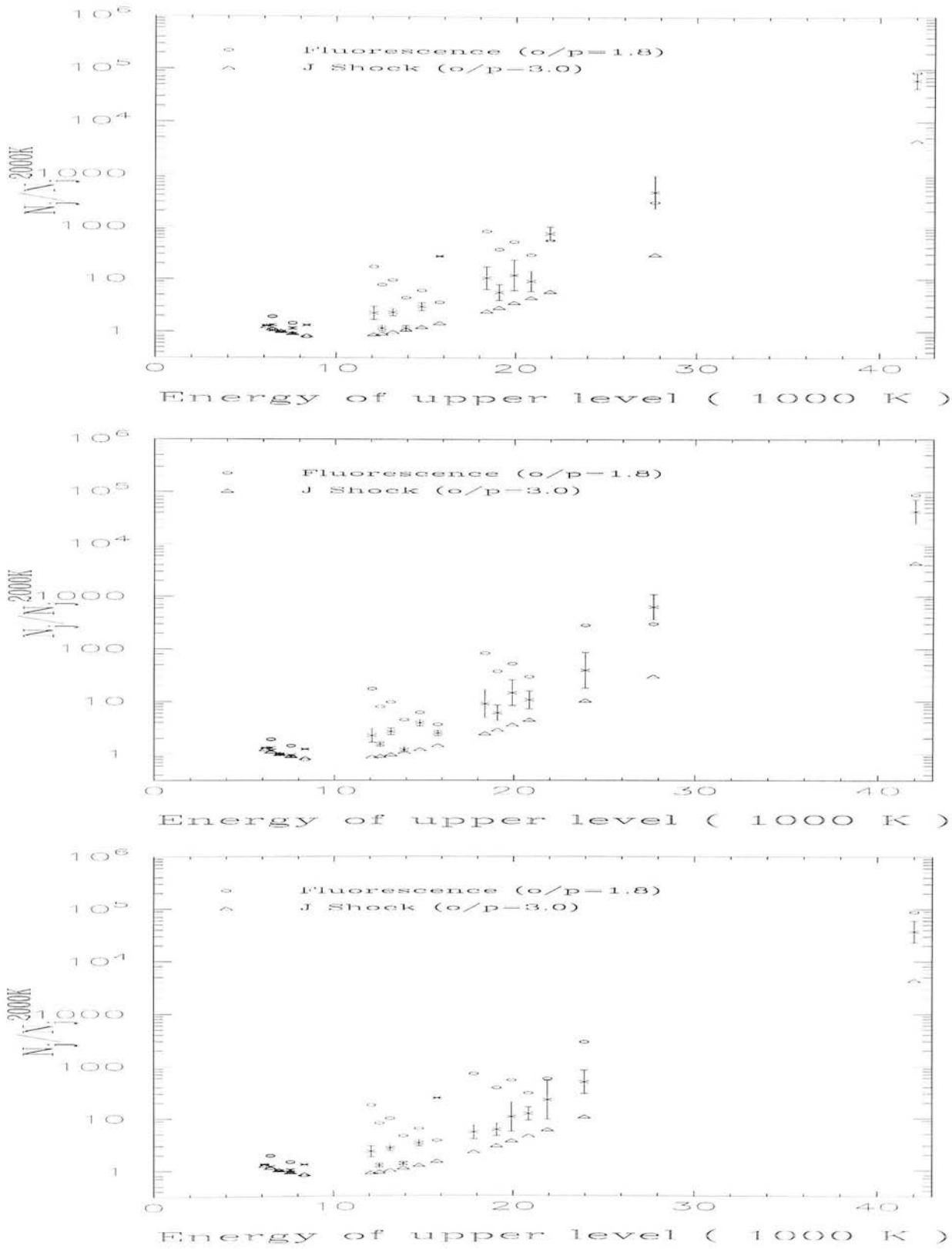


Figure 4.10: M42 HH120-114 - East slit - on wake CDR diagrams for rows 307,211 (top); 304,207 (middle); and 302,204 (bottom).

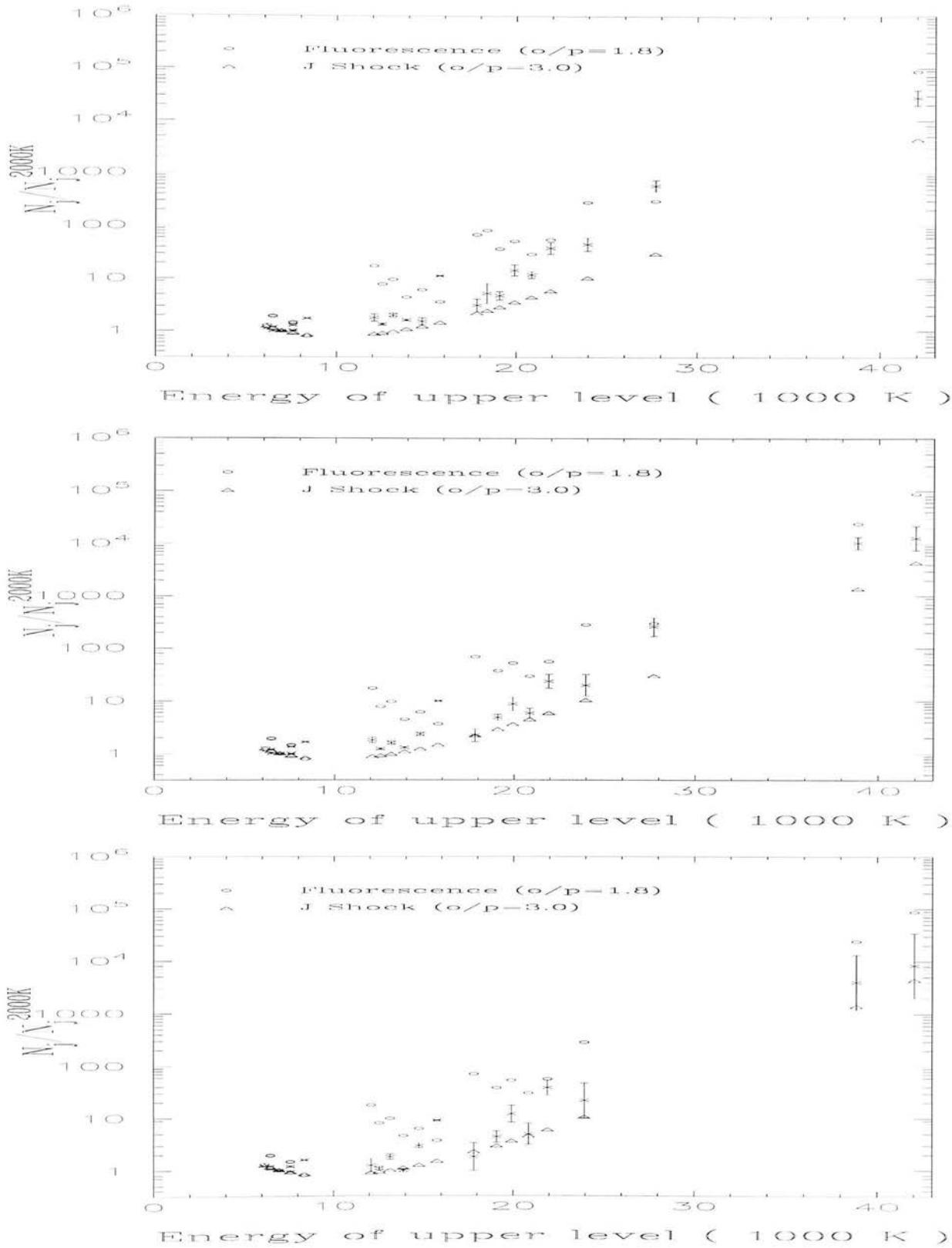


Figure 4.11: M42 HH120-114 - West slit - on wake CDR diagrams for rows 319,199 (top); 316,196 (middle); and 313,193 (bottom).

| East Slit | | Central Slit | | West Slit | |
|---|---|---|---|---|---|
| CGS4 Pixel Coords. (x,y) | $T_{ex}$ 1-0S(1)/2-1S(1) /K | CGS4 Pixel Coords. (x,y) | $T_{ex}$ 1-0S(1)/2-1S(1) /K | CGS4 Pixel Coords. (x,y) | $T_{ex}$ 1-0S(1)/2-1S(1) /K |
| - | - | 322,216 | 2419±20 | - | - |
| - | - | 319,212 | 2381±13 | - | - |
| - | - | 316,209 | 2310±15 | - | - |
| 307,211 | 2129±59 | 313,205 | 2334±14 | 319,199 | 2257±19 |
| 304,207 | 2382±82 | 310,202 | 2277±12 | 316,196 | 2177±19 |
| 302,204 | 2164±59 | 307,198 | 2194±13 | 313,193 | 2060±24 |

Table 4.5: Excitation temperature ($T_{ex}$) derived from the dereddened $H_2$ 1-0 S(1)/2-1 S(1) line ratio at the positions ($1.22\hat{''} \times 1.22\hat{''}$) centred at Allen & Burton (1993) image coordinates of the 3 slit positions indicated in Figure 4.1 in the M42 HH120-114 $H_2$ wake. Errors quoted are derived from the line-fitting routine only.

open "head" region of the wake, close to the averaged background $T_{ex}$ of 2416±173K, down to ≃2100K at the brightest on-wake positions. This is again consistent with our picture of an increasing background fluorescent contribution at fainter wake positions. The wake-only $H_2$ emission is therefore closer to the equivalent excitation temperature of 1900-2100K derived by Burton *et al.* (1989) in the four shocked sources HH7, CRL618, OMC-1 and IC443. We speculate that the ratio of wake-only to background fluorescent intensity dominates the observed decrease in $T_{ex}$ with position rather than being caused by any (small) intrinsic variations within the wake structure.

If the shocked $H_2$ emission is assumed to come from a region in which the gas is thermalized (o/p=3), this implies that the gas density must be in excess of the critical density for $H_2$ -$H_2$ collisions of order $10^6 cm^{-3}$. However, recent calculations by Mandy & Martin (1993) show that neutral hydrogen may be a more efficient collision partner because it has an unpaired electron and is a lighter species. They find the critical density for $H_2$ colliding with H in a 2000K gas is $6.5 \times 10^3 cm^{-3}$.

Figures 4.12 and 4.13 show the individual CDR diagrams for each of the positions

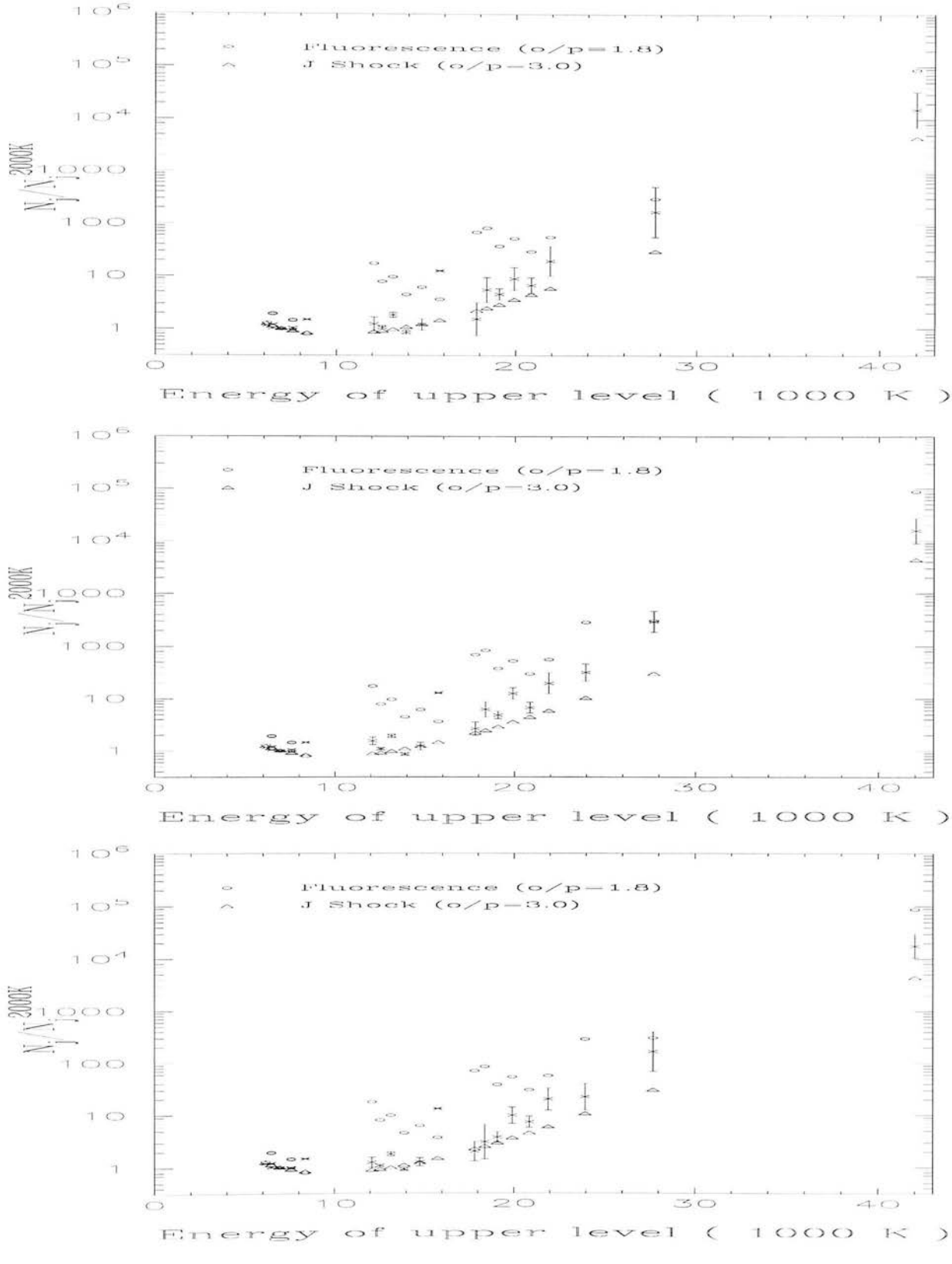


Figure 4.12: M42 HH126-053 - on wake CDR diagrams for rows 278,297 (top); 276,293 (middle); and 274,288 (bottom). Refer to Figure 4.2 for image coordinates.

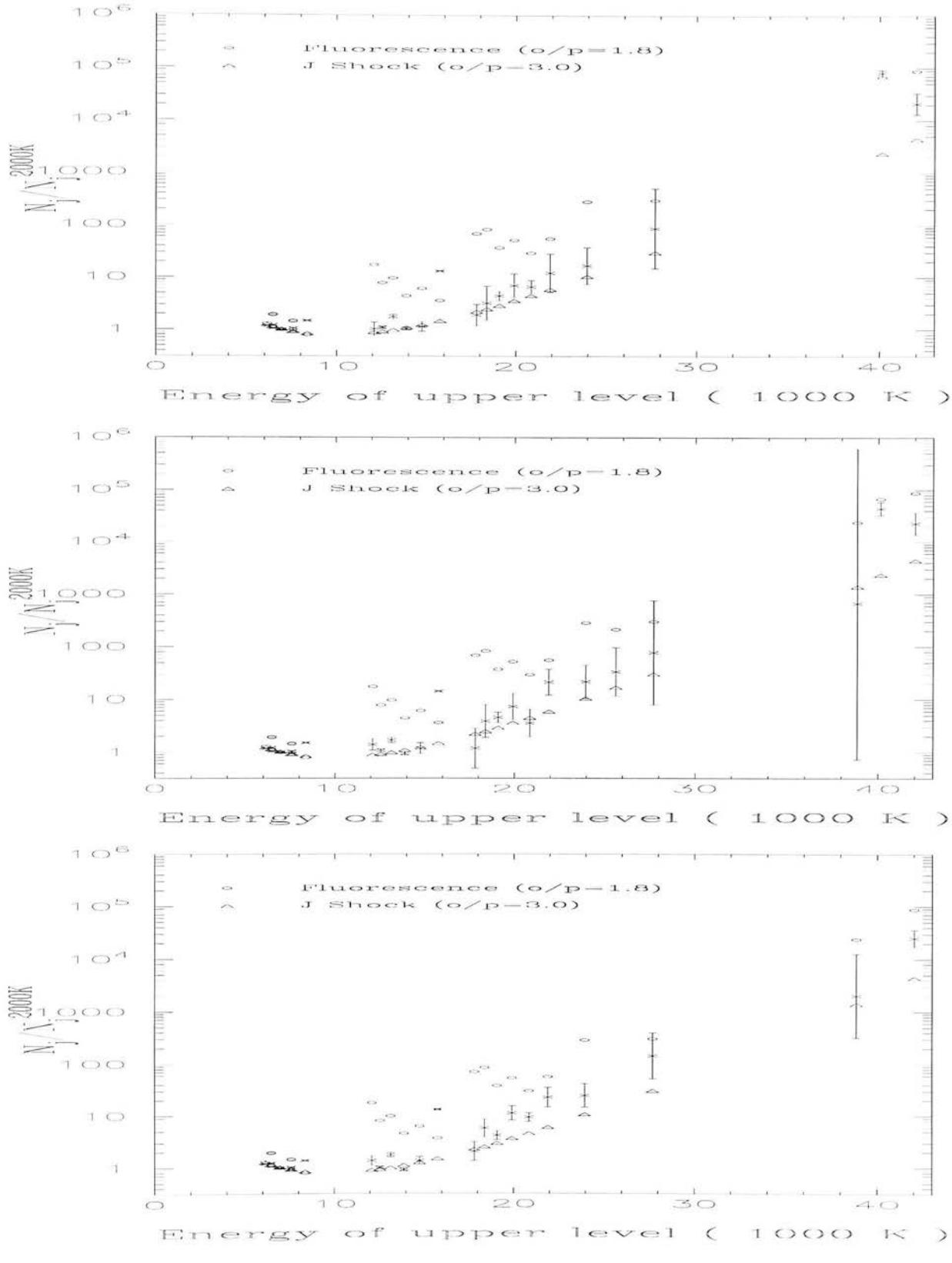


Figure 4.13: M42 HH126-053 - on wake CDR diagrams for rows 272,284 (top); 271,280 (middle); and 269,276 (bottom).

running along the axis indicated in Figure 4.2 for the M42 HH126-053 wake. As for M42 HH120-114, the excitation is quite closely matched at each position and follows a rather uniform curve which slightly steepens with increasing level energy. Just as before, neglecting the less reliable transitions, the scatter in data points about this smooth curve is minimised at the brightest wake positions where the relative background fluorescent contribution is smallest. Compared to the excitation in M42 HH120-114, however, we note systematically lower column densities in both the $v$=2 and 3 levels where the errors are small enough to facilitate comparison. The excitation here more closely resembles the pure J shock power-law cooling as fitted at OMC-1, suggesting lower pressure in such models. This is surprising given that the "bullet" associated with this wake is slightly faster than that associated with M42 HH120-114 (Chapter 3). However, M42 HH126-053 is situated at a larger radial distance from the densest BN-IRc2 region from which the "bullets" appear to emanate than M42 HH120-114. A lower ambient cloud density may therefore be responsible for this discrepancy. The fact that the excitation is relatively uniform within the wake is in agreement with M42 HH120-114 and suggests the same underlying mechanism in each case but with slightly different excitation conditions for each wake.

In Table 4.6 we present the associated 1-0 S(1)/2-1 S(1) excitation temperatures for these positions in M42 HH126-053, as shown in Figure 4.2. We here find that $T_{ex}$ remains constant within the errors of observation for all but the southernmost position (at which a second wake begins to overlap). The weighted mean value of $T_{ex}$ = 2065±4K is in close agreement to other shocked sources including OMC-1 and over 300K lower than the averaged background value. This constancy with position may reflect closely matched underlying $H_2$ intensities at these positions compared to M42 HH120-114, if we assume this to be the only significant factor affecting $T_{ex}$ (wake-only excitation mechanism is effectively constant).

We therefore conclude that although it is possible to fit composite bow shock + fluorescence models at any given individual position in the wakes, it is impossible to reconcile the near-constancy of the excitation with position in each individual wake with bow shock models. This is in agreement with our line profile observations. Unsurprisingly, in common with the profiles, the excitation appears to remain almost constant throughout each

| CGS4 Pixel Coords. (x,y) | $T_{ex}$ 1-0S(1)/2-1S(1) /K |
|---|---|
| 278,297 | 2055±18 |
| 276,293 | 2071±16 |
| 274,288 | 2059±21 |
| 272,284 | 2079±18 |
| 271,280 | 2064±14 |
| 269,276 | 2005±15 |

Table 4.6: Excitation temperature ($T_{ex}$) derived from the dereddened $H_2$ 1-0 S(1)/2-1 S(1) line ratio at the positions ($1.22\widehat{''} \times 1.22\widehat{''}$) centred at Allen & Burton (1993) image coordinates indicated in Figure 4.2 in the M42 HH126-053 $H_2$ wake.

wake suggesting a common underlying excitation mechanism, albeit with slightly different physical conditions in each case. The scatter in the CDR diagrams in the wakes can be explained by background and wake-only fluorescent components which are, however, relatively unimportant compared to collisional processes except for the most energetic $H_2$ levels. This is in contrast to the background $H_2$ level populations which are more strongly influenced by fluorescent excitation.

Alternatively, perhaps the scatter is a shock-related phenomenon unrelated to fluorescent processes. Perhaps shock inhomogeneities or some other neglected mechanism related to instabilities or supersonic turbulence produces the observed scatter, as speculated to explain the line profiles observed in Chapter 3. If enough dust grains survive passage of the shock front, perhaps re-formed $H_2$ could alter level populations. However, current theoretical models of $H_2$ re-formation predict a 1-0 S(1)/2-1 S(1) line ratio of ~2-3, for a range of densities $10^3$-$10^4 cm^{-3}$ and for shock speeds in the range 30-150km $s^{-1}$ (Hollenbach & McKee 1989). In contrast, the observed on-wake 1-0 S(1)/2-1 S(1) line ratios lie in the range 7.5 to 12.1. Hence any reformed $H_2$ should not have a significant effect on the observed fluorescent component.

Turbulence within downstream gas may cause mixing of the $H_2$ emitting sections so that a planar C shock approximation within the wake is invalidated since adjacent

emission sections must affect one another. Where the planar-element analysis is invalid (if the planar-shock thickness is much less than the overall bow size), then only three-dimensional numerical simulations can model the bows and associated $H_2$ line emission (Smith *et al.* 1991a). However, the predicted $H_2$ spectrum has not been modelled in detail although work is in progress (J. Stone, *Private Communication*).

### 4.5.4 Summary

We have confirmed our discovery in Chapter 3 of the existence of a near-constant background excitation mechanism pervading the entire Orion "bullets" region. The background $H_2$ emission can be modelled by a combination of fluorescent and shock excited mechanisms, in agreement with the broad $H_2$ line profiles observed in Chapter 3. It is thermalized in the $v$=1 levels but higher levels are dominated by fluorescence. Measurement of the $H_2$ excitation in the "bullet" wakes M42 HH126-053 and M42 HH120-114 shows a near constant emission spectrum, within each wake, that may be modelled by a combination of shocked and fluorescent excitation, now more strongly dominated by collisional processes but also containing an intrinsic wake-only fluorescent component. The column density ratios clearly show a range of gas temperatures as expected for cooling, post-shock gas. Furthermore, the uniformity of these ratios on small-scales (these observations) and also on large scales (Brand *et al.* 1989b), contradicts combinations of fundamentally different types of shock. However, the near constancy of this excitation with position *within* each individual wake is inconsistent with bow C shock models previously fitted at OMC-1, in which significantly different line ratios occur depending on the shock velocity which varies in the bow.

It might be possible to reproduce the observed spectrum if we are not resolving multiple shock fronts accelerated to a range of velocities by some mechanism other than the shock (Brand *et al.* 1989b) within each CGS4 pixel and there is a significant fluorescent background contribution. It is then necessary to explain the bow-shaped $H_2$ wake morphology. Alternatively, the effects of instabilities and turbulence may be dominating the $H_2$ level populations measured.

# Chapter 5

# Conclusions and Future Work

## 5.1 Summary of Results and Implications

The nature of molecular shocks is still uncertain. In Chapter 1 we outlined the importance of outflows as an integral part of the star forming process and demonstrated that the molecular shocks caused by the impact of such outflows with the ambient gas play a crucial role in the processes of momentum and energy transfer. We identified molecular hydrogen as the dominant constituent (by mass) in such molecular clouds and in Chapter 2 we described the unique properties of $H_2$ which allow us to directly probe these molecular shocks. The basic features of the competing models of shock excitation were then outlined and previous observations reviewed to demonstrate our current understanding and the outstanding problems to be addressed. Finally, a review of the near-infrared observational techniques required to study shocked $H_2$ and $Fe^+$ line emission was presented.

In Chapter 3 we identified the Orion star forming molecular cloud as the primary test-bed for such studies due to the brightness and proximity of the shocked molecular emission associated with it. In this thesis we have made the first measurements of the excitation and dynamics of molecular hydrogen in the bow-shaped wakes associated with the recently discovered Orion $Fe^+$ "bullets". We have demonstrated that integrated [FeII] 1.644$\mu$m line profiles in the Orion "bullets" are consistent with theoretical bow-shock

predictions and derived velocities and orientations of the "bullets" M42 HH126-053 and M42 HH120-114.

We have identified a uniform, broad background component pervading the Orion "bullets" region in both $Fe^+$ and $H_2$ tracers that is not consistent with a fluorescent component due to the ionizing radiation of the Trapezium stars alone. A collisionally broadened background component of unidentified origin is measured to have a near-constant intrinsic FWHM of $26\pm2.5\mathrm{km\,s^{-1}}$ in the $H_2$ 1-0 S(1) line and a constant peak velocity of $2.5\pm0.5\mathrm{km\,s^{-1}}$ , close to the local ambient rest velocity. The range of velocities, although significantly smaller than observed in the wakes, rules out a single planar J shock model or fluorescent emission alone which is characterised by intrinsically narrow, unresolved line profiles. Bow shock models are also ruled out, unless multiple and unresolved, given that the profile is always singly peaked. It may be possible to fit a highly magnetised planar C shock model, or else it will be necessary to model the effects of instabilities and turbulence. In Chapter 4 we found a near-constant background $H_2$ excitation spectrum that it is possible to model with a combination of fluorescent and shock excited mechanisms, in agreement with the broad $H_2$ line profiles observed in Chapter 3. This implies the collisional excitation mechanism and physical conditions throughout the region observed must remain almost constant at the $\sim1''$ resolution of these observations. The $H_2$ level populations are thermalized in the $v$=1 levels but higher levels are dominated by fluorescent excitation.

The extended $H_2$ "bullet" wakes have the appearance of limb-brightened bow shocks and so allowed us to dissect individual molecular bow shock structures for the first time in Orion. However, the broad, singly-peaked $H_2$ 1-0 S(1) profiles observed in the two most clearly resolved wakes associated with the "bullets" M42 HH126-053 and M42 HH120-114, oriented quite close to the plane-of-sky, challenge our present understanding. After subtraction of the averaged background component, we measure a broad, smooth profile well-fitted by a single Gaussian profile having an intrinsic FWHM that varies from $\sim26\mathrm{km\,s^{-1}}$ near the head of the wakes down to $\sim10\mathrm{km\,s^{-1}}$ near the tail. The peak velocity of the profiles is slightly shifted by up to $8\mathrm{km\,s^{-1}}$ from the background component with the maximum shift occurring at the head of each wake. In M42 HH126-053 the peak shift is blueshifted, whereas in the M42 HH120-114 wake the peak shift is

to the red. In addition to the main peak however, we find additional but much weaker velocity components that lie over the full velocity range of up to 150km s$^{-1}$ measured in the M42 HH126-053 $Fe^+$ "bullet". The peak shift and velocity width of these weak components is a maximum at the tips of the wakes, coincident with the "bullet" positions.

It is very difficult to reconcile *any* steady-state bow shock model with these observations in Orion. To fit a single C shock absorber model to individual profiles implies a magnetic field strength far in excess of observed estimates and is not consistent with the bow-shaped wake morphology. Measurement of the $H_2$ excitation in the "bullet" wakes M42 HH126-053 and M42 HH120-114 shows a near constant emission spectrum, within each wake, that may be modelled by a combination of shocked and fluorescent excitation, now more strongly dominated by collisional processes but also containing an intrinsic wake-only fluorescent component. The column density ratios clearly show a range of gas temperatures as expected for cooling, post-shock gas. Furthermore, the uniformity of these ratios on small-scales (these observations) and also on large scales at OMC-1 (Brand *et al.* 1989b), contradicts combinations of fundamentally different types of shock. However, the near constancy of this excitation with position *within* each individual wake is inconsistent with bow C shock models previously fitted at OMC-1, in which significantly different line ratios occur depending on the shock velocity which varies in the bow.

The detection of weak but extremely high velocity ($\lesssim$ -105km s$^{-1}$ ) $H_2$ emission features at positions close or coincident with the $Fe^+$ "bullet" emission in both wakes is inexplicable with any steady state molecular shock models unless we are not resolving multiple shock fronts along the line-of-sight. However, peak velocity of the individual features identified in M42 HH126-053 clearly moves closer to the main emission peak in moving down the wakes and so appears to be associated with the "bullets". It may be that $H_2$ reforming over the full range of velocities observed in the "bullets" is subsequently fluoresced by strong UV emission from the "bullets" themselves.

Alternatively, we may still not be resolving multiple shock fronts along the line-of-sight. For example, multiple overlapping bullet wakes could give rise to merged sets of doubly-peaked profiles resulting in approximately Gaussian shaped profiles. However,

given the appearance of single bow shaped wakes at many observed positions, the accuracy of Gaussian-shaped line-fits, the velocity resolution of our observations and that we see this phenomenon in *two* different wakes, this explanation is expected to be excluded. Or we are not resolving multiple shock fronts accelerated to a range of velocities by some mechanism other than the shock within each CGS4 pixel and there is a significant fluorescent background contribution. It remains possible that the scatter observed in the "bullet" wake $H_2$ level populations is a shock-related phenomenon unrelated to fluorescent processes. Perhaps shock inhomogeneities or some other neglected mechanism related to instabilities or supersonic turbulence produces the observed scatter, as speculated to explain the line profiles observed in Chapter 3. If enough dust grains survive passage of the shock front, perhaps re-formed $H_2$ could alter level populations. However, current theoretical models of $H_2$ re-formation predict a 1-0 S(1)/2-1 S(1) line ratio of ~2-3, for a range of densities $10^3$-$10^4 cm^{-3}$ and for shock speeds in the range 30-150km $s^{-1}$ (Hollenbach & McKee 1989). In contrast, the observed on-wake 1-0 S(1)/2-1 S(1) line ratios lie in the range 7.5 to 12.1, in agreement with other shocked sources. Hence any reformed $H_2$ should not have a significant effect on the observed fluorescent component.

Turbulence within downstream gas is likely to cause mixing of the $H_2$ emitting sections so that a planar C shock approximation within the wake is invalidated since adjacent emission sections must affect one another. However, the predicted $H_2$ spectrum has not yet been modelled in detail. Stone *et al.* (1995) were able to reproduce the observed morphology of the Orion "bullets" region by modelling two-dimensional, time-dependent numerical simulations of the fragmentation of a dense shell swept up by a poorly collimated, time-variable stellar wind. The "bullets" condense *in situ* within the high-velocity gas via Rayleigh-Taylor instabilities. The model predicts that the shell within the fingers (OMC-1 region) will be highly clumpy, now confirmed by spectroscopic imaging (McCaughren & Mac Low, *in press*), but that the $H_2$ wakes should be modelled by bow shocks. Schild *et al.* (*in press*), however, contend that instabilities in the thin layer of rapidly cooling radiative shocks created by the interaction of a stellar wind colliding with surrounding dense molecular material may be more important than Rayleigh-Taylor instabilities.

We note that individual column densities within the wakes can be modelled by in-

ferring fluorescence and a full range of bow C shock excitation conditions or a simple J shock power law cooling function. But the latter model poses severe theoretical problems as a J shock should only exist under these conditions if the magnetic field is unreasonably low ($B \leq 10\mu G$), or if the ionization fraction is unreasonably high. We expect fields of at least 1mG, which must have an important effect on the dynamics and necessitate a multi-fluid model. This model also assumes that $H_2$ is the dominant coolant, in contrast to chemical studies indicating that OH and $H_2O$ may significantly alter the emission spectrum.

Alternatively, we are left with the possibility that some important process in molecular physics or chemistry has been overlooked. For example, in low-fractional ionization gas such as in Orion, the dust grains play an important (but complicated) role in the dynamics (McKee & Draine 1991 and references therein). Given that high velocity molecular gas is clearly present, there are two possibilities to explain its formation. Either the molecules are formed or already present in the outflowing material or the molecules trace environmental material that has been entrained into the high velocity outflow (Raga and Canto 1996). The first possibility was explored by Rawlings, Williams and Cantó (1988) and by Glassgold, Mamon and Huggins (1989) who find that it is only possible to form molecules in a wind from a T Tauri star if the associated mass loss rate has values of $\dot{M} > 10^{-6} M_{\odot} yr^{-1}$, which might be rather high for outflows from some young stars. In the second scenario, the problem to be solved is how to entrain and accelerate molecular material to velocities comparable to the outflow velocity without dissociating the molecules.

## 5.2 Future Work

In order to model the detailed $H_2$ emission observed in the Orion "bullet" wakes it will be necessary to fit a multiple component model incorporating both foreground and background shock and fluorescent excitation mechanisms having variable ortho-to-para ratio and a range of physical parameters including magnetic field, density and the degree of ionization. In particular, a detailed two temperature component fit at each position will yield model-independent information about any small variations with position in

the wakes. For example, if the wake-only fluorescent excitation mechanism is directly associated with the "bullets" then this contribution will decrease with distance away from the "bullets". Our observations constrain such variations to be small, however.

To further our general understanding of $H_2$ emission in molecular shocks requires a number of observational and theoretical tasks. Observational work will continue to be driven by technological improvements resulting in higher spatial and spectral resolution near and mid-infrared spectroscopy and imaging of a range of shocked sources including Orion. We have begun a program utilising a new adaptive optics near-IR imaging instrument ADONIS mounted on the 3.6m ESO telescope. The significantly increased spatial resolution possible with this instrument should enable diffraction limited resolution of $\sim 0.14''$ which corresponds to a lengthscale of $\sim 10^{15}$cm at the distance of Orion. Since the shortest cooling lengths predicted in any shock models are of order $10^{16}$cm in C shocks and considerably less for J shocks, it will be possible to eliminate certain C shock models. However, this method is limited by the fact that the region imaged must lie within $\sim 20''$ of a suitable, optically visible star - a tall order in dense star forming regions. The NICMOS infrared imaging camera, to be fitted to HST in the next year, will dramatically improve spatial resolution obtainable in any source since it will be situated above the Earth's atmosphere.

Another program is now underway to repeat the same kind of detailed measurements of $H_2$ velocities and line intensities performed in this work, utilising the greatly increased sensitivity and resolution of CGS4 with the new array, in a range of other bright sources including HH7-11 and DR21. In particular, HH7-11 is perhaps the most clearly defined and bright individual bow-shaped source of this type and the detailed C shock + fluorescence model fitted to the brightest positions by Fernandes & Brand (1995) can be tested rigorously by searching for variations with position over the entire bow. K band spectra in this region are also free of the strong nebular emission observed throughout Orion. It should be possible to unambiguously detect unresolved fluorescent emission lines from the highest excitation energies where the model fitted predicts a negligible contribution from collisional excitation. Furthermore, it is important to test our understanding of shocked $H_2$ excitation in a range of conditions found in the interstellar medium. HH7-11 is situated in a low-mass star forming region in contrast to the massive clouds associated

with Orion and DR21. It is interesting that Davis *et al.* (1996b) observe $H_2$ 1-0 S(1) emission in the brightest positions in the DR21 outflow lobes that is generally dominated by a broad, singly-peaked line profile. Similar profiles are seen again in the observations by Richter *et al.* (1995c) of the supernova remnant IC443. More importantly, they also measure an $H_2$ excitation spectrum (Richter *et al.* 1995b) that matches the OMC-1 spectrum quite closely and suggests a common underlying model may be applicable in each case. It is speculated that the role of instabilities and/or supersonic turbulence may be significant.

McKee & Draine (1991) describe the significant differences seen in predictions of the relative strengths of $H_2O$ lines between C and J type models, with relatively stronger higher excitation lines in the C shocks. The recently launched ISO satellite will now hopefully begin to provide the observations to test this. The greater sensitivity and uniformity of optical CCD spectroscopy will enable observations of the optical transitions of $H_2$ , guided by high resolution infrared images, although these lines are weaker and the extinction at optical wavelengths is correspondingly higher. Ultimately, the observation of mid-infrared $H_2$ transitions from the ground (Michelle) and space (ISO and its successors) will be important. The next major increase in available spatial and spectral resolution that is likely to test models in more detail in Orion will be the 8m Gemini telescopes at the turn of the Century.

The most urgent theoretical work required is to investigate the emission from magnetic precursors and from unstable magnetic and non-magnetic shocks as these represent the remaining areas of the process not yet fully investigated. It is also necessary to further investigate turbulent boundary layers (e.g. Malone, Dyson & Hartquist 1994) in the context of new developments in non-linear C-shock instability growth (Wardle 1991) and the bow structures currently used to explain velocity profiles in sources such as HH7-11. The models must predict $H_2$ line intensities as determined for a range of parameter space in magnetic field, density, degree of ionization and so on. Where planar-element analysis is invalid (if the planar-shock thickness is much less than the overall bow size), then only three-dimensional numerical simulations can model the bows and associated $H_2$ line emission (Smith *et al.* 1991).

In the long term we wish to relate the high energy processes exciting $H_2$ , as traced by the shocking of molecular clouds by protostellar outflow and fluorescent $H_2$ emission near to massive young stars, to the primordial star formation process. Locally, we must investigate further the missing link between shocks in outflows and the drivers of the winds or jets, often intermittent, observed in sub-mm protostellar sources. On extra-galactic scales, it is necessary to constrain shock and PDR emission from high redshift galaxies in which, for example, elemental abundances will be different. This is of fundamental importance in understanding galactic evolution including actively star forming galaxies, where large $H_2$ fluxes are measured, and the relative contributions of shocked and fluorescent excitation at given positions can be related to detailed studies of individual sources in our own Galaxy. This thesis shows that we still have some way to go before we can say we understand molecular shocks but that the large number of sources now being analysed and the pace of technological improvements in near-infrared instrumentation auger well for the future of this work. It is to be hoped that the corresponding theoretical work required will match this pace of development.

# References


Abgrall H., Roueff E., 1989, A&AS, 79, 313

Allen D.A., Burton M.G., 1993, Nat, 363, 54

André P., 1995, Ap&SS, 224, 29

André P., Ward-Thompson D.W., Motte F., 1996, A&A, *in press*

Axon D.A., Taylor K., 1984, MNRAS, 207, 241

Balbus S.A., 1986, ApJ, 303, L79

Bally J., Lada C.J., 1983, ApJ, 265, 824

Bastien P., Bieging J., Henkel C., Martin R.N., Wamsley C.M., Wilson T.L., Ziurys L.M., Pauls T., 1981, A&A, 98, L4

Beckwith S., Persson S.E., Neugebauer G., Becklin E.E., 1978, ApJ, 223, 464

Beckwith S., Persson S.E., Neugebauer G., 1979, ApJ, 227, 436

Beckwith S., Evans N.J., Gatley I., Gull G., Russell R.W., 1983, ApJ, 264, 152

Black J.H., 1978, ApJ, 222, 125

Black J.H., Dalgarno A., 1976, ApJ, 203, 132

Black J.H., van Dishoeck E., 1987, ApJ, 322, 412

Brand P.W.J.L., Moorhouse A., Burton M.G., Geballe T.R., Bird M., Wade R., 1988, ApJ, 334, L103

Brand P.W.J.L., Toner M.P., Geballe T.R., Webster A., Williams P.M., Burton M.G., 1989a, MNRAS, 236, 929

Brand P.W.J.L., Toner M.P., Geballe T.R., Webster A., 1989b, MNRAS, 237, 1009

Burke J.R., Hollenbach D.J., 1980, NASA Tech. Memo 81163. Ames Res. Cent

Burton M.G., 1986, PhD Thesis, Univ. of Edinburgh

Burton M.G., Brand P.W.J.L., Moorhouse A., Geballe T., 1988, Proc. 22nd Eslab Symposium on IR spectroscopy in astronomy, ESA SP-290

Burton M.G., Brand P.W.J.L., Geballe T.R., Webster A.S., 1989, MNRAS, 236, 409

Burton M.G., Hollenbach D.J., Tielens A.G., 1990b, ApJ, 365, 620

Burton M.G., Hough J.H., Axon D.J., Hasegawa T., Tamura M., 1988, MNRAS, 235, 161

Burton M.G., Puxley P.J., 1990, *The Interstellar Medium in External Galaxies: Summaries of Contributed Papers*, ed. D. Hollenbach & H. Thronson, NASA CP, 3084, 238

Burton M.G., Geballe T.R., Brand P.W.J.L., Moorhouse A., 1990a, ApJ, 352, 625

Burton M.G., 1992, Aust. J. Phys., 45, 463

Cantó J., Rodriguez L.F., Barral J.F., Barral P., 1981, ApJ, 244, 102

Carr J., 1993, ApJ, 406, 553

Carruthers G.R., 1970, ApJ, 161, L81

Chernin L.M., Wright M.C.H., ApJ, 467, 676

Chernoff D.F., 1987, ApJ, 312, 143

Chernoff D.F., McKee C.F., Hollenbach D.J., 1982, ApJ, 259, 97

Chevalier R.A., 1980, *Astrophysical Letters*, 21, 57

Chrysostomou A., 1992, PhD Thesis, Univ. of Edinburgh

Chrysostomou A., Brand P.W.J.L., Burton M.G., Moorhouse A., 1992, MNRAS, 256, 528

Chrysostomou A., Hough J.H., Burton M.G., Tamura M., 1994, MNRAS, 268, 325

Dabrowski I., Herzberg G., 1984, Can. J. Phys., 62, 1639

Davis C.J., Eisloeffel J., Smith M.D., 1996, ApJ, 463, 246

Davis C.J., Smith M.D., 1996a, A&A, 309, 929

Davis C.J., Smith M.D., 1996b, A&A, 310, 961

Davis C.J., Smith M.D., 1995, ApJ, 443, L41

Draine B.T., 1980, ApJ, 241, 1021

Draine B.T., 1988, in *Interstellar Extinction in the Infrared*, 22nd Eslab Symposium on Infrared Spectroscopy in Astronomy, ESA SP-290, 93

Draine B.T., Roberge W.G., 1982, ApJ, 259, L91

Draine B.T., Roberge W.G., Dalgarno A., 1983, ApJ, 264, 485

Draine B.T., McKee C.F., 1993, Ann. Rev. Astron. Astrophys., 31, 373

Duley W.W., Williams D.A., 1986, MNRAS, 223, 177

Elmegreen B.G., 1985a,in *Protostars and Planets II* , ed. D. Black and M. Matthews (Tucson: University of Arizona Press), p. 33.

Elmegreen B.G., 1985b, ApJ, 299, 196

Elmegreen B.G., 1989, ApJ, 338, 178

Fernandes A.J.L., 1993, *PhD Thesis*

Fernandes A.J.L., Brand P.W.J.L., 1995, MNRAS, 274, 639

Field G.B., 1965, ApJ, 142, 531

Field G.B., Saslaw W.C., 1965, ApJ, 142, 568

Field G.B., Sommerville W.B., Dressler K., 1966, ARAA, 4, 207

Fleck R.C., 1988, ApJ, 328, 299

Flower D., Watt G., 1984, MNRAS, 209, 25

Franco J., Cox D.P., 1983, ApJ, 273, 243

Garden R.P., Russell A.P., Burton M.G., 1990, ApJ, 354, 232

Gatley I., Hasegawa T., Suzuki H., Garden R.P., Brand P.W.J.L., Lightfoot J., Glencross W., Okuda H., Nagata T., 1987, ApJ, 318, L73

Gautier T.N., Fink U., Larson H.P., 1976, ApJ, 207, L129

Genzel R., Stutzki J., 1989, ARAA, 27, 41

Glassgold A.E., Mamon G.A., Huggins P.J., 1989, ApJ, 336, L29

Goldreich P., Kwan J., 1974, ApJ, 189, 441

Goldsmith P.F., Plambeck R.L., Chiao R.Y., 1975, ApJ, 196, L39

Goodman F.O., 1978, ApJ, 226, 87

Grasdalen G.L., Joyce R.R., 1976, Bull. A.A.S, 8, 349

Gredel R., Dalgarno A., 1995, ApJ 446, 852

Habing H.J., 1968, *Bull. Ast. Inst. Netherlands*, 19, 421

Hartigan P., Carpenter J.M., Dougados C., Skrutskie M.F., 1996, AJ, 111, 1278

Hartigan P., Curiel S., Raymond J., 1989, ApJ, 347, L31

Hartigan P., Raymond J., Hartmann L., 1987, ApJ, 316, 323

Hartmann, L., Kenyon S.J., 1985, ApJ, 299, 462

Hartmann, L., Hewett R., Stahler S., Mathieu R.D., 1986, ApJ, 309, 275

He L., Whittet D.C.B., Kilkenny D., Spencer Jones J.H., 1995, ApJ Supplement, 101, 335

Heiles C., Goodman A.A., McKee C.F., Zweibel E.G., 1993, in *Protostars and Planets III* , ed. E.H. Levy and J.I. Lunine (Tucson: University of Arizona Press), p. 279.

Herzberg G., 1950, *Spectra of Diatomic Molecules.*, van Nostrand Reinhold, New York, pp658

Hirasawa T., 1969, Prog. Theor. Phys., 42, 523

Ho P.T.P., Barrett A.H., 1978, ApJ, 224, 223

Hollenbach D.J., McKee C.F., 1979, ApJ Suppl., 41, 553

Hollenbach D.J., McKee C.F., 1989, ApJ, 342, 306

Hollenbach D.J., Salpeter E.E., 1970, J. Chem. Phys., 53, 79

Hollenbach D.J., Salpeter E.E., 1971, ApJ, 163, 155

Hollenbach D.J., Shull J.M., 1977, ApJ, 216, 419

Hollenbach D.J., Chernoff D.F., McKee C.F., 1988, Proc. 22nd Eslab Symposium on IR spectroscopy in astronomy, ESA SP-290

Huber J.P., Herzberg G., 1979, *Constants of Diatomic Molecules*, van Nostrand, New York

Hutchins J.B., 1976, ApJ, 205, 103

Karpas Z., Anieieh V., Huntress W.T., 1979, J. Chem. Phys., 70, 2877

Kwan J., 1977, ApJ, 216, 713

Kwan J., Scoville N.Z., 1976, ApJ, 210, L39

Lada C.J., 1985, Ann. Rev. Ast. and Astrophys., 23, 267

Lada C.J., 1991, in *The Physics of Star Formation and Early Stellar Evolution* , eds. C.J. Lada & N.D. Kylafis, kluwer, p.329

Landau L.D., Lifshitz E.M., 1959a, Fluid Dynamics, Pergamon, Oxford

Landau L.D., Lifshitz E.M., 1959b, Statistical Physics, Pergamon, Oxford

Larson R.B., 1969, MNRAS, 145, 271

Larson R.B., 1981, MNRAS, 194, 809

Lepp S., McCray R., 1983, ApJ, 269, 560

London R., McCray R., Chu S., 1977, ApJ, 217, 442

Luhman M.L., Jaffe D.T., Keller L.D., Soojong Pak, 1994, ApJ, 436, L185

Luhman M.L., Jaffe D.T., 1996, ApJ, 463, 191

Lynden-Bell D., Pringle J.E., 1974, MNRAS, 168, 603

Maloney P., 1988, ApJ, 334, 761

Mandy M.E., Martin P.G., 1993, ApJS, 86, 199

Margulis M., Lada C.J., Snell R.L., 1988, ApJ, 333, 316

Mathis J.S., Rumpl W., Nordseick K., 1977, ApJ, 217, 425

Mathis J.S., 1990, ARAA, 28, 37

McCaughrean M.J., O'Dell C.R., 1996, AJ, 111, 1977

McKee C.F., 1989, ApJ, 345, 782

McKee C.F., Hollenbach D.J., 1980, ARAA, 18, 219

McKee C.F., Draine B.T., 1991, Science, 252, 397

Mestel L., Spitzer L., 1956, MNRAS, 116, 502

Moorhouse A., Brand P.W.J.L., Geballe T.R., Burton M.G., 1990, MNRAS, 242, 88

Mountain C.M., Selby M.J., Leggett S.K., Blackwell D.E., Petford A.D., 1985, A&A, 151, 399

Mountain C.M., Robertson D., Lee T., Wade R., 1990, *"An advanced cooled grating spectrometer for UKIRT"*, SPIE Symposium on Astronomical Telescopes and Instrumentation for the 21st Century, Tucson

Mouschovias T.C., 1991, in *The Physics of Star Formation and Early Stellar Evolution*, eds. Lada C.J., Kylafis N.D. (Kluwer), p. 449

Mundy L.G., Cornwell T.J., Masson C.R., Scoville N.Z., Baath L.B., Johansson L.E.B., 1988, ApJ, 325, 382

Myers P.C., 1985, in *Protostars and Planets II* , ed. D. Black and M. Matthews (Tucson: University of Arizona Press), p. 81.

Nadeau D., Geballe T.R., 1979, ApJ, 230, L169

Nadeau D., Geballe T.R., Neugebauer G., 1982, ApJ, 253, 154

Nakano T., 1984, in *Fundamental Cosmic Physics* , 9, 139

Norman C., Silk J., 1980, ApJ, 238, 158

Nussbaumer H., Storey P.J., 1988, A&A, 193, 327

O'Dell C.R., 1995, *Rev Mex A A (Serie de Conferencias)*, 1, 11

O'Dell C.R., Valk J.H., Wen Zheng, Meyer D.M., 1993, ApJ, 403, 678

O'Dell C.R., Wen Zheng, Hu Xihai, 1993, ApJ, 410, 696

O'Dell C.R., Wen Zheng, 1994, ApJ, 436, 194

O'Dell C.R., Wong Kwan, 1996, AJ, 111, 846

Ossenkopf V., Henning TH., 1994, A&A, 291, 943

Outred M., 1978, *J. Phys. Chem. Ref. Data*, 7, 81

Puxley P.J., Beard S.M., Ramsay S.K., 1992, *Proc. "Fourth Data Analysis Workshop"*, ESO/STECF, *ed.* Grosbol, P.

Raga A.C., Cantó J., 1996, submitted to Leiden conf. proceedings

Ramsay S.K., Mountain C.M., Geballe T.R., 1992, MNRAS, 259, 751

Rawlings J.M.C., Williams D.A., Cantó J., 1988, MNRAS, 230, 695

Ray T.P., Mundt R., Dyson J.E., Falle S.A.E.G., Raga A.C., 1996, ApJ, 468, L103

Rayner J., Hodapp K., Zinnecker H., 1991, *Astrophysics with Infrared Arrays*, ASP Conference Series, ed. R. Elston, 14

Rieke G.H.,Low F.J., Kleinmann D.E., 1973, ApJ, 186, L7

Richter M.J., Graham J.R., Wright G.S., 1995a, ApJ, 449, L83

Richter M.J., Graham J.R., Wright G.S., 1995b, ApJ, 454, 277

Roberge W.G., Dalgarno A., 1982, ApJ, 255, 176

Roberge W.G., Draine B.T., 1990, ApJ, 350, 700

Scalo J.M., Pumphrey W.A., 1982, ApJ, 258, L29

Scoville N., Hall D.N.B., Kleinmann S.G., Ridgway S.T., 1982, ApJ, 253, 136

Scoville N., Kleinmann S.G., Hall D.N.B., Ridgway S.T., 1983, ApJ, 275, 201

Shapiro P.R., Kang H., 1987, ApJ, 318, 32

Shortridge K., 1991, *FIGARO - General Data Reduction and Analysis"*

Shu F.H., 1977, ApJ, 214, 488

Shu F.H., 1987, in *Star Formationin Galaxies* , ed. C. Persson (Conference Publication 2466)(Washington: NASA OSSA), p. 743

Shu F.H., Adams F.C., Lizano S., 1987, ARAA, 25, 23

Shu F.H., 1991, *The Physics of Astrophysics Volume I: Radiation*, University Science Books, pp.341

Shull J.M., Beckwith S., 1982, ARAA, 20, 163

Shull J.M., Hollenbach D.J., 1978, ApJ, 220, 525

Silk J., Norman C., 1983, ApJ, 272, L49

Smith M.D., 1995, A&A, 296, 789

Smith M.D., 1994, MNRAS, 266, 238

Smith M.D., 1994, ApJ, 421, 400

Smith M.D., 1994, A&A, 289, 256

Smith M.D., 1993, ApJ, 406, 520

Smith M.D., 1992, ApJ, 390, 447

Smith M.D., 1991b, MNRAS, 253, 175

Smith M.D., 1991a, MNRAS, 252, 378

Smith M.D., 1989, MNRAS, 238, 235

Smith M.D., Brand P.W.J.L., 1990a, MNRAS, 242, 495

Smith M.D., Brand P.W.J.L., 1990b, MNRAS, 243, 498

Smith M.D., Brand P.W.J.L., 1990c, MNRAS, 245, 108

Smith M.D., Brand P.W.J.L., Moorhouse A., 1991a, MNRAS, 248, 451

Smith M.D., Brand P.W.J.L., Moorhouse A., 1991b, MNRAS, 248, 730

Smoluchowski R., 1981, ApSS, 75, 353

Snell R.L., Loren R.B., Plambeck R., 1980, ApJ, 239, L17

Solf J., Böhm K.H., 1987, AJ, 93, 1172

Soloman P.M., Sanders D.B., Rivolo A.R., 1985, ApJ, 292, L19

Soloman P.M., Rivolo A.R., Barrett J., Yahil A., 1987, ApJ, 319, 730

Spitzer L., Drake J.F., Jenkins E.B., Morton D.C., Rogerson J.B., York D.G., 1973, ApJ, 181, L116

Spitzer L., 1979, *Physical Processes in the Interstellar Medium* , Wiley, New York

Sternberg A., Dalgarno A., 1989, ApJ, 338, 197

Stone J.M., Xu J., Mundy L.G., 1995, Nat, 377, 315

Stutzki J., Genzel R., Harris A.I., Herman J., Jaffe D.T., 1988, ApJ, 330, L125

Suttner G., Smith M.D., Yorke H.W., Zinnecker H., 1996, submitted to A&A

Tedds J.A., Brand P.W.J.L., Burton M.G., Chrysostomou A., Fernandes A.J.L., 1994, in "Clouds, Cores and Low Mass Stars", ASP Conference Series, eds D.P. Clemens and R. Barvainis, 65, 375

Tedds J.A., Brand P.W.J.L., Burton M.G., Chrysostomou A., Fernandes A.J.L., 1995a, ApSS, 224, 139, "Circumstellar Matter" Conference, Edinburgh

Tedds J.A., Brand P.W.J.L., Burton M.G., Chrysostomou A., Fernandes A.J.L., 1995b, ApSS, 233, 39, "Shocks in Astrophysics", UMIST, ed. T. Millar

Tegmark M., Silk J., Rees M.J., Blanchard A., Abel T., Palla F., astro-ph/9603007, *in press*

Tóth G., Draine B.T., 1993, ApJ, 413, 176

Tóth G., 1994, ApJ, 425, 171

Tóth G., 1995, MNRAS, 274, 1002

Treffers R.R., Fink U., Larson H.P., Gautier T.N., 1976, ApJ, 209, 793

Turner J., Kirby-Docken K., Dalgarno A., 1977, ApJ *Suppl.*, 35, 281

Vogel S.N., Kuhi L.V., 1981, ApJ, 245, 960

Vogel S.N., Bieging J.H., Plambeck R.L., Welch W.J., Wright W.J., 1985, ApJ, 296, 600

Wardle M., Draine B.T., 1987, ApJ, 321, 321

Wardle M., 1990, MNRAS, 246, 968

Wardle M., 1991a, MNRAS, 250, 523

Wardle M., 1991b, MNRAS, 251, 119

Watson W.D., 1976, *Rev. Mod. Phys.*, 48, 513

Watson D.M., Genzel R., Townes C.H., Storey J.W.V., 1985, ApJ, 298, 316

Wen Zheng, O'Dell C.R., 1993, ApJ, 409, 262

Wen Zheng, O'Dell C.R., 1995, ApJ, 438, 784

White G.J., Avery L.W., Richardson K.J., Lesurf J.C.G., 1986, ApJ, 302, 701

Whittet D., 1988, in *Dust in the Universe*, ed. M.E. Bailey & D.A. Williams, Cambridge University Press, 25

Whitworth A., 1979, MNRAS, 186, 59

Wiseman J.J., Ho P.T.P., 1996, Nat, 382, 139

Wolfire C., Königl A., 1991, ApJ, 383, 205

Wright M.C.H., Plambeck R.L., Wilner D.J., 1996, ApJ, 469, 216

Wynn-Williams C.G., Genzel R., Becklin E.E., Downes D., 1984, ApJ, 281, 172

Yoneyama T., 1972, *Publ. Astr. Soc. Jpn.*, 24, 87

Zuckerman B., Evans N.J., 1974, ApJ, 192, L149

Zuckerman B., Palmer P, 1974, ARAA, 12, 279

Zuckerman B., Kuiper T.B.H., Rodriguez Kuiper E.N., 1976, ApJ, 209, L137